

STUDY OF LASER INDUCED COHERENT PHENOMENA
IN THE RUBIDIUM ATOMIC MEDIUM

By

Arpita Das

PHYS05201504017

Saha Institute of Nuclear Physics, Kolkata

*A thesis submitted to the
Board of Studies in Physical Sciences
In partial fulfillment of requirements
for the Degree of*

DOCTOR OF PHILOSOPHY

of

HOMI BHABHA NATIONAL INSTITUTE

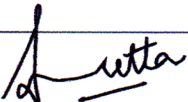
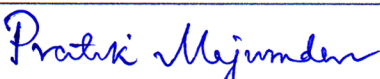
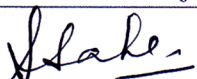
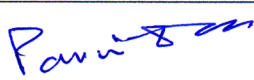


October, 2020

Homi Bhabha National Institute

Recommendations of the Viva Voce Committee

As members of the Viva Voce Committee, we certify that we have read the dissertation prepared by **ARPITA DAS** entitled “**STUDY OF LASER INDUCED COHERENT PHENOMENA IN THE RUBIDIUM ATOMIC MEDIUM**” and recommend that it may be accepted as fulfilling the thesis requirement for the award of Degree of Doctor of Philosophy.

Chairman	 Prof. Nayana Majumdar	Date 23/02/2021
Guide/Convener	 Prof. Sankar De	Date 23/2/2021
Co-guide (if any)		Date
Examiner	 Prof. Sourav Dutta	Date 23.02.2021
Member 1	 Prof. Pratik Majumdar	Date 23/2/2021
Member 2	 Prof. Satyajit Saha	Date 23/02/2021
Member 3	 Prof. Parnika Das	Date 23/2/2021

Final approval and acceptance of this thesis is contingent upon the candidate's submission of the final copies of the thesis to HBNI.

I/We hereby certify that I/ we have read this thesis prepared under my/our direction and recommend that it may be accepted as fulfilling the thesis requirement.

Date: 23/2/2021

Place: Kolkata - 64

Co-guide(if any)


Guide

STATEMENT BY AUTHOR

This dissertation has been submitted in partial fulfillment of requirements for an advanced degree at Homi Bhabha National Institute (HBNI) and is deposited in the Library to be made available to borrowers under rules of the HBNI.

Brief quotations from this dissertation are allowable without special permission, provided that accurate acknowledgment of source is made. Requests for permission for extended quotation from or reproduction of this manuscript in whole or in part may be granted by the Competent Authority of HBNI when in his or her judgment the proposed use of the material is in the interests of scholarship. In all other instances, however, permission must be obtained from the author.


(Arpita Das)

DECLARATION

I, hereby declare that the investigation presented in the thesis has been carried out by me. The work is original and has not been submitted earlier as a whole or in part for a degree / diploma at this or any other Institution/ University.

Arpita Das
(Arpita Das)

List of publication arising from thesis

Journal

1. “Effects of probe ellipticity and longitudinal magnetic field on the polarization rotation in a coherently prepared atomic medium”, **A. Das**, B.C. Das, D. Bhattacharyya and S. De, *OSA Continuum*, **2021**, *4*, 105-120.
2. “Angular dependency of the polarization rotation in a coherent atomic medium”, **A. Das**, B. C. Das, D. Bhattacharyya and S. De, *J. Phys. B: At. Mol. Opt. Phys.*, **2020**, *53*, 025502-025509.
3. “Polarization rotation with electromagnetically induced transparency in a V-type configuration of Rb in D_1 and D_2 transitions”, **A. Das**, B. C. Das, D. Bhattacharyya, S. Chakrabarti and S. De, *J. Phys. B: At. Mol. Opt. Phys.*, **2018**, *51*, 175502 - 175513.
4. “Observation and theoretical simulation of dispersive properties of an electromagnetically induced transparent ^{87}Rb atomic medium”, **A. Das**, B. C. Das, S. Chakrabarti, D. Bhattacharyya, and S. De, *Laser Phys.*, **2018**, *28*, 125205 - 125212.

Chapters in books and lecture notes NIL

Conferences

1. Poster Presentation: “Coherent Control of the optical Faraday rotation”, **A. Das**, B. C. Das, D. Bhattacharyya, and S. De, at Online International Conference on Fundamental Science and Quantum Technology using Atomic Systems (FSQT 2020), (**2020**). [Awarded Third Prize in poster presentation.](#)
2. Oral Presentation: “Polarization rotation with electromagnetically induced transparency (PREIT) in a V-type configuration of Rb D_1 and D_2 transitions”, at

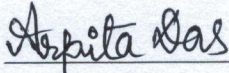
One Day Seminar on the Frontiers of Light-Matter Interactions, Aliah University, Kolkata, India, (2019).

3. Poster Presentation: “Polarization rotation in a coherent atomic medium”, **A. Das**, B. C. Das, D. Bhattacharyya, and S. De, at 13th European Conference on Atoms Molecules and Photons (ECAMP 13), Florence, Italy, (2019).
4. Poster Presentation: “Optical birefringence created in the atomic medium for the probe field with electromagnetically induced transparency”, **A. Das**, B. C. Das, D. Bhattacharyya, and S. De, at International Conference on Quantum and Atom Optics (ICQAO18), IIT Patna, Patna, India, (2018).
5. Poster Presentation: “Study of Polarization Rotation in an Electromagnetically Induced Transparent Atomic Medium”, **A. Das**, B. C. Das, D. Bhattacharyya, S. Chakrabarti and S. De, at National Laser Symposium (NLS-27), RRCAT, Indore, India, (2018). [Awarded Best Poster Prize, with contribution in KIRAN news-letters of Indian Laser Association \(ILA\).](#)
6. Poster Presentation: “Variation of group velocity with pump power in coherently prepared medium”, **A. Das**, S. Chakrabarti, at National Laser Symposium (NLS-25), KIIT, Bhubaneswar, India, (2016).
7. Poster Presentation: “Variation of group velocity with pump power in coherently prepared medium”, **A. Das**, S. Chakrabarti, at UGC sponsored national conference on The Central Role of Light in Science and the Importance of Optical Technologies (CRLSIOT), St. Paul’s Cathedral Mission College, Kolkata, India, (2016). [Awarded Best Poster Prize.](#)

Not related to thesis/Others

1. “Vector magnetometry using electromagnetically induced transparency with $lin \perp lin$ polarization”, B. C. Das, **A. Das**, D. Bhattacharyya and S. De, [J Opt Soc Am B](#), **2021**, *38*, 584-594.

2. "Interplay between electromagnetically induced transparency (EIT), absorption (EIA) and Autler-Townes (AT) splitting in \mathcal{N} -type atomic system: experiment and theory", B. C. Das, **A. Das**, D. Bhattacharyya, S. Chakrabarti and S. De, *OSA Continuum*, **2019**, *2*, 994-1010.
3. "Pulse delay and group velocity dispersion measurement in V -type electromagnetically induced transparency of hot ^{85}Rb atom", B. C. Das, D. Bhattacharyya, **A. Das**, S. Saha, S. Chakrabarti and S. De, *J. Phys. B: At. Mol. Opt. Phys.*, **2018**, *51*, 245501-245512.
4. "Simultaneous observation of Electromagnetically Induced Transparency (EIT) and Absorption (EIA) in a multi-level V -type system of ^{87}Rb and theoretical simulation of the observed spectra using a multi-mode approach", B. C. Das, D. Bhattacharyya, **A. Das**, S. Saha, S. Chakrabarti and S. De, *J. Chem. Phys.*, **2016**, *145*, 224312 - 224322.


(Arpita Das)

DEDICATIONS

To My Family

ACKNOWLEDGMENTS

The avenue towards this doctorate in physics is a big journey of my life. So, many people were involved with me. They need to be explicitly acknowledged and I would like to take this opportunity to thank them all who have got me to this point.

First of all, I would like to show my gratitude to Saha Institute of Nuclear Physics (SINP), for allocating me with an opportunity to pursue research at the “Laboratory of Light-matter interactions” in Applied Nuclear Physics Division (ANPD) and Department of Atomic Energy (DAE), Govt. of India for providing me financial support as a research fellowship.

I am thankful to my supervisor Prof. Sankar De for encouraging me and giving me freedom to venture whatever I want. He has also given me the opportunity of doing theoretical analysis of each of my thesis work which is based on experimental physics and developing the instruments. These practically helped me to carry out this journey with diverse and more profound knowledge.

I want to show my gratitude towards Prof. Dipankar Bhattacharyya with whom I have done detail discussion about the experiments as well as the theoretical analysis. His opinion assisted me in improving my work in both the directions and also took a complete picture. His research grants from the Department of Science and Technology (DST) and University Grants Commission (UGC) added additional fund in our lab to run all the experiments smoothly. I want to say thanks to Dr. Sharabana Chakrabarti, who was a DST women scientist in our lab. She helped me in the planning and designing of the magneto-optical trap.

I am also very grateful to my doctoral committee (DC) members, Prof. Nayana Majumdar, Prof. Pratik Majumdar, Prof. Satyajit Saha and Prof. Parnika Das. During all my renewal talks, their feedback helped me to improve my research skills.

This thesis would not have been possible without the initial guidance from my senior colleague Dr. Bankim Chandra Das. He was always supportive, friendly and ready to

discuss physics without any hesitation. He always encouraged me to endeavour until achieving the results. He has assisted me in various academic as well as non-academic purposes. Success, failure, pleasure, frustration and depression are the intertwined part of a PhD life. He always helped me to overcome the times of ups and downs.

I always got advice in various aspects of life, whenever I need, from Dr. Rajani Raman, one of my senior colleagues. I have met a few good human beings in SINP who enriched my life with music, art and philosophy e.g. Hitesh Da, Aminul Da, Maireyee Di, Sourav Da, Sukannya Di, Rome Da. I also want to thank my friends Sangeeta, Jaydeep, Sridhar, Apurba, Snehal and Prasant and my junior colleagues Sayan, Shubham, Promita, Ram and Vishal. Leisure time discussions with them gave me some relaxation.

I would like to show my gratitude to all my teachers, with whom I have met in different stages of my life. They have influenced my life with their diverse knowledge, philosophy and inspiration.

I am grateful to my parents, brother, parental uncle, aunts and cousins for their unconditional support, encouragement, love and care in every step of my life. My grandmother and parental aunt, who are no more with us, always motivated me to become an independent person and to chase my dream. They always inspire me in higher studies. It is my family who makes me a freebie. Here, I want to mention the name of my better half, Subhajit, who always supports and inspires me in all aspects of my life. He always enriches me about knowledge of programming languages. I have shared all my happiness, frustration and depression with him. I will be always thankful to him for all his love, care, support and inspiration.

In this opportunity, let me also thank the workshops of the SINP and the Variable Energy Cyclotron Center (VECC). I am also thankful to Mr. Sudipta Barman (SINP workshop) and Mr. Chandranath Marik (ANPD) who helped me to develop required instruments. Last but not the least, I would like to acknowledge all the instruments and the necessary scientific software which are an inseparable part of this journey. Without these, the journey may not end here.

Contents

Summary	xix
List of Figures	xxi
List of Tables	xxxiii
List of Acronyms	xxxv
List of Symbols	xxxvii
1 Introduction	1
1.1 Motivation and Goal	1
1.2 Thesis Overview	4
2 Experimental apparatus and methods	9
2.1 External cavity diode laser	10
2.2 Stabilization of frequency	12
2.3 Distributed feedback diode laser	13
2.3.1 Assembling and fabrication of DFBL	15
2.3.2 Characterization of DFBL	16
2.4 Atomic medium	17
2.4.1 Rb vapour cell	19
2.5 Cell heating arrangement	20
2.6 Solenoid	22

2.7	Magnetic shield	23
2.8	Saturation absorption spectroscopy	25
3	Theoretical framework	33
3.1	Semi-classical description of light-atom interaction	33
3.1.1	Formalism of density matrix: Equation of motion for density matrix	34
3.2	Two-level atom	38
3.2.1	Optical Bloch equation	42
3.2.2	Dressed states	45
3.3	Hyperfine levels	46
3.4	Zeeman shift	48
3.5	Doppler broadening	50
3.6	Three-level atoms: Electromagnetically induced transparency	52
3.6.1	Electromagnetically induced transparency (EIT)	52
4	Dispersive properties of a coherent atomic medium	59
4.1	Introduction	59
4.2	Experiment	61
4.3	Experimental results and analysis	64
4.4	Theory	69
4.5	Discussions	75
5	Polarization rotation with electromagnetically induced transparency	79
5.1	Introduction	79
5.2	Experiment	81
5.3	Experimental results and analysis	84
5.4	Theoretical Model	93
5.5	Discussions	102

6	Angular dependency of the polarization rotation in a coherent atomic medium	105
6.1	Introduction	105
6.2	Experiment	107
6.3	Experimental results and analysis	108
6.4	Theory	114
6.5	Discussions	122
7	Effects of ellipticity and magnetic field on the polarization rotation in a coherently prepared atomic medium	125
7.1	Introduction	125
7.2	Experiment	128
7.3	Experimental results and analysis	129
7.3.1	Dependency on the ellipticity	129
7.3.2	Dependency on the longitudinal magnetic field	132
7.4	Theoretical Analysis	135
7.4.1	Dependency on the ellipticity	136
7.4.2	Dependency on the longitudinal magnetic field	141
7.5	Discussions	145
8	Conclusion and Outlook	149
8.1	Peroration	149
8.2	Future trek	157
8.2.1	Storage and retrieval of information	157
8.2.2	Magnetometry	157
8.2.3	Birefringence lens effect	158
	Appendices	159
A	Solution of the OBE for a two-level atomic system	161

B Calculation of the output intensity difference in balanced homodyne detection technique	163
C Calculation of the output intensity in balanced polarimetric detection technique	165
D Assembling magneto-optical trap (MOT)	167
D.1 Assembling vacuum chambers for magneto-optical trap (MOT)	167
D.1.1 Scattering force on an atom	168
D.1.2 Doppler cooling: Optical molasses	169
D.1.3 Magneto-optical Trap (MOT)	173
D.1.4 Assembling vacuum chamber	175
D.1.5 Interlock to operate the turbo pump and the gate valve	177
D.1.6 Design and calibration of the anti-Helmholtz coils	180
D.1.7 Optical path for MOT	182
Bibliography	185

List of Figures

2.1	Tunable external cavity diode laser (ECDL) in (a) Littrow and (b) Littman-Metcalf configurations	10
2.2	An External cavity diode laser assembly of our laboratory. The adjustment screws are used for the course tuning of the external cavity. The piezo is used for fine-tuning and laser line scanning. The grating reflects the output beam and the -1 order beam is fed back to the laser. The lens is used to collimate the output laser beam.	11
2.3	A schematic representation of the structure of the distributed feedback diode laser.	14
2.4	Assembled DFBL with the collimating lens.	15
2.5	(a)Schematic diagram of the laser path for its characterization. DFBL: Distributed Feedback Diode Laser, O.I.: Optical Isolator, ND: Neutral Density filter, BS: Beam splitter, Rb cell: Rubidium vapour cell, BD: Beam Dump. (b) Power calibration plot for the laser beam from the assembled DFBL. The variations of power with current to the diode both before and after the isolator have been shown. The threshold current is about 38 mA.	16
2.6	Energy level diagram of ^{87}Rb and ^{85}Rb for (a) D_1 and (b) D_2 transitions with all corresponding hyperfine levels.	18

2.7	Cell characteristics with output power vs optical depth (OD, αL). With change in temperature of the vapour cell, the optical depth of the atomic medium was changed. From the absorption profile of the beam we have calculated the OD following the Beer-Lambert Law.	19
2.8	The temperature calibration curve of the home-build cell jacket with respect to time. It shows a fluctuations of $\pm 0.5^\circ$ C when the desired temperature is reached.	21
2.9	Magnetic field calibration along the axis of the solenoid.	22
2.10	One of the home-made cylindrical μ -metal shields. The black wire was wrapped in the cylinder with toroidal fashion for the degaussing process.	23
2.11	The general experimental setup to perform the saturation absorption spectroscopy with the ECDL and DFBL. ECDL: External Cavity Diode Laser, DFBL: Distributed Feedback Diode Laser, O.I.: Optical Isolator, BS: beam splitter, M: Mirror, Rb cell: Rubidium vapour cell, BD: Beam Dump, BDet: Balanced Photo-detector. The red line transmitted from the BS2 indicates the pump beam. The blue lines are the probe and the reference beams.	25
2.12	Doppler broadened profiles (black lines) of the reference beam, and the Lamb dips with Doppler background (red lines) of the probe beam for (a) D_1 and (b) D_2 transitions of both ^{87}Rb and ^{85}Rb . The hyperfine and the crossover line shapes (dark red lines) for (c) D_1 and (d) D_2 transitions of both ^{87}Rb and ^{85}Rb	28
2.13	Hyperfine and crossover peaks in case of D_1 transition corresponding to (a) $F = 2 \rightarrow F' = 1, 2$ transitions of ^{87}Rb and (b) $F = 3 \rightarrow F' = 2, 3$ transitions of ^{85}Rb . In case of for D_2 transition the hyperfine and crossover peaks for ^{87}Rb corresponding to (c) $F = 2 \rightarrow F' = 1, 2, 3$ transitions and (d) $F = 1 \rightarrow F' = 0, 1, 2$ transitions.	30
2.14	A representation of the real experimental setup of our laboratory	31

3.1	A two-level atomic system with ground state $ 1\rangle$ and excited state $ 2\rangle$ interacts with a laser of frequency ω . $\delta = (\omega_0 - \omega)$ is the detuning and Γ_2 is the decay rate from state $ 2\rangle$	38
3.2	Transient behaviour of the population terms corresponding to the ground state (ρ_{11}) and the excited state (ρ_{22}) and the coherence term (ρ_{21}). . . .	44
3.3	Steady state solution of the coherence term as a function of light detuning. Imaginary and real parts of the coherence term represent the absorption (red line) and dispersion (green line) profiles of the beam, interacting with the system respectively.	45
3.4	(a) Three level Λ -type system for EIT. (b) Coherent coupling between meta-stable state $ 2\rangle$ and excited state $ 3\rangle$ of the dressing (pump) field. (c) The formation of the dressed states in the atomic system. In this figure $ 1\rangle$, $ 2\rangle$ and $ 3\rangle$ correspond to the hyperfine levels $F = 1$, $F = 2$ and $F' = 3$ of ^{87}Rb respectively.	53
3.5	Probe coherence as a function of detuning at the steady-state. The red line represents the absorption profile with the transparency window in the vicinity of two photon resonance. The green line indicates probe dispersion with normal dispersion in the vicinity of the two photon resonance corresponding to the EIT.	57
4.1	Experimental Setup. ECDL : External cavity diode laser, OI : Optical isolator, HWP: Half-wave plate, PBS: Polarizing beam splitting cube, BS: Beam splitter, CBS : Non-polarizing beam splitting cube, M: Mirror, Rb Cell : Rubidium vapour cell, BD : Beam dump, Det : Single pin photodetector, B.Det : Balance detector, VND: Variable neutral density filter, SAS Setup: Saturation absorption spectroscopy setup, L: Convex Lens, PZT: Piezoelectric transducer.	61

- 4.2 Level scheme of ^{87}Rb with D_2 transition. This figure shows the Λ type configuration of the atomic system, where the pump beam (two-sided red arrow) is locked between the $F = 2(|2\rangle) \rightarrow F' = 2(|3\rangle)$ levels and the probe beam (one-sided blue arrow) is scanned through the $F = 1(|1\rangle) \rightarrow F' = 2(|3\rangle)$ levels. 64
- 4.3 (a) Experimental Doppler-broadened spectra of the probe beam when only the probe beam passed through the vapour cell. (b) Zoomed view (only the EIT portion) of the experimental Doppler broadened spectra of the probe beam when both the pump beam and the probe beam passed through the vapour cell at EIT condition. The probe Rabi frequency was 1.73 MHz in case of both (a) and (b), whereas the pump Rabi frequencies were 0 MHz and 32.74 MHz respectively. The black curve represents the probe transmission signal, and the red one denotes the probe dispersion profile. 65
- 4.4 Normalized dispersive EIT profiles corresponding to five pump Rabi frequencies ($\Omega_1 = 1.81 \pm 0.03$ MHz, $\Omega_2 = 6.3 \pm 0.01$ MHz, $\Omega_3 = 15.53 \pm 0.37$ MHz, $\Omega_4 = 25.84 \pm 0.22$ MHz, $\Omega_5 = 32.74 \pm 0.17$ MHz). The data were normalized only in the region of EIT. The probe Rabi frequency is 1.73 ± 0.34 MHz for all of the above spectra. 66
- 4.5 Variation of the group index with pump Rabi frequencies. The blue triangles show the experimental results (the line joining these experimental data points is given for eye guidance). The black line shows the variation of group index calculated analytically using Lorentzian velocity distribution of the atoms. The red dashed lines indicates the theoretical numerical variation considering the Maxwell-Boltzmann (MB) velocity distribution of the atoms. 67

-
- 4.6 Theoretical Doppler-broadened (a) absorption spectra and (b) dispersion spectra of the probe beam under EIT condition with both the M-B distribution and the Lorentzian distribution. The black lines and the red dashed lines in (a) and (b) correspond to the MB and the Lorentzian distribution respectively. In both (a) and (b) the probe Rabi frequency and the pump Rabi frequency are 1.73 MHz and 32.74 MHz respectively. 73
- 5.1 Experimental Setup. ECDL : External Cavity Diode Laser, DFBL: Distributed Feedback Diode Laser, O.I. : Optical Isolator, HWP: Half-wave Plate, QWP: Quarter-wave Plate, GL: Glan-laser Polarizer, PBS: Polarizing Beam Splitting Cube, BS: Beam Splitter, M: Mirror, Rb Cell : Rubidium Vapour Cell, BD : Beam Dump, ND: Neutral Density Filter, VND: Variable Neutral Density Filter, SAS Setup: Saturation Absorption Spectroscopy Setup, BDet: Balanced Detector. 81
- 5.2 (a) Energy level diagram for $^{85(87)}\text{Rb}$ for two cases. In case I, the pump beam was locked to $F = 3(2) \longrightarrow F' = 2(1)$ transition and then in case II, we locked the pump beam to $F = 3(2) \longrightarrow F' = 3(2)$ of D_1 transition for $^{85(87)}\text{Rb}$. The probe beam was scanned from $F = 3(2) \longrightarrow F' = 2(1), 3(2), 4(3)$ of D_2 transition for $^{85(87)}\text{Rb}$. (b) Simplified four level system modeled for theoretical analysis (for details see section (5.4)). 83

- 5.3 (a,c) Experimental Doppler-broadened absorption spectra for ^{85}Rb of the probe beam when one of the photo diodes of the balanced detector was blocked. (b,d) Experimental Doppler free spectra for ^{85}Rb of the probe beam when both the photo diodes of the balanced detector were opened. In the above figures the lock positions of the pump beam were at (a,b) $F = 3 \rightarrow F' = 2$ and at (c,d) $F = 3 \rightarrow F' = 3$ of D_1 transitions respectively. In all the plots, the probe intensity was $0.51 \pm 0.05 \text{ mW/cm}^2$ and the pump intensity was $1.53 \pm 0.15 \text{ mW/cm}^2$. In all the cases the probe beam was scanned from $F = 3 \rightarrow F' = 2, 3, 4$ of D_2 transition. The numbers in the figures are explained in Table (5.1). 86
- 5.4 (a,c) Experimental Doppler-broadened absorption spectra for ^{87}Rb of the probe beam when one of the photodiodes of the balanced detector was blocked. (b,d) Experimental Doppler free spectra for ^{87}Rb of the probe beam when both the photodiodes of the balanced detector were opened. In the above figures the lock positions of the pump beam were at (a,b) $F = 2 \rightarrow F' = 1$ and at (c,d) $F = 2 \rightarrow F' = 2$ of D_1 transitions respectively. In all the plots the probe intensity was $0.51 \pm 0.05 \text{ mW/cm}^2$ and the pump intensity was $1.53 \pm 0.15 \text{ mW/cm}^2$. In all the cases the probe beam was scanned from $F = 2 \rightarrow F' = 1, 2, 3$ of D_2 transition. The numbers in the figures are explained in Table (5.2). 87
- 5.5 Experimental dispersion spectrum in EIT region with three different pump beam intensities ($I_1 = 1.53 \pm 0.15 \text{ mW/cm}^2$, $I_2 = 10.76 \pm 0.54 \text{ mW/cm}^2$, $I_3 = 20.05 \pm 1.02 \text{ mW/cm}^2$) when the pump beam was locked (a) at $F = 3 \rightarrow F' = 2$ transition for ^{85}Rb , (b) at $F = 3 \rightarrow F' = 3$ transition for ^{85}Rb , (c) at $F = 2 \rightarrow F' = 1$ transition for ^{87}Rb and (d) at $F = 2 \rightarrow F' = 2$ transition for ^{87}Rb 89

-
- 5.6 Experimental variation of the angle of rotation of the polarization axis of the probe beam for different pump intensities in the EIT region for (a) ^{85}Rb and (b) ^{87}Rb (the lines are drawn for the eye guidance). The regions shown by the dashed lines in both the figures are zoomed in the insets given in each figure. The lock positions for the EIT peaks are shown in the legends. 91
- 5.7 Simulated (a) absorption and (b) dispersion spectra of the probe beam for ^{85}Rb . In both the spectra, the probe beam intensity and the pump beam intensity are set at 0.51 mW/cm^2 and 1.53 mW/cm^2 respectively. 96
- 5.8 Simulated (a) absorption and (b) dispersion spectra of the probe beam for ^{87}Rb . Both the spectra are plotted for the probe intensity 0.51 mW/cm^2 and the pump intensity was 1.53 mW/cm^2 98
- 5.9 (a) Complete energy level diagram with all sub levels in each F value for ^{85}Rb indicating the case when the pump beam was locked at $F = 3 \rightarrow F' = 3$. (b) Complete energy level diagram with all sub levels in each F value for ^{87}Rb showing the case when we locked the pump beam at $F = 2 \rightarrow F' = 2$. In both (a) and (b), the blue dashed lines indicate the transition for σ^+ component of the probe beam, orange lines are for the transitions corresponding to the σ^- component of the probe beam and the red lines are for the transition of the σ^+ component of the pump beam. 99
- 5.10 Variations of the angle of rotation corresponding to the EIT positions with pump intensities for (a) ^{85}Rb and (b) ^{87}Rb 101

- 6.1 (a) Experimental Setup. ECDL: External Cavity Diode Laser, DFBL: Distributed Feedback Diode Laser, O.I.: Optical Isolator, HWP: Half-wave Plate, QWP: Quarter-wave Plate, GL: Glan-laser Polarizer, PBS: Polarizing Beam Splitting Cube, CBS: Non-polarizing Cubic Beam Splitter, L: Lens, BS: Beam Splitter, M: Mirror, Rb Cell: Rubidium Vapour Cell, BD: Beam Dump, ND: Neutral Density Filter, VND: Variable Neutral Density Filter, SAS Setup: Saturation Absorption Spectroscopy Setup, BDet: Balanced Detector, DSO: Digital Storage Oscilloscope. (b) V-type configuration of ^{87}Rb combining D_1 and D_2 transitions for experimental observation of polarization rotation in the EIT medium. Here, $|1\rangle$, $|2\rangle$, $|3\rangle$ indicate the theoretical level scheme. (c) The orientation of the wave vector of the pump field (\vec{k}_c) with respect to the probe field wave vector (\vec{k}_p). 107
- 6.2 Polarization rotation signal of the probe beam with electromagnetically induced transparency (PREIT) as a function of probe detuning at three different angular mismatch ($\phi_1 = 0$ mrad, $\phi_2 = 14.49 \pm 3.68$ mrad and $\phi_1 = 36.23 \pm 3.75$ mrad) positions with the probe beam intensity as 0.47 ± 0.02 mW/cm² and that of the pump beam as 4.77 ± 0.03 mW/cm². In each case, $w_p = w_c = 1$ mm and the OD = 0.189 ± 0.003 109
- 6.3 Variation of angle of rotation of the plane of polarization of the probe beam taking (a) optical depth as a parameter with $w_c = 1$ mm and (b) pump beam spot size as a parameter with OD = 0.847 ± 0.004 . In both (a) and (b), the spot size of the probe was $w_p = 1$ mm. 111
- 6.4 Variation of group index of the medium with (a) optical depth and (b) pump beam spot size for $\phi = 0$ mrad. In (a) $w_p = w_c = 1$ mm and in (b) $w_p = 1$ mm and OD = 0.847 ± 0.004 113

-
- 6.5 Simulated polarization rotation spectrum of the probe beam with positive dispersion in the vicinity of the EIT resonance for different values of ϕ ($\phi_1 = 0$ mrad, $\phi_2 = 14.49$ mrad, $\phi_3 = 36.23$ mrad) with the probe intensity as 0.47 mW/cm² and that of the pump beam as 4.77 mW/cm². 119
- 6.6 Simulated variation of the angle of polarization rotation with the angular deviation between the pump and the probe beams taking (a) OD as a parameter and (b) the pump beam diameter as a parameter. In (a) $w_p = w_c = 1$ and in (b) $w_p = 1$ mm, OD = 0.847. 120
- 7.1 (a) Experimental Setup to study the polarization rotation in a coherently prepared atomic medium. ECDL: External Cavity Diode Laser, DFBL: Distributed Feedback Diode Laser, O.I.: Optical Isolator, HWP: Half-wave Plate, QWP: Quarter-wave Plate, GL: Glan-laser Polarizer, PBS: Polarizing Beam Splitting Cube, CBS: Non-polarizing Cubic Beam Splitter, BS: Beam Splitter, M: Mirror, Rb Cell: Rubidium Vapour Cell, BD: Beam Dump, ND: Neutral Density Filter, VND: Variable Neutral Density Filter, SAS Setup: Saturation Absorption Spectroscopy Setup, BDet: Balanced Detector, DSO: Digital Storage Oscilloscope. (b) V-type configuration of ⁸⁷Rb combining D₁ ($5S_{1/2} \rightarrow 5P_{1/2}$) and D₂ ($5S_{1/2} \rightarrow 5P_{3/2}$) transitions for experimental observation of polarization rotation in EIT medium. . . 128
- 7.2 (a) Experimental polarization rotation signal of the probe beam for different probe beam ellipticities in EIT medium. (b) Experimental variation of angle of PREIT with the probe ellipticity. 130
- 7.3 (a) Experimental polarization rotation signal of the probe beam for different magnetic fields ($B_1 = 0$ mT, $B_2 = 0.132 \pm 0.001$ mT, $B_3 = 0.300 \pm 0.001$ mT and $B_4 = 0.516 \pm 0.001$ mT) in the EIT medium. (b) Experimental variation of the angle of PREIT with the longitudinal magnetic field. . . 133

7.4	(a) Simplistic energy level diagram for theoretical analysis. See text for details. (b) All possible sub-level couplings of the degenerate sub-levels with both the components of the probe beam and the σ_+ pump beam in the complete atomic system. In both, the figures, the solid blue and the dotted blue one-sided arrows indicate the couplings due to the σ_+ and σ_- probe beams respectively. The solid red both sided arrows show the coupling for the σ_+ pump beam.	136
7.5	(a) Simulated polarization rotation signal of the probe beam for different probe beam ellipticities in the EIT medium. (b) Theoretical variation of the angle of PREIT with the probe ellipticity.	140
7.6	(a) A simple four-level V-type system to explain the magnetic field dependency on PREIT phenomenon. (b) Effect of the magnetic field with all the magnetic sub-levels in our experimental system. In both, the figures, the solid blue and the dotted blue one-sided arrows indicate the couplings due to the σ_+ and the σ_- probe beams respectively. The solid red both sided arrows show the coupling for the σ_+ pump beam.	141
7.7	(a) Simulated polarization rotation signal of the probe beam for different magnetic fields ($B_1 = 0$ mT, $B_2 = 0.132$ mT, $B_3 = 0.300$ mT and $B_4 = 0.516$ mT) in the EIT medium. (b) Theoretical variation of the angle of PREIT with the longitudinal magnetic field.	144
D.1	Three simple cases when an atom constrained to move in one dimension interacts with two laser beams of equal frequency incident from either side of the atom : (a) atom at rest, (b) atom moving left and (c) atom moving right.	170
D.2	Configuration for optical molasses.	171

D.3	The total force as a function of velocity in 1D optical molasses technique for $\delta = -\Gamma_2/2$. The force is plotted in units of $\hbar k\Gamma_2/2$, and the velocity is in units of Γ_2/k	172
D.4	(a) The mechanism of a magneto-optical trap illustrated for the case of an atom with $J = 0$ to $J = 1$ transition. In the magnetic field gradient, the Zeeman splitting of the sub-levels depends on the atom's position. (b) Configuration of a magneto-optical trap with three orthogonal pairs of laser beams which have the requisite circular polarization states and intersect at the centre of a pair of coils carrying opposite currents. The small arrows indicate the direction of the quadrupole magnetic field produced by the coils.	174
D.5	(a)-(c) Schematic diagrams of the vacuum system with the MOT chamber. The ports of the MOT chamber, where these two pumps are attached, are indicated with red and orange arrows respectively in (a).	177
D.6	Schematic diagram of home-made turbo interlock circuit. (a) Interlock for backing and (b) interlock to open the gate valve.	179
D.7	(a) Cylindrical coordinates for the magnetic field of a circular coil carrying current I at the axial position (z - direction). (b) The magnetic field along the axis of the pair of anti-Helmholtz coils.	180
D.8	Calibration of the magnetic field along the axial length of the coils in anti-Helmholtz configuration with current (a) $I = 6.0$ A, (b) $I = 7.0$ A, (c) $I = 7.5$ A, (d) $I = 8.0$ A.	181
D.9	Schematic presentation of the optical path from lasers to the MOT chamber. ECDL: External cavity diode laser, O.I.: Optical isolator, HWP: Half wave plate, PBS: Polarizing beam splitting cube, L: Lens, M: Mirror, SAS Setup: Saturation absorption spectroscopy setup.	182
D.10	An image of the MOT setup in our laboratory.	183

List of Tables

1	Acronyms used throughout in this thesis.	xxxvi
2	Symbols used throughout in this thesis.	xl
4.1	Experimentally measured values of the group velocities and the time delays for nine different pump Rabi frequencies.	68
5.1	Experimentally observed resonance positions for ^{85}Rb	86
5.2	Experimentally observed resonance positions for ^{87}Rb	88
5.3	Experimentally obtained maximum anisotropy in the Rb atomic medium at room temperature in the vicinity of the EIT.	92

List of Acronyms

A list of acronyms used throughout this thesis is given in the Table (1).

Acronyms	Full Form
CPT	Coherent Population Trapping
EIT	Electromagnetically Induced Transparency
EIA	Electromagnetically Induced Absorption
AT splitting	Autler-Townes splitting
LWI	Laser Without Inversion
PR	Polarization Rotation
OFR	Optical Faraday Rotation
MOR	Magneto-Optical Rotation
OR	Optical Rotation
PRS	Polarization Rotation Spectroscopy
^{87}Rb	Rubidium - 87
^{85}Rb	Rubidium - 85
SAS	Saturation Absorption Spectroscopy
RWA	Rotating wave approximation
PREIT	Polarization Rotation with Electromagnetically Induced Transparency
OD	Optical Depth

Acronyms	Full Form
MOT	Magneto-Optical Trap
ECDL	External Cavity Diode Laser
DFBL	Distributed Feedback Diode Laser
O.I.	Optical Isolator
ND	Neutral Density Filter
BS	Beam Splitter
Rb cell	Rubidium vapour cell
BD	Beam Dump
ND	Neutral Density Filter
M	Mirror
BDet	Balanced Photo-detector
PBS	Polarizing Beam Splitting Cube
HWP	Half-Wave Plate
QWP	Quarter-Wave Plate
PZT	Piezoelectric Transducer
VND	Variable Neutral Density Filter
Det	Single pin photodetector
L	Lens (in description of experimental setups and figures)
CBS	Non-Polarizing Cubic Beam Splitter
GL	Glan-Laser Polarizer
DSO	Digital Storage Oscilloscope

Table 1: Acronyms used throughout in this thesis.

List of Symbols

A list of symbols used throughout this thesis is given in the Table (2).

Symbols	Meaning
ν	Linear frequency of laser
ω	Circular frequency of laser
ω_0	Transition frequency
I	Intensity of laser
α	Absorption Coefficient of the atomic medium
L	Length of the atomic medium
μ_0	Free Space Permeability
l	Length of the solenoid
$ \psi\rangle$	State Vector
\hat{A}	Operator
ρ	Density matrix
ρ_{ii}	Diagonal element of the density matrix
ρ_{ij}	Off-diagonal element of the density matrix
\vec{P}	Polarization of the medium
χ	Susceptibility of the medium
N_0	Atomic number density

Symbols	Meaning
μ_{ij}	Dipole moment corresponding to the transition $ i\rangle \rightarrow j\rangle$
$\vec{\epsilon}$	Electric field Vector
E	Amplitude of the electric field
\hat{e}	Unit polarization vector
ϵ_0	Free space permittivity
H	Total Hamiltonian
H_0	Unperturbed Hamiltonian
H_p	Perturbed Hamiltonian
Γ_{ij}	Spontaneous decay rate
γ_{ij}	Coherence decay rate
\vec{k}	Wave-vector of the laser beam
k	Magnitude of the wave-vector
\vec{v}	Velocity of atom
v	Magnitude of velocity of atom
h	Planck's constant
Ω	Rabi frequency of laser
\mathcal{U}	Unitary matrix
Λ_0	Re-population matrix
$\delta_{p(c)}$	Detuning of probe (pump) laser
$\Delta_{p(c)}$	Doppler detuning of probe (pump) laser
D_{ij}	Complex detuning
β	Dispersion Coefficient of the medium (in chapter 4)

Symbols	Meaning
β	Ellipticity of probe beam (in chapter 7)
I_{sat}	Saturation intensity
P	Power of the laser beam
$N(kv)$ or $N(v)$	Velocity distribution of the atom
u	Value of most probable velocity of atom
ϕ	Angular mismatch between the probe and the pump beams
θ	Angle of polarization rotation at resonance as function of ϕ
$\theta(\omega_0)$	Angle of polarization rotation at resonance as function of pump intensity
$\theta(\beta)$	Angle of polarization rotation at resonance as function of probe ellipticity
$\theta(B)$	Angle of polarization rotation at resonance as function of magnetic field
v_g	Group velocity of probe beam
n_g	Group index of the medium
$\Delta n(\omega_p)$	Anisotropy for the refractive index
$w_{p(c)}$	Spot size of the probe (pump) beam
$\vec{r}_{p(c)}$	Propagation direction of the probe (pump) beam
r	radius of the beam
B	magnitude of the magnetic field
g_F	Lande g-factor
μ_B	Bohr Magneton

Symbols	Meaning
F_{rad}	Magnitude of radiation pressure force
A	Cross-sectional Area of laser beam
c	Speed of light in free space
R_{scatt}	Scattering rate of atom
F_s	Magnitude of scattering force
a_{max}	Maximum of magnitude of acceleration
M	Mass of an atom
λ	Wavelength of laser
τ	Lifetime of the excited state of atom
v_r	Magnitude of recoil velocity
η	damping coefficient
k_B	Boltzmann Constant
T_D	Doppler cooling limit temperature
ζ	Gradient of the magnetic field

Table 2: Symbols used throughout in this thesis.

1

1.1 Motivation and Goal

The light-atom interaction is one of the key research areas from the beginning of modern physics to the present time due to its vast applications in the various fields along with its elemental interest. Advancement in optical technology has made it happen so that one can control the properties of an atomic medium with laser and therefore can create a new medium with distinctive characteristics. It can be possible that an atomic medium may outshine the performance of many solid-state devices which are traditionally used in optics. Atoms can be prepared in a coherent superposition of energy states under the interaction of two or more laser fields which are resonant with various atomic transitions. There are several coherent phenomena being investigated, like coherent population trapping (CPT) [5–8], electromagnetically induced transparency (EIT) [9–12], electromagnetically induced absorption (EIA) [13–16], Autler-Townes (AT) splitting or AC-stark splitting [16–18], lasing without inversion (LWI) [19–23], polarization rotation (PR) or optical Faraday rotation (OFR) [24–27], magneto-optical rotation (MOR) [28–31] etc.

Among these, in a three-level atomic system, EIT becomes a noteworthy candidate.

Here a strong control or pump laser induces a narrow spectral transparency window at a highly absorbing atomic resonance for a weak probe laser beam by creating coherence between the relevant atomic states. As a result, the properties of the atomic vapour are changed dramatically [32, 33]. This coherent interaction of the laser with multilevel atomic or molecular system leads to quantum interference in the track of electronic excitation [12]. EIT was extensively studied since its first experimental observation [9] due to its potential applications in the non-linear optics and quantum information processing e.g., in the slow light and storage [34], atomic clocks [35], precision magnetometers [36–39], study of Rydberg states [40], non-linear wave mixing [41] and quantum information [42] etc. The fundamental effect of the “production of ultra-slow light” made possible the fact so that EIT is accompanied by a million-fold increase in the refractive index of the atomic vapour [43]. Thus, in the vicinity of EIT, the medium becomes very dispersive.

The polarization rotation (PR) is a type of coherent phenomenon where the polarization of the laser beams determine the coherent properties of the atomic medium. The rotation of the plane of polarization of an optical field can be induced by the intrinsic helicity of the atoms or the molecules in the medium or can be generated by applying external electric, magnetic and optical fields. A strong circularly polarized laser beam (pump beam) can induce the rotation of the original direction of linear polarization of a weak laser beam (namely, probe beam). This phenomenon is called polarization rotation (PR) [25, 44, 45] or optical rotation (OR) [26] or optical Faraday rotation (OFR) [27]. In this case, the pump beam creates non-uniform population distribution among the degenerate magnetic sub-levels due to both the optical pumping and the saturation effects. This non-uniform distribution of population, in turn, generates a difference in the

refractive index and a difference in the absorption of the atomic medium between the two circular components of the linearly polarized probe beam. The refractive index difference leads to optical birefringence, and the absorption difference produces circular dichroism in the medium. The circular dichroism leads to an elliptical polarization in the probe beam, while the optical birefringence creates a rotation in the plane of polarization of the probe beam. This birefringence can be measured by detecting the rotation of the polarization axis of the probe beam. If the external magnetic field is applied to rotate the polarization of the probe beam, then the phenomenon is known as the magneto-optical rotation (MOR) or Faraday rotation [28–31]. Now, if the magnetic field is applied in the direction of light propagation, the phenomenon is called the Faraday effect [28, 46, 47]. On the other hand, for the magnetic field applied in the transverse direction, the phenomenon is known as the Voigt effect [48, 49]. Therefore, we can say that if a strong circularly polarized pump beam is introduced in the atomic medium with proper conditions, it opens up the possibility of the medium becoming transparent as well as anisotropic to the weak probe beam.

The polarization rotation spectroscopy (PRS) [24] has applications in the various fields of atomic, molecular and optical (AMO) physics e.g. optical locking [25, 50, 51], linear and non-linear magneto-optical rotation [47, 52–54], atomic bandpass filter [55], all-optical switching and high-speed Stokesmetric imaging [56], squeezing of light [57–59], magnetometry [37, 53, 54], etc. Whereas the coherent control of the PR can be used in a variety of fields such as in precision measurements of parity violation in atoms [60], electron-spin-reversal phenomenon [61], to sort out the orbital angular momentum of light [62], detection of slow light [63], birefringence lens [64] etc. This plethora of the above

applications made the PR phenomenon draw our attention of investigation. If the angle of PR can be enhanced, then the results of all the above applications of the polarization rotation will also be improved.

The main objective of this research is to study the dispersive properties of the atomic medium, which exhibits coherent phenomena and to take the opportunity to investigate how the PR can be controlled coherently in an EIT medium.

1.2 Thesis Overview

Observation of the properties of a coherently prepared atomic medium is the main aim of my doctoral study. This research work contains both experiments and their corresponding theoretical models. We have performed all the experiments in Rubidium (Rb) atomic vapour cells which consists of ^{87}Rb and ^{85}Rb in their natural abundance with no buffer gas. The atomic states were dressed by applying perturbations from the electric fields of the lasers [1–3] and the external longitudinal magnetic field. We have studied how the system response can be modulated by controlling the amplitude of the electric fields in space and frequency domains and also by controlling the magnitude of the magnetic field. Our study mainly reveals the outcome of the interaction of the weak probe and the strong pump beams with the atomic medium in a suitable configuration so that the strong pump beam can induce EIT and PR in the atomic medium. The experiments were performed to study the polarization rotation and slow light phenomenon in the EIT medium. For these purposes, we have worked with three and four-level atomic systems.

The details of all the experimental apparatus that was used, developed and built for

this research work, are discussed elaborately in the chapter 2. Throughout this research work, we used a few commercially available instruments, while some necessary devices were developed in the laboratory. This chapter contains details about the procedure of their characterization, as well as the characterization of the atomic medium. Then, the saturation absorption spectroscopy (SAS) is discussed as one of the essential tools. Using SAS, we chose the hyperfine levels of Rb for our experiments.

In chapter 3, a general theoretical description of the light-atom interaction is discussed. Here, the essential theoretical tools, which have been used throughout my research work, have been emphasized. The density matrix equations of a two-level atomic system interacting with one electric field are solved with the semi-classical approach. The probe coherence of the medium has been solved to get an essence of the light-atom interaction. The probe coherence is related to the absorption and the dispersion signals of the probe. We have detected the absorption and dispersion spectra of the probe beam in our experiments. All of our experiments have been performed in the hyperfine states and the Zeeman sublevels of Rb. Therefore, the hyperfine levels and the Zeeman sub-levels structure is discussed to give completeness. Then we discuss a general three-level density matrix formalism as a general framework of our theoretical models which were developed during this research work. How EIT is formed in the atomic system has also been shown in this theoretical calculation.

Chapter 4 contains the discussion on the experimental and theoretical study of the dispersive properties of an EIT medium. In this work [1], we have reported the dispersive properties of ^{87}Rb in a Λ -type configuration with D_2 transition at room temperature. In this case, the probe beam was scanned from $F = 1 \rightarrow F' = 2$ hyperfine transition,

and the pump beam was locked at $F = 2 \rightarrow F' = 2$ hyperfine transition. Using the homodyne detection technique, we have observed the dispersion signal of the probe beam. The group index and the corresponding group velocity were calculated from the observed signal. It has been observed that the group index varies non-linearly with the pump Rabi frequency. Further, we have solved the Liouville equation for a three-level Λ -type system analytically to get the probe coherence term. Then to accumulate the contributions of atoms of all the velocities, we have considered the Lorentzian distribution. With this formulation, we were able to get an analytical solution to the total susceptibility of the medium and have examined the characteristic variation of the group index.

I have discussed about our study on the polarization rotation with electromagnetically induced transparency (PREIT) in a V-type system of both ^{85}Rb and ^{87}Rb [2] in the chapter 5. We observed two separate cases for each of the isotopes of Rubidium. In the first case, for ^{85}Rb , the pump beam was locked at $F = 3 \rightarrow F' = 2$ and in the second case, we locked the pump beam at $F = 3 \rightarrow F' = 3$ of D_1 transition. The probe beam was scanned from $F = 3 \rightarrow F' = 2, 3, 4$ of D_2 transition in both the cases of ^{85}Rb . Similarly, for ^{87}Rb at first, we locked the pump beam at $F = 2 \rightarrow F' = 1$ and in the second case, the pump beam was locked at $F = 2 \rightarrow F' = 2$ of D_1 transition. The probe beam was scanned from $F = 2 \rightarrow F' = 1, 2, 3$ of D_2 transition for both the cases of ^{87}Rb . We observed the polarization rotation spectrum experimentally with the help of balanced polarimetric detection technique. This rotation spectrum is dispersive. We got two EIT resonances in the case of ^{85}Rb and one EIT for ^{87}Rb . We have calculated the angle of rotation as a function of the pump intensity corresponding to each case. We observed that the angle of rotation increased first as we increased the pump intensity up

to a certain value. After that, it started to decrease with further increment in the pump intensity.

To understand this phenomenon, we considered a four-level V-type system. With this system, we were able to show two EIT resonances in the rotational spectra for ^{85}Rb and one EIT resonance for ^{87}Rb . To explain the polarization rotation phenomenon we also took into account, that the σ_+ component of the probe beam and the σ_+ component of the pump beam formed a V-type system, which gave a two-photon contribution to the medium. The σ_- component of the probe beam gave rise only to one photon contribution. Thus, this mismatch is responsible for the generation of the difference in the susceptibility of the medium. Thus, the anisotropy to the refractive index exhibited by the different components of the polarization of the probe beam is created in the medium. So, to get a theoretical idea about this, we solved the density matrix equations under steady-state condition. From the susceptibility, we calculated the angle of rotation in the vicinity of the EIT region. The theoretical and the experimental results have been compared in chapter 5.

Further, systematic investigations were performed with PREIT phenomenon in a V-type system of ^{87}Rb , where the pump beam was locked at $F = 2 \rightarrow F' = 2$ of D_1 transition and the probe beam was scanned from $F = 2 \rightarrow F' = 3$ of D_2 transition. In chapter 6, the dependencies of the angle of PREIT on the angular mismatch between the probe and the pump beams, the optical depth (OD) and the pump beam spot size have been investigated experimentally and theoretically [3]. The Liouville equation for a three-level V-type system has been solved analytically, and the characteristics of the angle of PREIT with the angular mismatch corresponding to both experiment and theory

are compared. Further, the group velocities of the probe beam without angular mismatch for maximum OD and pump beam spot size have been estimated.

Chapter 7 deals with the effects of the probe ellipticity and the external longitudinal magnetic field on the PREIT. Here also, we have chosen the same atomic configuration for our purpose of the study. It has been observed that the angle of PREIT shows a periodical variation of periodicity $\pi/2$ with the probe ellipticity. At the same time, it became non-linear with the variable longitudinal magnetic field. It is also observed that the PREIT phenomenon is sensitive to the low magnetic field as the angle of PREIT increased one order of magnitude by applying an external magnetic field comparable to the earth magnetic field than the angle of PREIT without any magnetic field. We have considered a four-level V-type system with degenerate and non-degenerate levels to explain our experimental findings. We have also compared our experimental observations with the theoretical results.

Lastly, in chapter 8, I have summarized all our studies with the importance and applications in the field of quantum optics. This chapter also contains a few proposals for the future experiments which can be done in continuation of the research work presented in my thesis.

As a part of this doctoral study, I was also involved in the assembling of the vacuum systems for the magneto-optical trap (MOT) [65–67]. Appendix D covers the method of achieving the ultra-high vacuum after assembling the MOT chamber with different vacuum pumps. It also deals with the design, fabrication and characterization of the required quadrupole magnetic field along with the optical path for MOT.

2

Experimental apparatus and methods

This chapter describes the experimental apparatus that was utilized or developed during this research work in an elaborating way. Even though some of them are commercially available, there are a few necessary apparatus that was developed in our laboratory. Since our research work is based on light-atom interactions, we need some essential instruments to do the experiments. External cavity diode laser (ECDL) and distributed feedback diode laser (DFBL) are the light sources, and the Rb vapour cell is the atomic medium in the purpose of our study. Indeed, other optical components and instruments were also used as per our experimental demand.

At first, the description of all the necessary apparatus, along with their working principles, are discussed in this chapter. It also narrates how the instruments were standardized and optimized for our experimental needs. Some standard results of the existing reports have been regenerated before doing the main experiment for a basic understanding of the light-atom interaction. It also helped us to characterize our atomic medium. Then, the saturation absorption spectroscopy (SAS) is discussed, which is one of the necessary techniques in our experiments.

2.1 External cavity diode laser

In the field of quantum optics or light-atom interaction experiments, light sources are one of the important elements. To do experiments in atomic physics, one needs to have a laser source of very narrow linewidth (a few MHz). In general, a laser diode itself consists of a gain medium which amplifies light through stimulated emission and a resonant cavity. The cavity is a set of reflectors which causes the light to bounce back and forth through the gain medium so that the light is continually amplified to a higher power. The linewidth of the emitted laser beam from a bare laser diode is not enough to study the atomic transition line. So, to get the required linewidth, we use the tunable ‘external cavity diode lasers’(ECDL), where an external cavity is created outside the gain medium with an extra reflector. The ECDL allows the cavity to be longer than when it was confined to the gain medium. Due to the large cavity length, the ECDL can be used as a light source of linewidth below or equal to 1 MHz. It can be reduced to a few tens of kHz in an ideal case. There are two basic types of configuration of tunable ECDL : (i) Littrow configuration [68, 69] and (ii) Littman-Metcalf configuration [70, 71].

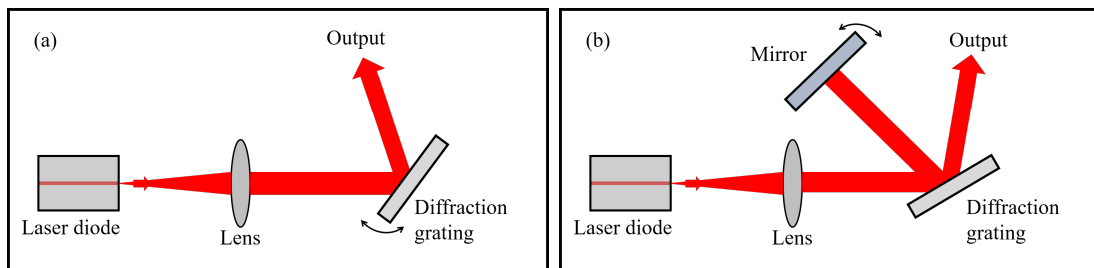


Figure 2.1: Tunable external cavity diode laser (ECDL) in (a) Littrow and (b) Littman-Metcalf configurations

The most common Littrow configuration (Fig.2.1(a)) contains a collimating lens and

a diffraction grating as the end reflector. The first-order diffracted beam provides optical feedback to the laser diode. The emission wavelength can be tuned by rotating the diffraction grating. A disadvantage of this configuration is that this also changes the direction of the output beam, which is inconvenient for many applications.

In the Littman-Metcalf configuration (Fig.2.1(b)), the grating orientation is fixed, and an additional mirror is used to reflect the first-order beam to the laser diode. By rotating that mirror, the wavelength can be tuned. This configuration offers a fixed direction of the output beam and also tends to exhibit a smaller linewidth, as the wavelength selectivity is more robust. Here, the wavelength-dependent diffraction occurs twice instead of once per resonator round trip. This configuration also has a disadvantage as the zero-order reflection of the beam reflected by the tuning mirror is lost, and this makes the output power lower than that for a laser in Littrow configuration.

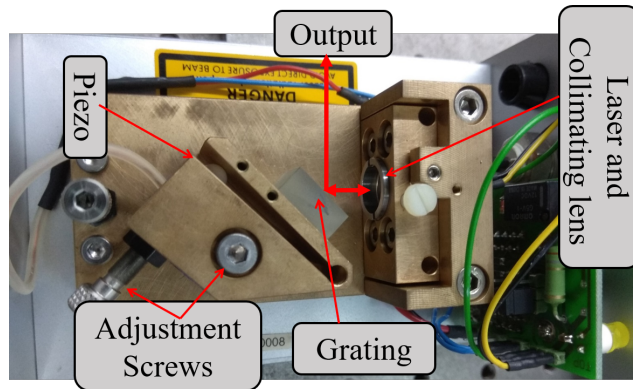


Figure 2.2: An External cavity diode laser assembly of our laboratory. The adjustment screws are used for the course tuning of the external cavity. The piezo is used for fine-tuning and laser line scanning. The grating reflects the output beam and the -1 order beam is fed back to the laser. The lens is used to collimate the output laser beam.

We have used the ECDL in Littrow configuration, which is composed of a semiconductor diode laser, an external grating and a collimating lens as shown in Fig 2.2. Generally,

bare laser diodes have a linewidth of the order of 100 MHz [68]. The linewidth can be reduced to below ≈ 1 MHz by using the external grating. The -1 order diffracted beam from the grating is fed into the laser source, while the zero-order diffracted beam is taken as the laser output. The diffraction grating is mounted on a piezoelectric crystal, which helps us to tune the wavelength. The cavity length can be adjusted, and the laser frequency can be scanned by modulating the piezo voltage. With the help of the lens, the zero-order diffracted beam of the grating is collimated, so that, throughout the experimental path, the beam does not diverge. The collimation of the laser beam is $\approx 4 - 5$ meters. Commercially available ECDL from Toptica, Germany (DL100) has been used in this research work. To emit the desired wavelength steadily, the ECDL further needs some electronic controls. These consist of a current controller to control the laser current as well as the laser output power and a temperature controller for the temperature stability of the diode laser. The emitted wavelength tremendously depends on current and temperature stability. Apart from these, the electronics also consists of a scan controller to control and scan the piezo of the external cavity and a lock-in-amplifier to stabilize the frequency of the desired laser line.

2.2 Stabilization of frequency

Generally, the ECDLs are very stable over a narrow bandwidth region. But for the experimental requirements, we need to stabilize the frequency over a concise spectral range \approx kHz or less as the laser frequency drifts within some time intervals. For this purpose, a lock-in-amplifier (Toptica LIR110) and a proportional integrator differentiator

(PID) circuit are used to lock the desired laser frequency on the top of a detected signal.

The laser frequency ν_0 is modulated by a small frequency $\Delta\nu$ with sinusoidal modulation to generate the derivative of the detected signal in the lock-in detection. Then the observed signal is compared with the signal of $\nu_0 \pm \Delta\nu$. Thus the LIR110 electronic box identifies whether the slope of the signal is positive or negative and calculates the absolute value of the signal slope. After that, the modulated signal is sent through a low pass filter to filter out the high-frequency components (ideally all the time-dependent contributions). The output of the lock-in signal is proportional to the derivative of the original signal. This output is called 1F signal, which is produced electronically. Now the LIR signal is fed into a PID feedback loop so that the frequency can be locked on the desired region of interest. When the frequency drifts, depending on the value of the slope, the feedback loop of the PID controller circuit adjusts the piezo current to re-establish the desired set point so that the laser frequency remains locked at the desired position.

2.3 Distributed feedback diode laser

A distributed feedback laser (DFBL) diode is a semiconductor laser diode, which contains a periodically structured element or diffraction grating as the active medium of the laser as shown in Fig.2.3. In contrast to ECDL, which consist of mirrors and diffraction gratings to form an external cavity, DFBL does not contain an external cavity. Instead, those lasers have a periodical internal feedback structure. The structure builds a one-dimensional interference grating (Bragg scattering), and the grating provides optical feedback for the laser. This longitudinal diffraction grating causes reflection back into the cavity.

This structure is a periodical variation of the refractive index or the same of the laser medium's gain or a combination of both. The grating operates in the first order, where the periodicity is a one-half wave, and the light is reflected backwards. Since the Bragg scattering is sensitive to the wavelength and the periodic structure has a certain length, only specific wavelengths can pass the structure. It leads to a spectral selection of the waves [72].

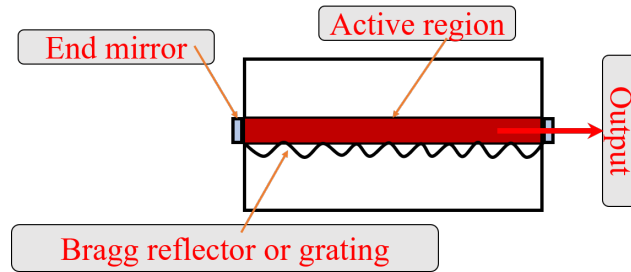


Figure 2.3: A schematic representation of the structure of the distributed feedback diode laser.

This periodic structure is highly dependent on the temperature of the diode. So by altering the temperature of the device, the pitch of the grating can be changed due to the dependence of refractive index on temperature. This change in the refractive index also alters the wavelength selection of the grating structure and therefore, the wavelength of the laser output. Thus by changing the temperature of the diode, we can get our specified wavelength. Changing the current of the device also causes a change in temperature inside the device. Therefore, by changing the current, we can also tune the device. To control the current and temperature of the device, we need electronics controllers, respectively.

2.3.1 Assembling and fabrication of DFBL

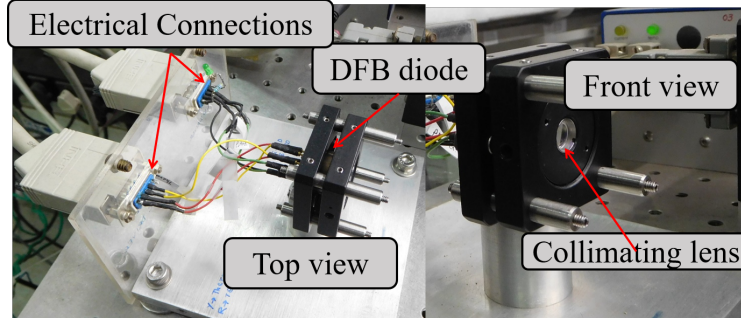


Figure 2.4: Assembled DFBL with the collimating lens.

We had a bare DFBL diode which was bought from Eagleyard with model no: EYP-DFB-0795-00080-1500-TOC03-005. The transition wavelength of the diode is 795 nm which is the wavelength of D_1 transition for Rb atom. To get the collimated laser beam from the diode, we used an aspheric lens of focal length $f = 6$ mm. We also bought a collimation mount kit from Thorlabs to set up the diode with the collimating lens. The collimating length is 4–5 m and we got the beam diameter as 2 mm with the formula, beam diameter $= 2 \times f \times \tan(\frac{\theta}{2})$ with the perpendicular beam divergence $\theta = 21^\circ$. An aluminium post and a rectangular aluminium base were made from our institute workshop to maintain the initial laser beam height 55 mm. We covered the entire assembly with a box made of perspex.

The laser system needs electrical connections to operate. We used a commercially bought temperature controller (Model no: TED 200 C) and current controller (Model no: LDC 205 C) from Thorlabs. Both the controllers have 9 pin output configurations. The bare diode has 8 individual specified pins. According to the pin configurations, we made connections between the laser diode and the two controllers via two D-connectors,

as mentioned above by soldering the joints. We have also made a connection for a LED to indicate the current controller is on. The image of the DFB laser assembly is shown in the Fig.2.4.

2.3.2 Characterization of DFBL

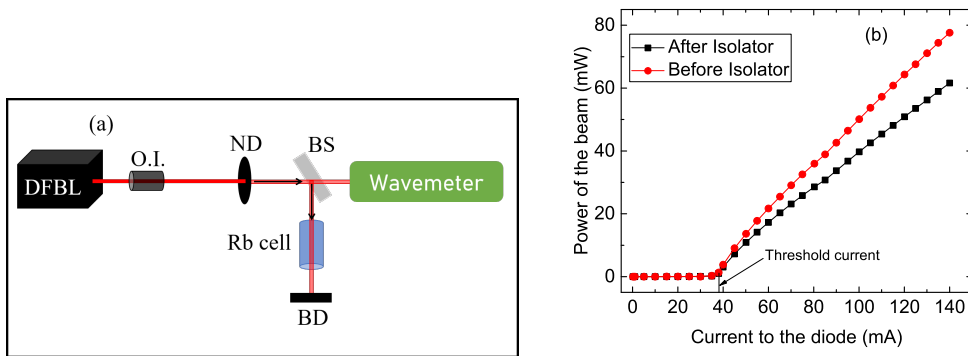


Figure 2.5: (a) Schematic diagram of the laser path for its characterization. DFBL: Distributed Feedback Diode Laser, O.I.: Optical Isolator, ND: Neutral Density filter, BS: Beam splitter, Rb cell: Rubidium vapour cell, BD: Beam Dump. (b) Power calibration plot for the laser beam from the assembled DFBL. The variations of power with current to the diode both before and after the isolator have been shown. The threshold current is about 38 mA.

An optical isolator (O.I.) was placed in the path of the output beam from the assembled laser to avoid back reflections to the diode from optical components. The isolator was adjusted so that we got 81% efficiency. Then the output wavelength was characterized using a wavemeter (From Coherent). The laser path diagram is shown in the Fig.2.5(a). The laser beam was passed through a neutral density filter (ND) of high optical density to protect the wavemeter from damage due to the high power of the laser. Then the beam was passed through a 50:50 beam splitter (BS). The transmitted part was sent to

the wavemeter, and the reflected part was passed through a 50 mm Rubidium vapour cell (Rb cell) to observe the fluorescence by an IR viewer. We observed fluorescence in the Rb cell when the wavemeter showed 794.978 nm wavelength with 129.76 mA to 131.50 mA current setting and 25°C temperature for 5 k Ω value of thermistor. It is the required wavelength of the D₁ transition for the Rb atom.

To get continuous tuning for each hyperfine line of Rb D₁ transition, we used an arbitrary function generator to give a ramp to the current of DFBL to scan it. We set the peak to peak modulation voltage at 160 mV, and the modulation frequency at 30 Hz. For safety, the limiting value of the current to the DFBL was set at 140 mA. The hyperfine spectra are shown in section 2.8 and are discussed in detail. Apart from this, the power of the laser beam from the DFBL was measured by changing the current to the diode from 0 mA to the limiting value. It was measured before and after the isolator. We observed the threshold current for this diode is \sim 38 mA. The characterization plot of power vs. current is shown in the Fig.2.5(b). Our DFBL has a linewidth \sim 2 MHz and temperature stability \sim 2 mK.

2.4 Atomic medium

Apart from the light source, the atomic medium is one of the important tools in our research of light-atom interaction. We have used room temperature or hot Rb atom in our experiments. Various lengths of the vapour cell of Rb containing its two main isotopes ⁸⁷Rb and ⁸⁵Rb in natural abundance without any buffer gas under 10⁻⁷ Torr pressure have been used in our experiments. Rb is an alkali atom with the atomic number 37.

The electronic configuration of the outermost orbit is $1s^2 2s^2 2p^6 3s^2 3p^6 4s^2 3d^{10} 4p^6 5s^1$. So, the total spin angular momentum of the outermost electron is $S = 1/2$, and the orbital angular momentum is $L = 0$ with the total angular momentum $J = 1/2$.

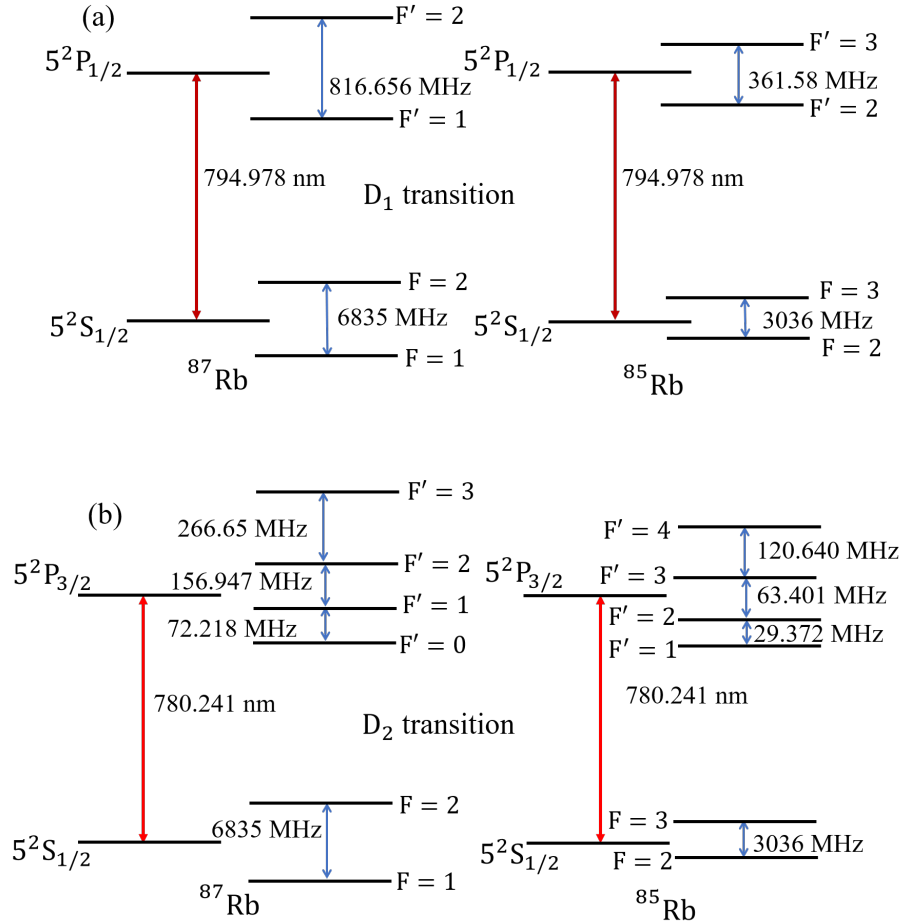


Figure 2.6: Energy level diagram of ^{87}Rb and ^{85}Rb for (a) D_1 and (b) D_2 transitions with all corresponding hyperfine levels.

The ground state is denoted by $5^2S_{1/2}$ and the first two excited states' configurations are $5^2P_{1/2}$ and $5^2P_{3/2}$. The transition from the ground state to the excited state $5^2P_{1/2}$ is called the D_1 transition with the wavelength of transition 794.978 nm. The transition from the ground state to the excited state $5^2P_{3/2}$ is called the D_2 transition with the transition wavelength 780.241 nm. In this research work, one experiment has been done

in D_2 transition, and the rest of the experiments have been done with the combination of D_1 and D_2 transitions.

The nuclear spin of the ^{87}Rb and ^{85}Rb are $I = 3/2$ and $I = 5/2$ respectively. Considering the hyperfine coupling (details are discussed in the section 3.3 of the chapter 3), the ground state $5^2S_{1/2}$ has two hyperfine levels $F = 1, 2$ and $F = 2, 3$ for ^{87}Rb and ^{85}Rb respectively. Correspondingly the excited state of D_1 line $5^2P_{1/2}$ has two hyperfine levels $F' = 1, 2$ and $F' = 2, 3$ respectively. Similarly the excited state of D_2 line $5^2P_{3/2}$ has four hyperfine levels $F' = 0, 1, 2, 3$ and $F' = 1, 2, 3, 4$ respectively. Fig.2.6(a) and Fig.2.6(b) represent the D_1 and D_2 transitions of ^{87}Rb and ^{85}Rb with the hyperfine lines respectively. Each of the hyperfine levels consists of $(2F + 1)$ Zeeman sub-levels (for details see section 3.4 of the chapter 3).

2.4.1 Rb vapour cell

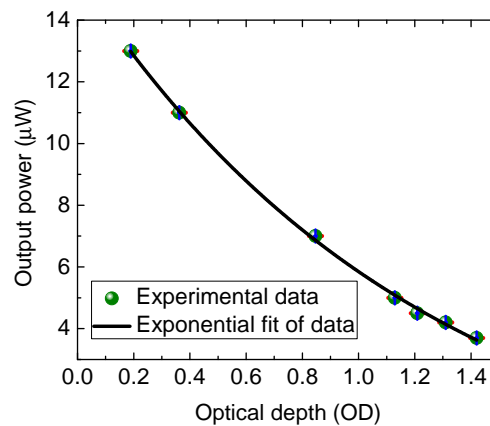


Figure 2.7: Cell characteristics with output power vs optical depth (OD, αL). With change in temperature of the vapour cell, the optical depth of the atomic medium was changed. From the absorption profile of the beam we have calculated the OD following the Beer-Lambert Law.

Since in a experiments we have studied the effect of OD on the observed phenomenon, to do the experiment with the cylindrical Pyrex cell, we need to study the absorption characteristics of the cell first to characterize the atomic medium. In this purpose, we have plotted the output power of a on-resonance beam as a function of the optical depth of the atomic medium in the Fig.2.7 and fit the data with an exponential function. The OD was changed as we changed the temperature of the vapour cell of length 50 mm. We have calculated the OD (αL) from the absorption profile of the resonant beam for each of the temperatures following the Beer-Lambert law, $I = I_0 e^{-\alpha L}$, where, I and I_0 are the output and the input intensities respectively with the absorption coefficient α and length of the atomic medium L . Since from the Fig.2.7 we have observed that the variation follows an exponential decay characteristics as the experimental data are fitted well with an exponential function, we can say that the absorption characteristics of cell follow the Beer-Lambert law.

2.5 Cell heating arrangement

The optical depth is an important parameter in the study of the interaction of the light with the atomic medium. The number density of the Rb atoms is $\sim 10^{15}/\text{m}^3$ in room temperature (21°C) under $\sim 10^{-7}$ Torr pressure. Due to the experimental needs, sometimes it is required to increase the number density or the optical depth (OD) of the atoms. For increment in the optical depth, the temperature of the Rb cell needs to be increased. To heat the cell, we used a home-build temperature controller with a double-walled cell jacket. The arrangement contains a double-walled jacket made of brass, silicon pipes, a

temperature controller, a pump to circulate hot water and a water heater.

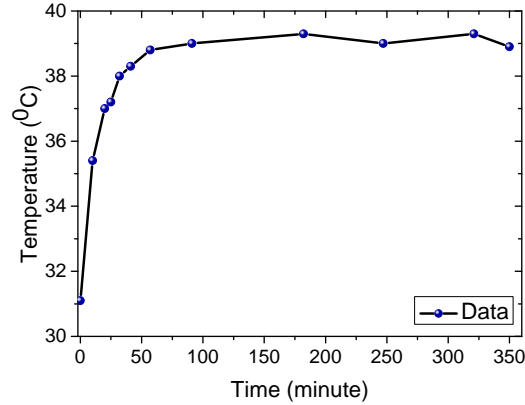


Figure 2.8: The temperature calibration curve of the home-built cell jacket with respect to time. It shows a fluctuations of $\pm 0.5^{\circ}\text{C}$ when the desired temperature is reached.

The inner cylinder of the double-walled jacket has an opening to place the Rb vapour cell inside it. After placing the Rb cell in the middle of the cell jacket, hot water was passed through the jacket. This home built temperature controller was used in our experiments. The temperature stability curve for 39°C is shown in the Fig.2.8. When the desired temperature was reached, its fluctuation was within $\pm 0.5^{\circ}\text{C}$. During heating, the atomic vapours were deposited on the cell window. Extra copper tapes were used to keep the window surfaces warmer than the rest of the cell body so that the vapour deposition can be avoided. This method is advantageous over the resistive heating technique because in that case, our experimental study can be affected due to the generated unwanted magnetic field.

2.6 Solenoid

There was only one perturbation in most of our experiments in this research work, i.e., the electric field of the laser beam. We gave an extra perturbation by applying external axial or longitudinal magnetic field along with the electric field of the laser in one of our experiments. As a result, the degeneracy between the magnetic or Zeeman sub-levels was removed. We used a home-made solenoid to generate the longitudinal magnetic field.

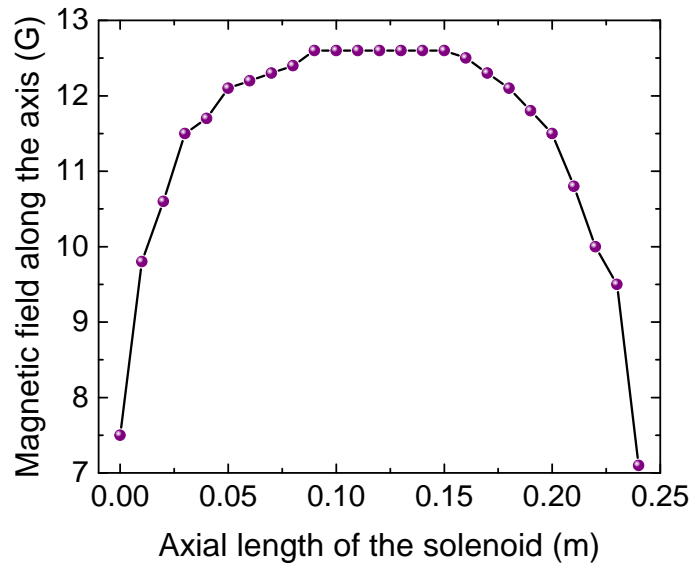


Figure 2.9: Magnetic field calibration along the axis of the solenoid.

A cylindrical paper board of length 0.24 m and diameter 0.05 m was chosen on which we wound copper wire of diameter ~ 1.1 mm. Since the length of the solenoid was larger than its diameter, we have calculated the value of magnetic field (B) generated inside the solenoid along its axis with the formula, $B = \frac{\mu_0 NI}{l}$. Here, μ_0 is the free space permeability, $N = 220$ is the total number of turns of wire, I is the current through the solenoid and $l = 0.24$ m is the length of the solenoid. Using this formula we got

$B = 12.67$ G for $I = 1.1$ A. After winding the wire, to calibrate the magnetic field we measured the field strength by a Hall probe with an accuracy of ± 0.01 G along the axis of the solenoid with a constant current $I = 1.1$ A. The variation is shown in the Fig.2.9. We observed the field was uniform over 0.06 m with the field strength $B = 12.60$ G. Since in our experiment the laser-atom interaction length was 50 mm or 0.05 m along the propagation direction, the magnetic field generated inside the solenoid is uniform within our experimental region. We used the relation $1 \text{ G} = 10^{-4} \text{ T}$ throughout our calculation in chapter 7 to maintain all units in S.I. system.

2.7 Magnetic shield



Figure 2.10: One of the home-made cylindrical μ -metal shields. The black wire was wrapped in the cylinder with toroidal fashion for the degaussing process.

The EIT based experiments are highly delicate to the external magnetic fields. When we perform high-resolution spectroscopy, it is mandatory to take care of the external magnetic fields, i.e., we need to control the magnetic field and also to maintain its homogeneity. The stray magnetic field, due to the earth, as well as generated from the nearby electronic instruments, bring a necessity to do experiments in a magnetically shielded environment. In this purpose, we have used μ -metal shields which are manufactured

with a high permeability material composition of nickel-iron alloy. The shields reduce the magnitude of the stray magnetic fields by several orders depending on the thickness of the shield. In most of our experiments, we have used one layer of thick μ -metal shield, which was commercially bought from Hamamatsu Photonics. This μ -metal shield has a diameter 0.1 m, length 0.2 m and thickness 0.002 m with attenuation factor ~ 911 . The efficiency of the shield can be improved further by using three or four layers of such shields. The shielding accuracy depends on the geometry of the shield. In one of our experiments, where we perturbed the atomic medium by the external magnetic field, to maintain homogeneity, we used three layers of cylindrical μ -metal shields of length 0.3 m each (see Fig.2.10). The three cylinders of μ -metal have diameters 0.07 m, 0.08 m and 0.09 m respectively. These cylinders were made from a sheet of μ -metal of thickness 0.001m at the workshop of our institute. The dimensions were so chosen such that the magnetic field generated inside the solenoid remains homogeneous and would not be affected by the stray magnetic fields.

The accuracy of the magnetic field shielding of the μ -metal degrades over time mostly due to the mechanical stress. To improve the efficiency of the shields, we used degaussing technique. The shield of each layer was wrapped with an electric wire in a toroidal approach shown in the Fig.2.10. Then the alternating current of 8 – 10 A was passed through the wire. With the help of a variac transformer, we slowly decreased the current over a few minutes. The process is repeated for several times. It, in turn, increase the efficiency of the shield. We have used a 10 Ω register in series with the wire to limit the current while using a variac.

2.8 Saturation absorption spectroscopy

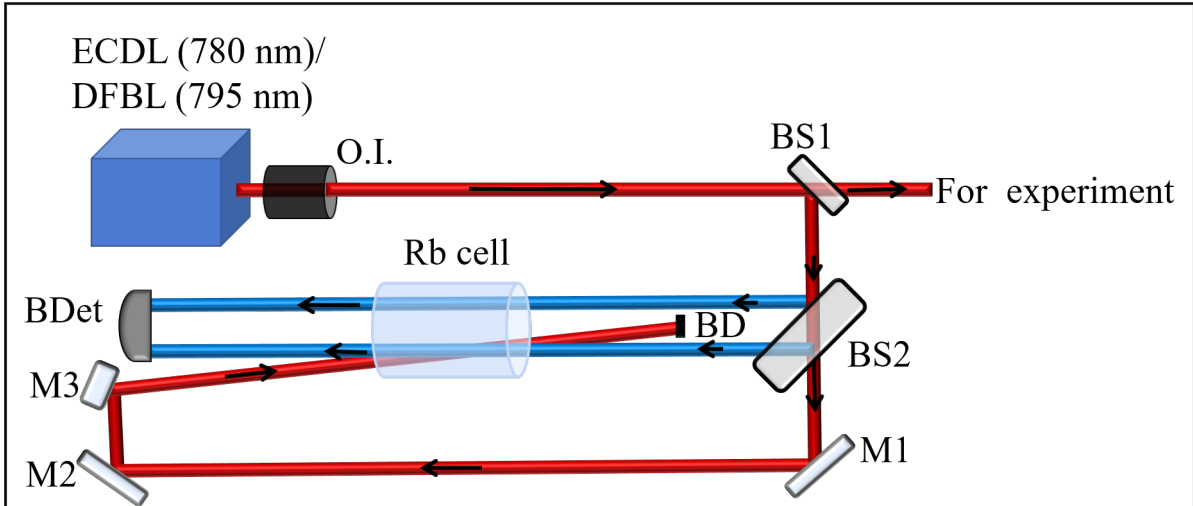


Figure 2.11: The general experimental setup to perform the saturation absorption spectroscopy with the ECDL and DFBL. ECDL: External Cavity Diode Laser, DFBL: Distributed Feedback Diode Laser, O.I.: Optical Isolator, BS: beam splitter, M: Mirror, Rb cell: Rubidium vapour cell, BD: Beam Dump, BDet: Balanced Photo-detector. The red line transmitted from the BS2 indicates the pump beam. The blue lines are the probe and the reference beams.

In the conventional laser spectroscopy, the closely spaced hyperfine transition lines are not resolvable due to the Doppler effect in the atomic medium. Since atoms have different velocities, due to the Doppler effect, instead of a narrow transition line, we observe a Doppler broadened absorption spectrum when laser passes through the atomic medium. The saturation absorption spectroscopy (SAS) technique helps us to get rid of the effect of Doppler broadening, which in turn helps us to resolve the hyperfine profiles of the atomic medium. To start any experiment related to the EIT phenomenon, first of all, we need to select particular hyperfine transitions so that a three-level atomic system can

be formed. Therefore, we had done the SAS for D_1 and D_2 transitions for both of the lasers. In SAS, a laser beam with a relatively higher intensity is sent through the atomic vapour (say Rb). This beam is called as the pump beam. Another counter-propagating weak beam is also sent through the atoms at the same frequency, which is known as the probe beam. The third beam, with almost the same intensity of the probe beam, is also sent through the atomic medium in parallel to the probe beam. This beam is called the reference beam. The experimental setup to perform the SAS is shown in the Fig.2.11. In this figure, it is shown that after coming out from the optical isolator (O.I.) the laser beam is split by a 10:90 (R:T) beam splitter (BS1). The reflection part is taken for the SAS, and the transmitted part is for the main spectroscopic experiments. After that, the reflected part is passed through a 30:70 thick beam splitter (BS2). The two reflected beams (blue lines) from the front (reference beam) and the rear surface (probe beam) of the BS2 are sent through the Rubidium vapour cell (Rb cell) parallel to each other. The transmitted beam (red line) is made counter-propagating with the probe beam and is sent through the Rb cell with the help of three mirrors (M1, M2 and M3). The pump is made overlapped with the probe beam inside the Rb cell. Then the reference beam and the probe beam are detected with a balanced photo-detector (BDet). The setup is similar for both the laser diodes (ECDL and DFBL), which are used in our experiments.

When only the reference beam is passed through the atomic medium, the Doppler broadened absorption profile was observed. It happened due to the thermal motion of the atoms. The atoms moving in the direction of the propagation of the beam are blue detuned with respect to the transition frequency and the atoms moving opposite to the beam propagation are red detuned. So we got a Doppler broadened absorption profile.

This is the case of moving atoms in a travelling wave. The linewidth of this Doppler broadened profile is a few hundred MHz while the natural linewidths of the hyperfine lines for the Rb atom are 5.76 MHz and 6 MHz for D_1 and D_2 transitions respectively. Due to this, the hyperfine lines can not be resolved by detecting only the reference beam. A standing wave is generated by the counter-propagating pump and probe beams in which the atoms are moving. Although the two beams are at the same frequency, they address a different set of atoms due to their natural thermal motion.

If the beams are red detuned with respect to the atomic transition frequency, the pump beam will be absorbed by the atoms moving towards the beam source. At the same time, the probe beam will be absorbed by the atoms moving away from that source at the same speed in the opposite direction. If the beams are blue detuned, the opposite phenomenon occurs. When the frequency of the applied field satisfy the resonance condition, the pump beam reduces the absorption of the probe beam for a very narrow frequency range [73, 74]. It leads to a Lamb dip in the Doppler background profile. This Lamb dip has a Lorentzian line shape with homogeneous linewidth. Here, the zero-velocity group of atoms are responsible for the hyperfine lines. Due to the velocity group of other atoms, additional resonances occur at the mid-value of the two consequent hyperfine transition frequencies. These resonances are called crossover peaks. These crossover peaks can be quite strong, often stronger than the main saturated absorption peaks.

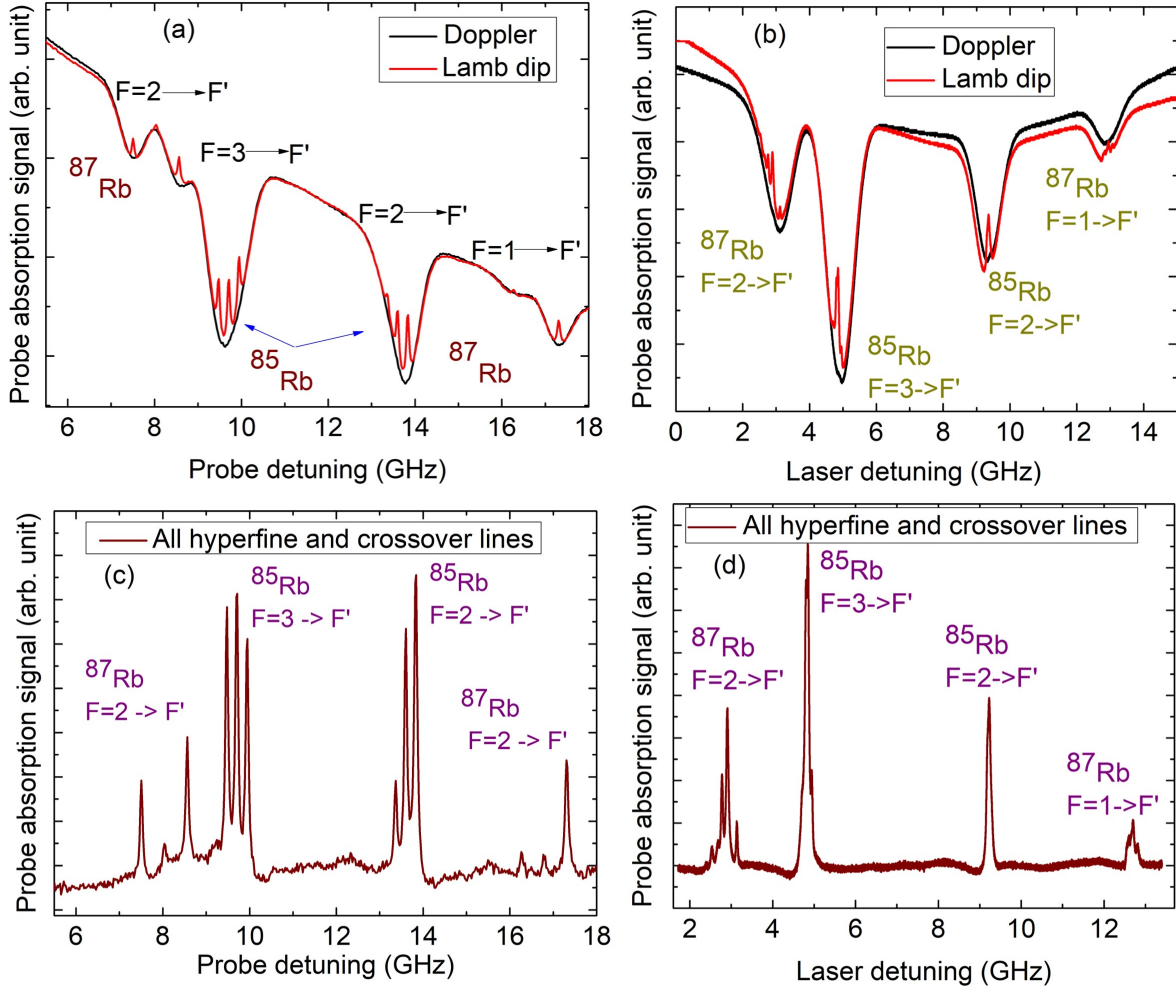


Figure 2.12: Doppler broadened profiles (black lines) of the reference beam, and the Lamb dips with Doppler background (red lines) of the probe beam for (a) D₁ and (b) D₂ transitions of both ⁸⁷Rb and ⁸⁵Rb. The hyperfine and the crossover line shapes (dark red lines) for (c) D₁ and (d) D₂ transitions of both ⁸⁷Rb and ⁸⁵Rb.

The Doppler broadened profiles of absorption for both D₁ and D₂ transitions are shown in Fig.2.12(a) and Fig.2.12(b) respectively with the black lines. The absorption profiles with the Lamb dips are shown with red lines in these two figures. Since there are two ground states for both the isotopes of Rb, we got four Doppler broadened absorption profiles for both D₁ and D₂ transitions. Now since the excited state separation of ⁸⁷Rb for D₁ transition is beyond the Doppler width at the room temperature of the Rb atom, one

Lamb dip was observed beyond the Doppler profile of ^{87}Rb in each case of D_1 transition as shown in the Fig.2.12(a). From this figure, we have also noticed that for each of the ground states of each of the isotopes, there are three Lamb dips because there are two excited states for each case. Two of the Lamb dips are the hyperfine lines, and the middle one is the crossover lines.

In case of the D_2 transitions since there are three excited states, transitions are allowed corresponding to each ground states of each of the isotopes of Rb atom. So in total six Lamb dips should be observed (see Fig.2.12(b)). All the narrow linewidth hyperfine and crossover peaks can be observed by subtracting the Doppler background from the Lamb dip profiles. For this reason, in this experiment, we used a BDet which produced the subtracted signal of the reference and the probe beam. In the Fig.2.12(c) and the Fig.2.12(d) the hyperfine and the crossover profiles for both D_1 and D_2 transitions are depicted. The peaks corresponding to ^{87}Rb and ^{85}Rb are marked in each of the plots of the Fig.2.12.

Most of our experiments had been performed with the D_1 transition of ^{87}Rb and ^{85}Rb and the D_2 transition of ^{87}Rb . In case of D_1 transition we mainly used the transitions of the excited states from the ground states $F = 2$ and $F = 3$ corresponding to ^{87}Rb and ^{85}Rb respectively. The hyperfine and crossover peaks corresponding to the above mentioned transitions are shown in Fig.2.13(a), Fig.2.13(b), Fig.2.13(c) and Fig.2.13(d) respectively.

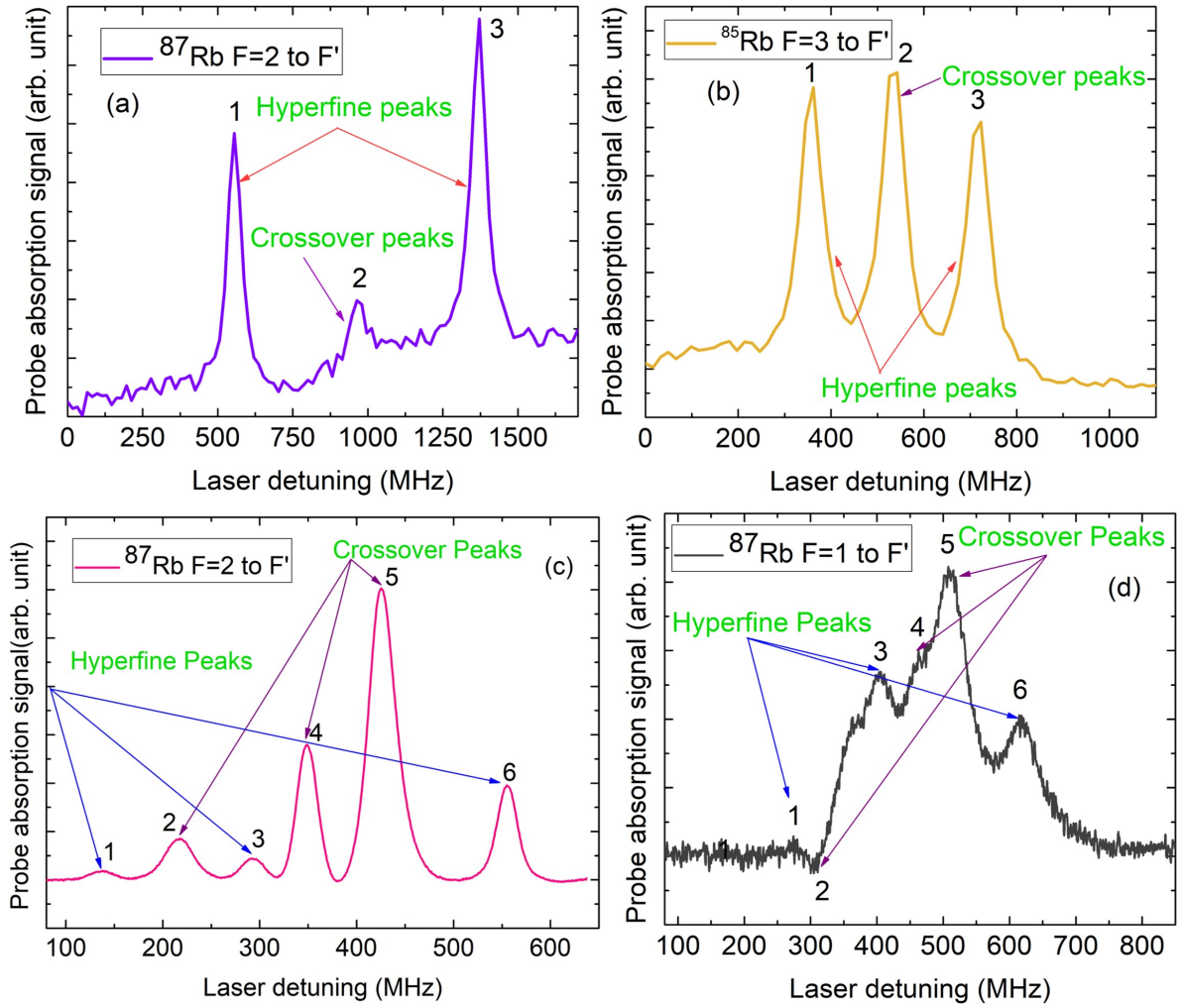


Figure 2.13: Hyperfine and crossover peaks in case of D_1 transition corresponding to (a) $F = 2 \rightarrow F' = 1, 2$ transitions of ^{87}Rb and (b) $F = 3 \rightarrow F' = 2, 3$ transitions of ^{85}Rb . In case of for D_2 transition the hyperfine and crossover peaks for ^{87}Rb corresponding to (c) $F = 2 \rightarrow F' = 1, 2, 3$ transitions and (d) $F = 1 \rightarrow F' = 0, 1, 2$ transitions.

In the Fig.2.13(a) and Fig.2.13(b) the peaks (1 and 3) indicated with red arrows are the hyperfine transition peaks due to $F = 2 \rightarrow F' = 1$ and $F = 2 \rightarrow F' = 2$ transitions for ^{87}Rb and transitions from $F = 3 \rightarrow F' = 2$ and $F = 3 \rightarrow F' = 3$ for ^{85}Rb respectively in D_1 transition. The peak 2, marked with the purple arrow is the crossover peak situated at the middle position between the two hyperfine peaks. In case of D_2 transitions the peaks 1, 3 and 6 designated with blue arrows are the hyperfine

peaks due to the transitions from $F = 2(1) \rightarrow F' = 1(0)$, $F = 2(1) \rightarrow F' = 2(1)$ and $F = 2(1) \rightarrow F' = 3(2)$ respectively for ^{87}Rb as shown in the Fig.2.13(c) and the Fig.2.13(d). The purple arrows show the crossover peaks 2, 4 and 5 of the corresponding transitions in the Fig.2.13(c) and the Fig.2.13(d) respectively.

The separations of the peaks depend on the separation of the hyperfine transitions. While the linewidth of the individual peaks depend on the relaxation rates as well as the intensity of the applied laser light [75].

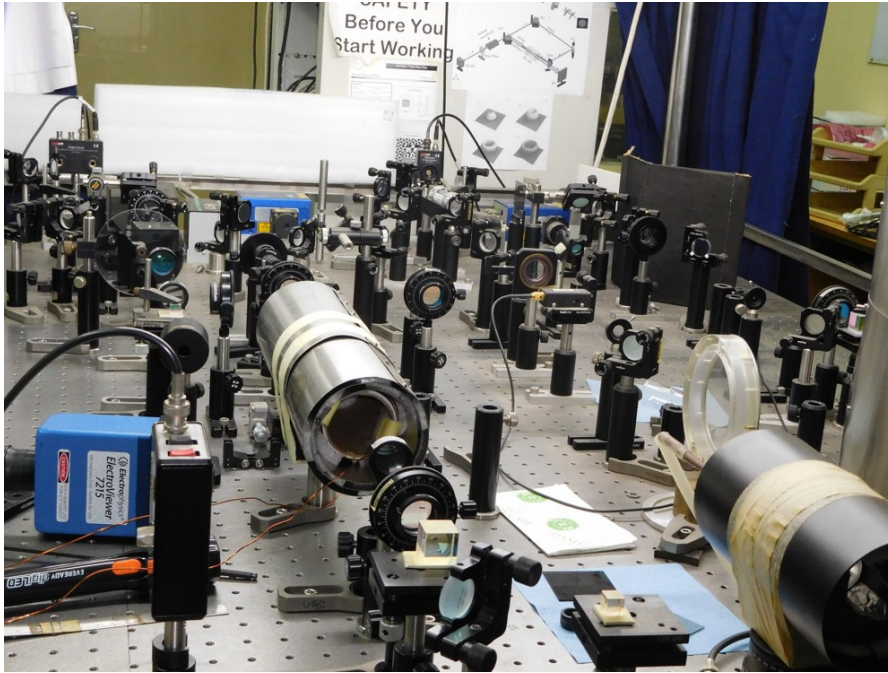


Figure 2.14: A representation of the real experimental setup of our laboratory

All the instruments mentioned above and accessories described in this chapter are needed to study the experiments related to quantum optics. Fig.2.14 shows a general image of the experimental setup in our laboratory with the accessories discussed above. Apart from these we also used a lot of optical components like mirrors (M), half-wave plates (HWP), quarter-wave plates (QWP), polarizing beam splitter cubes (PBS) etc.

according to our experimental needs.

3

Theoretical framework

To understand the physics behind our experimentally observed phenomena, we had built corresponding theoretical models. This research work also contains a theoretical analysis of atomic interactions with applied light fields in different configurations. In the first part of this chapter, we describe the semi-classical approach in density matrix formalism to calculate the atomic polarization, susceptibilities, atomic coherence, populations of the individual atomic levels, probe absorption and dispersion, etc. Then a two-level atomic system interacting with a classical field is discussed. After that, the hyperfine levels and the Zeeman levels of the atomic system are described. In the end, one of the atomic coherence effects with a general three-level atomic system is also discussed.

3.1 Semi-classical description of light-atom interaction

To describe the interaction of atoms with light fields, we have used the semi-classical representation [32, 33] in which the atom is considered as a quantum system in different configurations, e.g., two levels, three levels and four levels as the situation demand and the light, i.e. the laser field is treated as a classical electric field.

3.1.1 Formalism of density matrix: Equation of motion for density matrix

The wave function $|\psi\rangle$ contains complete information about a system in a pure state in the case of quantum mechanics. The state vector $|\psi\rangle$ can be written in a basis set $\{|i\rangle\}$ as,

$$|\psi\rangle = \sum_{i=1}^n c_i |i\rangle \quad (3.1.1)$$

While $|\psi\rangle$ carries all the possible information about a system, we cannot measure this quantity directly in an experiment. Instead of this, the expectation value of any quantum mechanical Hermitian operator (\hat{A}), which is a physical observable quantity, can be measured experimentally as,

$$\langle \hat{A} \rangle = \langle \psi | \hat{A} | \psi \rangle \quad (3.1.2)$$

where $|\psi\rangle$ is normalized as $\langle \psi | \psi \rangle = 1$. It can happen that for many situations, $|\psi\rangle$ is unknown and we know only the probability (P_ψ) of the system to be in the state $|\psi\rangle$. In such cases, not only the quantum mechanical average but also the ensemble average over many identical systems needs to be calculated. To do this we have defined the density operator as,

$$\rho = |\psi\rangle \langle \psi| \quad (3.1.3)$$

For a pure state, $P_\psi = 1$. Thus ρ can be written in terms of $n \times n$ density matrix, where n is the dimension of the Hilbert space. Therefore, the elements of the density matrix become

$$\rho_{ij} = \langle \psi | \rho | \psi \rangle \quad (3.1.4)$$

The normalization of the wave function gives $Tr[\rho] = \langle \psi | \psi \rangle = 1$. The diagonal terms are the probabilities $|c_i|^2$ for an atom to be in the state $|i\rangle$. The off-diagonal components $c_i c_j^*$ are called coherence since they are dependent on the phase difference between c_i and c_j . From Eq.(3.1.1) and Eq.(3.1.2) we get,

$$\langle \hat{A} \rangle = \sum_{i,j} c_i^* c_j \langle i | \hat{A} | j \rangle = \sum_{i,j} \rho_{ji} A_{ij} = \sum_j (\rho A)_{jj} = Tr[\rho A] \quad (3.1.5)$$

In above calculation we have considered the system to be in the pure state for which $Tr[\rho^2] = Tr[\rho] = 1$. For a mixed or impure state the density operator can be written as,

$$\rho = \sum_{\psi} P_{\psi} |\psi\rangle \langle \psi| \quad (3.1.6)$$

In this case $Tr[\rho^2] \leq Tr[\rho]$.

When light travels through an atomic medium, it polarizes that atomic medium. This in turn affects the propagation of the light field. Since we measure the experimental signal after it crosses the medium, it contains the changes occurred in the properties of light due to interaction with the atom. The polarization of the medium \vec{P} can be calculated from the density matrix as the expectation value of the dipole moment operator $\vec{\mu}$ as,

$$\vec{P} = N_0 Tr[\rho \vec{\mu}] = N_0 \sum_{i,j} \rho_{ji} \mu_{ij} \quad (3.1.7)$$

where N_0 is the atomic number density. From the above equation we can write,

$$\vec{P} = N_0 (\rho_{ji} \mu_{ij} + \rho_{ij} \mu_{ji}) \quad (3.1.8)$$

Again the atomic polarization can be expressed in terms of susceptibility χ of the medium as [32, 33],

$$\vec{P} = \frac{1}{2} \epsilon_0 E \hat{e} [\chi(\omega) e^{-i(\omega t - kz)} + \chi^*(\omega) e^{i(\omega t - kz)}] \quad (3.1.9)$$

where E is the amplitude of the electric field. Therefore, Eq.(3.1.8) and Eq.(3.1.9) yields,

$$\chi = \frac{2N_0\mu_{ij}}{\epsilon_0 E} \rho_{ji} \quad (3.1.10)$$

The susceptibility of the medium carries all the information about the absorption and the dispersion properties of the atomic medium when light interacts with it. The imaginary part (χ'') of the susceptibility carries the information about the absorption and the real part (χ') describes the information of the dispersion of the medium respectively. The dependency of the susceptibility on frequency is due to the coherence term of the density matrix as in Eq.(3.1.10), the other terms are independent of frequency. It makes the formulation of the time evolution of the density matrix important.

The equation of motion of the density matrix can be derived from Schrödinger equation [32],

$$\frac{d|\psi\rangle}{dt} = -\frac{i}{\hbar} H |\psi\rangle \quad (3.1.11)$$

Taking time derivative of the Eq.(3.1.6) and using Eq.(3.1.11) we obtain [32],

$$\frac{d\rho}{dt} = -\frac{i}{\hbar} [H, \rho] \quad (3.1.12)$$

Eq.(3.1.12) is known as the Liouville equation or the von Neumann equation of motion for the density matrix [32]. This equation is also called the master equation for the system. The Eq.(3.1.12) describes the statistical properties, as well as the quantum mechanical information about the system because it consists of a density operator rather than a specific state vector. In this equation, the decay of the atomic levels is not considered since it is derived from the Schrödinger wave equation. But the atoms decay with spontaneous emission. So we need to consider the relaxation terms for an atomic system. Again, the other decay mechanism like collisional decay persists in the atomic

systems. The relaxation terms can be added phenomenologically in the master equation. This relaxation operator can be defined as [76],

$$\langle i|\Gamma|j\rangle = \Gamma_j\delta_{ij} \quad (3.1.13)$$

This matrix can also be called as depopulation matrix. After considering the decay matrix phenomenologically the modified density matrix equation of motion becomes,

$$\frac{d\rho}{dt} = -\frac{i}{\hbar}[H, \rho] - \frac{1}{2}\{\Gamma, \rho\} \quad (3.1.14)$$

where $\{\}$ is the anti-commutator. If we assume the conservation of the number of atoms, the population which decay from the excited states must be repopulated to the ground states. Then the Eq.(3.1.14) can be modified further by considering the re-population matrix Λ_0 [76]. Therefore,

$$\frac{d\rho}{dt} = -\frac{i}{\hbar}[H, \rho] - \frac{1}{2}\{\Gamma, \rho\} + \Lambda_0 \quad (3.1.15)$$

Now the time evolution of an element of the density matrix can be written as,

$$\dot{\rho}_{ij} = -\frac{i}{\hbar} \sum_k (\mathcal{H}_{ik}\rho_{kj} - \rho_{ik}\mathcal{H}_{kj}) - \frac{1}{2} \sum_k (\Gamma_{ik}\rho_{kj} + \rho_{ik}\Gamma_{ik}) + \Lambda_{ij} \quad (3.1.16)$$

The Eq.(3.1.16) is useful in the treatment of the multilevel atomic system. Thus, We have added the re-population and the depopulation terms directly (as discussed above) in each of the density matrix equations phenomenologically in all of our theoretical models presented in the later chapters.

3.2 Two-level atom

A two-level atom [32, 33, 76] interacting with a classical optical field, $\vec{\varepsilon}(t)$ (see Fig.3.1) is considered in order to give an overview of the light-atom interactions. The external field $\vec{\varepsilon}(t)$ polarized along the direction \hat{e} is given as,

$$\vec{\varepsilon}(t) = E_0 \cos(\omega t) \hat{e} \quad (3.2.1)$$

where E_0 and ω are the amplitude and the frequency of the electric field respectively. To get the density matrix elements, we need to calculate the Hamiltonian of the system, relaxation matrices and re-population matrices as required by the Eq.(3.1.15) or Eq.(3.1.16).

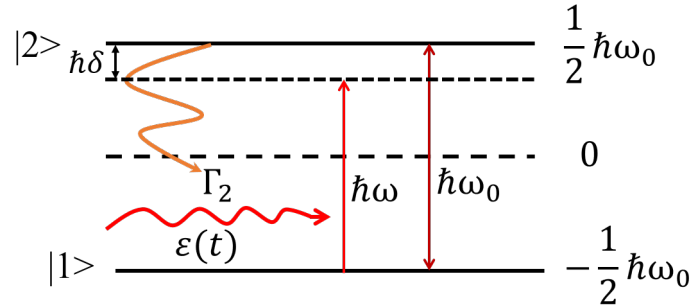


Figure 3.1: A two-level atomic system with ground state $|1\rangle$ and excited state $|2\rangle$ interacts with a laser of frequency ω . $\delta = (\omega_0 - \omega)$ is the detuning and Γ_2 is the decay rate from state $|2\rangle$.

The total Hamiltonian of the system is given by

$$H = H_0 + H_p \quad (3.2.2)$$

where H_0 and H_p are the unperturbed and the perturbed Hamiltonian of the system,

respectively. The unperturbed Hamiltonian of the two-level system is given by,

$$H_0 = \frac{\hbar}{2} \begin{bmatrix} -\omega_0 & 0 \\ 0 & \omega_0 \end{bmatrix} \quad (3.2.3)$$

with the transition frequency between the states $|1\rangle \rightarrow |2\rangle$ is ω_0 . The perturbed Hamiltonian with the electric dipole approximation can be written as,

$$H_p = -\vec{\mu} \cdot \vec{\varepsilon}(t) = -\frac{\hbar}{2} \begin{bmatrix} 0 & \Omega_{12}(e^{-i\omega t} + e^{i\omega t}) \\ \Omega_{21}(e^{-i\omega t} + e^{i\omega t}) & 0 \end{bmatrix} \quad (3.2.4)$$

where $\vec{\mu}$ is the dipole moment operator of the transition $|1\rangle \rightarrow |2\rangle$ and $\Omega_{12} = \Omega_{21}^* = E_0 \frac{\langle 1 | \vec{\mu} \cdot \hat{\varepsilon} | 2 \rangle}{\hbar}$ is the Rabi frequency of the applied electric field. Therefore the total Hamiltonian takes the form [76],

$$H = \frac{\hbar}{2} \begin{bmatrix} -\omega_0 & -\Omega_{12}(e^{-i\omega t} + e^{i\omega t}) \\ -\Omega_{21}(e^{-i\omega t} + e^{i\omega t}) & \omega_0 \end{bmatrix} \quad (3.2.5)$$

From Eq.(3.2.5), it can be seen that the Hamiltonian of the system depends on time. So, the polarization of the medium also becomes time-dependent, oscillating with the light frequency. But the explicit time dependency can be removed as this time scale is much shorter than any other time scale of the problem. Therefore, we have to do an average over many cycles of the optical oscillation for any measurement. It is also noticed from Eq.(3.2.5), that the optical field oscillates with a frequency ω having a coupling strength $\hbar\Omega_{12}$. This prompted a transition between the states $|1\rangle \rightarrow |2\rangle$ with transition frequency ω_0 . If $\omega \approx \omega_0$, then one component of the field is in near-resonant condition, termed as co-rotation and the other component 2ω which is in far detuned condition, is named as counter-rotation. In the case of the optical transition, we can neglect the far detuned term. Now if the operators are transformed in a new rotating basis with the co-rotating frame, then the measurements will be static with respect to the rotating frame

which is known as the rotating wave approximation (RWA) [32, 33, 76]. RWA¹ is an approximation used in atom optics and magnetic resonance. In this approximation, terms in a Hamiltonian which oscillate rapidly are neglected. When the applied electromagnetic radiation is near resonance with an atomic transition and the intensity is low or when the field-atom coupling strength is a small fraction of bare frequency of an uncoupled atom, we can apply the RWA. The name of the approximation originates from the form of the Hamiltonian in the interaction picture. Transforming to this picture the evolution of an atom due to the corresponding atomic Hamiltonian is absorbed into the state of the system, leaving only the evolution due to the interaction of the atom with the light field to consider. We can neglect the rapidly oscillating term in this picture. In other words, only the part of the electromagnetic wave which co-rotates with the system-state is kept while the counter rotating component is discarded, as we can think the interaction picture as rotating with the state of system.

Therefore, to make the transformation from the Schrödinger to the interaction picture or to find out a rotated basis we assume a unitary matrix,

$$\mathcal{U} = \begin{bmatrix} e^{i\omega t/2} & 0 \\ 0 & e^{-i\omega t/2} \end{bmatrix} \quad (3.2.6)$$

which satisfies the relation $\mathcal{U}^\dagger \mathcal{U} = 1$. In a rotating frame, the state vector $|\psi\rangle$ changes to $|\tilde{\psi}\rangle$ as

$$|\tilde{\psi}\rangle = \mathcal{U}^\dagger |\psi\rangle \quad (3.2.7)$$

¹When the driving field in a two-level system gets strong, e.g., atoms driven by a strong laser field or nuclear spins in NMR, driven by a strong oscillating magnetic field (radio frequency) then RWA is no longer valid. In 1940, Felix Bloch and Arnold Siegert showed that the dropped parts oscillating rapidly can give rise to a shift in the true resonance frequency of the dipoles. This shift is known as Bloch-Siegert shift (BSS). The corresponding shift is given by [77], $\Delta\omega_{BSS} = \frac{1}{4} \frac{\Omega_{21}^2}{\omega_0}$. The method to get a solution keeping the counter-rotating term for the strong field effects in the radio-frequency spectroscopy is discussed in details in the textbook [33]. In the mentioned reference, the result is shown in terms of a continued fraction, BSS and multiphoton resonances.

Similarly, on a rotating basis, the operators will also be modified. Now we start with the time-dependent Schrödinger equation in the laboratory frame,

$$H |\psi\rangle = i\hbar \frac{d}{dt} |\psi\rangle \quad (3.2.8)$$

Multiplying both sides by \mathcal{U}^\dagger and inserting the identity operator $\mathcal{U}\mathcal{U}^\dagger$ in front of the state ket on each side of the above equation yields,

$$\mathcal{U}^\dagger H \mathcal{U} \mathcal{U}^\dagger |\psi\rangle = i\hbar \mathcal{U}^\dagger \frac{d}{dt} \mathcal{U} \mathcal{U}^\dagger |\psi\rangle \quad (3.2.9)$$

Using Eq.(3.2.7), the above equation can be rearranged to form

$$(\mathcal{U}^\dagger H \mathcal{U} - i\hbar \mathcal{U}^\dagger \frac{d}{dt} \mathcal{U}) |\tilde{\psi}\rangle = i\hbar \frac{d}{dt} |\tilde{\psi}\rangle \quad (3.2.10)$$

Comparing Eq.(3.2.10) with Eq.(3.2.8), the effective Hamiltonian in the rotating frame can be written as

$$H_{eff} = (\mathcal{U}^\dagger H \mathcal{U} - i\hbar \mathcal{U}^\dagger \frac{d}{dt} \mathcal{U}) \quad (3.2.11)$$

Now,

$$\begin{aligned} \mathcal{U}^\dagger H \mathcal{U} &= \begin{bmatrix} e^{-i\omega t/2} & 0 \\ 0 & e^{i\omega t/2} \end{bmatrix} \frac{\hbar}{2} \begin{bmatrix} -\omega_0 & -\Omega_{12}(e^{-i\omega t} + e^{i\omega t}) \\ -\Omega_{21}(e^{-i\omega t} + e^{i\omega t}) & \omega_0 \end{bmatrix} \begin{bmatrix} e^{i\omega t/2} & 0 \\ 0 & e^{-i\omega t/2} \end{bmatrix} \\ &= \begin{bmatrix} e^{-i\omega t/2} & 0 \\ 0 & e^{i\omega t/2} \end{bmatrix} \frac{\hbar}{2} \begin{bmatrix} -\omega_0 e^{i\omega t/2} & -\Omega_{12}(e^{-3i\omega t/2} + e^{i\omega t/2}) \\ -\Omega_{21}(e^{-i\omega t/2} + e^{3i\omega t/2}) & \omega_0 e^{-i\omega t/2} \end{bmatrix} \\ &= \frac{\hbar}{2} \begin{bmatrix} -\omega_0 & -\Omega_{12}(e^{-2i\omega t} + 1) \\ -\Omega_{21}(1 + e^{2i\omega t}) & \omega_0 \end{bmatrix} \end{aligned} \quad (3.2.12)$$

and

$$\begin{aligned}
i\hbar\mathcal{U}^\dagger \frac{d}{dt}\mathcal{U} &= i\hbar \begin{bmatrix} e^{-i\omega t/2} & 0 \\ 0 & e^{i\omega t/2} \end{bmatrix} \frac{d}{dt} \begin{bmatrix} e^{i\omega t/2} & 0 \\ 0 & e^{-i\omega t/2} \end{bmatrix} \\
&= i\hbar \begin{bmatrix} e^{-i\omega t/2} & 0 \\ 0 & e^{i\omega t/2} \end{bmatrix} \begin{bmatrix} \frac{i\omega}{2}e^{i\omega t/2} & 0 \\ 0 & -\frac{i\omega}{2}e^{-i\omega t/2} \end{bmatrix} \\
&= \frac{\hbar}{2} \begin{bmatrix} -\omega & 0 \\ 0 & \omega \end{bmatrix}
\end{aligned} \tag{3.2.13}$$

Therefore using results of Eq.(3.2.12) and Eq.(3.2.13) in Eq.(3.2.11), We obtain the matrix form of the effective Hamiltonian as,

$$H_{eff} = \frac{\hbar}{2} \begin{bmatrix} -\delta & -\Omega_{12}(1 + e^{-2i\omega t}) \\ -\Omega_{21}(1 + e^{2i\omega t}) & \delta \end{bmatrix} \tag{3.2.14}$$

where $\delta = \omega_0 - \omega$ is the detuning of the applied electric field. The counter rotating 2ω frequency term can be neglected due to far off detuning. So, after the RWA, the effective Hamiltonian becomes,

$$H_{eff} = \frac{\hbar}{2} \begin{bmatrix} -\delta & -\Omega_{12} \\ -\Omega_{21} & \delta \end{bmatrix} \tag{3.2.15}$$

In this way, the effective Hamiltonian becomes time-independent or static after the RWA with respect to the rotating frame.

3.2.1 Optical Bloch equation

In case of a two level atomic system shown in the Fig.3.1 the density matrix can be written as,

$$\rho = \begin{bmatrix} \rho_{11} & \rho_{12} \\ \rho_{21} & \rho_{22} \end{bmatrix} \tag{3.2.16}$$

If the excited state can decay spontaneously at a rate of Γ_2 , then the relaxation matrix is given by,

$$\Gamma = \begin{bmatrix} 0 & 0 \\ 0 & \Gamma_2 \end{bmatrix} \quad (3.2.17)$$

Now, the population which decay from the upper level $|2\rangle$ can repopulate in the lower level of the atom $|1\rangle$. If the total population is conserved for a closed two level system then the re-population matrix becomes [76],

$$\Lambda_0 = \begin{bmatrix} \Gamma_2 \rho_{22} & 0 \\ 0 & 0 \end{bmatrix} \quad (3.2.18)$$

Using Eq.(3.2.15), Eq.(3.2.16), Eq.(3.2.17) and Eq.(3.2.18), the time evolution equations for the density matrix elements can be obtained in the rotating frame from the Eq.(3.1.16) as,

$$\begin{aligned} \dot{\rho}_{11} &= \Gamma_2 \rho_{22} + \frac{i}{2} \Omega_{12} \rho_{21} - \frac{i}{2} \Omega_{21} \rho_{12} \\ \dot{\rho}_{22} &= -\Gamma_2 \rho_{22} - \frac{i}{2} \Omega_{12} \rho_{21} + \frac{i}{2} \Omega_{21} \rho_{12} \\ \dot{\rho}_{12} &= -\left(\frac{\Gamma_2}{2} - i\delta\right) \rho_{12} - \frac{i}{2} \Omega_{12} (\rho_{11} - \rho_{22}) \\ \dot{\rho}_{21} &= -\left(\frac{\Gamma_2}{2} + i\delta\right) \rho_{21} + \frac{i}{2} \Omega_{12} (\rho_{11} - \rho_{22}) \end{aligned} \quad (3.2.19)$$

The equations in Eq.(3.2.19) are known as the optical Bloch equations (OBE) [32, 33, 76]. Here, $(\frac{\Gamma_2}{2} - i\delta)^{-1}$ is the complex detuning term. ρ_{ii} and ρ_{ij} are the population and the coherence terms, respectively. The population terms inform us about the scattering rates of the system, and the coherence terms give the essence of the absorption and the dispersion properties of the system. By solving the time-dependent solution of the OBE, we have plotted the transient behaviour of the excited state and the ground state along with the coherence term in the Fig.3.2.

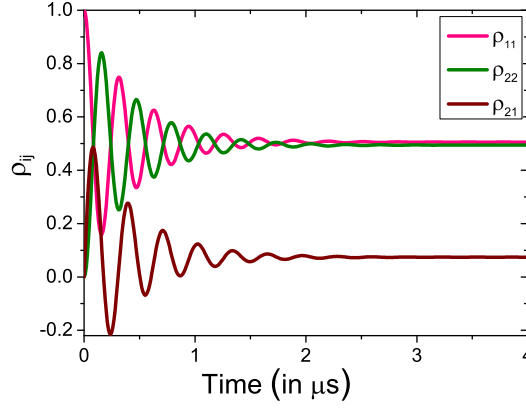


Figure 3.2: Transient behaviour of the population terms corresponding to the ground state (ρ_{11}) and the excited state (ρ_{22}) and the coherence term (ρ_{21}).

From the Fig.3.2 it can be noticed that ρ_{ij} shows oscillatory behaviour with respect to the time. These oscillations are the Rabi oscillations with a frequency Ω_{12} . The oscillations are dying down after some time as the system has decayed and it has reached the steady-state. The decay time depends on the natural linewidth Γ_2 .

The steady-state solution (see Appendix A for details) of the OBE can be obtained by considering $\dot{\rho}_{ij} = 0$. With the conservation of population i.e. $\rho_{11} + \rho_{22} = 1$, we can solve the OBE analytically and the solutions are given by,

$$\begin{aligned}
 \rho_{11} &= \frac{\Omega_{12}^2 + 4\left(\frac{\Gamma_2^2}{4} + \delta^2\right)}{2\{\Omega_{12}^2 + 2\left(\frac{\Gamma_2^2}{4} + \delta^2\right)\}} \\
 \rho_{22} &= \frac{\Omega_{12}^2}{2\{\Omega_{12}^2 + 2\left(\frac{\Gamma_2^2}{4} + \delta^2\right)\}} \\
 \rho_{21} &= i \frac{\Omega_{12}\left(\frac{\Gamma_2^2}{4} + \delta^2\right)}{\left(\frac{\Gamma_2}{2} + i\delta\right)\{\Omega_{12}^2 + 2\left(\frac{\Gamma_2^2}{4} + \delta^2\right)\}}
 \end{aligned} \tag{3.2.20}$$

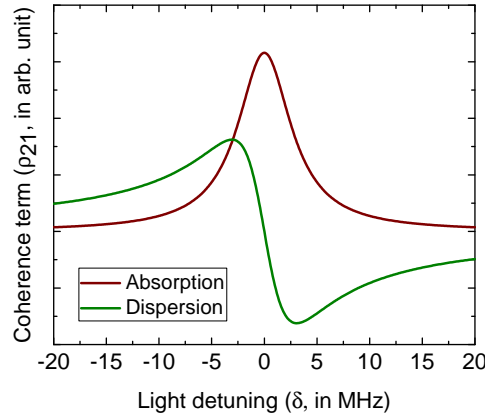


Figure 3.3: Steady state solution of the coherence term as a function of light detuning. Imaginary and real parts of the coherence term represent the absorption (red line) and dispersion (green line) profiles of the beam, interacting with the system respectively.

We have plotted the steady-state solution of the probe coherence as a function of the detuning in the Fig.3.3. $Im[\rho_{21}]$ and $Re[\rho_{21}]$ give the absorption and dispersion respectively. The absorption profile shows a Lorentzian behaviour due to the homogeneous decay of the system. The width of this profile is dependent on the Rabi frequency and the decay rate of the upper excited state. The width, $\sqrt{\Omega_{12}^2 + \Gamma_2^2/4}$, is called the power broadened width.

3.2.2 Dressed states

The rotating frame Hamiltonian in the Eq.(3.2.15) is presented in the bare state basis of the atomic levels $\{1, 2\}$. But, sometimes it is convenient to represent the phenomena on a different basis, e.g. the atom + photon basis where the photon dresses the bare atomic levels. This basis is known as the dressed state basis. For this purpose, we need to diagonalize the Hamiltonian matrix. By diagonalizing the Hamiltonian given in

Eq.(3.2.15) we have obtained the eigenvalues as [32],

$$R = \pm \sqrt{\Omega_{21}^2 + \delta^2} \quad (3.2.21)$$

and the corresponding eigenvectors are calculated by an effective rotation of the uncoupled basis states $|1\rangle$ and $|2\rangle$ as,

$$\begin{bmatrix} |+\rangle \\ |-\rangle \end{bmatrix} = \begin{bmatrix} \cos \theta |1\rangle + \sin \theta |2\rangle \\ -\sin \theta |1\rangle + \cos \theta |2\rangle \end{bmatrix} \quad (3.2.22)$$

The states represented in Eq.(3.2.22) are the dressed states of the two level system where, $\cos \theta = \frac{\Omega_{21}}{\sqrt{(R-\delta)^2 + |\Omega_{21}|^2}}$ and $\sin \theta = \frac{R-\delta}{\sqrt{(R-\delta)^2 + |\Omega_{21}|^2}}$. The eigenvalues represented in the Eq.(3.2.21) are called generalized Rabi frequencies. The energy corresponding to these frequencies have a shift from the energy of the bare state and is known as the AC-Stark shift.

3.3 Hyperfine levels

This research work is mainly based on alkali metals, which is a one-electron system. Most of the experiments were done in the hyperfine levels of Rubidium atom. Since the atom has nuclear spin, the hyperfine shifts exist in this type of system. This section will cover the discussion on the hyperfine coupling.

It is known that due to the coupling between the orbital angular momentum \vec{L} and the spin angular momentum \vec{S} of the electrons, the fine structure of the atom occurs. Again, the coupling of the \vec{L} and \vec{S} creates the total angular momentum \vec{J} of the atom as,

$$\vec{J} = \vec{L} + \vec{S} \quad (3.3.1)$$

where \vec{J} can take values in between,

$$|L - S| \leq J \leq |L + S| \quad (3.3.2)$$

On the other hand, the nucleus can have the spin angular momentum \vec{I} similar to the electrons. Similarly, the nuclear spin can couple to the total angular momentum. This leads to the hyperfine splitting of the atoms. So, the total hyperfine angular momentum \vec{F} becomes,

$$\vec{F} = \vec{J} + \vec{I} \quad (3.3.3)$$

and can take values in between,

$$|J - I| \leq F \leq |J + I| \quad (3.3.4)$$

The energy levels will be shifted due to the hyperfine coupling. The Hamiltonian describing the hyperfine splitting can be written as [78, 79],

$$\begin{aligned} H_{hfs} = & A_{hfs} \vec{I} \cdot \vec{J} + B_{hfs} \frac{3(\vec{I} \cdot \vec{J})^2 + \frac{3}{2} \vec{I} \cdot \vec{J} - I(I+1)J(J+1)}{2I(2I-1)J(2J-1)} \\ & + C_{hfs} \frac{10(\vec{I} \cdot \vec{J})^3 + 2(\vec{I} \cdot \vec{J})[I(I+1) + J(J+1) + 3] - 3I(I+1)J(J+1) - 5I(I+1)J(J+1)}{I(I-1)(2I-1)J(J-1)(2J-1)} \end{aligned} \quad (3.3.5)$$

The energy level splitting can be calculated from the above equation. The hyperfine energy shift becomes,

$$\begin{aligned} \Delta E_{hfs} = & \frac{1}{2} A_{hfs} K + B_{hfs} \frac{\frac{3}{2} K(K+1) - 2I(I+1)J(J+1)}{2I(2I-1)2J(2J-1)} \\ & + C_{hfs} \frac{5K^2(\frac{K}{4} + 1) + K[I(I+1) + J(J+1) + 3 - 3I(I+1)J(J+1)] - 5I(I+1)J(J+1)}{I(I-1)(2I-1)J(J-1)(2J-1)} \end{aligned} \quad (3.3.6)$$

where, $K = F(F+1) - I(I+1) - J(J+1)$. In the above Eq.(3.3.5) and Eq.(3.3.6), A_{hfs} , B_{hfs} and C_{hfs} are the magnetic dipole constant, the electric quadrupole constant and the magnetic octupole constant respectively. The terms corresponding to B_{hfs} and

C_{hfs} apply only to the excited state manifold of the D_2 transition and not to the D_1 transition.

3.4 Zeeman shift

The hyperfine levels have $(2F + 1)$ manifold, and the levels are degenerate in the absence of an external magnetic field. If the magnetic field is applied, the degeneracy of the energy levels will be broken. This phenomenon is known as the Zeeman effect. To describe the interactions of the atoms with the magnetic field, the Hamiltonian can be written as,

$$H_B = \frac{\mu_B}{\hbar} (g_S \vec{S} + g_L \vec{L} + g_I \vec{I}) \cdot \vec{B} \quad (3.4.1)$$

If the magnetic field is applied in the z direction, then the Hamiltonian becomes,

$$H_B = \frac{\mu_B}{\hbar} (g_S S_z + g_L L_z + g_I I_z) B_z \quad (3.4.2)$$

where, g_S , g_L and g_I are the g-factors of the electron spin, the electron orbital angular momentum and the nuclear spin respectively and μ_B is the Bohr magneton.

J will be a good quantum number where the energy shift is small comparable to the fine structure splitting and the corresponding Hamiltonian further becomes [78, 79],

$$H = \frac{\mu_B}{\hbar} (g_J J_z + g_I I_z) B_z \quad (3.4.3)$$

g_J is the Lande g-factor and is given by,

$$\begin{aligned} g_J &= g_L \frac{J(J+1) - S(S+1) + L(L+1)}{2J(J+1)} + g_S \frac{J(J+1) + S(S+1) - L(L+1)}{2J(J+1)} \\ &\simeq 1 + \frac{J(J+1) + S(S+1) - L(L+1)}{2J(J+1)} \end{aligned} \quad (3.4.4)$$

with $g_L = 1$ and $g_S = 2$.

In case of the applied ‘high’ magnetic field strength, Eq.(3.4.3) describes the appropriate interaction. This interaction term dominates the hyperfine energies so that the hyperfine Hamiltonian perturbs the strong-field eigenstate $|Jm_JIm_I\rangle$. The interaction of the atoms with high magnetic field is known as the *Paschen-Back effect*. In this case, the energies are given by [78, 79],

$$E_{|Jm_JIm_I\rangle} \approx A_{hfs}m_I m_J + B_{hfs} \frac{9m_I^2 m_J^2 - 3J(J+1)mI^2 - 3I(I+1)m_J^2 + I(I+1)J(J+1)}{4J(2J-1)I(2I-1)} + \mu_B(g_J m_J + g_I m_I)B \quad (3.4.5)$$

For the applied ‘small’ magnetic field where the energy splitting due to the magnetic field is small enough compared to the hyperfine splitting, \vec{F} will be a good quantum number. Assuming the quantization axis along the z -direction the corresponding interaction Hamiltonian becomes,

$$H_B = \frac{\mu_B}{\hbar} g_F F_z B_z \quad (3.4.6)$$

Here, the hyperfine Lande g-factor g_F is defined as,

$$g_F = g_J \frac{F(F+1) - I(I+1) + J(J+1)}{2F(F+1)} + g_I \frac{F(F+1) + I(I+1) - J(J+1)}{2F(F+1)} \simeq g_J \frac{F(F+1) - I(I+1) + J(J+1)}{2F(F+1)} \quad (3.4.7)$$

Moreover, the nuclear correction term g_I is neglected since $g_I \ll g_J$.

Thus when the energy level splitting is small due to the smaller applied magnetic field, the Hamiltonian in Eq.(3.4.6) describes the proper interaction. It perturbs the zero-field eigenstates of H_{hfs} . the level splitting is given to the lowest order by,

$$\Delta E_{|Fm_F\rangle} = \mu_B g_F m_F B_z \quad (3.4.8)$$

It is a linear Zeeman shift, and this regime is called the *anomalous Zeeman effect* or simply the *Zeeman effect*.

3.5 Doppler broadening

In the spectroscopy, no resonance line is infinitely narrow. A finite width is always associated with the resonance line. Spontaneous emission introduces a finite lifetime to the upper state (by the uncertainty principle). Therefore we can say that every transition has a natural width. Finite observation time, collisions, the motion of the atom, field inhomogeneity, pressure, etc. are the parameters which lead to an additional broadening of the spectral lines. These may be of two types, (i) homogeneous broadening and (ii) inhomogeneous broadening. Since the probability of absorption or emission of radiation is equal for all the atoms in an ensemble, natural linewidth having Lorentzian line shape is an example of homogeneous broadening. The transition probability is not equal for all atoms but depends on their velocity, e.g., Doppler broadening, which has a Gaussian line profile in case of inhomogeneous broadening. In this section, we will discuss Doppler broadening, which is very relevant to vapour cell experiments.

The relationship between the angular frequency ω of incident light field in the laboratory frame of reference and the angular frequency (ω') seen in a frame of reference moving at velocity v can be written using Doppler effect as,

$$\omega' = \omega - \vec{k} \cdot \vec{v} \quad (3.5.1)$$

where the wave-vector \vec{k} of the incident radiation has magnitude $k = \frac{\omega}{c} = \frac{2\pi}{\lambda}$. The component of the velocity along \vec{k} leads to the Doppler effect. Here, $\vec{k} \cdot \vec{v} = kv\cos\theta = kv$ as $\theta = 0$. The Doppler effect acts on the absorption by a gas where each atom absorbs radiation with frequency ω_0 in its rest frame, i.e. $\omega' = \omega_0$. Converting Eq.(3.5.1) to the

linear frequency scale we can write,

$$\nu_0 = \nu \left(1 - \frac{v}{c}\right) \quad (3.5.2)$$

Atoms in a vapour cell at room temperature, which are in thermal equilibrium, follow Maxwell-Boltzmann (MB) velocity distribution which is spherically symmetric. The fraction of atoms with velocity in the range v to $v + dv$ in atomic vapour is given by,

$$f(v)dv = \sqrt{\frac{M}{2\pi k_B T}} \exp\left(-\frac{v^2}{u^2}\right) dv \quad (3.5.3)$$

where $k_B = 1.38 \times 10^{23}$ J/K is the Boltzmann's constant and $u = \sqrt{\frac{2k_B T}{M}}$ is the most probable speed for atoms of mass M at absolute temperature T . Now, we can rewrite Eq.(3.5.3) in terms of frequency using Eq.(3.5.2) to obtain the Gaussian line shape function for absorption. This is given by,

$$G(\nu)d\nu = \frac{c}{\nu_0} \sqrt{\frac{M}{2\pi k_B T}} \exp\left\{-\frac{c^2}{u^2} \left(\frac{\nu - \nu_0}{\nu_0}\right)^2\right\} d\nu \quad (3.5.4)$$

Eq.(3.5.4) represents the Doppler line shape of an ensemble of atoms. Further, the FWHM of the absorption line shape from Eq.(3.5.4) is given by

$$\Delta\nu_D = \sqrt{\ln 2} \frac{u\nu_0}{c} = \sqrt{8k_B \ln 2} \frac{1}{\lambda_0} \sqrt{\frac{T}{M_N}} \quad (3.5.5)$$

where T is the temperature in absolute scale and M_N denotes the mass number. For example, $\Delta\nu_D = 504.34$ MHz for ^{87}Rb with $u = 236.32$ m/s at $T = 294$ K. We have convoluted the MB distribution to get the information of atoms of all velocities over the coherence term of the density matrix.

3.6 Three-level atoms: Electromagnetically induced transparency

When laser fields interact with three or multilevel atoms, many interesting phenomena like coherent population trapping (CPT), electromagnetically induced transparency (EIT), electromagnetically induced absorption (EIA), lasing without inversion (LWI) etc. can be observed. There are three kinds of three-level systems, such as Λ -type, V-type and cascade or ladder type. To observe the EIT phenomenon, one needs to have an alkali atomic system. Since this research work is mainly based on the EIT phenomenon in this section, a fundamental theoretical explanation of this phenomenon has been given.

3.6.1 Electromagnetically induced transparency (EIT)

As we discussed in chapter 1, EIT is a coherent phenomenon generated due to quantum interference-effect. To understand the physics behind this phenomenon, we have considered here a Λ -type system as shown in the Fig.3.4(a). The atomic levels are defined as $|1\rangle$, $|2\rangle$ and $|3\rangle$. The weak probe laser of frequency ω_p connects the transition between $|1\rangle \longrightarrow |3\rangle$ while the strong pump laser with frequency ω_c couples $|2\rangle \longrightarrow |3\rangle$ transition. The probe laser has Rabi frequency Ω_p and detuning δ_p while these quantities for the pump laser are Ω_c and δ_c respectively.

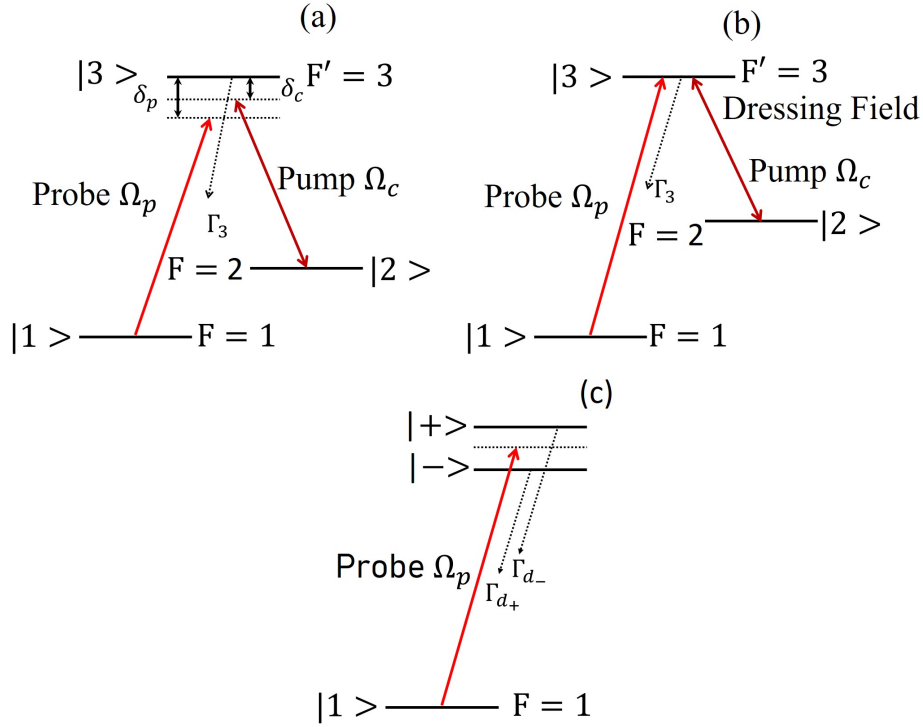


Figure 3.4: (a) Three level Λ -type system for EIT. (b) Coherent coupling between meta-stable state $|2\rangle$ and excited state $|3\rangle$ of the dressing (pump) field. (c) The formation of the dressed states in the atomic system. In this figure $|1\rangle$, $|2\rangle$ and $|3\rangle$ correspond to the hyperfine levels $F = 1$, $F = 2$ and $F' = 3$ of ^{87}Rb respectively.

Both these transitions are dipole allowed, and the involved levels have opposite parity. So, $|1\rangle \rightarrow |2\rangle$ transition involves the same parity levels and is dipole forbidden. Γ_3 is the spontaneous decay rate of level $|3\rangle$ and the ground states have zero decay rates. Since the pump beam is strong enough compared to the probe beam, it will act as the dressing field between the levels $|2\rangle$ and $|3\rangle$ (see Fig.3.4(b)). The pump field generates interference of excitation pathways through the doublet of dressed states $|\pm\rangle$ (Autler-Townes doublet), provided the decay out of state $|2\rangle$ is negligible compared to that of state $|3\rangle$ is shown in the Fig.3.4(c). Suppose the probe field is tuned precisely to the resonance frequency. In that case, the contributions to the linear susceptibility due to

the two resonances, $|1\rangle \rightarrow |+\rangle$ and $|1\rangle \rightarrow |-\rangle$, which are equally spaced but with opposite signs of detuning, will be equal and opposite. In this way, the cancellation of the response at this frequency due to a Fano-like interference [80] of the decay channels is created. In the probe absorption spectrum, we will get a transparency window at the resonance position.

To get a view about the dressed states of a three level system, let us consider that the probe and the pump fields are given by

$$\begin{aligned}\vec{\varepsilon}_p(t) &= E_{0p}\cos(\omega_p t)\hat{e}_p \\ \vec{\varepsilon}_c(t) &= E_{0c}\cos(\omega_c t)\hat{e}_c\end{aligned}\tag{3.6.1}$$

Following the derivation of the two-level system done in section 3.2, the effective Hamiltonian for the three-level Λ -type system with RWA becomes,

$$H_{eff} = \frac{\hbar}{2} \begin{bmatrix} 0 & 0 & -\Omega_p \\ 0 & -2(\delta_p - \delta_c) & -\Omega_c \\ -\Omega_p^* & -\Omega_c^* & -2\delta_p \end{bmatrix}\tag{3.6.2}$$

where, $\Omega_p = \frac{E_{0p}\langle 1|\vec{\mu}\cdot\hat{e}_p|3\rangle}{\hbar}$ and $\Omega_c = \frac{E_{0c}\langle 2|\vec{\mu}\cdot\hat{e}_c|3\rangle}{\hbar}$ are the Rabi frequencies for the probe and the pump beams respectively. Probe (pump) beam detuning is defined as $\delta_{p(c)} = (\omega_{31(32)} - \omega_{p(c)})$.

To express the eigenstates we consider the mixing angles θ and ϕ which depend in a simple way upon the Rabi frequencies as well as on the one photon detuning ($\delta_p = \delta$) and the Raman or two photon detuning ($\delta_R = (\delta_p - \delta_c)$). For Raman resonance condition i.e. at $\delta_R = 0$, the mixing angles are defined as [32],

$$\begin{aligned}\tan(\theta) &= \frac{\Omega_p}{\Omega_c} \\ \tan(2\phi) &= \frac{\sqrt{|\Omega_p|^2 + |\Omega_c|^2}}{\delta}\end{aligned}\tag{3.6.3}$$

Solving the characteristic equation for the Hamiltonian matrix of Eq.(3.6.2) at the Raman resonance condition, we have obtained the eigenvalues of the Hamiltonian as,

$$\begin{aligned}\lambda_0 &= 0 \\ \lambda_{\pm} &= \frac{\hbar}{2}[\delta \pm \sqrt{\delta^2 + |\Omega_p|^2 + |\Omega_c|^2}]\end{aligned}\tag{3.6.4}$$

The corresponding eigenstates are written in terms of the bare states as,

$$\begin{aligned}|0\rangle &= \cos(\theta) |1\rangle - \sin(\theta) |2\rangle \\ |+\rangle &= \sin(\theta)\sin(\phi) |1\rangle + \cos(\phi) |3\rangle + \cos(\theta)\sin(\phi) |2\rangle \\ |-\rangle &= \sin(\theta)\sin(\phi) |1\rangle - \sin(\phi) |3\rangle + \cos(\theta)\cos(\phi) |2\rangle\end{aligned}\tag{3.6.5}$$

The states $|\pm\rangle$ contain all the bare states' components while the bare state $|3\rangle$ has no contribution for the state $|0\rangle$. The state $|0\rangle$ is therefore called the dark state because there is no possibility of excitation to state $|3\rangle$ from it and subsequent spontaneous emission for the atoms who are in this state $|0\rangle$.

Now for the case of EIT considering a weak probe beam, i.e., $\Omega_p \ll \Omega_c \implies \tan(\theta) \ll 1 \implies \sin(\theta) \rightarrow 0, \cos(\theta) \rightarrow 1$ and if the probe beam is on resonance, i.e., $\delta = 0 \implies \tan(2\phi) = \infty \implies \phi = \frac{\pi}{4}$, Eq.(3.6.5) becomes,

$$\begin{aligned}|0\rangle &= |1\rangle \\ |+\rangle &= \frac{1}{\sqrt{2}}(|2\rangle + |3\rangle) \\ |-\rangle &= \frac{1}{\sqrt{2}}(|2\rangle - |3\rangle)\end{aligned}\tag{3.6.6}$$

The states described in the Eq.(3.6.6) are the usual dressed states created in the EIT phenomenon with the condition of strong pump beam and weak probe beam as shown in the Fig.3.4(c).

To get the probe absorption and the dispersion spectra we have to solve the master

Eq.(3.1.16). Here the relaxation matrix of the system is given by

$$\Gamma = \begin{bmatrix} 0 & 0 & 0 \\ 0 & 0 & 0 \\ 0 & 0 & \Gamma_3 \end{bmatrix} \quad (3.6.7)$$

The re-population matrix of this three level system can be written as,

$$\Lambda_0 = \begin{bmatrix} \frac{\Gamma_3 \rho_{33}}{2} & 0 & 0 \\ 0 & \frac{\Gamma_3 \rho_{33}}{2} & 0 \\ 0 & 0 & 0 \end{bmatrix} \quad (3.6.8)$$

Using Eq.(3.6.2), Eq.(3.6.7) and Eq.(3.6.8), from Eq.(3.1.16), the OBE for the three level Λ -type system can be obtained as,

$$\begin{aligned} \dot{\rho}_{11} &= \Gamma_{31} \rho_{33} + \frac{i}{2} \Omega_p (\rho_{31} - \rho_{13}) \\ \dot{\rho}_{22} &= \Gamma_{32} \rho_{33} + \frac{i}{2} \Omega_c (\rho_{32} - \rho_{23}) \\ \dot{\rho}_{33} &= -(\Gamma_{31} + \Gamma_{32}) \rho_{33} - \frac{i}{2} \Omega_p (\rho_{31} - \rho_{13}) - \frac{i}{2} \Omega_c (\rho_{32} - \rho_{23}) \\ \dot{\rho}_{31} &= -D_{31}^{-1} \rho_{31} - \frac{i}{2} \Omega_p (\rho_{33} - \rho_{11}) + \frac{i}{2} \Omega_c \rho_{21} \\ \dot{\rho}_{32} &= -D_{32}^{-1} \rho_{32} - \frac{i}{2} \Omega_c (\rho_{33} - \rho_{22}) + \frac{i}{2} \Omega_p \rho_{12} \\ \dot{\rho}_{21} &= -D_{21}^{-1} \rho_{21} + \frac{i}{2} \Omega_c \rho_{31} - \frac{i}{2} \Omega_p \rho_{23} \end{aligned} \quad (3.6.9)$$

Here, D_{ij} is the complex detuning defined as $D_{ij}^{-1} = \gamma_{ij} + i\delta_{ij}$, γ_{ij} is the coherence decay for the corresponding transition $|i\rangle \rightarrow |j\rangle$ and δ_{ij} is the detuning of the corresponding levels. Under the steady state condition, with the first order perturbation for the probe beam, the probe coherence term is obtained as,

$$\rho_{31} = \frac{i}{2} \frac{\Omega_p D_{31}}{1 + \frac{\Omega_c^2}{4} D_{21} D_{31}} \quad (3.6.10)$$

While calculating the coherence term we have assumed that $\rho_{11} = 1$ and $\rho_{22} = \rho_{33} = 0$

for the sake of simplicity. Here, we have calculated the probe coherence term only for the atoms which are at rest.

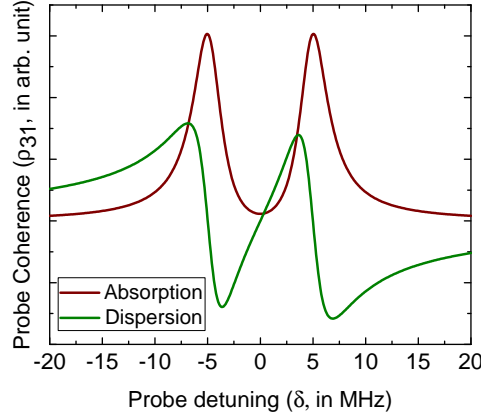


Figure 3.5: Probe coherence as a function of detuning at the steady-state. The red line represents the absorption profile with the transparency window in the vicinity of two photon resonance. The green line indicates probe dispersion with normal dispersion in the vicinity of the two photon resonance corresponding to the EIT.

In the Fig.3.5 the probe absorption and the probe dispersion profiles for a three-level Λ -type system are shown. We have observed the transparency window in the absorption profile and the normal dispersion in the dispersion spectrum in the vicinity of the resonance. For the interaction of only the probe beam, we would have observed just an absorption and an anomalous dispersion, as shown in Fig.3.3. Thus, the atomic medium becomes very dispersive when EIT resonance occurs in the medium. It leads to the phenomenon of slowing down of light while the light interacts with an EIT medium. So, the EIT medium becomes very interesting to investigate the light-atom interactions. We had explored several phenomena with this quantum interference effect, as described in the later chapters of this thesis.

On the other hand, for both of the EIT and the Autler-Townes (AT) effect one can

observe a transparency window at the resonance position, but origins of these two phenomena are different. In the spectroscopy, the AT effect (AC Stark effect) shows a change in shape of absorption spectra of a spectral line when an oscillating electric field is tuned in resonance to the transition frequency of that spectral line. The AC Stark effect was discovered by Stanley Autler and Charles Townes in 1955 [17]. This effect is more pronounced when the field is tuned to the frequency of a two-level transition. Here, the oscillating field has the effect of splitting the two bare transition states into doublets or “dressed states” which are separated by the corresponding Rabi frequency. On the other hand, EIT is coming mainly due to the Fano interference effect [80]. In both the cases of AT effects and EIT we can observe a transparency window at the resonance position in an absorption background. In the EIT, the transparency is induced coherently by a pump field even if the pump is relatively weak. Here, the coherence between the relevant atomic levels is achieved due to the Fano interference between the two atomic transitions. In the atomic system, for very high pump Rabi frequency, the Fano interference starts to wash out. Then the transparency occurs simply due to a doublet structure in the absorption profile resulting from electromagnetic pumping and this is known as AT splitting (ATS). For a three-level Λ -type system the strong EIT occurs for the condition $\Omega_c \leq (\Gamma_{31} - \gamma_{21})/2$ and ATS starts to appear for $\Omega_c \gg \Gamma_{31}$ [81–83].

4

Dispersive properties of a coherent atomic medium¹

4.1 Introduction

In this work, we have reported the experimental and theoretical study of the dispersive properties of ^{87}Rb in D_2 transition with Λ -type configuration at room temperature [1]. Experimentally, we observed the dispersion profile of the probe beam with the help of the balanced homodyne detection technique [84]. The dispersive signal carries information about the phase difference between the reference and the probe signal beams which formed the two arms of a Mach-Zehnder interferometer. There are several previous studies where the dispersive properties of the atomic medium under the EIT resonance condition have been investigated. The change in the refractive index can be observed by studying the dispersion signal when the probe beam interacts with an EIT medium. Xiao et al. [85], using homodyne detection technique, measured the dispersive properties of an EIT medium. They observed rapidly varying refractive index under EIT condition in a cascade-type system of $\text{Rb-}D_2$ transition and achieved a reduced group velocity of $\frac{c}{13.2}$ m/s at room temperature. Schmidt et al. [86] showed the group velocity was

¹This chapter is based on the publication Das et al. *Laser Phys.*, **2018**, *28*, 125205 - 125212. The experiment and the theoretical calculations presented in this chapter have been entirely done by Arpita Das.

near about $\frac{c}{3000}$ m/s at room temperature with a 20 mm Cs cell. They observed the dispersion signal for the CPT phenomenon. In the theoretical work of Harris et al. [87], the dispersive properties of a Pb vapour in a cell were studied, and they predicted a group velocity of $\frac{c}{250}$ m/s. Measurement of the dispersive profile of a multi-window EIT spectrum in Rb atomic medium had also been reported recently [88]. The authors studied both experimentally and theoretically, how under the EIT effect, an anomalous dispersive region of the medium got modified into multiple normal and anomalous dispersive regions. Liu et al. [89] experimentally demonstrated a measurement method to get high-precision refractive index spectrum using the phase interferometry setup of ^{87}Rb . They performed the experiment in the hyperfine spectrum. Recently, the subluminal light propagation in the EIT medium forming a V-type configuration in ^{85}Rb has been studied [90]. In this work, the system was studied in the time domain. The slow light phenomenon has also been observed in GaAs/AlGaAs solid-state medium configuring a V-type system [91]. Beil et al. [92] also studied both Λ -type and V-type systems in $\text{Pr}^{3+} : \text{Y}_2\text{SiO}_5$ crystal for this purpose.

In our experiment, we determined the group index of the medium within the EIT region from the slope of the probe dispersion signal. Then we have studied the variation of the group index of the medium with respect to the pump power (or the pump Rabi frequency). From our study, we calculated the group velocity of light, which passes through the atomic medium. We theoretically supported our observation by solving the density-matrix equation of motion (Liouville equation) analytically using the semi-classical approach. We have found out an analytical expression of the group index assuming Lorentzian velocity distribution of the atom. We have also shown that the ana-

lytical solution matched precisely with the numerical solution of the group index for the Maxwell-Boltzmann (MB) velocity distribution of the atoms. Finally, we have compared our experimental findings with our theoretical calculations.

4.2 Experiment

To study the dispersive properties of ^{87}Rb atoms, an EIT setup was made using the concept of a Mach-Zehnder interferometer.

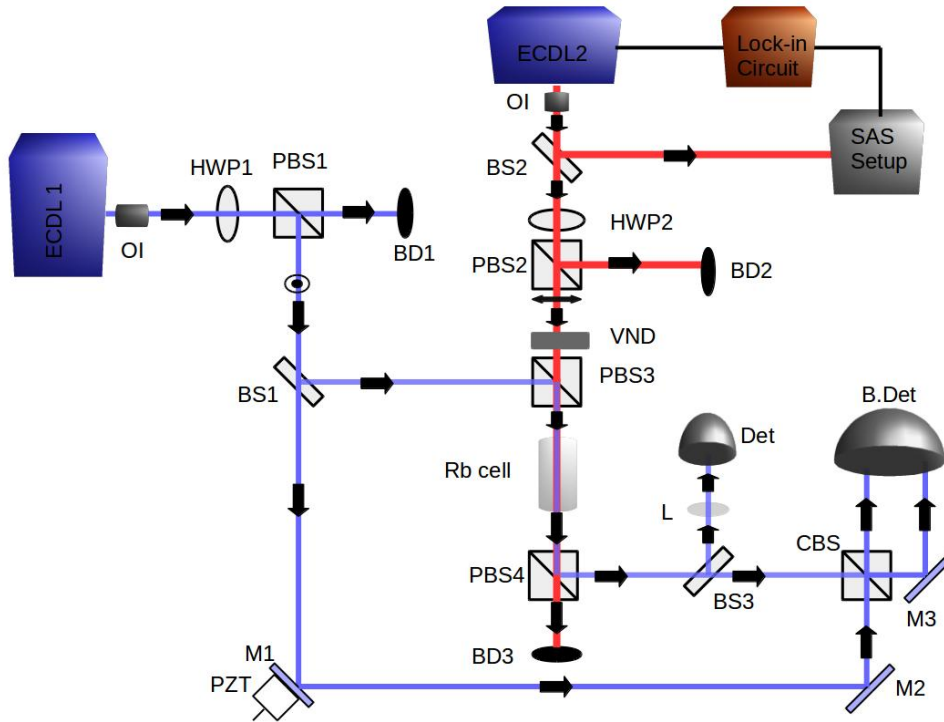


Figure 4.1: Experimental Setup. ECDL : External cavity diode laser, OI : Optical isolator, HWP: Half-wave plate, PBS: Polarizing beam splitting cube, BS: Beam splitter, CBS : Non-polarizing beam splitting cube, M: Mirror, Rb Cell : Rubidium vapour cell, BD : Beam dump, Det : Single pin photodetector, B.Det : Balance detector, VND: Variable neutral density filter, SAS Setup: Saturation absorption spectroscopy setup, L: Convex Lens, PZT: Piezoelectric transducer.

We used two external cavity diode lasers (ECDLs) for the probe and the pump beams.

The probe beam was taken from ECDL1, and the pump beam was drawn from ECDL2 as shown in Fig.4.1. Both the beams were passed through the optical isolators (OI) to prevent back reflection into the laser diodes. The probe and the pump beams were made orthogonally polarized with the combination of the half-wave plates (HWP) and polarizing beam splitters (PBS). The pump beam from ECDL2 was passed through a 30:70 plate beam splitter (BS2). The reflected part of the beam was taken for saturation absorption spectroscopy (SAS) setup. The transmitted part of the pump beam was taken for our experiment after passing through HWP2 and PBS2. For the probe beam, we took the reflected part after it passed through HWP1 and PBS1. The probe beam was then passed through a 30:70 plate beam splitter (BS1) and divided into the probe signal beam and the reference beam.

The probe signal beam and the pump beam were combined in PBS3, and the combined beams are co-propagated through the 50 mm long cylindrical Rubidium vapour cell (Rb cell) of diameter 25 mm. It formed one arm of the interferometer. The reference beam travelled along another arm of the interferometer, which consists of a piezoelectric transducer (PZT) attached to a mirror (M1). To detect only the probe signal, we separated the probe signal and the pump beams after the Rb cell by using another polarizing beam splitter (PBS4). The probe signal beam was again divided into two parts by another 30:70 plate beam splitter (BS3). The reflected part was focused into a single pin photodetector (Det, New Focus Model: 2001) by a convex lens (L) of focal length 10 cm to observe the probe transmission signal. The transmitted part of the probe signal beam and the reference beam were recombined in a 50:50 non-polarizing cubic beam splitter (CBS). The probe dispersion signal was observed by a balanced photodetector (New Fo-

cus Model: 2307) using the homodyne detection technique. The dispersion profile carries a small phase difference $\beta(\omega)L$ between the two arms of the interferometer due to the EIT created in the Rb atomic medium, where $\beta(\omega)$ is the dispersion coefficient of the medium and L is the length of the Rb cell.

The difference signal from the balanced photodetector (B.Det) is given by (see Appendix B)

$$\Delta I_d(\omega) \propto 2E_r E_p \exp\left(-\frac{\alpha(\omega)L}{2}\right) \cos(\phi_r + \beta(\omega)L) \quad (4.2.1)$$

where E_r and E_p are the amplitudes of the electric fields of the reference beam and the probe signal beam respectively. $\alpha(\omega)$ is the absorption coefficient of the medium, and ϕ_r is the reference phase of the interferometer. Thus the phase difference between the probe signal beam and the reference beam due to an EIT medium is manifested by the dispersion signal. We adjusted the phase of the reference arm of the Mach-Zehnder interferometer using a PZT by changing the voltage on it such that the phase becomes $\pi/2$. Then, the difference signal becomes, $\Delta I_d(\omega) \propto \exp\left(-\frac{\alpha(\omega)L}{2}\right)\beta(\omega)L$ for $|\beta(\omega)L| \ll 1$ [85]. The Rb cell contains both ^{87}Rb and ^{85}Rb in their natural abundance and no buffer gas. The pressure of the cell is of the order of 10^{-7} Torr at the room temperature. Throughout our experiment, we have kept the powers of the probe signal beam and that of the reference beam constant at $13 \pm 0.5 \mu\text{W}$ and $4 \pm 0.05 \text{ mW}$ respectively. We varied the pump power from $14 \pm 0.5 \mu\text{W}$ to $5 \pm 0.05 \text{ mW}$ using a variable neutral density filter (VND) placed in the path of the pump beam. We recorded both the probe absorption and the probe dispersion signals using a digital storage oscilloscope (Rohde and Schwarz).

4.3 Experimental results and analysis

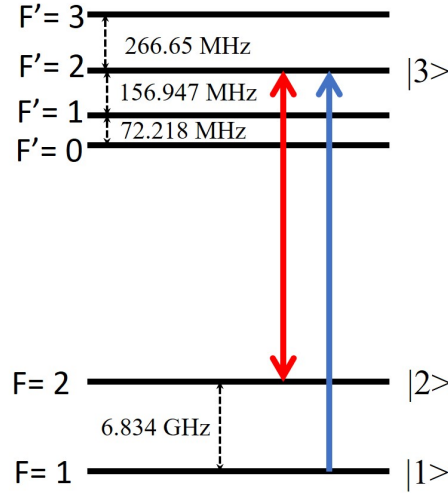


Figure 4.2: Level scheme of ^{87}Rb with D_2 transition. This figure shows the Λ type configuration of the atomic system, where the pump beam (two-sided red arrow) is locked between the $F = 2(|2\rangle) \rightarrow F' = 2(|3\rangle)$ levels and the probe beam (one-sided blue arrow) is scanned through the $F = 1(|1\rangle) \rightarrow F' = 2(|3\rangle)$ levels.

In our experiment, we focused only on the D_2 transition of ^{87}Rb . We locked the pump beam at $F = 2 \rightarrow F' = 2$ hyperfine transition with the help of SAS setup, the lock-in circuit and the PID control loop. The probe beam was scanned from $F = 1 \rightarrow F' = 2$ transition as shown in Fig.4.2. When only the probe beam passed through the Rb cell, we got the Doppler-broadened transmission and dispersion profiles of the probe signal beam as shown in Fig.4.3(a). When both the pump and the probe beams travelled through the cell at the two-photon resonance condition, we observed an EIT peak in the probe transmission profile. Corresponding to the EIT peak in the transmission profile, we got the normal dispersion in the probe dispersion profile. A zoomed view of the probe transmission spectrum with the EIT and the dispersive EIT profile are shown in

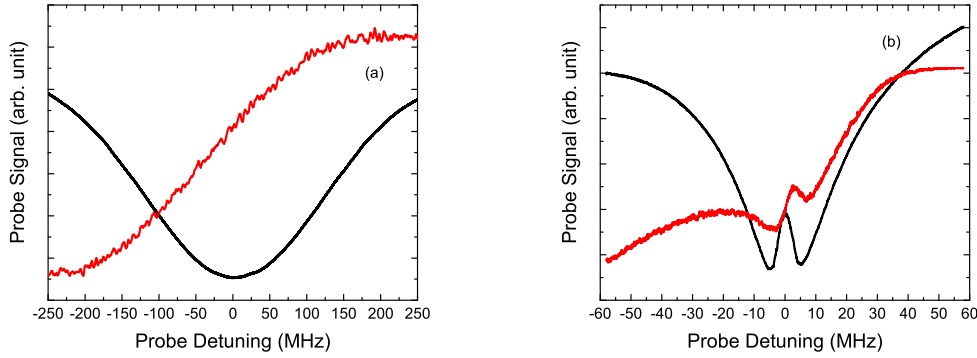


Figure 4.3: (a) Experimental Doppler-broadened spectra of the probe beam when only the probe beam passed through the vapour cell. (b) Zoomed view (only the EIT portion) of the experimental Doppler broadened spectra of the probe beam when both the pump beam and the probe beam passed through the vapour cell at EIT condition. The probe Rabi frequency was 1.73 MHz in case of both (a) and (b), whereas the pump Rabi frequencies were 0 MHz and 32.74 MHz respectively. The black curve represents the probe transmission signal, and the red one denotes the probe dispersion profile.

Fig.4.3(b).

We studied the pump power variation of the dispersion signal. In Fig.4.4 the dispersion profiles corresponding to five pump Rabi frequencies are shown. It was observed that as we increased the pump beam power or the pump Rabi frequency, the slope of the dispersive EIT signal became steeper upto a certain value of the pump power. After that, the slope gradually decreased as we increased the pump beam power. Although the strength of the EIT in the dispersion profile always kept increasing.

The Rabi frequencies of both the probe and the pump beams in our experiment were calculated using the formula, $\frac{I}{I_{sat}} = 2 \left(\frac{\Omega}{\Gamma}\right)^2$ [78], where I_{sat} is the saturation intensity and Γ is the natural linewidth of the medium. We have the atom density as, $N_0 \approx 4 \times 10^{15}/m^3$ [78] since our laboratory temperature during the experiment was 21°C. The intensities of either the probe or the pump beams $I_{p(c)}$ can be obtained from the relation $I_{p(c)} = \frac{P_{p(c)}}{A}$,

where $P_{p(c)}$ is the the probe (pump) power and A is the cross sectional area of the laser beam respectively. In our case, the diameter of each beam was 2 mm.

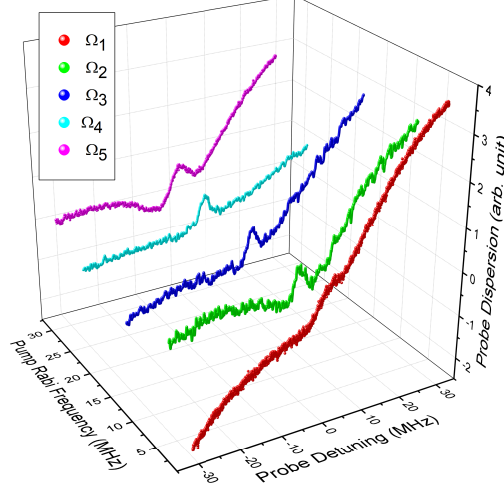


Figure 4.4: Normalized dispersive EIT profiles corresponding to five pump Rabi frequencies ($\Omega_1 = 1.81 \pm 0.03$ MHz, $\Omega_2 = 6.3 \pm 0.01$ MHz, $\Omega_3 = 15.53 \pm 0.37$ MHz, $\Omega_4 = 25.84 \pm 0.22$ MHz, $\Omega_5 = 32.74 \pm 0.17$ MHz). The data were normalized only in the region of EIT. The probe Rabi frequency is 1.73 ± 0.34 MHz for all of the above spectra.

From the slope of the dispersive EIT signal we got $L \frac{d\beta(\omega)}{d\omega} |_{\omega_0}$. We calculated $\frac{d\beta(\omega)}{d\omega} |_{\omega_0}$ from it, where ω_0 is the resonance frequency of the probe. With this value, the group index $n_g = 1 + c \frac{d\beta}{d\omega} |_{\omega_0}$ was calculated. We noticed that the nature of variation of the group index with the pump Rabi frequency was similar to that of the slope of the dispersive EIT signal with the pump beam power. The value of the group index increased as the pump Rabi frequency was increased, upto a certain value. But beyond that value, the group index decreased as the value of pump Rabi frequency was increased. From this behaviour, we can say that the medium became more dispersive when the pump Rabi frequency was increased in the low pump power region. Although beyond a critical point of the pump Rabi frequency, power broadening phenomenon started dominating over the

dispersive behaviour of the atomic medium, even if the strength of the dispersive EIT signal was always increasing. The variation of the group index with the pump Rabi frequencies, which was observed experimentally, is shown in Fig.4.5 by the blue triangles. The theoretical plots are explained in section 4.4.

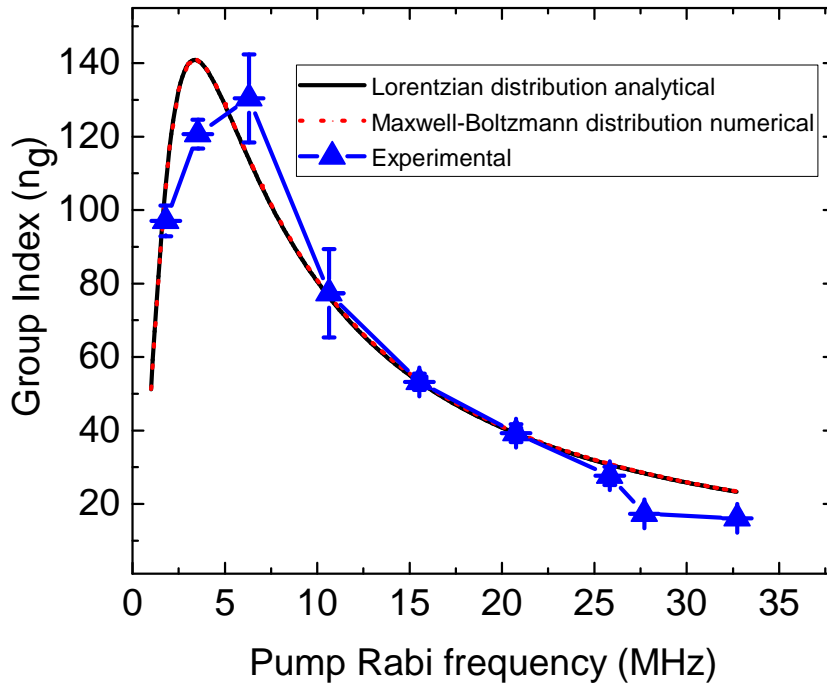


Figure 4.5: Variation of the group index with pump Rabi frequencies. The blue triangles show the experimental results (the line joining these experimental data points is given for eye guidance). The black line shows the variation of group index calculated analytically using Lorentzian velocity distribution of the atoms. The red dashed lines indicates the theoretical numerical variation considering the Maxwell-Boltzmann (MB) velocity distribution of the atoms.

From the group index we can calculate the group velocity, $v_g = c/n_g$ where c is the velocity of light in free space. v_g was calculated with the help of the relation $v_g = \frac{c}{1+c\frac{d\beta}{d\omega}|_{\omega_0}}$, where ω_0 is the resonance frequency of the probe beam. The time delay (Δt_g) can also be

calculated as $\Delta t_g = (L/v_g - L/c) \approx L/v_g = Ln_g/c$. The values of the group velocities and the time delays corresponding to each pump Rabi frequency are mentioned in the Table (4.1). We got the maximum time delay corresponding to the maximum group index.

Pump Rabi frequency (MHz)	Group velocity (m/s)	Time delay (ns)
1.81 ± 0.03	$\frac{c}{97.04 \pm 4.2}$	16.17 ± 0.70
3.54 ± 0.02	$\frac{c}{120.65 \pm 3.9}$	20.11 ± 0.65
6.3 ± 0.01	$\frac{c}{130.40 \pm 12}$	21.73 ± 1.99
10.64 ± 0.01	$\frac{c}{77.33 \pm 12}$	13.87 ± 1.99
15.53 ± 0.37	$\frac{c}{53.24 \pm 2.2}$	8.87 ± 0.37
20.76 ± 0.27	$\frac{c}{39.24 \pm 2.4}$	6.54 ± 0.4
25.84 ± 0.22	$\frac{c}{27.65 \pm 2.5}$	4.61 ± 0.42
27.71 ± 0.21	$\frac{c}{17.30 \pm 0.38}$	2.88 ± 0.06
32.74 ± 0.17	$\frac{c}{16.06 \pm 0.43}$	2.68 ± 0.07

Table 4.1: Experimentally measured values of the group velocities and the time delays for nine different pump Rabi frequencies.

From the values of group velocity in Table (4.1) one can see that the group velocity reduced as we increased the pump Rabi frequency upto a certain value. Then the group velocity increased with increase in the pump Rabi frequency as the group velocity is inversely proportional to the group index. Therefore we can say that to get the most reduced group velocity; we have to select the pump Rabi frequency or the pump power carefully. We achieved the most reduced group velocity in our EIT medium as $v_g = \frac{c}{130.40 \pm 12}$ m/s with the pump Rabi frequency 6.3 ± 0.01 MHz at 21°C for a 50 mm Rb vapour cell. This corresponds to a time delay of 21.73 ± 1.99 ns in a Λ -type configuration of ^{87}Rb with D_2 transition.

4.4 Theory

To support our experimental observations theoretically and to explain the non-linear behaviour of the group index, we used a semi-classical approach of density matrix formalism. We considered a three-level Λ type configuration as shown in Fig.4.2. The states $|3\rangle$ and $|2\rangle$ are coupled by the strong pump beam while the weak probe beam couples the states $|3\rangle$ and $|1\rangle$. The transitions $|1\rangle \rightarrow |3\rangle$ and $|2\rangle \rightarrow |3\rangle$ are dipole allowed, while the transition between $|1\rangle$ and $|2\rangle$ is dipole-forbidden. The pump beam has the frequency ω_c and the electric field amplitude E_c , while for the probe beam, those quantities are ω_p and E_p respectively. In general we can define the electric fields of both the lasers as, $\varepsilon_q(\omega_q, z) = \text{Re}[E_q e^{-i(\omega_q t - k_q z)}]$, where $q = c, p$. Here c stands for the pump beam and p stands for the probe beam. We assumed that the fields propagate along the z -direction. Here, k_q is the wave propagation vector which is defined as $k_q = 2\pi/\lambda_q$. The wave vectors of the pump and the probe beams are almost equal, so we took $k_p = k_c = k$ in our calculation. Here our total Hamiltonian of the system is the sum of unperturbed and perturbed Hamiltonian of the system.

For our system H_0 is the unperturbed Hamiltonian that can be written as,

$$H_0 = \sum_{j=1}^3 \hbar\omega_j |j\rangle \langle j|, \quad (4.4.1)$$

where $\hbar\omega_j$ is the energy of j -th level. H_I is the perturbation or the atom-field interaction Hamiltonian. It can be written as,

$$H_I = -\frac{\hbar}{2} [\Omega_p |3\rangle \langle 1| (e^{-i(\omega_p t - k_p z)} + e^{i(\omega_p t - k_p z)}) + \Omega_c |3\rangle \langle 2| (e^{-i(\omega_c t - k_c z)} + e^{i(\omega_c t - k_c z)}) + c.c.]. \quad (4.4.2)$$

Here, $\Omega_p = \mu_{31} E_p / \hbar$ is the probe Rabi frequency and $\Omega_c = \mu_{32} E_c / \hbar$ is the pump Rabi

frequency with μ_{31} and μ_{32} as the dipole moments of the respective dipole allowed transitions. For the dipole forbidden transition, $\mu_{12} = 0$. We considered the Rabi frequencies to be real. The time evolution of the atomic density matrix operator can be derived from the Liouville equation (Eq.(3.1.16)), after including the decay terms phenomenologically. Therefore, assuming RWA the time evolution can be expressed as following,

$$\begin{aligned}
\dot{\rho}_{11} &= \Gamma_{31}\rho_{33} + \Gamma_{21}\rho_{22} - \Gamma_{12}\rho_{11} + \frac{i}{2}\Omega_p(\rho_{31} - \rho_{13}) \\
\dot{\rho}_{22} &= \Gamma_{32}\rho_{33} - \Gamma_{21}\rho_{22} + \Gamma_{12}\rho_{11} + \frac{i}{2}\Omega_c(\rho_{32} - \rho_{23}) \\
\dot{\rho}_{33} &= -(\Gamma_{31} + \Gamma_{32})\rho_{33} - \frac{i}{2}\Omega_p(\rho_{31} - \rho_{13}) - \frac{i}{2}\Omega_c(\rho_{32} - \rho_{23}) \\
\dot{\rho}_{31} &= -D_{31}^{-1}\rho_{31} - \frac{i}{2}\Omega_p(\rho_{33} - \rho_{11}) + \frac{i}{2}\Omega_c\rho_{21} \\
\dot{\rho}_{32} &= -D_{32}^{-1}\rho_{32} - \frac{i}{2}\Omega_c(\rho_{33} - \rho_{22}) + \frac{i}{2}\Omega_p\rho_{12} \\
\dot{\rho}_{21} &= -D_{21}^{-1}\rho_{21} + \frac{i}{2}\Omega_c\rho_{31} - \frac{i}{2}\Omega_p\rho_{23}
\end{aligned} \tag{4.4.3}$$

Here, $\Gamma_{31} = \Gamma_{32} = \frac{\Gamma}{2}$, where Γ is the spontaneous decay rate from the excited state $|3\rangle$. Γ_{12} and Γ_{21} are the non radiative decay rates between the two ground levels $|1\rangle$ and $|2\rangle$ respectively. We have assumed that $\Gamma_{21} = \Gamma_{12}$. γ_{31} and γ_{32} are the coherence decay rates and are defined as, $\gamma_{31} = \frac{\Gamma_{31} + \Gamma_{32}}{2}$ and $\gamma_{32} = \frac{\Gamma_{31} + \Gamma_{32}}{2}$.

In the equations, Δ_p and Δ_c are the probe and the pump laser detunings respectively after taking the Doppler shift into account and they are defined as, $\Delta_p = (\delta_p + kv)$ and $\Delta_c = (\delta_c + kv)$ respectively. $\delta_p = (\omega_p - \omega_{13})$ and $\delta_c = (\omega_c - \omega_{23})$ are the probe and the pump laser detunings without the Doppler shifts, where, ω_{13} and ω_{23} are the frequencies of the allowed atomic transitions. We denoted $\omega_{13} = \omega_0$ in our further calculation. Under the steady state condition we have solved the Eq.(4.4.3) analytically. Since in our experiment the intensity of probe beam was very low than the pump beam, we took the first order

perturbation for the probe beam. We have obtained the zeroth order population of $|3\rangle$ from the Eq.(4.4.3),

$$\rho_{33}^0 = -\frac{i\Omega_c}{2\Gamma_3}(\rho_{32}^0 - \rho_{23}^0) \quad (4.4.4)$$

and the zeroth order pump-coherence term,

$$\rho_{32}^0 = -\frac{i\Omega_c}{2} \frac{(\rho_{33}^0 - \rho_{22}^0)}{\gamma_{32} - i\Delta_c} \quad (4.4.5)$$

Using Eq.(4.4.5), Eq.(4.4.4) becomes,

$$\begin{aligned} \rho_{33}^0 &= -\frac{i\Omega_c}{2\Gamma_3} \left\{ -\frac{i\Omega_c}{2} \frac{(\rho_{33}^0 - \rho_{22}^0)}{\gamma_{32} - i\Delta_c} - \frac{i\Omega_c}{2} \frac{(\rho_{33}^0 - \rho_{22}^0)}{\gamma_{32} + i\Delta_c} \right\} \\ &= \frac{\Omega_c^2 \gamma_{32}}{2\Gamma_3(\gamma_{32}^2 + \Delta_c^2) + \Omega_c^2 \gamma_{32}} \rho_{22}^0 \end{aligned} \quad (4.4.6)$$

Again, from Eq.(4.4.3) the zeroth order population of $|1\rangle$ becomes,

$$\rho_{11}^0 = \frac{\Gamma_{31}\rho_{33}^0 + \Gamma_{21}\rho_{22}^0}{\Gamma_{12}} \quad (4.4.7)$$

Assuming population conservation, i.e. $\rho_{11}^0 + \rho_{22}^0 + \rho_{33}^0 = 1$, using Eq.(4.4.6) and Eq.(4.4.7) we have obtained,

$$\rho_{11}^0 + \rho_{22}^0 + \rho_{33}^0 = 1 \quad (4.4.8)$$

$$\Rightarrow \frac{\Gamma_{31} \frac{\Omega_c^2 \gamma_{32}}{2\Gamma_3(\gamma_{32}^2 + \Delta_c^2) + \Omega_c^2 \gamma_{32}} \rho_{22}^0 + \Gamma_{21}\rho_{22}^0}{\Gamma_{12}} + \rho_{22}^0 + \frac{\Omega_c^2 \gamma_{32}}{2\Gamma_3(\gamma_{32}^2 + \Delta_c^2) + \Omega_c^2 \gamma_{32}} \rho_{22}^0 = 1 \quad (4.4.9)$$

$$\Rightarrow \frac{\Gamma_{31} \frac{\Omega_c^2 \gamma_{32}}{2\Gamma_3(\gamma_{32}^2 + \Delta_c^2) + \Omega_c^2 \gamma_{32}} \rho_{22}^0 + \Gamma_{21}\rho_{22}^0}{\Gamma_{12}} + \rho_{22}^0 + \frac{\Omega_c^2 \gamma_{32}}{2\Gamma_3(\gamma_{32}^2 + \Delta_c^2) + \Omega_c^2 \gamma_{32}} \rho_{22}^0 = 1 \quad (4.4.10)$$

$$\Rightarrow \rho_{22}^0 = \frac{2\Gamma_{12}\Gamma_3(\gamma_{32}^2 + \Delta_c^2) + \Gamma_{12}\gamma_{32}\Omega_c^2}{4\Gamma_{12}\Gamma_3(\gamma_{32}^2 + \Delta_c^2) + (3\Gamma_{12} + \Gamma_{31})\gamma_{32}\Omega_c^2} \quad (4.4.11)$$

Therefore, Eq.(4.4.6) and Eq.(4.4.6) become,

$$\rho_{33}^0 = \frac{\Gamma_{12}\gamma_{32}\Omega_c^2}{4\Gamma_{12}\Gamma_3(\gamma_{32}^2 + \Delta_c^2) + (3\Gamma_{12} + \Gamma_{31})\gamma_{32}\Omega_c^2} \quad (4.4.12)$$

and

$$\rho_{11}^0 = \frac{2\Gamma_{12}\Gamma_3(\gamma_{32}^2 + \Delta_c^2) + (\Gamma_{12} + \Gamma_{31})\gamma_{32}\Omega_c^2}{4\Gamma_{12}\Gamma_3(\gamma_{32}^2 + \Delta_c^2) + (3\Gamma_{12} + \Gamma_{31})\gamma_{32}\Omega_c^2} \quad (4.4.13)$$

Thus we got the probe coherence under steady state condition,

$$\rho_{31} = -\frac{\frac{i}{2}\Omega_p D_{31}[(\rho_{33}^0 - \rho_{11}^0) - \frac{\Omega_c^2}{4}D_{23}D_{21}(\rho_{33}^0 - \rho_{22}^0)]}{(1 + \frac{\Omega_c^2}{4}D_{31}D_{21})} \quad (4.4.14)$$

Where we have assumed that $(k_p - k_c) \approx 0$ and

$$\begin{aligned} D_{31} &= \frac{1}{(\gamma_{31} - i\Delta_p)} \\ D_{23} &= \frac{1}{(\gamma_{32} + i\Delta_c)} \\ D_{21} &= \frac{1}{[\gamma_{21} - i(\Delta_p - \Delta_c)]} \end{aligned} \quad (4.4.15)$$

Now, to get the group index we have to calculate the susceptibility of the medium since the refractive index of the medium is related to the susceptibility as, $n(\omega) = 1 + \frac{1}{2}\chi'(\omega)$. Therefore the group index at the transition frequency can be calculated from the relation, $n_g = n(\omega_0) + \omega_0 \frac{dn}{d\omega}|_{\omega_0}$, where $n(\omega_0) = 1$. χ' is the real part of the susceptibility. Considering the contribution of all velocities of the atoms the complex susceptibility at the probe field frequency can be determined from the probe coherence by the following equation,

$$\chi(\omega_p) = \frac{2\mu_{31}}{\epsilon_0 E_p} \int_{-\infty}^{+\infty} \rho_{31} N(kv) d(kv) \quad (4.4.16)$$

where, μ_{31} is the dipole moment for the transition from $|1\rangle$ to $|3\rangle$. $N(kv)$ is the velocity distribution of the atoms. Generally, the atoms obey Maxwell-Boltzmann (MB) distribution which can be written as,

$$N(kv) = \frac{N_0}{\sqrt{\pi}(ku)^2} \exp\left[-\frac{(kv)^2}{(ku)^2}\right] \quad (4.4.17)$$

Here, u is the most probable velocity and it is related to the Doppler width of the absorption of the probe response. Eq.(4.4.16) for the susceptibility is not analytically

integrable with the MB distribution of Eq.(4.4.17). So, to get an analytical expression of the susceptibility we assumed the velocity distribution to be a Lorentzian function of the same FWHM as the MB distribution, i.e. $2W_D = 2\sqrt{\ln 2}ku$. This Lorentzian velocity distribution [93] is given by,

$$N(kv) = N_0 A_0 \frac{W_D/\pi}{W_D^2 + (kv)^2} \quad (4.4.18)$$

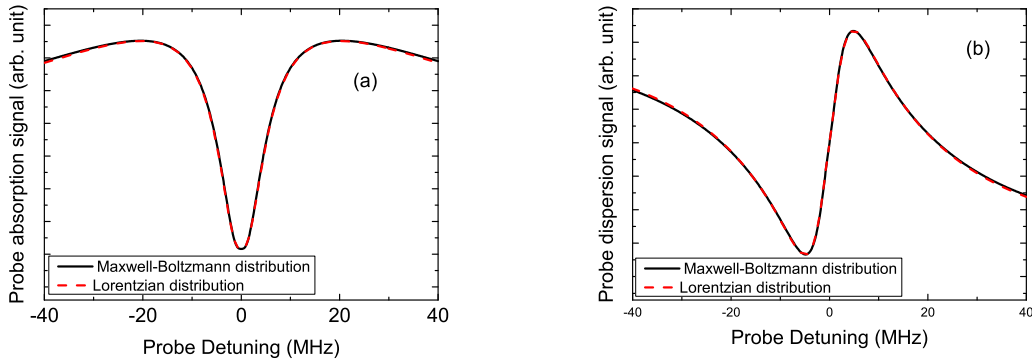


Figure 4.6: Theoretical Doppler-broadened (a) absorption spectra and (b) dispersion spectra of the probe beam under EIT condition with both the M-B distribution and the Lorentzian distribution. The black lines and the red dashed lines in (a) and (b) correspond to the MB and the Lorentzian distribution respectively. In both (a) and (b) the probe Rabi frequency and the pump Rabi frequency are 1.73 MHz and 32.74 MHz respectively.

In both the Eq.(4.4.17) and Eq.(4.4.18), N_0 is the number density of atoms, k is the wave vector and $A_0 = \sqrt{\pi \ln 2}$ in equation Eq.(4.4.18) is a constant. Therefore, with this Lorentzian distribution, Eq.(4.4.16) becomes,

$$\chi(\omega_p) = \frac{2\mu_{31}N_0A_0}{\epsilon_0 E_p} \int_{-\infty}^{+\infty} \rho_{31} \frac{W_D/\pi}{W_D^2 + (kv)^2} d(kv) \quad (4.4.19)$$

It is observed that the numerical solutions of Eq.(4.4.16) by taking both of the above distributions of Eq.(4.4.17) and Eq.(4.4.18) are completely overlapped in the vicinity of the EIT region from Fig.4.6(a) and Fig.4.6(b). So, we have taken the Lorentzian velocity

distribution instead of the MB distribution to calculate χ analytically and also the values of the group index (n_g) from the susceptibility.

Solving the integral of the Eq.(4.4.19) by the contour integral method we found five poles of χ . They are $\pm iW_D$, $\pm \frac{i\sqrt{16\Gamma^2\Gamma_{12}^2 + 4\Gamma_{12}(\Gamma + 6\Gamma_{12})\Omega_c^2}}{8\Gamma_{12}}$ and $-i\Gamma/2 - \Delta_p - \frac{i\Omega_c^2/4}{(\gamma_{21} - i\Delta_p)}$. Among these we took two poles situated in the upper half plane i.e. $+iW_D$ and $+\frac{i\sqrt{16\Gamma^2\Gamma_{12}^2 + 4\Gamma_{12}(\Gamma + 6\Gamma_{12})\Omega_c^2}}{8\Gamma_{12}}$. Therefore, the total susceptibility is, $\chi = \chi_1 + \chi_2$, where χ_1 and χ_2 are the contributions of the two above said poles respectively.

The contribution of the pole $kv = +iW_D$ to $\frac{d\chi}{d\omega}|_{\omega_0}$, when the pump and the probe beams are on resonance, is given by,

$$\begin{aligned} \frac{d\chi_1}{d\omega}|_{\omega_0} = & \frac{2\mu_{31}^2}{\epsilon_0\hbar} N_0 A_0 \left[-\frac{2[8(4W_D^2 - \Gamma^2)\Gamma_{12}\gamma_{21}^2 + 4(2W_D\Gamma_{12}(\Gamma + \gamma_{21}))]}{(4W_D\gamma_{21} + 2\Gamma\gamma_{21} + \Omega_c^2)^2(16W_D^2\Gamma_{12} - 4\Gamma^2\Gamma_{12} - (\Gamma + 6\Gamma_{12})\Omega_c^2)} \right. \\ & \left. - \frac{2[\Gamma(\Gamma\Gamma_{12} + (\Gamma_{12} - \gamma_{21})\gamma_{21}))\Omega_c^2 + \Gamma\Omega_c^4]}{(4W_D\gamma_{21} + 2\Gamma\gamma_{21} + \Omega_c^2)^2(16W_D^2\Gamma_{12} - 4\Gamma^2\Gamma_{12} - (\Gamma + 6\Gamma_{12})\Omega_c^2)} \right] \\ kv = & \frac{i\sqrt{16\Gamma^2\Gamma_{12}^2 + 4\Gamma_{12}(\Gamma + 6\Gamma_{12})\Omega_c^2}}{8\Gamma_{12}} \text{ pole contributes to the } \frac{d\chi}{d\omega}|_{\omega_0} \text{ as,} \end{aligned} \quad (4.4.20)$$

$$\begin{aligned} \frac{d\chi_2}{d\omega}|_{\omega_0} = & \frac{2\mu_{31}^2}{\epsilon_0\hbar} N_0 A_0 \left[\frac{8W_D\Gamma_{12}^3\Omega_c^2[4\Gamma^2\Gamma_{12} + \Gamma(4\Gamma_{12}\gamma_{21} - 2\gamma_{21}^2 + \Omega_c^2)]}{\sqrt{\Gamma_{12}\{4\Gamma^2\Gamma_{12} + (\Gamma + 6\Gamma_{12})\Omega_c^2\}}\{-16W_D^2\Gamma_{12} + 4\Gamma^2\Gamma_{12} + (\Gamma + 6\Gamma_{12})\Omega_c^2\}} \right. \\ & \left. + \frac{2\Gamma\sqrt{\Gamma_{12}\{4\Gamma^2\Gamma_{12} + (\Gamma + 6\Gamma_{12})\Omega_c^2\}} + 2\Gamma_{12}[6\Gamma_{12}\gamma_{21} + \sqrt{\Gamma_{12}\{4\Gamma^2\Gamma_{12} + (\Gamma + 6\Gamma_{12})\Omega_c^2\}}]}{\sqrt{\Gamma_{12}\{4\Gamma^2\Gamma_{12} + (\Gamma + 6\Gamma_{12})\Omega_c^2\}}\{-16W_D^2\Gamma_{12} + 4\Gamma^2\Gamma_{12} + (\Gamma + 6\Gamma_{12})\Omega_c^2\}} \right] \end{aligned} \quad (4.4.21)$$

From these Eq.(4.4.20) and Eq.(4.4.21) the group index (n_g) can be calculated. Throughout our calculation we maintained the condition $\delta_c = 0$, as in our experiment the pump beam is locked. In our simulation we have used $\Gamma = 6$ MHz, $\Gamma_{12} = 150$ KHz, $\gamma_{21} = 300$ KHz and $\mu_{31} = 3.58 \times 10^{-29}$ C.m .

In the Fig.4.5 the black line shows the variation of the group index with the pump Rabi frequency for the analytical solutions of the group index. In this figure the red dot line indicates the same variation for the numerical solution of the group index considering the MB distribution shown in Eq.(4.4.17). The characteristics of the variations corresponding to the analytical and the numerical solutions are exactly overlapped with each other and these are almost matched with our experimental observations. Now when $\Omega_c \rightarrow \infty$, then

$$\frac{d\chi}{d\omega}|_{\omega_0} \rightarrow \frac{2\mu_{31}^2}{\epsilon_0\hbar} N_0 A_0 \left[-\frac{2\Gamma}{(\Gamma + 6\Gamma_{12})\Omega_c^2} \right] \quad (4.4.22)$$

Therefore from the Eq.(4.4.22) we see that in the high pump power region, $\frac{d\chi}{d\omega}|_{\omega_0} \sim \frac{1}{\Omega_c^2}$. Thus for high pump Rabi frequency region, the group index decreases with increasing pump Rabi frequency as shown in the Fig.4.5. Thus from both the numerical and analytical solutions, we have found that for maximum reduction of group velocity, we have to optimize the pump Rabi frequency. It depends only on the system parameters like the decay rates (the spontaneous decay rate (Γ) and the non-radiative decay rate (γ_{21})), the saturation intensity (I_{sat}), the optical depth (αL) of the medium and the pump beam detuning (δ_c). We have chosen the same values of these parameters for both the numerical and analytical solutions. So both of these solutions were overlapped on each other as shown in the Fig.4.5.

4.5 Discussions

In the study of the dispersive properties of an EIT medium in room temperature, we have taken a Λ - type configuration of ^{87}Rb . The dispersion signal with the normal dispersion

in the vicinity of the EIT region has been observed by measuring the phase difference between the two arms of the Mach-Zehnder interferometer. The signal was detected by a balanced homodyne detection technique. From the detected intensity profile, we have calculated the group index of the medium. The corresponding group velocity and the time delay of the probe beam have also been estimated. We have observed a non-linear dependency of the group index on the pump Rabi frequency. To explain our experimental observation theoretically, we have considered a three-level Λ type system. The optical Bloch equations have been solved analytically to get the probe coherence term. We have also obtained analytical expression for the population of the individual atomic states. To get an analytical expression for the susceptibility (χ), we assumed the velocity distribution to be Lorentzian distribution. Then the susceptibility was calculated by the contour integral method. We have shown that the group index varies with $\frac{1}{\Omega_c^2}$ at the high pump power region. On the other hand, as we know that the group velocity can be calculated from the group index. Therefore such a behaviour of the group index of the medium with the pump Rabi frequency implies that one has to optimize the pump power, which is related to the pump Rabi frequency, to get the most reduced group velocity. The maximum reduced group velocity obtained in our experiment was $v_g = \frac{c}{130.40 \pm 12}$ m/s.

Observation of group velocity using a Mach-Zehnder interferometer is an application of interferometry technique. Our experimental setup can be used to observe the slow light phenomenon indirectly. Since the dispersion slope or the group index depends on the coherence relaxation times of the two ground levels in a Λ -type system, we can prolong this time to achieve further reduced group velocity of light by introducing a buffer gas

cell [94] or a cell with paraffin coated wall [95] in place of a normal glass vapour cell. The group velocity of the beam can be reduced further if the atomic density in the medium is increased either by increasing the temperature of the vapour cell or by experimenting with cold atoms. Using our setup, we can also study the dispersive properties in the electromagnetically induced absorption (EIA) region. We can use our setup as phase shift interferometer [89] to study phase shift measurements in the observation of absorptive EIT to dispersive EIT transformation. Our setup has a potential application in optical magnetometer [96–98] as the dispersion in EIT is very sensitive to the magnetic field.

5

Polarization rotation with electromagnetically induced transparency¹

5.1 Introduction

In the previous work (described in chapter 4), we have observed the dispersion signal of the atomic medium by homodyne detection technique with the help of Mach-Zehnder interferometry setup. This technique is very noise sensitive. Therefore, the signal to noise ratio (S/N) of our observed signal was low. To get rid of the noise, we have chosen to experiment with polarization rotation spectroscopy (PRS) setup where the observed signal is dispersive, and the S/N ratio of the signal is very high.

There are many previous works on PRS where authors detected the rotation signal due to the atomic medium in two-level [25] and three-level [44, 45, 99] systems. Kulatunga et al. [44] studied two colour polarization spectroscopy in room temperature Rb vapour with a cascade configuration. They used the PRS signal to lock the 776 nm laser. Carr et al. [45] demonstrated polarization spectroscopy of an excited state in room-temperature Cs-vapour also with a cascade configuration. Pandey et al. [31] experimentally studied the rotation of the polarization axis of the probe beam with or without the magnetic

¹This chapter is based on the publication Das et al. *J. Phys. B: At. Mol. Opt. Phys.*, **2018**, *51*, 175502 - 175513. The experiment and the theoretical calculations presented in this chapter have been entirely done by Arpita Das.

field for the room temperature Rb vapour. They studied their system in a cascade configuration. Polarization-rotation has also been studied in a ΛV -type system of the Rb D_2 transition in room temperature vapour cell [100]. Polarization effects in the interaction between multi-level atoms and two optical fields have been studied in ^{85}Rb in a Λ type, and a cascade-type configuration [101]. Absorption, polarization rotation and the visible fluorescence that result from the decay of the excited states were also measured in Rb atom with a cascade configuration [102]. Cha et al. [99] presented a two colour spectroscopy in a V -type configuration using the D_1 and D_2 transitions of Rb with co-propagating and counter-propagating geometry. However, EIT was not observed in their experimentally observed spectrum. Kang et al. [103] did an experiment with the D_1 and D_2 transitions of Rb atom where they studied the coherence effect of the EIT with the absorption properties in a V -type system of ^{87}Rb using the polarization spectroscopy setup.

This chapter contains the process of finding out how the quantum interference effect of the V -type Rb system affects the rotation of the plane of polarization of the probe beam [2]. For this purpose, we made a polarization spectroscopy setup. We used two laser sources of 795 nm and 780 nm wavelengths for the circularly polarized strong pump beam and the linearly polarized weak probe beam respectively. We studied the phenomenon of rotation of the plane of polarization in the EIT region [9, 12] at room temperature (21°C). We named this phenomenon as polarization rotation with electromagnetically induced transparency (PREIT). In this study, we have investigated the optical rotation from the dispersion signal under EIT condition both for ^{85}Rb and ^{87}Rb . We have also studied the dependency of the optical rotation for the probe field in the EIT region on the

intensity of the pump field. We have modelled a four-level atomic system to understand the physics behind the experimentally observed phenomenon. We have solved the four-level density matrix equation under the steady-state condition analytically to get the probe coherence term. The variation of polarization rotation with the pump intensity has also been shown. The experimental and the theoretical characteristic variation of the angle of rotation with the intensity of the pump beam are compared.

5.2 Experiment

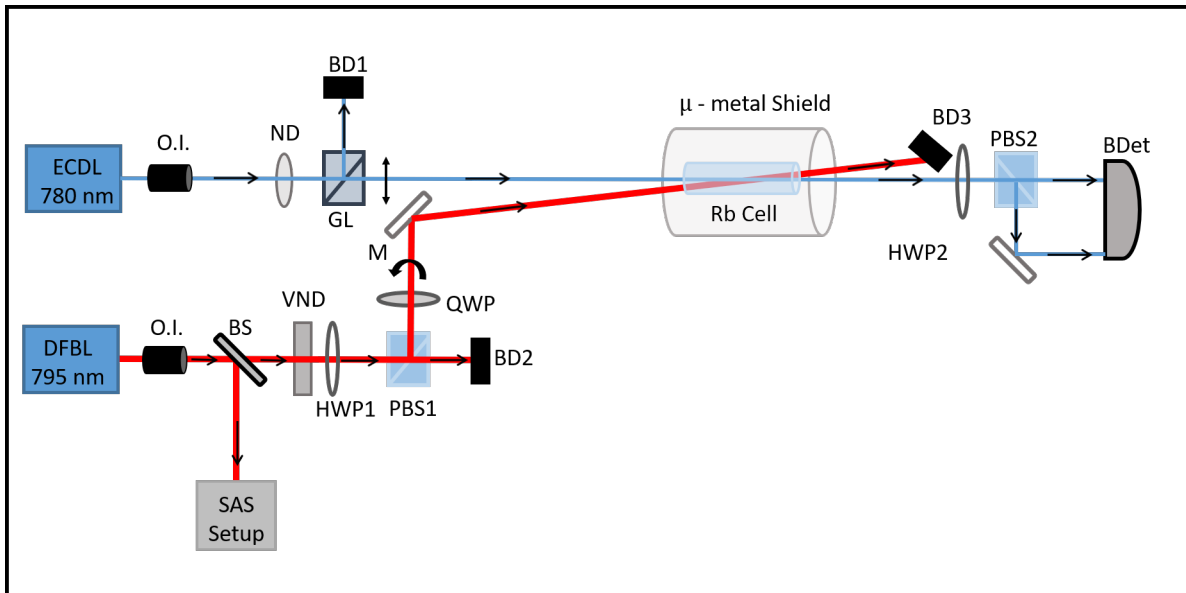


Figure 5.1: Experimental Setup. ECDL : External Cavity Diode Laser, DFBL: Distributed Feedback Diode Laser, O.I. : Optical Isolator, HWP: Half-wave Plate, QWP: Quarter-wave Plate, GL: Glan-laser Polarizer, PBS: Polarizing Beam Splitting Cube, BS: Beam Splitter, M: Mirror, Rb Cell : Rubidium Vapour Cell, BD : Beam Dump, ND: Neutral Density Filter, VND: Variable Neutral Density Filter, SAS Setup: Saturation Absorption Spectroscopy Setup, BDet: Balanced Detector.

The experimental setup to study the PREIT is shown in the Fig.5.1. We used an external cavity diode laser (ECDL) of 780 nm with linewidth ~ 1 MHz for the probe beam, and a home built distributed feedback diode laser (DFBL) of 795 nm for the pump beam. The DFBL has a linewidth ~ 2 MHz and temperature stability ~ 2 mK. Both the beams have a diameter ~ 2 mm. Optical isolators (O.I.) were used to avoid back reflections to both the diodes. A neutral density filter (ND) was used to reduce the probe beam power. With the help of a glan-laser polarizer (GL), the probe beam was made p-polarized. A 10:90 (R:T) beam splitter (BS) was used in the path of the pump beam. The reflected part of the beam was used to lock the pump beam to a particular hyperfine level using the saturation absorption spectroscopy setup (SAS setup), and the transmitted part was taken for the polarization spectroscopy experiment. Using a polarizing beam splitting cube (PBS1), the pump beam was made s-polarized, and with the help of a half-wave plate (HWP1), the intensity of the pump beam was adjusted. A quarter-wave plate (QWP) after PBS1 made the pump beam σ^+ polarized. The probe and the pump beams co-propagated with a certain angle through a 75 mm long Rubidium vapour cell (Rb cell) of 25 mm diameter. Our Rb cell contained both ^{85}Rb and ^{87}Rb in their natural abundance without any buffer gas under $\sim 10^{-7}$ Torr pressure. The angle between the pump and the probe beams was kept very small, about ~ 8 mrad so that only the probe beam can reach the balanced detector (BDet; New Focus, Model No:2307). To avoid interference due to the stray magnetic field of the earth, the Rb cell was covered by a thick μ -metal shield. After coming out from the atomic medium, the probe beam was passed through a half-wave plate (HWP2) and a polarizing beam splitting cube (PBS2). The combination of HWP2 and PBS2, oriented at an angle (ϕ) of $\pi/4$ helped in resolving

the electric field of the probe beam into two orthogonal components. The components were detected by the BDet. This detection technique is known as balanced polarimetric detection technique [25, 104]. We recorded the Doppler-free dispersion spectrum of the probe beam with a digital storage oscilloscope (Rohde and Schwarz, Model No: RT01004) since the polarization spectroscopy is a Doppler-free technique. Beam dumps (BD1, BD2, BD3) were used for laser safety in the path of the unused beams.

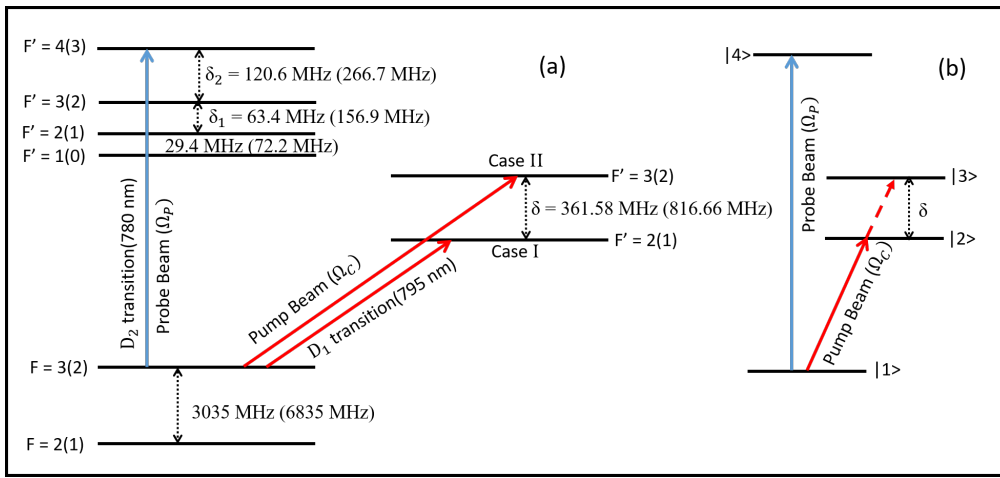


Figure 5.2: (a) Energy level diagram for $^{85(87)}\text{Rb}$ for two cases. In case I, the pump beam was locked to $F = 3(2) \rightarrow F' = 2(1)$ transition and then in case II, we locked the pump beam to $F = 3(2) \rightarrow F' = 3(2)$ of D₁ transition for $^{85(87)}\text{Rb}$. The probe beam was scanned from $F = 3(2) \rightarrow F' = 2(1), 3(2), 4(3)$ of D₂ transition for $^{85(87)}\text{Rb}$. (b) Simplified four level system modeled for theoretical analysis (for details see section (5.4)).

We have observed the phenomenon of rotation of the polarization axis of the probe beam for both ^{85}Rb and ^{87}Rb at EIT condition in room temperature. We observed two separate cases for each of ^{85}Rb and ^{87}Rb . In the first case, for ^{85}Rb , the pump beam was locked at $F = 3 \rightarrow F' = 2$ and in the second case, we locked the pump beam at $F = 3 \rightarrow F' = 3$ of D₁ transition. The probe beam was scanned from $F = 3 \rightarrow F' = 2, 3, 4$ of D₂ transition in both the cases of ^{85}Rb . Similarly, for ^{87}Rb

at first, we locked the pump beam at $F = 2 \rightarrow F' = 1$ and in the second case, the pump beam was locked at $F = 2 \rightarrow F' = 2$ of D_1 transition. The probe beam was scanned from $F = 2 \rightarrow F' = 1, 2, 3$ of D_2 transition for both the cases of ^{87}Rb . The corresponding level schemes are shown in Fig.5.2(a). Since in each case the pump and the probe beams shared a common ground state, the V-type system was formed. Throughout our experiment we had fixed the probe beam power to $16.02 \pm 1.01 \mu\text{W}$ and varied the pump beam power from $18.00 \pm 1.2 \mu\text{W}$ to $5.05 \pm 0.25 \text{ mW}$ for each of the cases of ^{85}Rb and ^{87}Rb .

5.3 Experimental results and analysis

The experimental spectra of both the absorption (a and c in Fig.5.3) and the dispersion (b and d in Fig.5.3) for ^{85}Rb when the pump beam was locked at $F = 3 \rightarrow F' = 2$ (a and b in Fig.5.3) and at $F = 3 \rightarrow F' = 3$ (c and d in Fig.5.3) are shown in Fig.5.3. In both the cases we got two EIT peaks since the pump beam can couple both the excited states i.e. $F' = 2$ and $F' = 3$ simultaneously. This is because the separation between them in the D_1 transition for ^{85}Rb ($\delta = 361.58 \text{ MHz}$) is within the Doppler width ($\sim 510 \text{ MHz}$) at room temperature. The EIT peaks were observed for the closed transition of the probe beam and they were separated by $\delta = 361.58 \pm 0.05 \text{ MHz}$. We defined the EIT peak appearing at the lock position as ‘EIT peak’ and the EIT peak situated at the coupled position as ‘EIT peak due to coupling’. Besides these two EIT peaks, we also observed four velocity selective resonance (VSR) peaks [105] corresponding to the excited states of D_2 transition for the probe beam. In general, VSR peaks occur due to

Doppler effect of the atom. When the pump beam is locked at a particular transition and the probe beam is scanned through all the allowed dipole transitions, then due to velocity effect, the atoms with different group of velocities are in resonance with pump beam. Since we observed the absorption profile of the probe beam, we got peaks in the absorption profile. The peak, which occurred at the closed transition of the probe beam, satisfies the Raman detuning condition. It is therefore called an EIT peak. Other peaks are known as velocity selective resonance (VSR) [105, 106]. For example, let us consider the case of ^{85}Rb where the pump beam was locked at $F = 3 \rightarrow F' = 3$ of D_1 transition line. When pump beam is on resonance with this transition it can absorb the atoms of such velocity groups where their Doppler shifts are equal to the transition frequencies of $F = 3 \rightarrow F' = 2$, $F = 3 \rightarrow F' = 3$ and $F = 3 \rightarrow F' = 4$ of D_2 transition line of the probe beam. Therefore, being a closed transition, $F = 3 \rightarrow F' = 4$ gives EIT peak, while the other peaks are coming purely from velocity effects of the atom and are known as VSR peaks.

On the other hand, in case of ^{85}Rb the system behaves as a double V-type system as the pump beam can couple both the excited states simultaneously. The Raman detuning condition was satisfied for both the three-level systems when the probe is on-resonance with the closed transition ($F = 3 \rightarrow F' = 4$). Therefore, we observed two EIT peaks in the absorption profile and correspondingly two normal dispersions in the dispersion signal separated by 361.58 ± 0.05 MHz. So, in total, we got four VSR peaks along with two EIT peaks for ^{85}Rb . The resonance positions of the peaks in Fig.5.3 are given in Table (5.1).

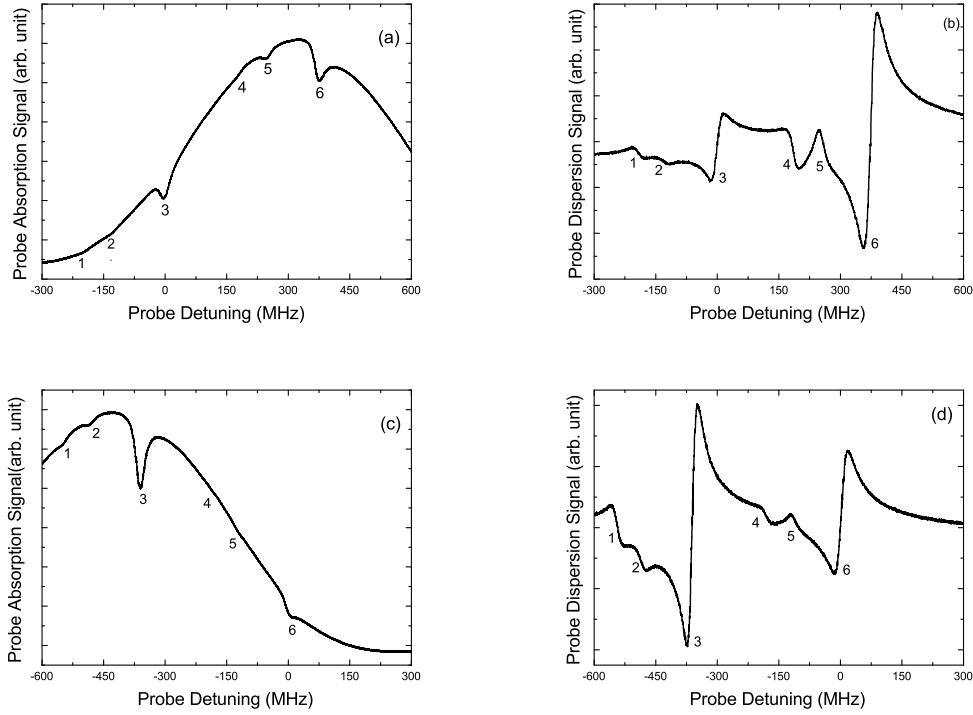


Figure 5.3: (a,c) Experimental Doppler-broadened absorption spectra for ^{85}Rb of the probe beam when one of the photo diodes of the balanced detector was blocked. (b,d) Experimental Doppler free spectra for ^{85}Rb of the probe beam when both the photo diodes of the balanced detector were opened. In the above figures the lock positions of the pump beam were at (a,b) $F = 3 \rightarrow F' = 2$ and at (c,d) $F = 3 \rightarrow F' = 3$ of D_1 transitions respectively. In all the plots, the probe intensity was $0.51 \pm 0.05 \text{ mW/cm}^2$ and the pump intensity was $1.53 \pm 0.15 \text{ mW/cm}^2$. In all the cases the probe beam was scanned from $F = 3 \rightarrow F' = 2, 3, 4$ of D_2 transition. The numbers in the figures are explained in Table (5.1).

Rb isotope	Lock position	Peak 1	Peak 2	Peak 3	Peak 4	Peak 5	Peak 6
85	$F = 3 \rightarrow F' = 2$	-184.04 ± 0.05 MHz	-120.64 ± 0.05 MHz	0 MHz	177.54 ± 0.05 MHz	240.94 ± 0.05 MHz	361.58 ± 0.05 MHz
85	$F = 3 \rightarrow F' = 3$	-545.62 ± 0.05 MHz	-482.22 ± 0.05 MHz	-361.58 ± 0.05 MHz	-184.04 ± 0.05 MHz	-120.64 ± 0.05 MHz	0 MHz

Table 5.1: Experimentally observed resonance positions for ^{85}Rb .

From Fig.5.3, we observed that the strength of the ‘EIT peaks due to coupling’ is more than the strength of the ‘EIT peaks’. The number of atoms interacting with the coupling transition, which is 361.58 ± 0.05 MHz shifted from the locked transition of the pump beam, is less than the number of atoms interacting with the locked transition. Due to this reason the EIT peaks due to coupling were observed with more transparency background than the EIT peaks [107].

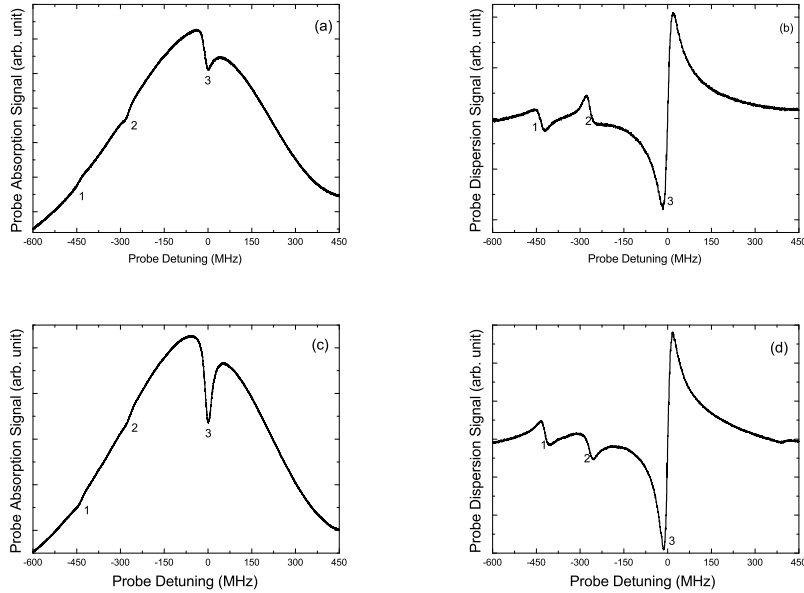


Figure 5.4: (a,c) Experimental Doppler-broadened absorption spectra for ^{87}Rb of the probe beam when one of the photodiodes of the balanced detector was blocked. (b,d) Experimental Doppler free spectra for ^{87}Rb of the probe beam when both the photodiodes of the balanced detector were opened. In the above figures the lock positions of the pump beam were at (a,b) $F = 2 \rightarrow F' = 1$ and at (c,d) $F = 2 \rightarrow F' = 2$ of D_1 transitions respectively. In all the plots the probe intensity was 0.51 ± 0.05 mW/cm² and the pump intensity was 1.53 ± 0.15 mW/cm². In all the cases the probe beam was scanned from $F = 2 \rightarrow F' = 1, 2, 3$ of D_2 transition. The numbers in the figures are explained in Table (5.2).

Rb isotope	Lock position	Peak 1	Peak 2	Peak 3
87	$F = 2 \rightarrow F' = 1$	-423.60 ± 0.07 MHz	-266.65 ± 0.07 MHz	0 MHz
87	$F = 2 \rightarrow F' = 2$	-423.60 ± 0.07 MHz	-266.65 ± 0.07 MHz	0 MHz

Table 5.2: Experimentally observed resonance positions for ^{87}Rb .

Similarly, the experimental spectra of the absorption (a and c in Fig.5.4) and the dispersion (b and d in Fig.5.4) for ^{87}Rb when the pump beam was locked at $F = 2 \rightarrow F' = 1$ (a and b in Fig.5.4) and at $F = 2 \rightarrow F' = 2$ (c and d in Fig.5.4) are shown in Fig.5.4. Here, we got only one EIT peak at the closed transition position as the pump beam can not couple the two excited states simultaneously since they are separated by 861.66 MHz which is beyond the Doppler limit at the room temperature. We also observed two VSR peaks. The resonance positions of the peaks in Fig.5.4 are given in the Table (5.2).

We observed that it is difficult to resolve the VSR peaks from the absorption spectra of the probe beam as shown in Fig.5.3(a), Fig.5.3(c), Fig.5.4(a) and Fig.5.4(c) respectively. This happens possibly due to the optical pumping effect (which broadened the peaks) and also due to the positions of the VSRs are at the tailing end of the Doppler profile. But in the dispersion spectra of Fig.5.3(b), Fig.5.3(d), Fig.5.4(b) and Fig.5.4(d) respectively, the resonances are well resolved since these spectra are Doppler free.

Since our aim was to measure the angle of rotation of the plane of polarization of the probe beam in the EIT region, so we focused only on the dispersion spectra. We observed from the above spectra that the slope corresponding to the EIT position is ‘positive’ due

to normal dispersion. By varying the pump beam intensity in each case for both ^{85}Rb and ^{87}Rb , we observed that the intensity of the dispersion signal near the resonance of the probe beam was increasing with the increment in the intensity of the pump beam. The variations of the intensity, as well as the slope for both of ^{85}Rb and ^{87}Rb , are shown in the Fig.5.5, where we can observe the increasing intensity of the spectra.

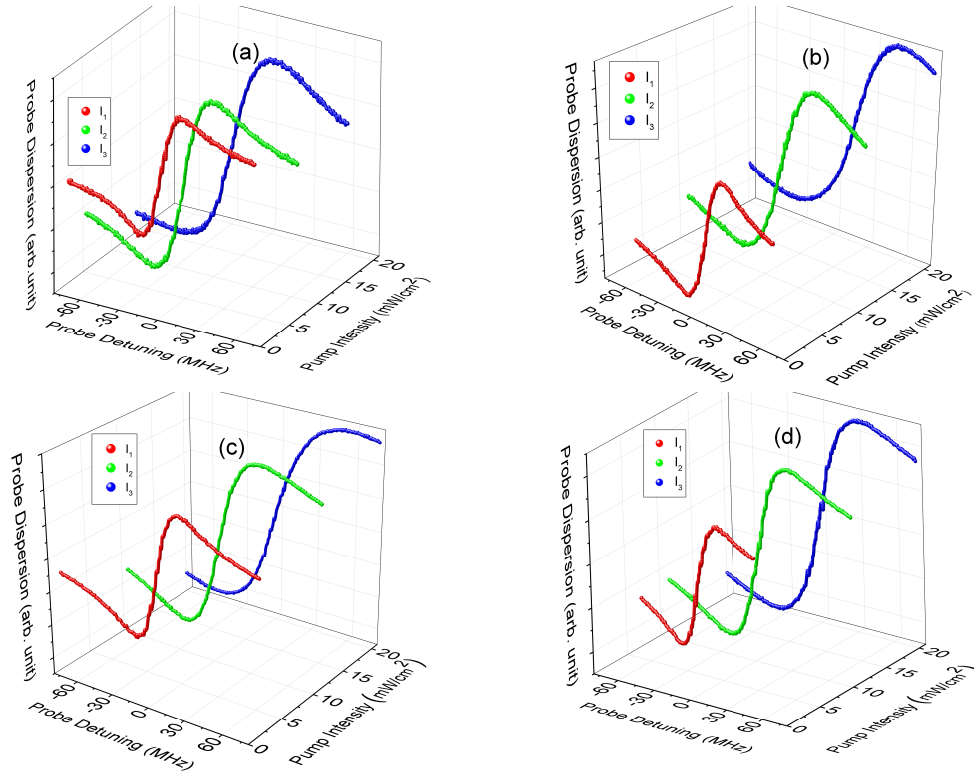


Figure 5.5: Experimental dispersion spectrum in EIT region with three different pump beam intensities ($I_1 = 1.53 \pm 0.15 \text{ mW/cm}^2$, $I_2 = 10.76 \pm 0.54 \text{ mW/cm}^2$, $I_3 = 20.05 \pm 1.02 \text{ mW/cm}^2$) when the pump beam was locked (a) at $F = 3 \rightarrow F' = 2$ transition for ^{85}Rb , (b) at $F = 3 \rightarrow F' = 3$ transition for ^{85}Rb , (c) at $F = 2 \rightarrow F' = 1$ transition for ^{87}Rb and (d) at $F = 2 \rightarrow F' = 2$ transition for ^{87}Rb .

Since we detected the signal to measure the polarization rotation from a balanced detector, we got a Doppler free dispersion signal of the probe beam. The angle of polarization rotation in the EIT region can be calculated from the slope of the dispersion

signal. The output intensity of the rotational signal can be written as (see Appendix C),

$$\Delta I(\omega_p) \approx I_0 \exp(-\alpha L) \theta(\omega_p) \quad (5.3.1)$$

Here, $\theta(\omega_p) = \frac{\Delta n(\omega_p) \omega_0 L}{c}$ is the angle of rotation of the polarization axis of the probe beam. c is the velocity of light in free space. $\Delta n(\omega_p) = n_+(\omega_p) - n_-(\omega_p)$ measures the anisotropy created in the atomic medium corresponding to the refractive index and $\alpha = (\alpha_+ + \alpha_-)$ gives the total absorption in the medium due to the different polarization components of the probe field. Since $\theta \ll 1$, from Eq.(5.3.1) at $\omega_p = \omega_0$ we can write the angle of rotation as,

$$\theta(\omega_0) = \frac{1}{I_0 \exp(-\alpha L)} \left. \frac{d(\Delta I(\omega_p))}{d\omega_p} \right|_{\omega_0} \Delta\omega_p \quad (5.3.2)$$

Eq.(5.3.2) is a general equation to calculate the rotation angle for any resonance position. Following this equation we have calculated the angle of rotation θ in the vicinity of the EIT resonance. The corresponding anisotropy for the refractive index at the resonance frequency can be calculated as,

$$\Delta n(\omega_0) = \frac{c \theta(\omega_0)}{\omega_0 L} \quad (5.3.3)$$

Following Eq.(5.3.2), from the slope of the dispersive EIT signal, we calculated the angle of rotation of the plane of polarization of the probe beam for increasing pump beam intensity. The angle of rotation has been calculated in each case for both ^{85}Rb and ^{87}Rb . We have plotted the angle of rotation as a function of the pump intensity and got a non-linear variation, as shown in Fig.5.6. From Fig.5.6(a) and Fig.5.6(b) we see that with the increase in the pump intensity upto a certain value, the rotation of the probe field increases gradually (see the insets of these figures), then it decreases with further

increase in the pump intensity. Even at high pump power (or, intensity), the variation maintains a decreasing trend. This phenomenon can be explained in the following way.

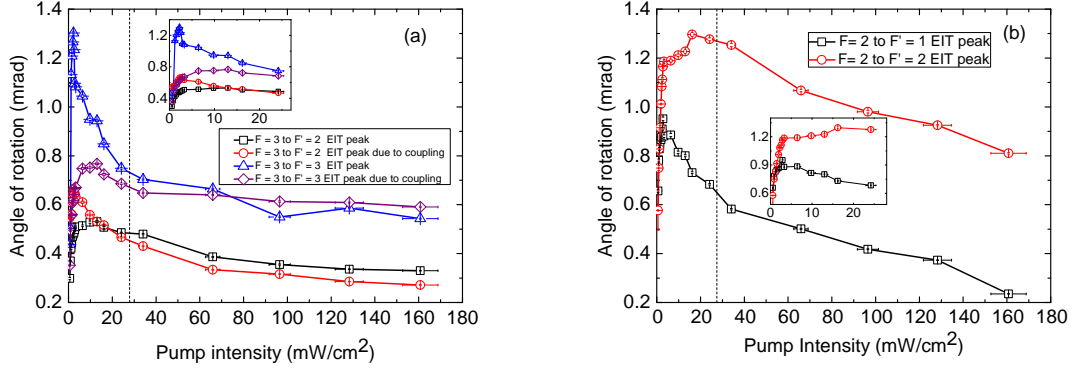


Figure 5.6: Experimental variation of the angle of rotation of the polarization axis of the probe beam for different pump intensities in the EIT region for (a) ^{85}Rb and (b) ^{87}Rb (the lines are drawn for the eye guidance). The regions shown by the dashed lines in both the figures are zoomed in the insets given in each figure. The lock positions for the EIT peaks are shown in the legends.

The anisotropy of the refractive index for the probe field or the circular birefringence in the medium and the dispersive behaviour increases as the intensity of the pump beam increases in the low pump power region. Then in the vicinity of the saturation intensity of the pump beam, we get the maximum rotation. In the high pump power region, the power broadening phenomenon dominates over the anisotropic, as well the dispersive, behaviour of the medium for the probe field. On increasing the pump intensity further, the medium gets saturated, and the rotation is maximized. Beyond this, i.e. in the high pump power region, no further distribution of the population is possible, so the angle rotation decrease. In the high pump intensity region, the interference effect of the EIT is dominated by the power broadening phenomenon. This results an increase in the slope of the normal dispersion corresponding to EIT resonance. As a result the angle of rotation

decreases.

From these variations we have also observed that the value of the angle of rotation is always more for the transition $F = 3 \rightarrow F' = 3$ than that for the transition $F = 3 \rightarrow F' = 2$ in case of ^{85}Rb . We mentioned earlier that the anisotropy created in the medium, which leads to the rotation of plane of polarization, occurred mainly due to the non-uniform distribution of population between the sub-levels. Therefore, we might say that for a particular pump intensity, this non-uniform distribution of population is more for the transition from $F = 3 \rightarrow F' = 3$ than that for the transition from $F = 3 \rightarrow F' = 2$. So we got more rotation for $F = 3 \rightarrow F' = 3$ than that for $F = 3 \rightarrow F' = 2$. Similarly, since for a particular pump intensity, the non-uniform distribution of population is more for the transition $F = 2 \rightarrow F' = 2$ than that for the transition $F = 2 \rightarrow F' = 1$, we observed that the value of rotation is more for the earlier case than that for the later for ^{87}Rb . Thus, we can conclude that to get maximum rotation we have to be selective about the pump intensity and the transition where the pump beam had to be locked.

Rubidium isotope	Lock position of the pump beam	Value of anisotropy ($\Delta n(\omega_0)$)
85	$F = 3 \rightarrow F' = 2$	35.2 ± 0.17 & 44.34 ± 0.12
85	$F = 3 \rightarrow F' = 3$	106.4 ± 0.83 & 65.2 ± 0.20
87	$F = 2 \rightarrow F' = 1$	80.55 ± 0.58
87	$F = 2 \rightarrow F' = 2$	108 ± 0.88

Table 5.3: Experimentally obtained maximum anisotropy in the Rb atomic medium at room temperature in the vicinity of the EIT.

We have also estimated the maximum value of anisotropy for the difference in the refractive index ($\Delta n(\omega_0)$) at the resonance frequency, i.e., corresponding to each EIT position in the atomic medium. It arises due to the different components of the polarization of the probe field in the EIT condition. The maximum values of anisotropy towards

refractive index are calculated from the maximum values of the angle of rotation with the help of Eq.(5.3.3). The corresponding values for both ^{87}Rb and ^{85}Rb due to all the transitions are shown in the Table (5.3). There are two values of anisotropy for ^{85}Rb corresponding to the two EIT positions, as shown in the table. The first one is for the EIT peak, and the second one is for the EIT peak due to coupling.

5.4 Theoretical Model

To explain the formation of double EIT in the case of ^{85}Rb and the optical rotation phenomenon in EIT, we have considered a four-level system. The simplified system is shown in the Fig.5.2(b), where the probe beam interacts with the levels $|1\rangle$ and $|4\rangle$ and the pump beam couples the levels $|1\rangle$ and $|2\rangle$. The pump beam can also couple the level $|3\rangle$ with the level $|1\rangle$ simultaneously while interacting with the level $|2\rangle$ if the separation (δ) between $|2\rangle$ and $|3\rangle$ is within the Doppler limit. Transitions between $|1\rangle$ and $|4\rangle$, $|1\rangle$ and $|2\rangle$ and $|1\rangle$ and $|3\rangle$ are dipole allowed transitions. Transitions between $|4\rangle$ and $|3\rangle$, $|4\rangle$ and $|2\rangle$ and $|2\rangle$ and $|3\rangle$ are dipole forbidden transitions. Since in the case of ^{85}Rb , $\delta = 361.58$ MHz, the pump beam can couple both the excited states due to thermal velocity. Thus in the case of ^{85}Rb , we defined the system as a double V-type, which is formed only with two beams. This leads us to two EIT peaks for ^{85}Rb . For ^{87}Rb , $\delta = 816.66$ MHz, the separation being beyond the Doppler width, the pump beam cannot couple the excited states. Therefore, in this case, the four-level system is reduced to a three-level V-type system, and we get one EIT peak for ^{87}Rb .

To get the probe coherence term, we have solved the master equation, Eq.(3.1.12)

with phenomenologically included decay terms described in Eq.(3.1.16). In this case, ρ is a 4×4 density matrix. We took the probe field as $\varepsilon_p = E_p \cos(\omega_p t - k_p z)$ and the pump field as $\varepsilon_c = E_c \cos(\omega_c t - k_c z)$ where $E_{p(c)}$ is the amplitude of the electric field of frequency $\omega_{p(c)}$ and $k_{p(c)} = 2\pi/\lambda_{p(c)}$ is the wave vector for the probe (pump) field. With the above definitions, the perturbed Hamiltonian becomes, $H_I = -\hbar(\Omega_{21} \cos(\omega_c t - k_c z) |1\rangle \langle 2| + \Omega_{31} \cos(\omega_c t - k_c z) |1\rangle \langle 3| + \Omega_{41} \cos(\omega_p t - k_p z) |1\rangle \langle 4| + c.c.)$. In this case the optical Bloch equations for the four level system assuming RWA are given by,

$$\begin{aligned}
\dot{\rho}_{11} &= \Gamma_{41} \rho_{44} + \Gamma_{31} \rho_{33} + \Gamma_{21} \rho_{22} + \frac{i}{2} \Omega_{21} (\rho_{21} - \rho_{12}) + \frac{i}{2} \Omega_{31} (\rho_{31} - \rho_{13}) + \frac{i}{2} \Omega_{41} (\rho_{41} - \rho_{14}) \\
\dot{\rho}_{22} &= -\Gamma_{21} \rho_{22} - \frac{i}{2} \Omega_{21} (\rho_{21} - \rho_{12}) \\
\dot{\rho}_{33} &= -\Gamma_{31} \rho_{33} - \frac{i}{2} \Omega_{31} (\rho_{31} - \rho_{13}) \\
\dot{\rho}_{44} &= -\Gamma_{41} \rho_{44} - \frac{i}{2} \Omega_{41} (\rho_{41} - \rho_{14}) \\
\dot{\rho}_{i3} &= -D_{13}^{-1} \rho_{13} + \frac{i}{2} \Omega_{31} (\rho_{33} - \rho_{11}) + \frac{i}{2} \Omega_{21} \rho_{23} + \frac{i}{2} \Omega_{41} \rho_{43} \\
\dot{\rho}_{i2} &= -D_{12}^{-1} \rho_{12} + \frac{i}{2} \Omega_{21} (\rho_{22} - \rho_{11}) + \frac{i}{2} \Omega_{31} \rho_{32} + \frac{i}{2} \Omega_{41} \rho_{42} \\
\dot{\rho}_{41} &= -D_{41}^{-1} \rho_{41} - \frac{i}{2} \Omega_{41} (\rho_{44} - \rho_{11}) - \frac{i}{2} \Omega_{21} \rho_{42} - \frac{i}{2} \Omega_{31} \rho_{43} \\
\dot{\rho}_{43} &= -D_{43}^{-1} \rho_{43} + \frac{i}{2} \Omega_{41} \rho_{13} - \frac{i}{2} \Omega_{31} \rho_{41} \\
\dot{\rho}_{42} &= -D_{42}^{-1} \rho_{42} + \frac{i}{2} \Omega_{41} \rho_{12} - \frac{i}{2} \Omega_{31} \rho_{41} \\
\dot{\rho}_{32} &= -D_{32}^{-1} \rho_{32} + \frac{i}{2} \Omega_{31} \rho_{12} - \frac{i}{2} \Omega_{21} \rho_{31}
\end{aligned} \tag{5.4.1}$$

Here, Ω_{i1} is the Rabi frequency of the pump beam for the transition from $|1\rangle$ to $|i\rangle$ ($i = 2, 3$) and Ω_{41} is the probe Rabi frequency for the transition from $|1\rangle$ to $|4\rangle$. Since the probe resonance frequency is $\omega_{41} = \omega_0$, $\delta_p = \delta_{41} = (\omega_0 - \omega_p)$ is the probe detuning. The Doppler detuning of the probe is $\Delta_p = \Delta_{41} = (\delta_p + k_p v)$, where v is the component of the velocity of one of the atoms in the propagation direction (z) of the beam through the atomic medium. Similarly, we have defined $\delta_{21} = (\omega_{21} - \omega_c)$ and $\delta_{31} = (\omega_{31} - \omega_c) =$

$(\omega_{21} - \omega_c + \delta) = (\delta_{21} + \delta)$ as the detunings of the pump beam while it coupled the levels $|2\rangle$ and $|3\rangle$ with the Doppler detunings of the pump beam as $\Delta_{21} = (\delta_{21} + k_c v)$ and $\Delta_{31} = (\delta_{31} + k_c v) = (\Delta_{21} + \delta)$ respectively.

Now, solving Eq.(5.4.1) under steady state condition we obtained the probe coherence term ρ_{41} as,

$$\rho_{41} = \frac{i\frac{\Omega_{41}}{2}D_{41}}{(1 + \frac{\Omega_{21}^2}{4}D_{41}D_{42} + \frac{\Omega_{31}^2}{4}D_{41}D_{43})} \left\{ \rho_{11}^0 + \frac{\Omega_{21}^2}{4}(D_{42}C_{12} - \frac{\Omega_{31}^2}{4}D_{43}d)(\rho_{22}^0 - \rho_{11}^0) \right. \\ \left. + \frac{\Omega_{31}^2}{4}(D_{43}C_{13} - \frac{\Omega_{21}^2}{4}D_{42}d^*)(\rho_{33}^0 - \rho_{11}^0) \right\} \quad (5.4.2)$$

We have calculated the probe coherence term contained in the Eq.(5.4.2) under the first order perturbation for the probe beam. In this equation ρ_{11}^0 , ρ_{22}^0 and ρ_{33}^0 are the zeroth order populations of the levels $|1\rangle$, $|2\rangle$ and $|3\rangle$ respectively. The zeroth order population (ρ_{44}^0) for the level $|4\rangle$ was assumed to be zero. The parameters used in Eq.(5.4.2) are described as follows,

$$\rho_{11}^0 = \frac{1}{1 + P}$$

$$\rho_{jj}^0 = \frac{E_{jj}^{-1}F_{jj} - i\frac{\Omega_{j1}^2\Omega_{k1}}{8}E_{kk}^{-1}E_{jj}^{-1}F_{kk}(d + d^*)}{G_{jj}(1 + P)}, \quad j = 2, 3 \quad \text{and} \quad k = 3, 2$$

$$P = G_{22}^{-1}E_{22}^{-1}F_{22} + G_{33}^{-1}E_{33}^{-1}F_{33} - i\frac{\Omega_{21}\Omega_{31}}{8}E_{33}^{-1}E_{22}^{-1}(d + d^*)(\Omega_{21}G_{33}^{-1}F_{33} + \Omega_{31}G_{22}^{-1}F_{22})$$

$$G_{jj} = 1 + \frac{\Omega_{j1}^2\Omega_{k1}^4}{64}E_{kk}^{-1}E_{jj}^{-1}(d + d^*)^2, \quad j = 2, 3 \quad \text{and} \quad k = 3, 2$$

$$F_{jj} = (-1)^j \frac{\Omega_{j1}^2\Omega_{k1}^2}{16\Gamma_{j1}}(d + d^*) + \frac{\Omega_{j1}^2}{4\Gamma_{j1}}(C_{j1} + C_{j1}^*), \quad j = 2, 3 \quad \text{and} \quad k = 3, 2$$

$$E_{jj} = 1 + \frac{\Omega_{j1}^2}{4\Gamma_{j1}}(C_{j1} + C_{j1}^*), \quad j = 2, 3$$

$$d = \frac{D_{13}D_{21}D_{23}}{A_{13}A_{12}B}$$

$$C_{1j} = \frac{D_{1j}}{A_{1j}B}, \quad j = 2, 3$$

$$B = 1 - \frac{\Omega_{21}^2\Omega_{31}^2}{16}A_{13}^{-1}A_{12}^{-1}D_{21}D_{13}D_{23}^2$$

$$\begin{aligned}
A_{12} &= 1 + \frac{\Omega_{31}^2}{4} D_{21} D_{23} \\
A_{13} &= 1 + \frac{\Omega_{21}^2}{4} D_{13} D_{23} \\
D_{j1}^{-1} &= \gamma_{j1} + i\Delta_{j1}, \quad j = 2, 3, 4 \\
D_{4k}^{-1} &= \gamma_{4k} + i(\Delta_{41} - \Delta_{k1}), \quad k = 2, 3 \\
D_{32}^{-1} &= \gamma_{32} + i(\Delta_{31} - \Delta_{21})
\end{aligned} \tag{5.4.3}$$

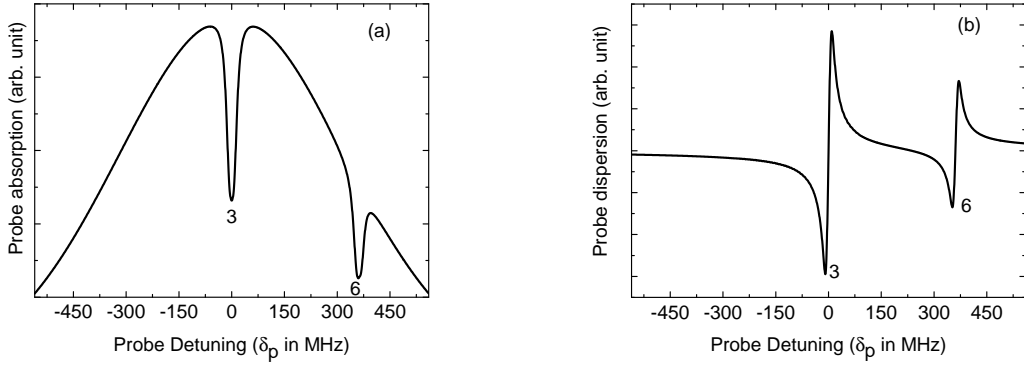


Figure 5.7: Simulated (a) absorption and (b) dispersion spectra of the probe beam for ^{85}Rb . In both the spectra, the probe beam intensity and the pump beam intensity are set at 0.51 mW/cm^2 and 1.53 mW/cm^2 respectively.

Since in our experiment we have scanned the probe beam and have locked the pump beam, to maintain the same experimental condition in the simulation, we varied the detuning (δ_p) of the probe beam and set the detuning of the pump beam $\delta_{21} = 0$. The $\text{Im}(\rho_{41})$ is related to the absorption of the medium and the $\text{Re}(\rho_{41})$ gives the response of the dispersion of the medium. The Rabi frequencies were calculated from the relation, $\Omega = \Gamma \sqrt{\frac{I}{2I_{sat}}}$ [78, 79], where Γ is the natural linewidth, I is the intensity of the beam and I_{sat} is the saturation intensity of the medium.

For ^{85}Rb , the simulated absorption and the dispersion spectra are shown in Fig.5.7(a) and Fig.5.7(b) respectively, where we have set $\delta_{31} = (\delta_{21} + 361.58)$ MHz and got two EIT peaks. Peak 3 at $\delta_p = 0$ MHz and peak 6 at $\delta_p = 361.58$ MHz are the two EIT peaks shown in Fig.5.7(a) and Fig.5.7(b) (similar to the peaks as marked in Fig.5.3(a) and Fig.5.3(b)) of the experimental spectra. Here, peak 3 and the peak 6 are the EIT peak and the EIT peak due to coupling respectively. Other way round, if we had set $\delta_{31} = 0$ MHz and $\delta_{21} = (\delta_{31} - 361.58)$ MHz, then we would get the two EIT peaks at $\delta_p = -361.58$ MHz (EIT peak due to coupling) and at $\delta_p = 0$ MHz (EIT peak) respectively. So for ^{85}Rb our model behaves like a double V-type system though it is coupled with only two laser beams. Since we assumed a simple four level model we did not get any VSR peaks in our simulation. Further, for this reason we did not observe any asymmetry in the absorption and the dispersion profiles in theoretical simulation. Whereas, those asymmetries were present in the experimental spectra.

The simulated absorption and the dispersion spectra for ^{87}Rb are shown in the Fig.5.8(a) and Fig.5.8(b) respectively. In this case the probe detuning δ_p was varied and the pump detunings were set at $\delta_{21} = 0$ MHz and $\delta_{31} = (\delta_{21} + 816.66)$ MHz. Here the separation δ is beyond the Doppler limit, so we got only one EIT peak (peak 3 in Fig.5.8) for ^{87}Rb . Thus for ^{87}Rb our model is reduced to a three-level V-type system. In our simulation we took $\Gamma_{41} = 6$ MHz, $\Gamma_{31} = \Gamma_{21} = 5.7$ MHz, $\gamma_{41} = \frac{\Gamma_{41}}{2}$, $\gamma_{21} = \frac{\Gamma_{21}}{2}$, $\gamma_{31} = \frac{\Gamma_{31}}{2}$ and for the dipole forbidden transitions, $\gamma_{42} = \frac{\Gamma_{41} + \Gamma_{21}}{2}$, $\gamma_{43} = \frac{\Gamma_{41} + \Gamma_{31}}{2}$ and $\gamma_{32} = 100$ kHz.

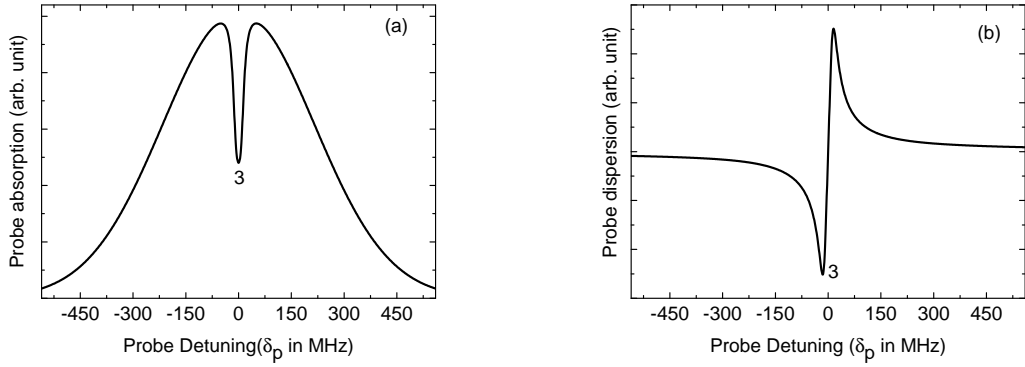


Figure 5.8: Simulated (a) absorption and (b) dispersion spectra of the probe beam for ^{87}Rb . Both the spectra are plotted for the probe intensity 0.51 mW/cm^2 and the pump intensity was 1.53 mW/cm^2 .

The anisotropy was created in the medium due to the non-uniform distribution of population in the sub-levels when the circularly polarized strong pump beam and the linearly polarized weak probe beam interacted with the medium simultaneously. In our case we considered, that the σ^+ component of the probe beam (the blue dashed lines in Fig.5.9) and the σ^+ component of the pump beam (the red lines) formed a V-type system, which gave two photon contribution to the medium. The σ^- component of the probe beam (the orange lines) gave rise only to one photon contribution. Thus this mismatch is responsible for the generation of the difference in the susceptibility of the medium. The real part of the susceptibility (χ) is related to the refractive index of the medium by, $n = 1 + \frac{1}{2}\text{Re}[\chi]$.

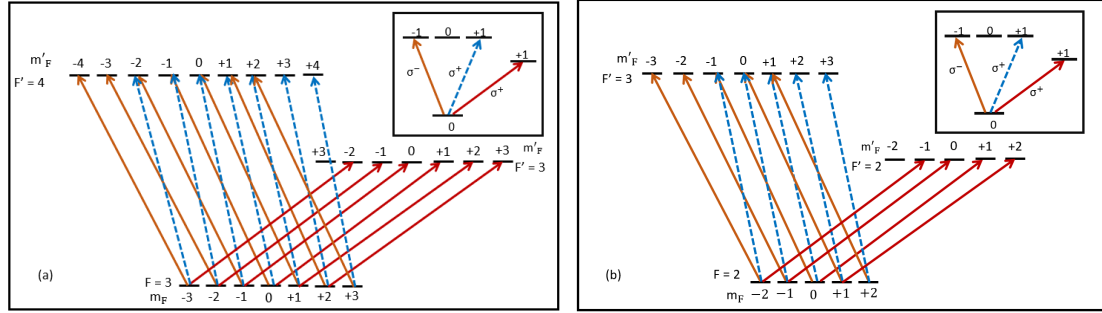


Figure 5.9: (a) Complete energy level diagram with all sub levels in each F value for ^{85}Rb indicating the case when the pump beam was locked at $F = 3 \rightarrow F' = 3$. (b) Complete energy level diagram with all sub levels in each F value for ^{87}Rb showing the case when we locked the pump beam at $F = 2 \rightarrow F' = 2$. In both (a) and (b), the blue dashed lines indicate the transition for σ^+ component of the probe beam, orange lines are for the transitions corresponding to the σ^- component of the probe beam and the red lines are for the transition of the σ^+ component of the pump beam.

In this way, the anisotropy to the refractive index exhibited by the different components of polarization of the probe beam is created in the medium. The situation is shown in the Fig.5.9 and the simplistic view of the two photon and one photon contributions are shown in the insets of both the figures. In the Fig.5.9(a) we have shown only the case when the pump beam is locked at $F = 3 \rightarrow F' = 3$ transition for ^{85}Rb and the Fig.5.9(b) shows only the case when the pump beam is locked at $F = 2 \rightarrow F' = 2$ transition for ^{87}Rb . For ^{85}Rb , if the pump beam is locked at $F = 3 \rightarrow F' = 2$, then the number of sub-levels in the excited state will be less. Similar things will happen to the case when the lock transition for the pump beam is $F = 2 \rightarrow F' = 1$ for ^{87}Rb .

Thus the difference in the refractive index can cause circular birefringence which produced the rotation in the plane of polarization of the probe field. The angle of rotation (θ) can be written in terms of the difference in the real parts of the susceptibility due to

different polarized components of the probe field from Eq.(5.3.3) as,

$$\theta(\omega_p) = \frac{\omega_0 L}{2c} \text{Re}(\chi_+(\omega_p) - \chi_-(\omega_p)) \quad (5.4.4)$$

where $\chi_{\pm}(\omega)$ is the susceptibility for σ^{\pm} components of the probe field. These can be calculated from the probe coherence ρ_{41+} and ρ_{41-} of the density matrix component, where ρ_{41+} gives the two-photon contribution to the system and ρ_{41-} carries information about the one photon contribution.

Now, from Eq.(5.4.2) we can write the two photon contribution of probe coherence (ρ_{41+}) as,

$$\begin{aligned} \rho_{41+} = & \frac{i\frac{\Omega_{41}}{2} D_{41}}{(1 + \frac{\Omega_{21}^2}{4} D_{41} D_{42} + \frac{\Omega_{31}^2}{4} D_{41} D_{43})} \left\{ \rho_{11}^0 + \frac{\Omega_{21}^2}{4} (D_{42} C_{12} - \frac{\Omega_{31}^2}{4} D_{43} d) (\rho_{22}^0 - \rho_{11}^0) \right. \\ & \left. + \frac{\Omega_{31}^2}{4} (D_{43} C_{13} - \frac{\Omega_{21}^2}{4} D_{42} d^*) (\rho_{33}^0 - \rho_{11}^0) \right\} \end{aligned} \quad (5.4.5)$$

and the one photon probe coherence (ρ_{41-}) as,

$$\rho_{41-} = i\frac{\Omega_{41}}{2} D_{41} \rho_{11}^0 \quad (5.4.6)$$

Considering atoms of all velocities the susceptibilities can be written as,

$$\chi_{\pm}(\omega_p) = \frac{2\mu_{41}}{\epsilon_0 E_p} \int_{-\infty}^{+\infty} \rho_{41\pm} N(v) dv \quad (5.4.7)$$

Here, $N(v) = \frac{N_0}{u\sqrt{\pi}} e^{-v^2/u^2}$ is the Maxwell-Boltzmann velocity distribution with the most probable velocity u of the atoms at temperature ‘T’ K and the number density N_0 . Γ_{j1} and γ_{jk} are the natural decay rates to the ground state $|1\rangle$ and the coherence decay rate respectively, where $j = 4, 3, 2$ and $k = 1, 2, 3$. In our simulation, we took $N_0 = 4 \times 10^{15} / \text{m}^3$ and the magnitude of the dipole matrix element μ_{41} is taken as 1.79×10^{-29} C.m for ^{85}Rb [79] and 1.73×10^{-29} C.m for ^{87}Rb [78].

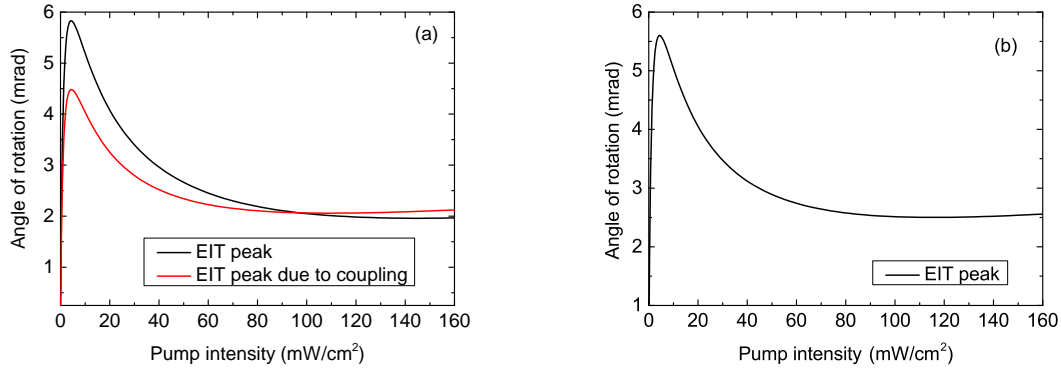


Figure 5.10: Variations of the angle of rotation corresponding to the EIT positions with pump intensities for (a) ^{85}Rb and (b) ^{87}Rb .

Now expanding Eq.(5.4.4) at $\omega = \omega_0$ we got an explicit expression for the angle of rotation (θ) at the resonance frequency as,

$$\theta(\omega_0) = \frac{\omega_0 L}{2c} \frac{d[\text{Re}(\chi_+(\omega_p) - \chi_-(\omega_p))]}{d\omega} \Big|_{\omega_0} \Delta\omega_p \quad (5.4.8)$$

The variation of the angle of rotation calculated from the Eq.(5.4.8) is plotted as a function of the pump intensity.

The variations of the angle of rotation at EIT condition for ^{85}Rb and ^{87}Rb are shown in Fig.5.10(a) and Fig.5.10(b) respectively. In Fig.5.10(a) the variation of angle of rotation for the probe beam are shown corresponding to both the EIT positions for ^{85}Rb . The characteristics behaviour is the same as we found in our experiment. In the region of the low pump Rabi frequency, the angle of rotation increased as the pump intensity was increased, upto a certain value of that intensity. This indicates that in this region, the anisotropy created in the medium was increasing. It also means that the circular birefringence was increasing in the medium, upto a certain maximum value. Then as the pump intensity was further increased, the value of the angle of rotation decreased. It means that the power broadening phenomenon dominates over the anisotropic behaviour

of the medium. Finally, at the high pump power (or, intensity) region, the angle of rotation became almost constant. It happened because the pump created the anisotropy due to the non-uniform distribution of the population. In the high pump power region, the medium got saturated for which further redistribution of the population was not possible.

5.5 Discussions

In conclusion, we have observed experimentally as well as theoretically PREIT in rubidium vapour at room temperature in the absence of any magnetic field. In this work, we studied PREIT for both ^{85}Rb and ^{87}Rb combining the D_1 and the D_2 transitions with a V-type configuration. In our experiment, we observed two EIT peaks for ^{85}Rb and one EIT peak for ^{87}Rb . We have modelled our system in such a way so that we can explain the occurrence of double EIT in case of ^{85}Rb . We can further explain the rotation of the plane of polarization which occurred in the probe beam. The occurrence of one EIT peak for ^{87}Rb was also explained by our model. We have studied both experimentally and theoretically, the variation of the angle of rotation with the pump intensity. Here, we got a similar type of non-linear behaviour of the variation of the angle of rotation with the pump intensities in both the experiment and the theory. But the experimental values differ from the theoretical values possibly due to (a) the angular broadening as there was a mismatch in the overlapping between the probe and the pump beams inside the atomic medium, (b) the difficulty to relate the measured power to what is actually seen by the atoms inside the vapour cell and (c) in the experimental system, there are

other energy levels where the population may decay, but in our theoretical formulation, we have taken a four-level system. So the extra decays in the real system can also introduce this discrepancy. From the dispersion spectra, we observed that for the EIT, we got positive rotation because, in the case of EIT, normal dispersion occurred. We also observed that the maximum rotation not only depends on the pump power, but it also depends on the number of sub-levels where the pump beam is locked. The value of rotation can be increased if the Rb cell is heated because the number density is increased by increasing the temperature of the cell and if the angular mismatch between the pump and the probe beams is reduced further.

From the absorption and the dispersion spectra, it is clear that this experimental technique can be used to identify any resonance position which is smeared out in the absorption spectrum due to the power broadening or the angular broadening phenomenon. All the resonances are well resolved in the dispersion spectrum. As we got a sharp rotation in the vicinity of the probe resonance, i.e., at the EIT position, we can use this signal as an error signal for frequency stabilization of the probe beam at the EIT position without using a lock-in-amplifier circuit. Such an optical locking method is advantageous because the dispersion signal is modulation free and noise insensitive signal. As the rotation can be changed by introducing the magnetic field [31] so our experimental technique can be used to measure an unknown magnetic field by knowing the rotation.

6

Angular dependency of the polarization rotation in a coherent atomic medium¹

6.1 Introduction

In our previous study discussed in chapter 5, we have shown how the EIT phenomenon influences the polarization rotation (PR) of the probing field by forming a V-type system for both ^{87}Rb and ^{85}Rb with D_1 and D_2 transitions. It was also shown how this polarization rotation with electromagnetically induced transparency (PREIT) could be modified with the pump field intensity. We realize that the study of the dependencies of the angle of rotation on other system parameters is needed. On the other hand, the V-type system was used to study absorptive, and dispersive properties of the atomic medium under the EIT condition [92, 108–111]. With D_1 and D_2 transitions of the ^{87}Rb , the coherence effect of EIT in a V-type system was studied recently [103]. However, the polarization rotation phenomenon was not explored much in the V-type system. Cha et al. [99] studied the two colour polarization spectroscopy (TCPS) in rubidium vapour at room temperature but they did not get any EIT resonance in their system due to weak pump beam. Carvalho et al. [112] studied the angular dependence of EIT in Cs vapour

¹This chapter is based on the publication Das et al. *J. Phys. B: At. Mol. Opt. Phys.*, **2020**, *53*, 025502-025509. The experiment and the theoretical calculations presented in this chapter have been entirely done by Arpita Das.

with a Λ type configuration. They observed how the EIT linewidth depends on the angle between the coupling and the probe beams. Angular dependence of Dicke-narrowed EIT was also studied using a Λ type system of ^{87}Rb atomic vapour with buffer gas [113]. However, to the best of our knowledge, there is no work done with the V-type system to study the angular dependence of EIT. Therefore, how the angle between the pump and the probe beams affect the coherent control of the polarization rotation under the EIT condition needs to be ventured. In the present study [3], our aim was to systematically investigate how the PREIT angle for the probe beam can be controlled by (a) the angular mismatch between the pump and the probe beams, (b) the optical depth (OD) of the medium and (c) the spot size or the radius of the pump beam in ^{87}Rb atomic medium. For this purpose, we have used a V-type system combining the D_1 and D_2 transitions of the ^{87}Rb . The effect of the OD of the medium was studied by changing the temperature of the atomic medium.

We have also calculated the group velocity from the PREIT spectrum. Although, there are two techniques of detection for the subluminal light propagation through the atomic medium. One is an indirect process [1], and the other one is a direct process [90]. Our detection technique of group velocity is advantageous than the balanced homodyne detection technique using the Mach-Zehnder interferometer [1] because the PREIT spectrum has a high signal to noise (S/N) ratio. For a theoretical explanation of these experimentally observed phenomena, we have considered a three-level V-type system and solved the master equation analytically in steady-state condition to get the susceptibility of the medium. We have also considered the probe field and the pump field to be Gaussian distribution functions to study the spot size effect in the theoretical model.

6.2 Experiment

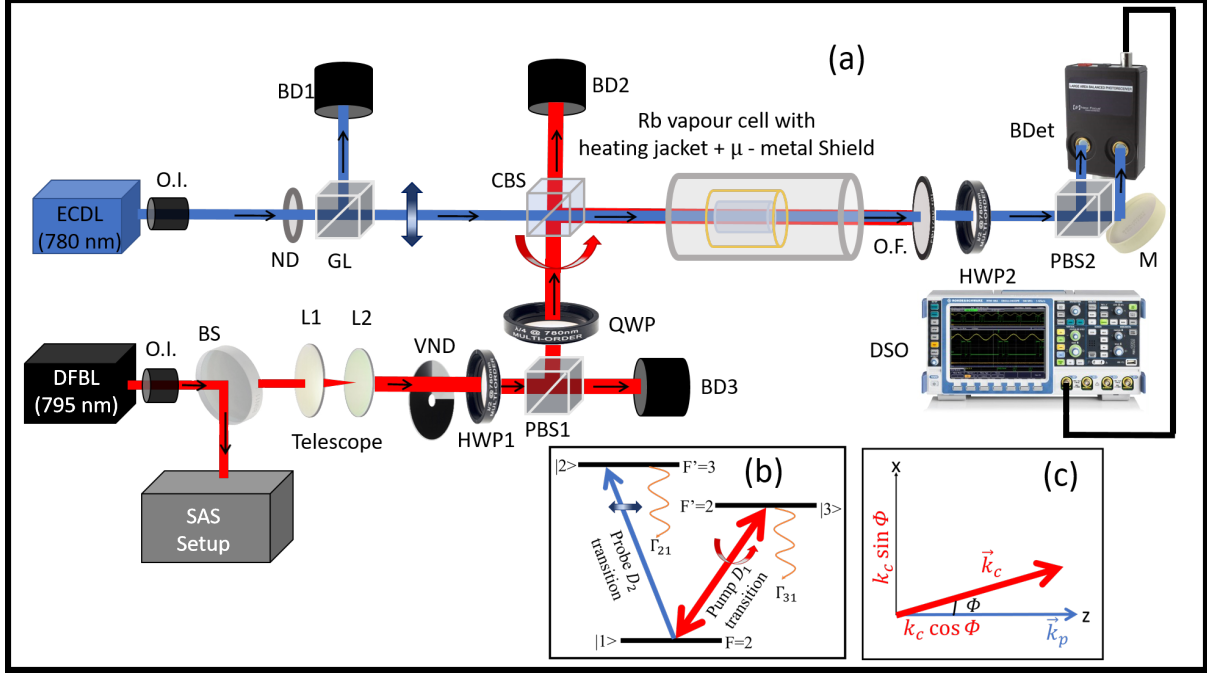


Figure 6.1: (a) Experimental Setup. ECDL: External Cavity Diode Laser, DFBL: Distributed Feedback Diode Laser, O.I.: Optical Isolator, HWP: Half-wave Plate, QWP: Quarter-wave Plate, GL: Glan-laser Polarizer, PBS: Polarizing Beam Splitting Cube, CBS: Non-polarizing Cubic Beam Splitter, L: Lens, BS: Beam Splitter, M: Mirror, Rb Cell: Rubidium Vapour Cell, BD: Beam Dump, ND: Neutral Density Filter, VND: Variable Neutral Density Filter, SAS Setup: Saturation Absorption Spectroscopy Setup, BDet: Balanced Detector, DSO: Digital Storage Oscilloscope. (b) V-type configuration of ^{87}Rb combining D_1 and D_2 transitions for experimental observation of polarization rotation in the EIT medium. Here, $|1\rangle$, $|2\rangle$, $|3\rangle$ indicate the theoretical level scheme. (c) The orientation of the wave vector of the pump field (\vec{k}_c) with respect to the probe field wave vector (\vec{k}_p).

Fig.6.1(a) shows the experimental setup to study the effect of the angular mismatch between the pump and the probe beams (ϕ) on the PREIT without applying any external magnetic field. The experimental setup is more or less same as the previous one, except here the probe and the pump beams were mixed in a 50:50 non-polarizing cubic beam

splitter (CBS). This CBS was placed on a combination of the kinematic rotational mount and a translational stage to create an angle between the path of the pump beam and the probe beam. The probe and the pump beams were co-propagated through a 50 mm \times 25 mm cylindrical Rubidium vapour cell (Rb cell). The Rb cell was placed inside a heating jacket to change the temperature of the medium for OD variation. The OD of the atomic medium was increased by increasing the Rb cell temperature from 21°C to 45°C. We used a bandpass optical filter (O.F., Thorlabs FBH780-10 with a central wavelength of 780 nm and an OD 6 for 795 nm) after the Rb cell to block the pump beam (795 nm) so that only the probe beam (780 nm) can be detected. After passing through the atomic medium and the O.F., the probe beam was detected with the help of balanced polarimetric technique [25, 104], to get the polarization rotation signal.

In this experiment, we have also observed how the spot size of the pump beam (w_c) can affect the angle of rotation of the polarization of the probe beam. To study this, we made a telescopic arrangement in the path of the pump beam with the combination of L1 and L2 lenses so that the beam size can be changed. The intensities of the probe and the pump beams were set at 0.47 ± 0.02 mW/cm² and 4.77 ± 0.03 mW/cm², respectively. These intensities were kept fixed throughout the experiments even when we changed the spot sizes of the pump beam by changing the corresponding laser power accordingly.

6.3 Experimental results and analysis

In our experiment we have locked the pump beam from $F = 2 \rightarrow F' = 2$ of D_1 transition and scanned the probe beam from $F = 2 \rightarrow F' = 3$ of D_2 transition of ^{87}Rb

(see Fig.6.1(b)).

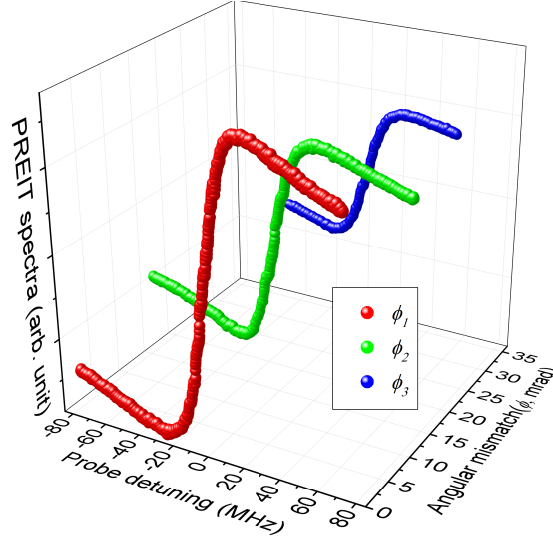


Figure 6.2: Polarization rotation signal of the probe beam with electromagnetically induced transparency (PREIT) as a function of probe detuning at three different angular mismatch ($\phi_1 = 0$ mrad, $\phi_2 = 14.49 \pm 3.68$ mrad and $\phi_3 = 36.23 \pm 3.75$ mrad) positions with the probe beam intensity as 0.47 ± 0.02 mW/cm² and that of the pump beam as 4.77 ± 0.03 mW/cm². In each case, $w_p = w_c = 1$ mm and the OD = 0.189 ± 0.003 .

Fig.6.2 shows the polarization rotation signals of the probe beam at the EIT condition at three different angular mismatch positions between the pump beam and the probe beam. From this figure, we have seen that due to the EIT condition we got normal dispersion signal at the vicinity of resonance. It is also clear from the Fig.6.2 that the intensity, as well as the slope of the spectra, got reduced as we increased the angle ϕ . This indicates that the two-photon coherence contribution, i.e. the coherence effect due to EIT, decreases with the increase in the angular mismatch between the pump and the probe beams. From the slope of the dispersion spectrum, we have calculated the angle of PREIT (θ). The output intensity difference ($\Delta I(\omega_p)$) depends on the phase shift due to the refractive index difference (anisotropy in refractive index ($\Delta n(\omega_p) = n_+(\omega_p) - n_-(\omega_p)$))

for the two circular components (σ_+ and σ_-) of the probe beam as [2],

$$\Delta I(\omega_p) \approx I_0 \exp(-\alpha L) \frac{\Delta n(\omega_p) \omega_0 L}{c} \quad (6.3.1)$$

The angle of polarization rotation which we detected is defined [63] as,

$$\theta(\omega_p) = \frac{\Delta n(\omega_p) \omega_0 L}{2c} \quad (6.3.2)$$

Therefore the angle of PREIT can be calculated by Taylor series expansion of Eq.(6.3.1) as,

$$\theta = \frac{1}{2I_0 \exp(-\alpha L)} \left. \frac{d(\Delta I)}{d\omega} \right|_{\omega_0} \Delta\omega \quad (6.3.3)$$

where, ω_0 is the resonance frequency of the probe beam, $\Delta\omega$ is the smallest division of frequency, α is the absorption coefficient of the medium and L is the interaction length of the atomic medium. In our case $L = 50$ mm is the Rb cell length.

In this study, we choose the pump intensity to be 4.77 ± 0.03 mW/cm² so that there was no power broadening due to the pump beam in the medium. We have plotted the angle of PREIT (θ) with the angular mismatch (ϕ). From the Fig.6.3(a) and Fig.6.3(b), it is seen that θ decreases as ϕ increases.

This may be due to the reasons that (i) as we increased ϕ the residual Doppler broadening effect increased in the medium, (ii) increment in ϕ also decreased the two-photon coherence effect and (iii) since we changed the angle between the pump and the probe, it changed the effective number of interacting atoms in the interaction cross-section. Moreover, the number density of atomic medium can be changed by changing the OD and the spot size of the pump beam. Therefore, we have also studied the dependency of θ on the OD and on the pump beam spot sizes. At first, we kept the spot size of the pump (w_c) and that of the probe beam (w_p) same, i.e. $w_c = w_p = 1$ mm and changed

the angle between the pump and probe beam taking OD as a parameter.

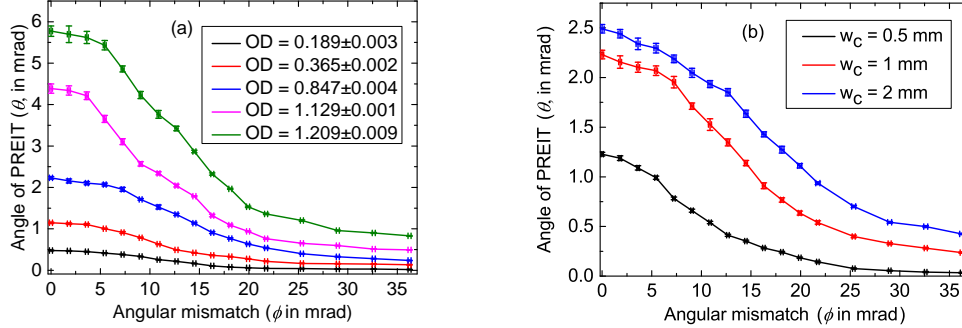


Figure 6.3: Variation of angle of rotation of the plane of polarization of the probe beam taking (a) optical depth as a parameter with $w_c = 1$ mm and (b) pump beam spot size as a parameter with $OD = 0.847 \pm 0.004$. In both (a) and (b), the spot size of the probe was $w_p = 1$ mm.

We have observed that for a particular OD, as we increased the angle between the pump and the probe beams the angle of polarization rotation was decreased as shown in the Fig.6.3(a). Due to the angular mismatch between the pump and the probe beams, the residual Doppler broadening effect was increased, which hindered the process of Doppler narrowing effect in the medium. Thus the anisotropic behaviour of the medium was dominated by this residual Doppler broadening phenomenon for a particular OD. Since the anisotropy created in the medium led to the rotation of the plane of polarization of the probe beam, increasing the angular mismatch decreased the rotation angle. Besides, the increase in an angular mismatch between the pump and the probe beams also decreased the two-photon coherence contribution in the medium continuously because the contribution of the pump beam in the propagation direction of the probe beam was reducing (see Fig.6.1(c)). For this reason, also the anisotropy in the medium, as well as the angle of polarization rotation, was decreased. From this figure, we have also observed that the

angle of rotation was increased as the OD was increased by increasing the temperature of the medium for a particular ϕ . With the increment in OD, the number density of the atoms was increased. Therefore the angle of rotation was also increased since it depends on the number density of the atomic medium.

We also changed the pump beam spot size with respect to the probe beam spot size keeping the OD of the medium fixed at 0.847. For each w_c we have changed the ϕ . The corresponding variation is shown in Fig.6.3(b), where we have found that for a particular w_c , θ shows similar variation with respect to ϕ as it shows in Fig.6.3(a). As shown in Fig.6.3(b), we took three different w_c ; one is smaller than the probe beam, $w_c = 0.5$ mm, the second one is comparable to the probe beam, $w_c = 1$ mm and the last one is greater than that of the probe beam, $w_c = 2$ mm. For different spot sizes of the pump beam at a particular ϕ , we have observed that the value of θ increases as we increased w_c . This happened because as we increased w_c , the cross-sectional area for the two-photon interaction was also increased. Therefore, the two-photon contribution was increased, which in turn increased θ . From this study we have observed that though it may seem that when the probe beam is fully inside the pump beam, the rotation may be insensitive to ϕ , but from the Fig.6.3(b) we have found that ϕ is always an important parameter even if the probe beam is fully overlapped by the pump beam. From both the Fig.6.3(a) and Fig.6.3(b) we have observed that to get enhanced rotation we have to take care of the value of ϕ together with the OD and w_c , since the angular mismatches between the pump and the probe not only change the effective number of atoms in the interaction cross-section but also enhance the residual Doppler broadening effect and decrease the two-photon contribution.

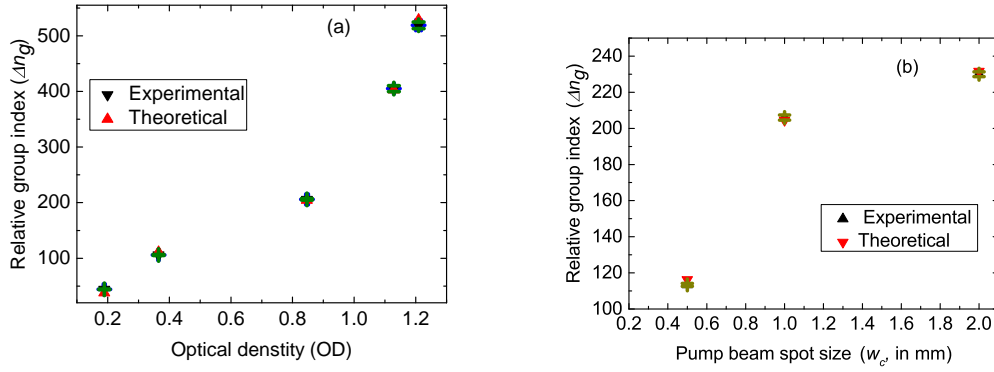


Figure 6.4: Variation of group index of the medium with (a) optical depth and (b) pump beam spot size for $\phi = 0$ mrad. In (a) $w_p = w_c = 1$ mm and in (b) $w_p = 1$ mm and OD = 0.847 ± 0.004 .

Apart from the determination of the angle of PREIT, the polarization rotation spectra can be used to estimate the group velocity of the probe beam. We have calculated the relative group index of the medium from the slope of the rotational spectra of PREIT at $\phi = 0$ mrad as $\Delta n_g = \Delta n(\omega_0) + \omega_0 \frac{d\Delta n}{d\omega} \Big|_{\omega_0} = \frac{c}{I_0 \exp(-\alpha L) L} \frac{d(\Delta I)}{d\omega} \Big|_{\omega_0}$ from Eq.(6.3.1). In Fig.6.4(a), the variation of the relative group index (Δn_g) with the OD of the medium is shown. As the number density increased with the increment of the OD, Δn_g has also increased. So, the group velocity was reduced with the increasing OD of the atomic medium as $v_g = \frac{c}{\Delta n_g}$. We have observed the maximum reduced group velocity, $v_g = \frac{c}{518.82 \pm 5.82}$ m/s for $OD = 1.209 \pm 0.009$ at $w_p = 1$ mm and $w_c = 1$ mm. We have also plotted the group index as a function of w_c . It increased with increasing w_c since the effective number of atoms exhibiting the two-photon contribution was increased as shown in the Fig.6.4(b). In this case we got the maximum reduced group velocity, $v_g = \frac{c}{230 \pm 1.34}$ m/s for $w_c = 2$ mm at and $w_p = 1$ mm $OD = 0.847 \pm 0.004$. From the Fig.6.4(b) it seems that the group index has a tendency of saturation as w_c becomes

larger than w_p . This indicates that the effective number of atoms in the overlapping cross-section of the probe and the pump beams, which were exhibiting the two photon contribution, was getting maximized. From the Fig.6.4(a) and Fig.6.4(b) it is apparent that the parameter OD is more sensitive to the two photon coherence contribution than the parameter w_c after a certain value. Therefore to get enhanced coherence control on the polarization rotation, a very large spot size of the pump beam will not be effective but a very large OD will be effective.

6.4 Theory

We have considered a three-level V-type system as shown in Fig.6.1(b) to explain the experimentally observed phenomena, where the probe beam interacts with the levels $|1\rangle$ and $|2\rangle$ and the pump beam couples the levels $|1\rangle$ and $|3\rangle$. Since the probe beam is linearly polarized, we have assumed that it carries both the σ_+ and σ_- components of polarization equally. Therefore in our system, the σ_+ component of the probe beam and the σ_+ polarized pump beam formed a three-level system and gave a two-photon contribution to the atomic medium. While the σ_- component of the probe beam gave only one photon contribution to the medium. Thus a mismatch in the population distribution was generated, which in turn produced anisotropy towards the refractive index in the atomic medium. As a result, polarization rotation occurred for the probe beam [2]. Since the refractive index ($n = 1 + \frac{1}{2}\chi'$) is related to the real part of the complex susceptibility (χ') of the medium, to generate the polarization spectrum and to get the angle of polarization rotation at the EIT condition we have to find the difference in susceptibilities (χ) in the

atomic medium corresponding to the two circular components of the probe beam. These can be calculated from the probe coherence terms ρ_{21+} and ρ_{21-} of the density matrix component, where these two terms carry information about the two-photon and the one-photon contribution of the probe field to the medium respectively. To get these terms we have solved the master equation, Eq.(3.1.12) where we phenomenologically included the decay terms. In this case our unperturbed (H_0) and perturbed (H_p) Hamiltonians are given by respectively,

$$H_0 = \sum_{i=1}^{i=3} \hbar\omega_{ii} |i\rangle \langle i| \quad (6.4.1)$$

$$H_p = -\hbar\{\Omega_{21}(r)\cos(\omega_p t - \vec{k}_p \cdot \vec{r}_p) |1\rangle \langle 2| + \Omega_{31}(r)\cos(\omega_c t - \vec{k}_c \cdot \vec{r}_c) |1\rangle \langle 3| + c.c.\}$$

Here, ρ is a 3×3 density matrix; diagonal terms of which give the populations for the individual energy levels and the off-diagonal terms indicate the coherence terms of the system. We have considered the probe field as $\varepsilon_p(r) = E_p(r)\cos(\omega_p t - \vec{k}_p \cdot \vec{r}_p)$ and the pump field to be $\varepsilon_c(r) = E_c(r)\cos(\omega_c t - \vec{k}_c \cdot \vec{r}_c)$ where, $E_{p(c)}(r)$ being the amplitude of the electric field of frequency $\omega_{p(c)}$, $k_{p(c)} = 2\pi/\lambda$ is the wave vector and $\vec{r}_{p(c)}$ is the propagation direction of the probe (pump) field. $\Omega_{ji}(r) = \mu_{ji}E_{p(c)}(r)/\hbar$, $j = 2, 3$ and $i = 1$, are the Rabi frequencies for the probe and the pump fields respectively. Using Eq.(3.1.16) and assuming the RWA we have obtained the optical Bloch equations for this three level V-type system as follows,

$$\begin{aligned} \dot{\rho}_{11} &= \Gamma_{31}\rho_{33} + \Gamma_{21}\rho_{22} + \frac{i}{2}\Omega_{21}(r)(\rho_{21} - \rho_{12}) + \frac{i}{2}\Omega_{31}(r)(\rho_{31} - \rho_{13}) \\ \dot{\rho}_{22} &= -\Gamma_{21}\rho_{22} - \frac{i}{2}\Omega_{21}(r)(\rho_{21} - \rho_{12}) \\ \dot{\rho}_{33} &= -\Gamma_{31}\rho_{33} - \frac{i}{2}\Omega_{31}(r)(\rho_{31} - \rho_{13}) \\ \dot{\rho}_{21} &= -D_{21}^{-1}\rho_{21} - \frac{i}{2}\Omega_{21}(r)(\rho_{22} - \rho_{11}) - \frac{i}{2}\Omega_{31}(r)\rho_{23} \\ \dot{\rho}_{13} &= -D_{13}^{-1}\rho_{13} + \frac{i}{2}\Omega_{31}(r)(\rho_{33} - \rho_{11}) + \frac{i}{2}\Omega_{21}(r)\rho_{23} \\ \dot{\rho}_{23} &= -D_{23}^{-1}\rho_{23} - \frac{i}{2}\Omega_{31}(r)\rho_{21} + \frac{i}{2}\Omega_{21}(r)\rho_{13} \end{aligned} \quad (6.4.2)$$

Where the parameters can be described as follows,

$$D_{21} = \frac{1}{\gamma_{21} + i\Delta_p}, \quad D_{13} = \frac{1}{\gamma_{31} - i\Delta_c}, \quad D_{23} = \frac{1}{\gamma_{23} + i(\Delta_p - \Delta_c)} \quad (6.4.3)$$

$\gamma_{j1} = \frac{\Gamma_{j1}}{2}$ are the coherence decay rates, where $j = 2, 3$ and Γ_{j1} is the natural decay rate from $|j\rangle$ to $|1\rangle$. $\gamma_{23} = \frac{\Gamma_{31} + \Gamma_{21}}{2}$ is the non-coherence decay rate between the dipole forbidden transitions.

Using the first order perturbation for the probe field under steady state condition from Eq.(6.4.2) we can write the zeroth order pump coherence as,

$$\begin{aligned} \rho_{13}^0 &= i \frac{\Omega_{31}(r)}{2} D_{13} (\rho_{33}^0 - \rho_{11}^0) \\ &= i \frac{\Omega_{31}(r)}{2} \frac{(\rho_{33}^0 - \rho_{11}^0)}{(\gamma_{13} - i\Delta_c)} \end{aligned} \quad (6.4.4)$$

Again, from Eq.(6.4.2) under steady state condition with first order perturbation for the probe field we can write the zeroth order population of the levels $|3\rangle$ and $|2\rangle$ as,

$$\rho_{33}^0 = i \frac{\Omega_{31}(r)}{2\Gamma_{31}} (\rho_{13}^0 - \rho_{31}^0) \quad (6.4.5)$$

and

$$\rho_{22}^0 = 0 \quad (6.4.6)$$

Now, from Eq.(6.4.4) we can write,

$$\begin{aligned} (\rho_{13}^0 - \rho_{31}^0) &= i \frac{\Omega_{31}(r)}{2} D_{13} (\rho_{33}^0 - \rho_{11}^0) + i \frac{\Omega_{31}(r)}{2} D_{31} (\rho_{33}^0 - \rho_{11}^0) \\ &= i \frac{\Omega_{31}(r)}{2} (\rho_{33}^0 - \rho_{11}^0) \left[\frac{1}{(\gamma_{13} - i\Delta_c)} + \frac{1}{(\gamma_{13} + i\Delta_c)} \right] \\ &= i \frac{\Omega_{31}(r) \gamma_{31} (\rho_{33}^0 - \rho_{11}^0)}{(\gamma_{31}^2 + \Delta_c^2)} \end{aligned} \quad (6.4.7)$$

Therefore using Eq.(6.4.7), Eq.(6.4.5) can be written as,

$$\begin{aligned} \rho_{33}^0 &= - \frac{\Omega_{31}^2(r) \gamma_{31}}{2\Gamma_{31}(\gamma_{31}^2 + \Delta_c^2)} (\rho_{33}^0 - \rho_{11}^0) \\ &= \frac{\Omega_{31}^2(r) \gamma_{31}}{2\Gamma_{31}(\gamma_{31}^2 + \Delta_c^2) + \Omega_{31}^2(r) \gamma_{31}} \rho_{11}^0 \end{aligned} \quad (6.4.8)$$

Since we assumed the population conservation, i.e. $\rho_{11}^0 + \rho_{22}^0 + \rho_{33}^0 = 1$, the zeroth order population of the ground state is given by,

$$\begin{aligned}\rho_{11}^0 &= 1 - \rho_{33}^0 \\ &= 1 - \frac{\Omega_{31}^2(r)\gamma_{31}}{2\Gamma_{31}(\gamma_{31}^2 + \Delta_c^2) + \Omega_{31}^2(r)\gamma_{31}} \rho_{11}^0 \\ &= \frac{\Omega_{31}^2(r)\gamma_{31} + 2\Gamma_{31}(\gamma_{31}^2 + \Delta_c^2)}{2\{\Gamma_{31}(\gamma_{31}^2 + \Delta_c^2) + \Omega_{31}^2(r)\gamma_{31}\}}\end{aligned}\quad (6.4.9)$$

Where we have used Eq.(6.4.6) and Eq.(6.4.8). Following this Eq.(6.4.8) becomes,

$$\rho_{33}^0 = \frac{\Omega_{31}^2(r)\gamma_{31}}{2\{\Gamma_{31}(\gamma_{31}^2 + \Delta_c^2) + \Omega_{31}^2(r)\gamma_{31}\}} \quad (6.4.10)$$

Using all the above equations, we obtained the probe coherence (ρ_{21+}) containing two photon contribution as,

$$\rho_{21+} = \frac{i\frac{\Omega_{21}(r)}{2}D_{21}[\rho_{11}^0 + \frac{\Omega_{31}^2(r)}{4}D_{13}D_{23}(\rho_{33}^0 - \rho_{11}^0)]}{(1 + \frac{\Omega_{31}^2(r)}{4}D_{21}D_{23})} \quad (6.4.11)$$

and putting $\Omega_{31}(r) = 0$ in the Eq.(6.4.11), we get the one photon probe coherence term (ρ_{21-}) as,

$$\rho_{21-} = i\frac{\Omega_{21}(r)}{2}D_{21}\rho_{11}^0 \quad (6.4.12)$$

Since our V-type system is a combination of D_1 and D_2 transition of ^{87}Rb , we have taken $\Gamma_{21} = 6$ MHz and $\Gamma_{31} = 5.75$ MHz. Since in our experiment we have varied the spot size of the pump beam, in the above Eq.(6.4.11), Eq.(6.4.12), Eq.(6.4.10) and Eq.(6.4.9), we have considered, $\Omega_{21}(r) = \Omega_p \exp(-r^2/w_p^2)$ and $\Omega_{31}(r) = \Omega_c \exp(-r^2/w_c^2)$ to include the spot size variation in the simulation as we have assumed Gaussian distribution of the probe and the pump fields. Here, Ω_p and Ω_c are the peak values of the probe and the pump Rabi frequencies respectively. The peak values of Rabi frequencies were calculated from the relation, $\Omega = \Gamma\sqrt{\frac{I}{2I_{sat}}}$ [78], where Γ is the natural linewidth, I is the intensity and I_{sat} is the saturation intensity of the laser beam. In our simulation we have assumed

that the peak value of the pump Rabi frequency is constant for all the cases of different spot sizes similar to our experiment.

Since the probe resonance frequency is $\omega_{21} = \omega_0$, the probe detuning is $\delta_p = (\omega_0 - \omega_p)$. As we have taken the propagation direction of the probe beam along the z -axis, the Doppler detuning of the probe is $\Delta_p = (\delta_p + \vec{k}_p \cdot \vec{v}) = (\delta_p + k_p v_z)$. Similarly, we have defined the detuning of the pump beam as $\delta_c = (\omega_{31} - \omega_c)$ with the Doppler detuning of the pump beam $\Delta_c = (\delta_c + \vec{k}_c \cdot \vec{v})$. Since the pump field wave vector \vec{k}_c is rotated in the xz plane as shown in Fig.6.1(c), $\Delta_c = (\delta_c + k_c v_x \sin \phi + k_c v_z \cos \phi) \approx (\delta_c + k_c v_x \phi + k_c v_z)$. Here ϕ is the angular mismatch between the pump and the probe beams. We have assumed ϕ to be small enough so that we can write $\sin \phi \rightarrow \phi$ and $\cos \phi \rightarrow 1$. Therefore the two photon Doppler detuning becomes, $(\Delta_p - \Delta_c) = (\delta_p - \delta_c) + (k_p - k_c)v_z - k_c v_x \phi$. This $(k_p - k_c)v_z - k_c v_x \phi$ introduces the residual Doppler broadening effect in the atomic medium. It may be noted that, in general the residual Doppler effect $((\vec{k}_p - \vec{k}_c) \cdot \vec{v})$ due to the wavelength mismatch is negligible because $(\vec{k}_p - \vec{k}_c)$ is very small. But in our case the term $k_c v_x \phi$ is playing a dominating role. So due to the angular mismatch the residual Doppler broadening effect is increased in our system.

Considering atoms of all velocities and integrating over space, the susceptibilities can be written as,

$$\chi_{\pm} = \frac{2\mu_{31}}{\epsilon_0 E_p} \int_{v_z=-\infty}^{+\infty} \int_{v_x=-\infty}^{+\infty} \int_{r=0}^{+\infty} \rho_{21\pm}(r, v_x, v_z) N(v_x, v_z) dr dv_x dv_z \quad (6.4.13)$$

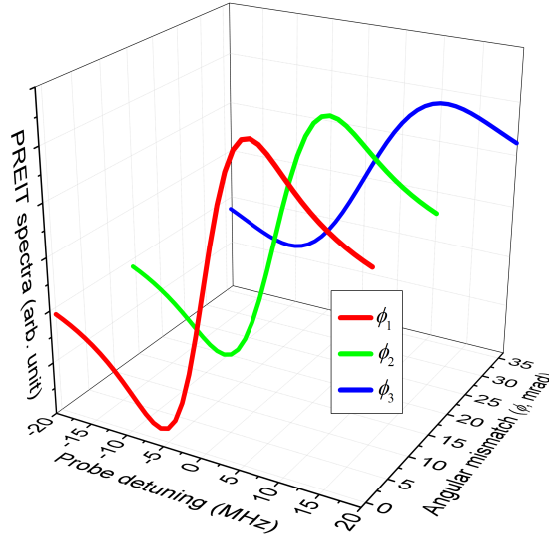


Figure 6.5: Simulated polarization rotation spectrum of the probe beam with positive dispersion in the vicinity of the EIT resonance for different values of ϕ ($\phi_1 = 0$ mrad, $\phi_2 = 14.49$ mrad, $\phi_3 = 36.23$ mrad) with the probe intensity as 0.47 mW/cm^2 and that of the pump beam as 4.77 mW/cm^2 .

Here, as \vec{k}_c lies in the xz plane, we have considered the two-dimensional Maxwell-Boltzmann (MB) velocity distribution assuming that the third component of velocity does not affect the phenomenon,

$$N(v_x, v_z) = \frac{N_0}{\pi u^2} \exp\left\{-\frac{(v_x^2 + v_z^2)}{u^2}\right\} \quad (6.4.14)$$

In the above Eq.(6.4.14), u is the most probable velocity of the atoms and N_0 is the number density of the atoms at temperature 'T'K. The dipole moment, $\mu_{31} = 1.73 \times 10^{-29}$ C.m [78]. The simulated polarization rotation spectrum with a positive slope in the vicinity of the EIT resonance is shown in the Fig.6.5 for three different values of ϕ . Here also we have observed that the intensity of the spectrum is reducing as ϕ is increasing similar to what we observed in our experiment. We have varied the detuning of the probe beam while the detuning of the pump beam was set at 0 MHz in our theoretical

calculation to match the experimental condition.

The angle of polarization rotation can be related with the real part of the susceptibilities for the two photon (χ'_+) and one photon contribution (χ'_-) to the medium as,

$$\theta(\omega_p) = \frac{\omega_0 L}{4c} (\chi'_+(\omega_p) - \chi'_-(\omega_p)) \quad (6.4.15)$$

Therefore, θ can be calculated using the Eq.(6.4.15) at the EIT resonance position as,

$$\theta = \frac{\omega_0 L}{4c} \frac{d(\chi'_+ - \chi'_-)}{d\omega} \Big|_{\omega_0} \Delta\omega \quad (6.4.16)$$

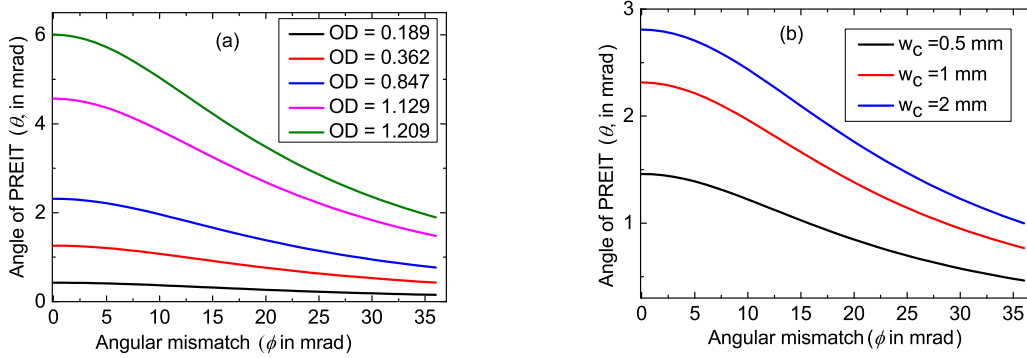


Figure 6.6: Simulated variation of the angle of polarization rotation with the angular deviation between the pump and the probe beams taking (a) OD as a parameter and (b) the pump beam diameter as a parameter. In (a) $w_p = w_c = 1$ and in (b) $w_p = 1$ mm, OD = 0.847.

We have calculated the angle of rotation (θ) of the plane of polarization of the probe beam from Eq.(6.4.16) in the vicinity of the EIT resonance. The variation of θ with ϕ was studied with the OD and w_c as parameters similar to our experiment. In the first case, we have fixed the pump beam spot size $w_c = 1$ mm and changed the OD of the medium. In the second case, the OD of the medium was kept constant, and we changed the pump beam spot size w_c . In both, the cases the probe beam spot size was taken as $w_p = 1$ mm.

From the Fig.6.6(a) and Fig.6.6(b) we have found that the characteristics of variation of θ with ϕ for both the cases are similar to what we have observed in our experiment (shown in Fig.6.3). One could also see that the angle of polarization rotation is decreasing as the angular mismatch is increased due to the residual Doppler broadening effect similar to the experimental result. From Fig.6.6(a) it is observed that the angle of polarization rotation increases as we increased the OD. From Eq.(6.4.13) and Eq.(6.4.14) we have found that the susceptibility is directly proportional to the atomic number density. Since on increasing the OD of the medium, the number density of the interacting atoms also increased, as a result, more non-uniform population distribution between the sub-levels occurred. As more anisotropy was created in the medium, the angle of polarization rotation increased. When we kept the OD fixed and changed w_c , we noticed that θ increased as we increased w_c similar to the experiment. On increasing w_c , the two-photon contribution in the medium increased. So, the chiral behaviour of the medium, as well as the angle of polarization rotation, was also increased as shown in the Fig.6.6(b). But there is some mismatch between the experimental and the theoretical results as we have observed from the Fig.6.3 and Fig.6.6. This difference between the experimental and theoretical observations occurs due to certain reasons. In the case of the experiment, the effective interaction length is always changing as we changed ϕ . In theory, for simplicity, we have assumed that this remains constant for a particular OD and w_c . In the experimental system, there are other energy levels where the population may decay, but in our theoretical formulation, we have taken a three-level closed system. So the extra decays in the real system can also introduce this discrepancy.

Further, this theoretical formulation can be used to calculate the relative group index

(Δn_g) and then the group velocity (v_g) of the probe beam as $\Delta n_g = \frac{\omega_0}{2} \frac{d(\chi'_+ - \chi'_-)}{d\omega} \Big|_{\omega_0}$.

We have compared the variation of Δn_g as a function of OD of the system and pump beam spot size w_c . In Fig.6.4(a) and Fig.6.4(b) the red up triangles show the theoretically calculated values of Δn_g as a function of OD and w_c respectively. The values match well with our experimental observations.

6.5 Discussions

We have investigated how the angle of polarization rotation of the probe beam at the EIT region can be tuned by changing the overlapping cross-section between the pump and the probe beams, by increasing the optical depth of the medium and by changing the spot size of the pump beam. The linear polarized probe beam and the circularly polarized pump beam interacted simultaneously with the atomic vapour medium. We have noticed that the angle of PREIT depends non-linearly on the angular mismatch between the pump and the probe beams. It has also been observed that this value of angle θ for a particular angular mismatch increases as we increased the optical depth of the medium or as the pump beam spot size was increased. From the study, we can conclude that the angular mismatch between the pump and the probe beams will always remain as an essential parameter whatever be the OD and the pump beam spot size. The final findings of our study say that this is the way where one can control the enhancement of the two-photon contribution in the medium to enhance the anisotropy, as well as the chiral behaviour, of the medium. This enhanced PREIT spectrum can be used for optical locking purpose as we got a sharp rotation at the vicinity of the EIT region, and the spectrum is modulation

free as well as has a high S/N ratio. The generated $1F$ signal is modulation free because we get it directly out of the atomic birefringent phenomenon.

Since we have shown that we can use the PREIT spectrum to calculate the group velocity of light, this experimental technique can be useful for the study of subluminal light propagation. For better estimation of the group velocity of light, the enhancement of the coherent control of the polarization rotation is needed. Thus our systemic study of the dependency of PREIT on the angular mismatch carries significance.

7

Effects of ellipticity and magnetic field on the polarization rotation in a coherently prepared atomic medium¹

7.1 Introduction

From our earlier studies [2, 3] depicted in the chapters 5 and 6, it is realized that to get an enhanced polarization rotation in the medium the system should be optimized for the corresponding parameters. The non-linear dependency on the pump beam intensity of the polarization rotation with electromagnetically induced transparency (PREIT) condition has been studied [2]. We have also investigated the effects of the angular mismatch between the pump and the probe beams, the change in the optical depth (OD) of the medium, and the change in the spot size or the radius of the pump beam on the angle of PREIT of the probe beam in ^{87}Rb atomic medium for same system configuration [3]. Further, the ellipticity of the beam and the external magnetic field are the two essential parameters in the case of study of the coherent phenomenon.

The effect of incident field ellipticity on the coherent phenomenon in Hanle configuration [5, 114] has been studied well both experimentally and theoretically [115, 116].

¹This chapter is based on the publication Das et al. *OSA Continuum*, **2021**, *4*, 105-120. The experiment and the theoretical calculations presented in this chapter have been entirely done by Arpita Das.

Generally, study of the coherence phenomenon in Hanle configuration [5, 115–118] has been done by using a σ_+ probe and σ_- pump beam. Both the beams are locked at a desired hyperfine transition and the externally applied magnetic field is scanned. By scanning this magnetic field when the Raman detuning condition is achieved one can observe the interference effect (CPT or EIT). The effect of quantum interference due to the spontaneous emission on the linear magneto-optical rotation (MOR) has been studied [119]. In MOR or Faraday rotation [28], the birefringence is created due to the applied magnetic field. In this case, one need only the linearly polarized probe beam and the external magnetic field. Here, the probe field is locked at a particular atomic transition and the magnetic field is scanned. Coherent control of MOR has also been investigated in a cascade system theoretically [29, 30] and experimentally [31], where along with the magnetic field a circularly polarized or linearly polarized pump beam is applied. There is one similar experimental technique by which one can study the spin dynamics of the medium. This phenomenon is known as spin-noise spectroscopy [120]. The idea of SNS is to detect intrinsic fluctuations of spin magnetization. In this technique the concept of Faraday rotation is used and the fluctuation of the angle of rotation is measured. To do this, after detecting the rotation signal by balanced polarimetric detection technique, the signal is fed into a spectrum analyzer instead of a oscilloscope. The fluctuation of angle of rotation is related with the magnetization fluctuation [120, 121]. Recently M. Swar et al. [122] using the Faraday rotation technique, explores the application of the spin noise spectroscopy (SNS) to detect the spin properties of atomic ensembles in and out of equilibrium. Besides, there are several studies on the Faraday rotation in cold atoms [123], hot atomic vapour [26], in a tripod system [124] and in multi-Zeeman levels [125] of room

temperature atomic vapour. In contrast to these, in our experiment the birefringence is created at first due to the circularly polarized pump beam and the EIT condition was created in the medium. Therefore, we called this phenomenon as polarization rotation with electromagnetically induced transparency (PREIT). In this chapter, we present how the angle of PREIT can be controlled by changing the ellipticity of the linearly polarized probe beam in the absence of an external magnetic field [4]. This work also involves an observation on the modification of polarization rotation due to the application of static longitudinal magnetic field in the EIT medium. We have shown that due to application of the magnetic field an additional birefringence effect is generated in the medium. To observe these phenomena, we have considered a V-type system of ^{87}Rb with D_1 and D_2 transitions in room temperature. To explain the experimentally observed phenomena theoretically, we have considered a four-level system combining the magnetic sub-levels of the corresponding hyperfine transitions. We have also followed a semi-classical approach to get the probe response of the medium.

7.2 Experiment

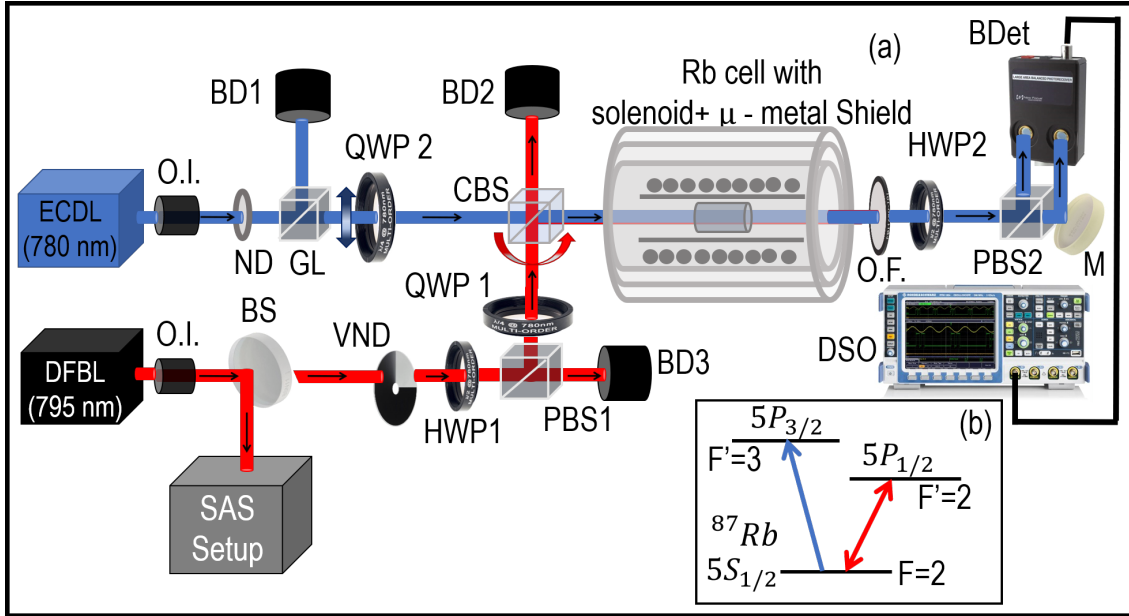


Figure 7.1: (a) Experimental Setup to study the polarization rotation in a coherently prepared atomic medium. ECDL: External Cavity Diode Laser, DFBL: Distributed Feedback Diode Laser, O.I.: Optical Isolator, HWP: Half-wave Plate, QWP: Quarter-wave Plate, GL: Glan-laser Polarizer, PBS: Polarizing Beam Splitting Cube, CBS: Non-polarizing Cubic Beam Splitter, BS: Beam Splitter, M: Mirror, Rb Cell: Rubidium Vapour Cell, BD: Beam Dump, ND: Neutral Density Filter, VND: Variable Neutral Density Filter, SAS Setup: Saturation Absorption Spectroscopy Setup, BDet: Balanced Detector, DSO: Digital Storage Oscilloscope. (b) V-type configuration of ^{87}Rb combining D_1 ($5S_{1/2} \rightarrow 5P_{1/2}$) and D_2 ($5S_{1/2} \rightarrow 5P_{3/2}$) transitions for experimental observation of polarization rotation in EIT medium.

Fig.7.1(a) describes our experimental setup to study how the polarization rotation of the probe beam in an EIT medium can be affected by changing the ellipticity of the probe beam and also by applying an external magnetic field in the medium. The experimental setup is almost similar to the experimental setup to study angular dependency of PREIT

shown in Fig.6.1 of chapter 6. The difference lies in the fact that here we have used a quarter-wave plate (QWP2) in the path of the linearly polarized probe beam to change its ellipticity and a Rb vapour cell of length 0.05 m is placed inside a solenoid to observe the effect of the magnetic field. The entire arrangement of the Rb cell along with the solenoid was covered by three layers of μ -metal shields to avoid interference due to the stray magnetic field of the earth. The probe beam was detected with the help of balanced polarimetric technique [25, 104] to get the polarization rotation signal. To study this phenomenon in an EIT or coherently prepared medium, we have chosen a V-type level scheme with D_1 and D_2 hyperfine transitions of ^{87}Rb as shown in Fig.7.1(b). The probe beam was scanned from $F = 2 \rightarrow F' = 3$ of D_2 transition, and the pump beam was locked at $F = 2 \rightarrow F' = 2$ of D_1 line. Throughout our experiment, the intensities of the probe and the pump beams before the Rb cell were kept constant at $0.47 \pm 0.02 \text{ mW/cm}^2$ and $5.09 \pm 0.02 \text{ mW/cm}^2$, respectively.

7.3 Experimental results and analysis

7.3.1 Dependency on the ellipticity

To study the behaviour of the angle of polarization rotation in a coherently prepared atomic medium due to the ellipticity of the probe beam, we have varied this parameter by rotating QWP2 as shown in the Fig.7.1(a)). The polarization rotation signals with EIT (PREIT signals) for different ellipticities with normal dispersion is shown in the Fig.7.2(a). From this figure, we have seen that the intensities, as well as the slopes of the signals, are changing periodically as the ellipticity of the probe beam (β) was

changed. It indicates that the birefringence created in the medium due to the difference in contributions of σ_+ and σ_- components of the probe beam is changing periodically with the change in probe ellipticity. It happens because the intensities of both components were changing as the ellipticity was varied.

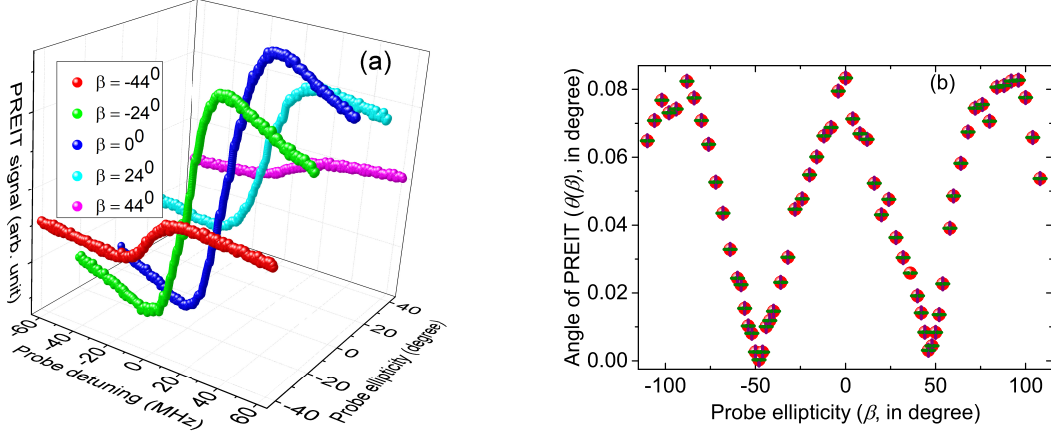


Figure 7.2: (a) Experimental polarization rotation signal of the probe beam for different probe beam ellipticities in EIT medium. (b) Experimental variation of angle of PREIT with the probe ellipticity.

The output intensity difference ($\Delta I(\omega_p)$), detected by the balanced photo-detector (B.Det in Fig.7.1(a)), can be written as (see appendix 2),

$$\Delta I(\omega_p, \beta) \approx I_0 \exp(-\alpha(\omega_p, \beta)L) \frac{\Delta n(\omega_p, \beta)\omega_0 L}{c} \quad (7.3.1)$$

The detected angle of polarization rotation is defined [3] as,

$$\theta(\omega_p, \beta) = \frac{\Delta n(\omega_p, \beta)\omega_0 L}{2c} \quad (7.3.2)$$

So, the angle of rotation in the vicinity of the EIT resonance is calculated by Taylor series expansion around $\omega_p \approx \omega_0$ of Eq.(7.3.1) as,

$$\theta(\beta) = \frac{1}{2I_0 \exp(-\alpha_0(\beta)L)} \left. \frac{d(\Delta I(\omega_p, \beta))}{d\omega} \right|_{\omega_0} \Delta\omega \quad (7.3.3)$$

where, ω_0 is the resonance frequency of the probe beam, $\Delta\omega$ is the smallest division of the frequency, $\alpha_0(\beta)$ is the absorption coefficient of the medium at the resonance condition corresponding to the probe ellipticity β and $L = 0.05$ m is the interaction length of the atomic medium.

From the slope of the rotation signal we have calculated the angle of polarization rotation at the vicinity of EIT i.e. the angle of PREIT using Eq.(7.3.3). In the Fig.7.2(b), we have plotted the angle of PREIT ($\theta(\beta)$) as a function of the probe beam ellipticity (β). From this plot we have observed that $\theta(\beta)$ shows a periodical behaviour with the variation of β . It shows maxima at $\beta = m\frac{\pi}{4}$ while the minima occur at $\beta = (m + 1)\frac{\pi}{4}$, where $m = 0, 2, 4, \dots$. To explain the physics behind this phenomenon let us express the electric field of the probe beam along with its ellipticity as,

$$\vec{\varepsilon}_p(\vec{r}_p, t) = E_p \hat{e} \cos(\omega_p t - \vec{k}_p \cdot \vec{r}_p) \quad (7.3.4)$$

where E_p is the complex amplitude and \hat{e} is the unit polarization vector. The polarization vector can be written as,

$$\hat{e} = \hat{e}_x \cos(\beta) + i \hat{e}_y \sin(\beta) = -\hat{e}_{+1} \cos(\beta - \frac{\pi}{4}) + \hat{e}_{-1} \cos(\beta + \frac{\pi}{4}) \quad (7.3.5)$$

where \hat{e}_z is directed along the propagation direction (\vec{k}_p) and $\hat{e}_{x,y}$ is directed along the polarization ellipse semi-axes. $\hat{e}_{\pm 1} = \mp \frac{(\hat{e}_x \pm i \hat{e}_y)}{\sqrt{2}}$ are the cyclic basis vectors and β is the ellipticity of the probe beam.

Now from Eq.(7.3.4) and Eq.(7.3.5) we can say that when $\beta = m\frac{\pi}{4}$, our probe beam became linearly polarized and both σ_+ and σ_- components of the beam were equal in intensities. So the birefringence created due to the difference between the contributions of the σ_+ and the σ_- components of the probe beam in the medium was maximum. As

a result, we got a maximum rotation in the medium. Again for $\beta = (m + 1)\frac{\pi}{4}$ the probe beam became circularly polarized. Depending on the value of β , it had either σ_+ or σ_- component in the medium and we got minimum rotation as the birefringence was minimum in this condition. In the intermediate value of β , the intensities of σ_+ and σ_- components were not equal, and we got an intermediate value of rotation. Therefore, we got a periodical variation of the angle of PREIT with the probe beam ellipticity with a $\pi/2$ period. Another way round, depending on the value of rotation, we can find the corresponding ellipticity from this variation. After getting the value of β from Eq.(7.3.5), we can say whether the beam is linearly or circularly or elliptically polarized. So, our study becomes important to find the unknown state of polarization of the probe beam. In our previous studies [2, 3] we have shown that from the angle of PREIT, one can calculate the refractive index of the medium. So our study becomes useful when one uses this experimental technique to find the group velocity of light as the refractive index is directly proportional to the angle of rotation. Our study also confirms that we need to use a linearly polarized probe with circularly polarized pump in the polarization spectroscopy technique to get the most reduced group velocity of the probe beam; as the angle of rotation for a linearly polarized probe beam is maximum.

7.3.2 Dependency on the longitudinal magnetic field

To venture into the effect of the longitudinal magnetic field on the angle of PREIT, we kept the probe beam as linearly polarized and the pump beam as circularly polarized. We have recorded the polarization rotation signal first without an external magnetic field under the EIT condition. Then we varied the magnetic field inside the solenoid. For each

magnetic field, we took the data corresponding to the PREIT signal of the probe beam.

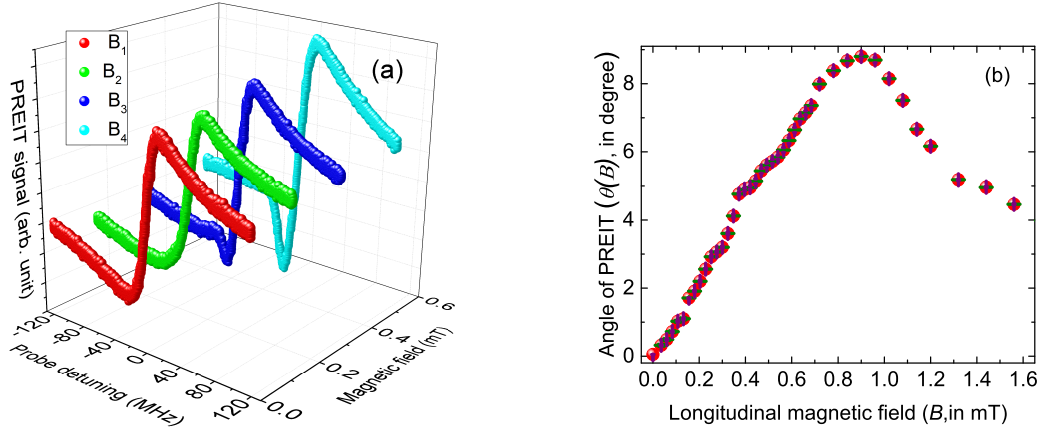


Figure 7.3: (a) Experimental polarization rotation signal of the probe beam for different magnetic fields ($B_1 = 0$ mT, $B_2 = 0.132 \pm 0.001$ mT, $B_3 = 0.300 \pm 0.001$ mT and $B_4 = 0.516 \pm 0.001$ mT) in the EIT medium. (b) Experimental variation of the angle of PREIT with the longitudinal magnetic field.

In this case, the anisotropy in the refractive index was also created due to the applied magnetic field (\vec{B}). Therefore, the output intensity difference is written as,

$$\Delta I(\omega_p, B) \approx I_0 \exp(-\alpha(\omega_p, B)L) \frac{\Delta n(\omega_p, B)\omega_0 L}{c} \quad (7.3.6)$$

This gives the angle of rotation at the EIT resonance condition as,

$$\theta(B) = \frac{\Delta I(B)}{2I_0 \exp(-\alpha_0(B)L)} \quad (7.3.7)$$

In the Fig.7.3(a) the PREIT signals have been shown for different longitudinal magnetic fields. We have calculated the angles of PREIT ($\theta(B)$) from these signals, as a function of the magnetic field using Eq.(7.3.7).

The variation of the angle of PREIT with the applied magnetic field is shown in the Fig.7.3(b). We have observed that in the beginning, $\theta(B)$ increased with the increment of B field upto a specific value. After that, $\theta(B)$ decreased for further increased B field. A

qualitative explanation behind this phenomenon is that when we apply the longitudinal magnetic field, the degeneracy among the magnetic sub-levels is removed (see Fig.7.6(b)). Since our medium is interacting with both circularly polarized pump beam and external magnetic field, both of these effects create a circular birefringence in the medium due to the non-uniform population distribution among the magnetic sub-levels of the atom [2, 25, 31, 45]. Again, due to the fixed intensity of the pump beam, in this case, the applied longitudinal magnetic field is the only reason for the enhancement of the circular birefringence for more non-uniform population redistribution. It increased the anisotropy of the refractive indices for the σ_+ and σ_- components of the probe beam, which in turn augmented the angle of PREIT as we increased the magnetic field. For this reason, we got an increasing behaviour in $\theta(B)$ with increasing B field till a specific value is reached where the population redistribution saturated. After this, as we have seen from the Fig.7.3(b), further increment in the B field worsen the birefringence effect in the medium due to the decreasing coherence as the population redistribution got saturated. Because in this region as the separation between individual magnetic-sublevels is increased, it in turn decreases the slope of the dispersion signal corresponding to the EIT resonance. So, $\theta(B)$ shows a decreasing trend with increasing B in this region. Thus we observed a non-linear variation of $\theta(B)$ with the B field.

Further, we can also comment that the angle of polarization rotation in the EIT medium is sensitive towards the magnetic field. From our experiment, we got the angle of rotation as $0.0267^\circ \pm 0.0002^\circ$ without any external magnetic field, while the angle of rotation was $0.32^\circ \pm 0.01^\circ$ for $B = 0.036 \pm 0.001$ mT. This got maximized as $8.79^\circ \pm 0.05^\circ$ at 0.900 ± 0.001 mT. So, the angle of rotation was increased by one order of magnitude

on introducing a magnetic field comparable to the earth's magnetic field in comparison to the value of rotation without any magnetic field. Moreover, it got maximized with two orders of magnitude using our atomic system. Thus our study becomes important when one uses the polarization spectroscopy technique to measure an unknown magnetic field.

7.4 Theoretical Analysis

To describe the experimentally observed phenomena for the dependency of the angle of PREIT on the probe beam ellipticity and the magnetic field, we have constructed two four-level systems as shown in the Fig.7.4(a) and Fig.7.6(a) with degenerate and non-degenerate excited states respectively. As shown in these figures, the σ_+ and σ_- components of the probe beam interact between $|1\rangle \rightarrow |3\rangle$ and $|1\rangle \rightarrow |4\rangle$ respectively, while the σ_+ pump beam couples between $|1\rangle \rightarrow |2\rangle$ states. To calculate the angle of PREIT theoretically, we need the susceptibilities (χ_+ and χ_-) corresponding to the σ_+ and σ_- components of the probe beam since the refractive index of an atomic medium is related to the real part of the susceptibility of the medium. Therefore, we have to calculate the probe coherence terms ρ_{31} and ρ_{41} of the density matrix component, where these two terms carry information about the contribution of the σ_+ and σ_- components of the probe field to the medium respectively. To get these terms, we need to solve the master equation Eq.(3.1.12). Here, $H_0 = \sum_{n=1}^{n=4} \hbar\omega_n |n\rangle \langle n|$ is the unperturbed Hamiltonian for both the cases of study. The perturbed Hamiltonian (H_p) will be different for the two cases. In Eq.(3.1.12), ρ is a 4×4 density matrix, whose diagonal terms contain the information of the population for the individual energy levels and the off-diagonal terms

give the information about the coherence contributions corresponding to the respective electric fields.

7.4.1 Dependency on the ellipticity

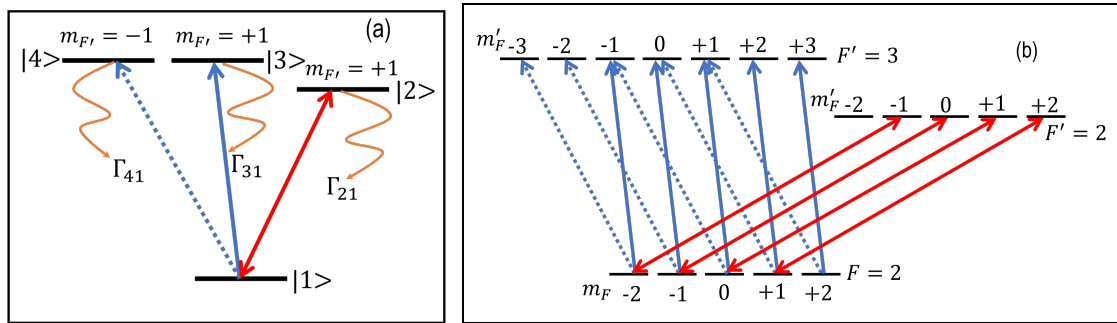


Figure 7.4: (a) Simplistic energy level diagram for theoretical analysis. See text for details. (b) All possible sub-level couplings of the degenerate sub-levels with both the components of the probe beam and the σ_+ pump beam in the complete atomic system. In both, the figures, the solid blue and the dotted blue one-sided arrows indicate the couplings due to the σ_+ and σ_- probe beams respectively. The solid red both sided arrows show the coupling for the σ_+ pump beam.

To explain how the rotation phenomenon occurred in the study of dependency of the angle of PREIT on the ellipticity of the probe beam, we considered that both the σ_+ and σ_- components of the probe beam contributes to the two-photon coherence contribution in the medium along with the σ_+ pump beam. But there was a mismatch between the contributions of the σ_+ and the σ_- probe beams depending on their amplitudes of the electric fields as the ellipticity of the probe beam was varied. Thus anisotropy was created between the refractive indices of the two circular polarization components of the probe beam leading to the rotation of its plane of polarization. Fig.7.4(b) represents the energy level diagram with σ_+ and σ_- polarization components of the probe beam and

σ_+ component of the pump beam, where all the possible degenerate sub-level couplings for both the components of the probe beam and that for the σ_+ pump beam have been shown. From this figure, it is also clear how the contributions can differ due to the different intensities of the components. For simplicity, we have taken only four sub-levels (see Fig.7.4(a)) to explain the phenomenon theoretically.

In this case, the perturbation in the system was only due to the electric fields of the applied beams so the perturbed Hamiltonian can be written as,

$$\begin{aligned} H_p = H_E = & -\hbar\{\Omega_{21}\cos(\omega_c t - \vec{k}_c \cdot \vec{r}_c) |2\rangle \langle 1| + \Omega_{31}(\beta)\cos(\omega_p t - \vec{k}_p \cdot \vec{r}_p) |3\rangle \langle 1| \\ & + \Omega_{41}(\beta)\cos(\omega_p t - \vec{k}_p \cdot \vec{r}_p) |4\rangle \langle 1| + c.c\} \end{aligned} \quad (7.4.1)$$

We have considered the probe field as in equation (7.3.4) and the pump field to be $\vec{E}_c(\vec{r}_c, t) = E_c \hat{e}_z \cos(\omega_c t - \vec{k}_c \cdot \vec{r}_c)$, where, E_c being the amplitude of the electric field of frequency ω_c , $\vec{k}_c = 2\pi/\lambda$ is the wave vector and $\vec{r}_{p(c)}$ is the propagation direction of the fields. Here, $|\Omega_{31}(\beta)| = \frac{\mu_{31} E_p \cos(\beta - \frac{\pi}{4})}{\hbar} = \Omega_p \cos(\beta - \frac{\pi}{4})$ and $|\Omega_{41}(\beta)| = \frac{\mu_{41} E_p \cos(\beta + \frac{\pi}{4})}{\hbar} = \Omega_p \cos(\beta + \frac{\pi}{4})$ are the Rabi frequencies for the σ_+ and σ_- components of the probe field respectively and $|\Omega_{21}| = \frac{\mu_{21} E_c}{\hbar} = \Omega_c$ is the pump Rabi frequency. The optical Bloch equations (OBE) in this case can be written as,

$$\begin{aligned} \dot{\rho}_{11} &= \Gamma_{21}\rho_{22} + \Gamma_{31}\rho_{33} + \Gamma_{41}\rho_{44} + \frac{i}{2}\Omega_p(\beta)(\rho_{31} - \rho_{13}) + \frac{i}{2}\Omega_p(\beta)(\rho_{41} - \rho_{14}) - \frac{i}{2}\Omega_c(\rho_{21} - \rho_{12}) \\ \dot{\rho}_{22} &= -\Gamma_{21}\rho_{22} - \frac{i}{2}\Omega_c(\rho_{21} - \rho_{12}) \\ \dot{\rho}_{33} &= -\Gamma_{31}\rho_{33} - \frac{i}{2}\Omega_p(\beta)(\rho_{31} - \rho_{13}) \\ \dot{\rho}_{44} &= -\Gamma_{41}\rho_{44} - \frac{i}{2}\Omega_p(\beta)(\rho_{41} - \rho_{14}) \\ \dot{\rho}_{12} &= -D_{12}^{-1}(\omega_c, \nu)\rho_{12} + \frac{i}{2}\Omega_p(\beta)\rho_{32} + \frac{i}{2}\Omega_p(\beta)\rho_{42} + \frac{i}{2}\Omega_c(\rho_{22} - \rho_{11}) \\ \dot{\rho}_{31} &= -D_{31}^{-1}(\omega_p, \nu)\rho_{31} - \frac{i}{2}\Omega_p(\beta)(\rho_{33} - \rho_{11}) - \frac{i}{2}\Omega_c\rho_{32} - \frac{i}{2}\Omega_p(\beta)\rho_{34} \end{aligned}$$

$$\begin{aligned}
\rho_{41} &= -D_{41}^{-1}(\omega_p, v)\rho_{41} - \frac{i}{2}\Omega_p(\beta)(\rho_{44} - \rho_{11}) - \frac{i}{2}\Omega_c\rho_{42} - \frac{i}{2}\Omega_p(\beta)\rho_{43} \\
\rho_{32} &= -D_{32}^{-1}(\omega_p, \omega_c, v)\rho_{32} + \frac{i}{2}\Omega_p(\beta)\rho_{12} - \frac{i}{2}\Omega_c\rho_{31} \\
\rho_{42} &= -D_{42}^{-1}(\omega_p, \omega_c, v)\rho_{42} + \frac{i}{2}\Omega_p(\beta)\rho_{12} - \frac{i}{2}\Omega_c\rho_{41} \\
\rho_{43} &= -D_{32}^{-1}(\omega_p, v)\rho_{43} + \frac{i}{2}\Omega_p(\beta)\rho_{13} - \frac{i}{2}\Omega_p(\beta)\rho_{41}
\end{aligned} \tag{7.4.2}$$

Using the rotating wave approximation (RWA) and the first order perturbation for the probe field, solving Eq.(7.4.2) under steady state condition, we obtained the two photon contribution terms (ρ_{31} and ρ_{41}) as,

$$\begin{aligned}
\rho_{31}(\omega_p, \omega_c, \beta, v) &= \frac{i\frac{\Omega_p \cos(\beta - \frac{\pi}{4})}{2} D_{31}(\omega_p, v)}{[1 + \frac{\Omega_c^2}{4} D_{31}(\omega_p, v) D_{32}(\omega_p, \omega_c, v)]} \{\rho_{11}^0(\omega_c, v) \\
&+ \frac{\Omega_c^2}{4} D_{12}(\omega_c, v) D_{32}(\omega_p, \omega_c, v) (\rho_{22}^0(\omega_c, v) - \rho_{11}^0(\omega_c, v))\}
\end{aligned} \tag{7.4.3}$$

and

$$\begin{aligned}
\rho_{41}(\omega_p, \omega_c, \beta, v) &= \frac{i\frac{\Omega_p \cos(\beta + \frac{\pi}{4})}{2} D_{41}(\omega_p, v)}{[1 + \frac{\Omega_c^2}{4} D_{41}(\omega_p, v) D_{42}(\omega_p, \omega_c, v)]} \{\rho_{11}^0(\omega_c, v) \\
&+ \frac{\Omega_c^2}{4} D_{12}(\omega_c, v) D_{42}(\omega_p, \omega_c, v) (\rho_{22}^0(\omega_c, v) - \rho_{11}^0(\omega_c, v))\}
\end{aligned} \tag{7.4.4}$$

$\rho_{11}^0(\omega_c, v)$, $\rho_{22}^0(\omega_c, v)$ are the zeroth order populations of the levels $|1\rangle$, and $|2\rangle$ respectively. They were calculated analytically as,

$$\rho_{11}^0(\omega_c, v) = \frac{\Omega_c^2 \gamma_{21} + 2\Gamma_{21}(\gamma_{21}^2 + \Delta_c^2(\omega_c, v))}{2[\Omega_c^2 \gamma_{21} + \Gamma_{21}(\gamma_{21}^2 + \Delta_c^2(\omega_c, v))]} \tag{7.4.5}$$

$$\rho_{22}^0(\omega_c, v) = \frac{\Omega_c^2 \gamma_{21}}{2[\Omega_c^2 \gamma_{21} + \Gamma_{21}(\gamma_{21}^2 + \Delta_c^2(\omega_c, v))]} \tag{7.4.6}$$

The parameters used in Eq.(7.4.3) , Eq.(7.4.4), Eq.(7.4.5) and Eq.(7.4.6) are described as follows,

$$D_{m1}(\omega_p, v) = \frac{1}{\gamma_{m1} + i\Delta_p(\omega_p, v)}; \quad m = 3, 4 \quad (7.4.7)$$

$$D_{12}(\omega_c, v) = \frac{1}{\gamma_{21} - i\Delta_c(\omega_c, v)}; \quad (7.4.8)$$

$$D_{m2}(\omega_p, \omega_c, v) = \frac{1}{\gamma_{m2} + i(\Delta_p(\omega_p, v) - \Delta_c(\omega_c, v))}; \quad m = 3, 4 \quad (7.4.9)$$

where, $\gamma_{m1} = \frac{\Gamma_{m1}}{2}$ are the coherence decay rates, where $m = 2, 3, 4$ and Γ_{m1} is the natural decay rate from $|m\rangle$ to $|1\rangle$. $\gamma_{32} = \frac{\Gamma_{31} + \Gamma_{21}}{2}$ and $\gamma_{42} = \frac{\Gamma_{41} + \Gamma_{21}}{2}$ are the non-coherence decay rates between the dipole forbidden transitions. In our calculations we have taken $\Gamma_{31} = \Gamma_{41} = 3$ MHz and $\Gamma_{21} = 5.75$ MHz. Following our experiment, when we have varied the ellipticity of the probe beam, the probe Rabi frequencies for both the components containing the ellipticity information had also changed accordingly. The amplitudes of Rabi frequencies have been calculated using, $\Omega = \Gamma \sqrt{\frac{I}{2I_{sat}}}$ [78], where Γ is the natural linewidth, I is the intensity and I_{sat} is the saturation intensity of the laser beam.

The probe resonance frequency is $\omega_{21} = \omega_0$ and the probe detuning is $\delta_p(\omega_p) = (\omega_0 - \omega_p)$. As we have taken the propagation direction of the probe beam along the z -axis, the Doppler detuning of the probe is $\Delta_p(\omega_p, v) = (\delta_p(\omega_p) + \vec{k}_p \cdot \vec{v}) = (\delta_p(\omega_p, v) + k_p v)$ (as, $\vec{v} = v\hat{z}$). Similarly, we have defined the detuning of the pump beam as $\delta_c(\omega_c) = (\omega_{31} - \omega_c)$ with the Doppler detuning of the pump beam $\Delta_c(\omega_c, v) = (\delta_c(\omega_c) + k_c v)$. Since in our experiment the pump beam was locked so in our calculation we have taken $\omega_{31} = \omega_c$. Therefore, in our calculation, $\delta_c = 0$ and $\Delta_c(v) = k_c v$.

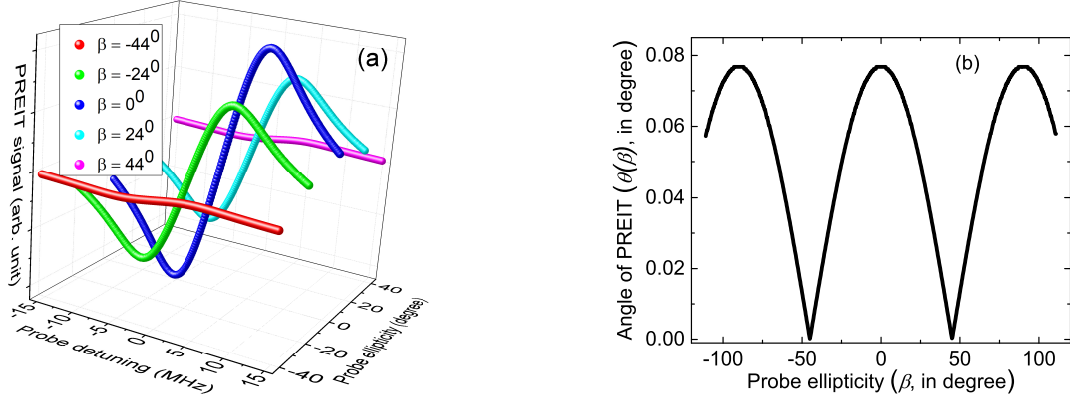


Figure 7.5: (a) Simulated polarization rotation signal of the probe beam for different probe beam ellipticities in the EIT medium. (b) Theoretical variation of the angle of PREIT with the probe ellipticity.

Convoluting the velocity distribution for the atoms, the susceptibilities can be written as,

$$\chi_{31(41)}(\omega_p, \beta) = \frac{2\mu_{31(41)}}{\epsilon_0 E_p} \int_{v=-\infty}^{+\infty} \rho_{31(41)}(\omega_p, \beta, v) N(v) dv \quad (7.4.10)$$

In the above equation, $N(v) = \frac{N_0}{\sqrt{\pi}u^2} \exp\left[-\frac{v^2}{u^2}\right]$ is Maxwell-Boltzmann (MB) velocity distribution, where u is the most probable velocity of the atoms and N_0 is the number density of the atoms at temperature 'T'K. The dipole moment, $\mu_{31(41)} = 1.73 \times 10^{-29}$ C.m [78]. The simulated polarization rotation spectra with positive slope in the vicinity of the EIT resonance are shown in the Fig.7.5(a) for different values of β . Here also we have observed the same periodical variations in the intensity of the rotational spectra with changing β as we had observed in our experiment.

With help of Eq.(7.4.10) we have calculated the angle of rotation according to,

$$\theta(\omega_p, \beta) = \frac{\omega_0 L}{4c} (\chi'_{31}(\omega_p, \beta) - \chi'_{41}(\omega_p, \beta)) \quad (7.4.11)$$

Therefore, $\theta(\beta)$ at the EIT resonance position can be calculated by expanding the Eq.(7.4.11)

in Taylor-series upto the first order term as,

$$\theta(\beta) = \frac{\omega_0 L}{4c} \left\{ (\chi'_{31}(\omega_0) - \chi'_{41}(\omega_0)) + \frac{d(\chi'_{31}(\omega_p, \beta) - \chi'_{41}(\omega_p, \beta))}{d\omega} \Big|_{\omega_0} \Delta\omega \right\} \quad (7.4.12)$$

In the above equations χ' is the real part of the susceptibility. In Eq.(7.4.12), $\chi'_{31}(\omega_0) = \chi'_{41}(\omega_0) = 0$. Therefore, $\theta(\beta)$ entirely depends on the derivatives of $\chi'_{31}(\omega_p, \beta)$ and $\chi'_{41}(\omega_p, \beta)$ at the resonance position. Since the susceptibilities depend on β as shown in the Eq.(7.4.10), the angle of PREIT is also a dependent of β . Using Eq.(7.4.12) we have calculated $\theta(\beta)$ for different values of β . In the Fig.7.5(b) we have shown the theoretical variation of the angle of PREIT with the probe beam ellipticity β . We got similar periodical variation of θ as a function of β with a period of $\frac{\pi}{2}$.

7.4.2 Dependency on the longitudinal magnetic field

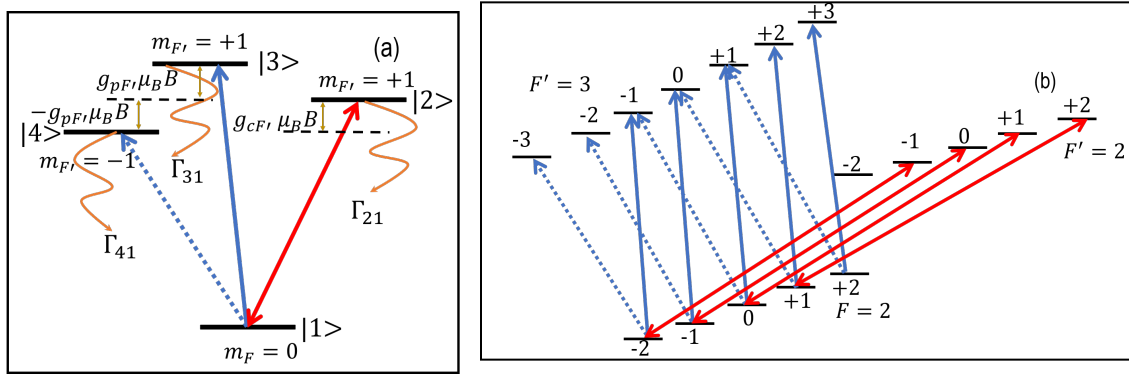


Figure 7.6: (a) A simple four-level V-type system to explain the magnetic field dependency on PREIT phenomenon. (b) Effect of the magnetic field with all the magnetic sub-levels in our experimental system. In both, the figures, the solid blue and the dotted blue one-sided arrows indicate the couplings due to the σ_+ and the σ_- probe beams respectively. The solid red both sided arrows show the coupling for the σ_+ pump beam.

In the Fig.7.6(a), a simplistic level scheme has been shown, where the σ_+ and σ_- components of the probe beam and the σ_+ component of the pump beam coupled the non-

degenerate magnetic sub-levels. In this case, we have considered that the σ_+ component of the probe beam along with the σ_+ pump beam created the EIT condition which contributed to the two-photon coherence effect in the medium. Whereas, the σ_- component of the probe beam gave only one photon contribution to the medium. Thus, there was a mismatch between the contributions of the σ_+ and the σ_- probe beams due to the non-uniform population distribution.

Further, as we applied the magnetic field along the direction of propagation of the pump beam, here, both the pump beam and the longitudinal magnetic field created circular birefringence in the medium. Therefore, an anisotropy was generated between the refractive indices of the two polarization components of the probe beam leading to the rotation of its plane of polarization. In the Fig.7.6(b) we have shown the effect of the magnetic field (B), which is responsible for splitting the magnetic sub-levels by an amount of $g_F\mu_B m_F B$. For simplicity, we have taken only four sub-levels (Fig.7.6(a)) to describe the phenomenon theoretically.

In this case, both the external magnetic field and the electric fields of the applied laser beams perturbed the system. Therefore, H_p can be written as,

$$\begin{aligned}
 H_p &= H_B + H_E \\
 &= \sum_{n=1}^{n=4} \hbar g_{F_n} \mu_B m_{F_n} B |n\rangle \langle n| - \hbar \{ \Omega_{21} \cos(\omega_c t - \vec{k}_c \cdot \vec{r}) |2\rangle \langle 1| + \Omega_{31} \cos(\omega_p t - \vec{k}_p \cdot \vec{r}) |3\rangle \langle 1| \\
 &\quad + \Omega_{41} \cos(\omega_p t - \vec{k}_p \cdot \vec{r}) |4\rangle \langle 1| + c.c \} \tag{7.4.13}
 \end{aligned}$$

Where g_{F_n} is the Lande g-factor, μ_B is the Bohr magneton, m_{F_n} is the magnetic quantum number corresponding to the hyperfine state F . For $n = 3, 4$, we can write g_{F_n} as g_p and for $n = 2$ g_{F_n} can be written as g_c . According to the Fig.7.6(a), $m_{F_1} = 0$, $m_{F_2} = +1$,

$m_{F_3} = +1$, and $m_{F_4} = -1$. Since, in this case our probe beam is linearly polarized ($\beta = 0$), so the probe Rabi frequencies are no longer a function of ellipticity. Therefore, the probe Rabi frequencies can be written as, $|\Omega_{31}| = \frac{\mu_{31}E_p}{\hbar} = \Omega_p$ and $|\Omega_{41}| = \frac{\mu_{41}E_p}{\hbar} = \Omega_p$. In this case the OBE can be written as,

$$\begin{aligned}
\rho_{11} &= \Gamma_{21}\rho_{22} + \Gamma_{31}\rho_{33} + \Gamma_{41}\rho_{44} + \frac{i}{2}\Omega_p(\rho_{31} - \rho_{13}) + \frac{i}{2}\Omega_p(\rho_{41} - \rho_{14}) - \frac{i}{2}\Omega_c(\rho_{21} - \rho_{12}) \\
\rho_{22} &= -\Gamma_{21}\rho_{22} - \frac{i}{2}\Omega_c(\rho_{21} - \rho_{12}) \\
\rho_{33} &= -\Gamma_{31}\rho_{33} - \frac{i}{2}\Omega_p(\rho_{31} - \rho_{13}) \\
\rho_{44} &= -\Gamma_{41}\rho_{44} - \frac{i}{2}\Omega_p(\rho_{41} - \rho_{14}) \\
\rho_{12} &= -D_{12}^{-1}(\omega_c, B, v)\rho_{12} + \frac{i}{2}\Omega_p\rho_{32} + \frac{i}{2}\Omega_p\rho_{42} + \frac{i}{2}\Omega_c(\rho_{22} - \rho_{11}) \\
\rho_{31} &= -D_{31}^{-1}(\omega_p, B, v)\rho_{31} - \frac{i}{2}\Omega_p(\rho_{33} - \rho_{11}) - \frac{i}{2}\Omega_c\rho_{32} - \frac{i}{2}\Omega_p\rho_{34} \\
\rho_{41} &= -D_{41}^{-1}(\omega_p, B, v)\rho_{41} - \frac{i}{2}\Omega_p(\rho_{44} - \rho_{11}) - \frac{i}{2}\Omega_c\rho_{42} - \frac{i}{2}\Omega_p\rho_{43} \\
\rho_{32} &= -D_{32}^{-1}(\omega_p, \omega_c, B, v)\rho_{32} + \frac{i}{2}\Omega_p\rho_{12} - \frac{i}{2}\Omega_c\rho_{31} \\
\rho_{42} &= -D_{42}^{-1}(\omega_p, \omega_c, B, v)\rho_{42} + \frac{i}{2}\Omega_p\rho_{12} - \frac{i}{2}\Omega_c\rho_{41} \\
\rho_{43} &= -D_{32}^{-1}(\omega_p, B, v)\rho_{43} + \frac{i}{2}\Omega_p\rho_{13} - \frac{i}{2}\Omega_p\rho_{41}
\end{aligned} \tag{7.4.14}$$

After taking RWA, the analytical solution of Eq.(7.4.14) under steady state condition yields the probe coherence terms as,

$$\begin{aligned}
\rho_{31}(\omega_p, \omega_c, B, v) &= \frac{i\frac{\Omega_p}{2}D_{31}(\omega_p, B, v)}{(1 + \frac{\Omega_c^2}{4}D_{31}(\omega_p, B, v)D_{32}(\omega_p, \omega_c, B, v))} \{\rho_{11}^0(\omega_c, B, v) \\
&+ \frac{\Omega_c^2}{4}D_{12}(\omega_c, B, v)D_{32}(\omega_p, \omega_c, B, v)(\rho_{22}^0(\omega_c, B, v) - \rho_{11}^0(\omega_c, B, v))\}
\end{aligned} \tag{7.4.15}$$

and

$$\rho_{41}(\omega_p, \omega_c, B, v) = i\frac{\Omega_p}{2}D_{41}(\omega_p, B, v)\rho_{11}^0(\omega_c, B, v) \tag{7.4.16}$$

The zeroth order populations are given by,

$$\rho_{11}^0(\omega_c, B, v) = \frac{\Omega_c^2 \gamma_{21} + 2\Gamma_{21}(\gamma_{21}^2 + \Delta_c(\omega_c, B, v)^2)}{2[\Omega_c^2 \gamma_{21} + \Gamma_{21}(\gamma_{21}^2 + \Delta_c(\omega_c, B, v)^2)]} \quad (7.4.17)$$

$$\rho_{22}^0(\omega_c, B, v) = \frac{\Omega_c^2 \gamma_{21}}{2[\Omega_c^2 \gamma_{21} + \Gamma_{21}(\gamma_{21}^2 + \Delta_c(\omega_c, B, v)^2)]} \quad (7.4.18)$$

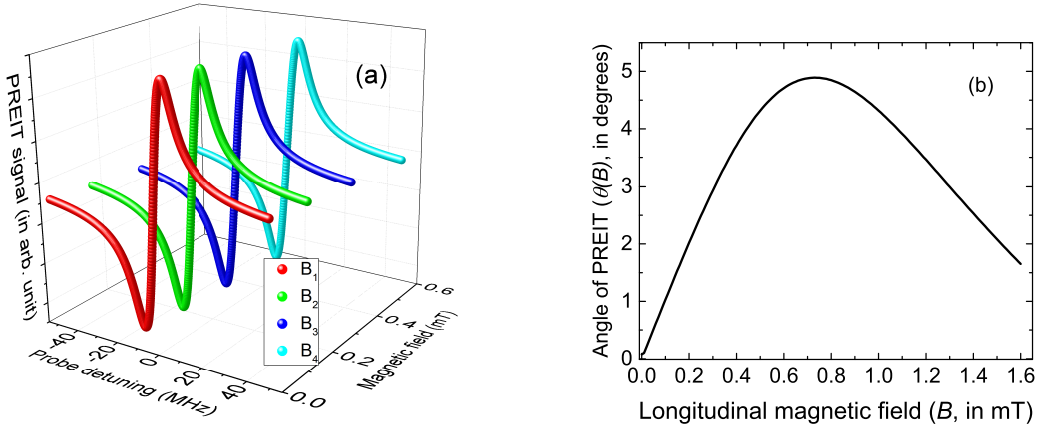


Figure 7.7: (a) Simulated polarization rotation signal of the probe beam for different magnetic fields ($B_1 = 0$ mT, $B_2 = 0.132$ mT, $B_3 = 0.300$ mT and $B_4 = 0.516$ mT) in the EIT medium. (b) Theoretical variation of the angle of PREIT with the longitudinal magnetic field.

The parameters in Eq.(7.4.15) , Eq.(7.4.16), Eq.(7.4.17) and Eq.(7.4.18) are described as follows,

$$D_{31}(\omega_p, B, v) = \frac{1}{\gamma_{31} + i\Delta_{p+}(\omega_p, B, v)} \quad (7.4.19)$$

$$D_{41}(\omega_p, B, v) = \frac{1}{\gamma_{41} + i\Delta_{p-}(\omega_p, B, v)} \quad (7.4.20)$$

$$D_{12}(\omega_c, B, v) = \frac{1}{\gamma_{21} - i\Delta_{cB}(\omega_c, B, v)} \quad (7.4.21)$$

$$D_{32}(\omega_p, \omega_c, B, v) = \frac{1}{\gamma_{32} + i(\Delta_{p+}(\omega_p, B, v) - \Delta_{cB}(\omega_c, B, v))} \quad (7.4.22)$$

$$D_{42}(\omega_p, \omega_c, B, v) = \frac{1}{\gamma_{42} + i(\Delta_{p-}(\omega_p, B, v) - \Delta_{cB}(\omega_c, B, v))} \quad (7.4.23)$$

The Doppler detunings for both the probe and the pump beams have been changed to $\Delta_{p+}(\omega_p, B, v) = \{\Delta_p(\omega_p, v) + g_p\mu_B B\}$, $\Delta_{p-} = \{\Delta_p(\omega_p, v) - g_p\mu_B B\}$ and $\Delta_{cB} = \{\Delta_c(\omega_c, v) + g_c\mu_B B\}$ respectively. Since our atomic system is a V-type system of ^{87}Rb with the combination of D₁ and D₂ transitions, we have taken $g_p = \frac{2}{3}$, $g_c = \frac{1}{6}$ and $\mu_B = 1.4h$ MHz/G [78]. In this case, $\Delta_{cB} = \{\Delta_c(v) + g_c\mu_B B\}$ since $\delta_c = 0$. All the values of decay parameters are the same as in the earlier case of ellipticity dependence. Therefore, integrating over all the velocity range, the susceptibilities are given by,

$$\chi_{31(41)}(\omega_p, B) = \frac{2\mu_{31(41)}}{\epsilon_0 E_p} \int_{v=-\infty}^{+\infty} \rho_{31(41)}(\omega_p, B, v) N(v) dv \quad (7.4.24)$$

The simulated PREIT spectra with different magnetic fields are shown in the Fig.7.7(a). The angle of polarization rotation at the EIT resonance position is calculated theoretically with the help of,

$$\theta(B) = \frac{\omega_0 L}{4c} (\chi'_{31}(B) - \chi'_{41}(B)) \quad (7.4.25)$$

After calculating $\theta(B)$ using Eq.(7.4.25), we have numerically plotted it as a function of the magnetic field(B). The theoretical characteristic variation of $\theta(B)$ with respect to B is shown in the Fig.7.7(b), where it can be seen that $\theta(B)$ increases with the B field upto a specific value. Then further increase in B decreases the value of $\theta(B)$ similar to what we have observed in the experiment.

7.5 Discussions

In this work, we have investigated how the angle of polarization rotation of the probe beam at the EIT region can be modified by changing the ellipticity of the probe beam without the external magnetic field in ^{87}Rb atomic vapour at room temperature. We had

also studied how the polarization rotation in the EIT region can be affected by applying the longitudinal magnetic field when the probe beam was linearly polarized, and the pump beam was circularly polarized. We had observed that the angle of PREIT shows a periodical behaviour of periodicity $\frac{\pi}{2}$ when the ellipticity of the probe beam was varied. The angle of PREIT became maximum when the probe beam was linearly polarized and became minimum when the probe beam was circularly polarized. It has been noticed that the angle of PREIT depends non-linearly on the applied longitudinal magnetic field. The circular birefringence was increased due to the increment in the applied magnetic field upto a specific value; after which, the circular birefringence decreases due to the decreasing coherent effect. Therefore, we can say that one can control the enhancement of polarization rotation occurring in the atomic medium at the EIT condition by controlling the ellipticity of the probe beam as well as by controlling the longitudinal magnetic field. Thus we can also enhance the anisotropy, as well as the chiral behaviour of the atomic medium.

To understand the experimental observations, we have analytically solved the density matrix equation for a four-level system. We have considered the excited states of the system to be degenerate for the case of ellipticity variation as there was no external magnetic field. Whereas, the excited states were considered to be non-degenerate for the magnetic field variation. From our theoretical calculation, we got a good agreement in the characteristic variation of the angle of rotation with the experimental observations.

As discussed in section 7.3, we can find the ellipticity of an unknown polarized probe beam from our study of dependency on the probe ellipticity of the angle of PREIT. Therefore, we can use the plot of $\theta(\beta)$ vs β as a calibration curve for this purpose. From

our observation, we can also say that the polarization rotation is highly dependent on the magnetic field. We found out that the angle of polarization rotation increased by one order of magnitude when 0.036 ± 0.001 mT magnetic field was applied compared to the angle of rotation without the magnetic field. Therefore, this experimental technique of detecting rotation spectrum can be useful to detect an unknown magnetic field.

8

Conclusion and Outlook

8.1 Peroration

Exploring the coherent phenomena for the application of the atomic medium in real life is a deep-rooted objective in physics. Even though the basic research focused on the interaction of laser with the atomic medium in different configurations, certainly in-situ measurements with high precision are needed for real-world applications. My thesis work has dealt with the experiment and theory behind the coherent control of light-atom interactions as a part of the ongoing research. We have studied how the atomic properties have changed as the EIT condition was created inside the Rb medium. It has been observed that we can control various phenomena by manipulating several system parameters like the intensity and the polarization of the beams, beam size, OD, residual Doppler broadening and the magnetic field.

Experiments have been carried out in multilevel Rb vapour medium. We have selected the probe and the pump transitions so that we can observe the interference effect, namely the EIT, in the medium. Main aim of this thesis was to study the dispersive properties of the atomic medium under several laser induced coherent phenomena, in terms of light-atom interaction. We have observed from one of our experiments that the group velocity

of light depends on the pump intensity non-linearly and to get a maximum reduction in the group velocity one needs to optimize the pump intensity. The experiment related to polarization rotation with electromagnetically induced transparency (PREIT) reveals that to get a maximum angle of rotation we have also to optimize the pump intensity. We have also observed that the angle of PREIT will be enhanced if the angular mismatch between the probe and the pump beam is minimized, the OD of the medium is increased and the spot size of the pump beam is increased. From our study we have found that the angle of PREIT became more sensitive to the OD than the pump beam's spot size after a certain value. We have also shown that the angle of PREIT will be maximum only for the linearly polarized probe beam. The characteristics curve for the variation of the angle of PREIT with the ellipticity of the probe beam can be used as a calibration curve to get an idea about the polarization of the beam. The angle of PREIT also depends on the external static magnetic field non-linearly. To get an enhanced rotation, the strength of the applied magnetic field should be optimized. Moreover, our studies find application in the light-storage experiments, the frequency stabilization or the optical locking in the EIT transition, in the field of magnetometry etc. The atomic medium can be used as a polarization rotator and also used as a birefringence lens. Along with the experiments we have built corresponding theoretical models. In all the cases we have taken a semi-classical approach for light-atom interaction and have solved the OBE for the multi-level atomic systems to get the probe coherence term. With the models we were able to understand the phenomena in a qualitative way. Although there are some mismatches observed between the theory and experiments due to various reasons.

In the study of the dispersive properties of an EIT medium in room temperature, the

susceptibility of the medium for a three level Λ - type system was calculated analytically assuming the Lorentzian (Lz) velocity distribution of the atom. We have numerically plotted the imaginary and the real parts of the probe coherence term as a function of the probe detuning for both the Lz and the MB distributions to check the correctness of our assumption. We have obtained a complete overlap of the coherence terms corresponding to both distributions in the EIT region for the two distributions. Analytical expressions for the susceptibility and the group index of the medium have also been derived. The characteristic variation of the group index with the Rabi frequency of the pump beam matches well with our experimental findings. Although there are some discrepancies in the numerical values, we think that it can happen due to certain reasons. In our experiment, we have measured the power of the beams before the Rb cell, but there was power loss in the glass windows of the cell when the beams enter the medium. We did not incorporate this power loss in our theory. It is well known that the magnetic field can affect the EIT phenomenon. In this particular experiment, we did not use any magnetic shielding for the Rb cell. So the earth's magnetic field may have affected the numerical values of the group index. In the real experimental system there are other hyperfine states which can affect the observed phenomenon, but in theory we have considered only a three level system and the effect of the hyperfine levels has been ignored. The reduction of the group velocity and the maximization of the time delay of the probe beam under the EIT condition are the important parameters to optimize the efficiency of light storage and retrieval. The maximum storage efficiency depends on the optical depth, and this can be achieved by optimization of the probe and the pump pulse shapes. We can take the help of a powerful time-reversal-based optimization process which allows us

to find the pulse shape of a weak input field iteratively until the shape of the retrieved pulse becomes identical to the reversed profile of the input pulse [126]. Thus, our study becomes important in the field of storage of light experiments since it gives an indirect measurement of slow light.

PREIT phenomenon has been studied in a V-type system for both ^{87}Rb and ^{85}Rb combining both D_1 and D_2 transitions. For this purpose, a polarization spectroscopy setup has been made, and the polarization rotation signal of the probe beam has been detected with the help of a balanced polarimetric detection technique. Therefore, we have obtained a Doppler-free dispersion signal with positive slope and high S/N ratio. For ^{85}Rb , we observed two EIT peaks simultaneously and one EIT peak for ^{87}Rb . From the detected signal, we have estimated the angle of rotation. The angle of rotation gave a non-linear characteristic variation. We have also measured the maximum birefringence created in the medium calculating the relative refractive index of the medium. We have considered a four-level V-type system, where the pump beam couples two excited states to explain the occurrence of two EITs in the medium for ^{85}Rb . Using our theoretical model, we have justified the reason behind the creation of one EIT resonance for ^{87}Rb , as well as two EIT resonances for ^{85}Rb . Following our model, we were able to understand the rotation phenomenon. To get the probe response, we have solved the OBE for a four-level system analytically under the steady-state condition. The susceptibilities corresponding to the σ_+ and the σ_- components of the probe beam have been calculated numerically using the 1D MB velocity distribution of the atoms. The angle of rotation has been calculated numerically in theory for the atoms of all velocities. Theoretical characteristics of the angle of PREIT with the intensity of the pump beam matches consistently with

our experimental observations. In a realistic system, there are more hyperfine levels which also contributed to our experiment due to which we got the VSR peaks. We have considered a simple four-level system in our theoretical model with no extra energy levels. It may generate discrepancy in the numerical values between the experimental and the theoretical results. The discrepancy also comes due to the angular broadening effect, which was not included in our theoretical model. Difficulty in the measurement of exact Rabi frequency seen by the atom may additionally affect the value of the angle of rotation. Therefore, considering all the energy levels, as well as the angular broadening effect in our theoretical model, can improve the similarities between the experimental and theoretical results. Knowing the ratio between the output and input powers of a non-resonant beam passing through the vapour cell, we can get an idea about loss of power due to scattering, reflection or absorption in the cell window. This will help us to calculate Rabi frequency closer to the exact value seen by an atom.

From this study, we can say that for a particular pump intensity, there exists a maximum rotation in the plane of polarization of the probe beam when it passes through an EIT medium. The system can be optimized to get maximum rotation using our theoretical calculations. The atomic medium can be used as atomic polarization rotator using this experimental technique. Further, from the absorption and the dispersion spectra, it is clear that we can use this experimental technique to identify any resonance position, which is smeared out in the absorption spectrum due to the power broadening or due to the angular broadening. All resonance positions can easily be resolved in the dispersion spectrum. As we got a sharp rotation in the vicinity of the probe resonance, i.e., at EIT position, we can use this signal as a 1F signal for frequency stabilization of the probe

beam at the EIT position without using a lock-in-amplifier circuit. Such an optical locking method is advantageous because the dispersion signal is a modulation free and has high S/N ratio.

A further experiment was carried out to find how the PREIT phenomenon in a V-type system of ^{87}Rb can be affected by the residual Doppler broadening. To do this, we have changed the overlapping angle (angular mismatch) between the probe and the pump beams inside the atomic medium. While increasing the angular mismatch, the number of interacting atoms in the interaction region was also changed along with residual Doppler broadening in the medium. Therefore, we have taken the OD and the pump beam spot size as two separate parameters in our study. For a particular OD and pump beam diameter, we observed that the angle of PREIT decreased as the angular mismatch was increased. For a particular angular mismatch, the angle of PREIT increases with OD and the pump beam diameter with having a saturation tendency in case of pump beam diameter variation. So, OD is more effective in this case than the pump beam diameter after a specific value. From the angle of PREIT, we have also calculated the group velocity of the probe beam for zero angular mismatch. In support of our experiment, we have solved the OBE analytically for a three-level V-type system. The theoretical results show a consistent agreement with the experimental observations in most of the cases. However, there are possible causes of some discrepancies. The effective interaction length is always changing as we changed the angle between the probe and the pump beams in our experiment, but in theory, we have assumed that this remains constant for a particular OD and w_c for the sake of simplicity. There are other energy levels where the population may decay in the existing experimental system. But we have taken a three-level closed

system in our theoretical formulation. So the extra decays in the real system can also introduce this discrepancy. This experimental technique can be used to get slow light, and the atomic medium can be prepared with the proper choice of the system parameters using our theoretical model.

Effects of ellipticity of the probe beam and the external longitudinal magnetic field on the PREIT with the same atomic system and configuration has been studied. We have observed a periodic variation of the angle of PREIT with the probe ellipticity when there is no external magnetic field. A non-linear variation of the angle of PREIT was seen with the external longitudinal magnetic field when the probe beam was linearly polarized. To understand the experimental observation, we have analytically solved the OBE for a four-level system. We have considered the excited states of the system to be degenerate in the case of ellipticity variation. On the other hand, the excited states were deemed to be non-degenerate in the case of magnetic field variation. The characteristic variations of the angle of rotation corresponding to the experimental observations and the theoretical results matches well. As discussed in the section 7.3 of the chapter 7, we can find the ellipticity of an unknown polarized probe beam from our study for the dependency of the angle of PREIT on the ellipticity of the probe beam. Therefore, we can use the plot of the angle of PREIT vs the ellipticity of the probe beam as a calibration curve for this purpose. From our observation, we can also say that the polarization rotation is highly dependent on the magnetic field because the angle of polarization rotation increased by one order of the magnitude when we applied 0.036 ± 0.001 mT compared to the angle of rotation without the magnetic field. Therefore, this experimental technique of observing rotation spectrum can be useful to detect an unknown magnetic field. Although there

are some discrepancies between the experiment and the theory. It may be due to the reason that in the theoretical model for sake of simplicity we have reduced our system to a four-level system, whereas in our real system there seventeen non-degenerate sublevels which will also affect the rotation phenomenon. If we consider all the sub-levels then the numerical solution will be helpful. Instead of this, one can get an idea about the magnetic field using our theoretical model to get the maximum rotation using our experimental method.

On the other hand, in the polarization measurement the stress induced birefringence in glass may play an important role. It results when isotropic materials are stressed or deformed causing a loss of physical isotropy. In our experiments, circularly polarized pump creates the birefringence in the atomic medium, as a result the direction of linearly polarized probe beam is rotated. This rotational signal was detected with help of balanced polarimetric detection technique. When there is only linearly polarized probe beam, then no dispersion signal was observed. This implies that no rotation occurred in the direction of polarization of the probe beam. We have observed the same when we heated the atomic cell at 45⁰C. Therefore, we can say that in our case there is no stress induced birefringence which can affect the observed phenomenon. Even if, there is any stress induced birefringence, it is so small that it cannot affect our measurements. Therefore, we did not consider this effect in our all of our analysis.

Finally, we can comment that the systematic study with PREIT phenomenon becomes important in the field of the applications of the PR phenomenon. In each case, to optimize the system, our theoretical models can be helpful.

8.2 Future trek

The studies carried out in this thesis unlocks several possibilities in the future direction. It can be done in the experimental and as well as theoretical directions.

8.2.1 Storage and retrieval of information

The study of dispersive properties in the Λ -type configuration and also the study of PREIT phenomenon in the V-type system open up the chance of the storage and the retrieval the light in the EIT medium. The study can be performed in the cold atoms, which is in the building stage in our laboratory (see appendix D). Use of the polarization rotation spectroscopy (PRS) technique is advantageous as it gives high S/N ratio signals in case of indirect detection of slow light. Moreover, the noise generated in the interferometric setup can be overcome by using the PRS technique. The results will be improved with cold atoms because in this case, we can get a high optical density, and we can get rid of the Doppler broadening of the medium. Use of the V-type system gives a possibility of getting larger storage time [92].

8.2.2 Magnetometry

Since the PREIT technique is sensitive to the low magnetic field, we can detect such fields using this experimental technique. It can be said that our study is the building stage of the magnetometry experiment. Therefore, this experimental process of PREIT can be used in the field of magnetometry [37, 47, 53, 54]. To detect an unknown magnetic field with this technique, we need to scan the magnetic field. The system needs to be

optimized with various system parameters for this purpose. It can be done following the studies contained in this research work. In this case, for theoretical calculation, we need to consider all the sub-levels acting in the experimental system to get a realistic estimate.

8.2.3 Birefringence lens effect

The atomic medium can behave as a birefringence lens when polarization rotation occurred in the medium. Generating EIT in the medium gives rise the possibility of increasing birefringence in the medium. Therefore, the PREIT technique can be used to prepare a more active birefringence lens experimentally. In this case, the pump beam should be highly intense and spatially inhomogeneous. This effect will be more in a tripod system since this system can be treated as a double Λ - type system. The divergence to convergence transition of the lens like effect can be enhanced in the double-EIT configuration [64]. This study can be done in Rb vapour as well as in cold atoms.

Summary

Experiments have been performed with multilevel Rb atomic vapour to understand the quantum interference effect in the light-atom interactions. An indirect measurement of the slowing down of the group velocity has been studied by using the dispersive properties of electromagnetically induced transparency (EIT) in a Λ -type system at room temperature with D_2 transition of ^{87}Rb [1]. It has been observed that the group index of the medium varies non-linearly with the pump Rabi frequency. This observation indicates that to get maximum reduction in the group velocity, one needs to optimize the system. Moreover, the dispersive properties of the atomic medium can be modified by controlling the polarization of laser, which in turn can create birefringence in the medium. An experiment on polarization rotation spectroscopy (PRS) has been performed by forming EIT in a V-type configuration combining D_1 and D_2 transitions for both Rb isotopes to understand the phenomenon mentioned above in detail. This technique is named as polarization rotation with electromagnetically induced transparency (PREIT) [2]. PREIT gives a non-linear characteristic variation of the rotation angle with the pump intensity. The amount of anisotropy in the refractive index is also estimated. Dependence of the angle of PREIT on the angular mismatch between the probe and the pump beams has been studied in the ^{87}Rb with a similar configuration [3]. Effects of the optical depth (OD) and spot size (w_c) of the pump beam on the PREIT phenomenon have also been explored. From the angle of PREIT, the relative group indices of the medium are measured for variable OD and w_c respectively, without any angular mismatch between the probe and the pump beams. Reduced group velocities of the probe beam corresponding

to maximum OD and w_c are also estimated from this study. Other two parameters, the ellipticity of the probe beam (β) and the external longitudinal magnetic field (B), can also modify PREIT [4]. Therefore, the effect of β on the angle of PREIT has been investigated, and a periodical variation is observed in a V-type system of ^{87}Rb combining its D_1 and D_2 transitions. From this periodicity, one can comment about the unknown state of polarization of the beam if the angle of rotation is known. Further, the dependence of the angle of PREIT on B has been studied, which gives non-linear characteristics. This study also indicates that the PREIT is sensitive to the low magnetic field. Thus, the effects of the system-parameters on PREIT help us to understand how we can control the system so that we can get an enhanced rotation in the system. All the above studies are explained with corresponding theoretical models. The Liouville equation for three and the four-level systems have been solved analytically under the steady-state condition to get the probe coherence term. We have considered the velocity of the atom by convoluting its velocity distribution with the analytically derived susceptibility. We have also compared our experimental findings with our theoretical calculations and found consistent agreement between them.

Appendices

A

Solution of the OBE for a two-level atomic system

Under the steady state condition ($\frac{d\rho}{dt} = 0$), from Eq.(3.2.19) we obtain,

$$\Gamma_2\rho_{22} + \frac{i}{2}\Omega_{12}\rho_{21} - \frac{i}{2}\Omega_{21}\rho_{12} = 0 \quad (\text{A.0.1})$$

Since, $\Omega_{12} = \Omega_{21}$. Therefore, Eq.(A.0.1) gives,

$$\rho_{22} = \frac{i}{2\Gamma_2}\Omega_{12}(\rho_{12} - \rho_{21}) \quad (\text{A.0.2})$$

Similarly, from Eq.(3.2.19) we get,

$$\rho_{12} = -\frac{i\Omega_{12}}{2(\frac{\Gamma_2}{2} - i\delta)}(\rho_{11} - \rho_{22}) \quad (\text{A.0.3})$$

and

$$\rho_{21} = \frac{i\Omega_{12}}{2(\frac{\Gamma_2}{2} + i\delta)}(\rho_{11} - \rho_{22}) \quad (\text{A.0.4})$$

Subtracting Eq.(A.0.4) from Eq.(A.0.3) we get,

$$(\rho_{12} - \rho_{21}) = -\frac{i\Omega_{12}\Gamma_2(\rho_{11} - \rho_{22})}{2(\frac{\Gamma_2^2}{4} + \delta^2)} \quad (\text{A.0.5})$$

Using Eq.(A.0.5), Eq.(A.0.2) yields,

$$\rho_{22} = \frac{\Omega_{12}^2}{4(\frac{\Gamma_2^2}{4} + \delta^2)}(\rho_{11} - \rho_{22}) \quad (\text{A.0.6})$$

Since we have considered that $\rho_{11} + \rho_{22} = 1$, i.e. the population is conserved. With this assumption Eq.(A.0.6) gives,

$$\rho_{22} = \frac{\Omega_{12}^2}{4(\frac{\Gamma_2^2}{4} + \delta^2)}(1 - 2\rho_{22}) \quad (\text{A.0.7})$$

$$\implies \rho_{22} = \frac{\Omega_{12}^2}{2\{\Omega_{12}^2 + 2(\frac{\Gamma_2^2}{4} + \delta^2)\}} \quad (\text{A.0.8})$$

Therefore using $\rho_{11} + \rho_{22} = 1$,

$$\rho_{11} = 1 - \frac{\Omega_{12}^2}{2\{\Omega_{12}^2 + 2(\frac{\Gamma_2^2}{4} + \delta^2)\}} \quad (\text{A.0.9})$$

$$\implies \rho_{11} = \frac{\Omega_{12}^2 + 4(\frac{\Gamma_2^2}{4} + \delta^2)}{2\{\Omega_{12}^2 + 2(\frac{\Gamma_2^2}{4} + \delta^2)\}} \quad (\text{A.0.10})$$

Using Eq.(A.0.8) and Eq.(A.0.10), Eq.(A.0.4) can be written as,

$$\rho_{21} = i \frac{\Omega_{12}(\frac{\Gamma_2^2}{4} + \delta^2)}{(\frac{\Gamma_2}{2} + i\delta)\{\Omega_{12}^2 + 2(\frac{\Gamma_2^2}{4} + \delta^2)\}} \quad (\text{A.0.11})$$

Eq.(A.0.8), Eq.(A.0.10) and Eq.(A.0.11) are the analytical solutions of Eq.(3.2.19) under steady state condition.

The numerical solution has been done in Mathematica using NDSolve technique.

B

Calculation of the output intensity difference in balanced homodyne detection technique

After mixing the probe signal and the reference beams in the 50:50 CBS shown in the Fig.4.1, there were two outputs from it. If we assume them to be ε_1 and ε_2 respectively then we can write [84],

$$\begin{aligned}\varepsilon_1 &= \frac{1}{\sqrt{2}}[E_r \exp\{i(\phi_r + \beta(\omega)L)\} + E_p \exp\{-\alpha(\omega)L/2\}] \\ \varepsilon_2 &= \frac{1}{\sqrt{2}}[E_r \exp\{i(\phi_r + \beta(\omega)L)\} - E_p \exp\{-\alpha(\omega)L/2\}]\end{aligned}\tag{B.0.1}$$

The intensities at the two photo detectors of the balanced detector I_1 and I_2 can be written as,

$$\begin{aligned}\Delta I_1(\omega) &\propto \varepsilon_1 \varepsilon_1^* \\ &\propto \frac{1}{2}[E_r^2 + E_r E_p \exp\{-\alpha(\omega)L/2\}(\exp\{i(\phi_r + \beta(\omega)L)\} + \exp\{-i(\phi_r + \beta(\omega)L)\}) \\ &\quad + E_p^2 \exp\{-\alpha(\omega)L\}]\end{aligned}\tag{B.0.2}$$

and

$$\begin{aligned}\Delta I_2(\omega) &\propto \varepsilon_2 \varepsilon_2^* \\ &\propto \frac{1}{2}[E_r^2 - E_r E_p \exp\{-\alpha(\omega)L/2\}(\exp\{i(\phi_r + \beta(\omega)L)\} + \exp\{-i(\phi_r + \beta(\omega)L)\}) \\ &\quad + E_p^2 \exp\{-\alpha(\omega)L\}]\end{aligned}\tag{B.0.3}$$

Therefore, the output of the balanced homodyne detector is given by,

$$\begin{aligned} \Delta I_d(\omega) &= I_1 - I_2 \\ &\propto 2E_r E_p \exp\{-\alpha(\omega)L/2\} \cos(\phi_r + \beta(\omega)L) \end{aligned} \tag{B.0.4}$$

C

Calculation of the output intensity in balanced polarimetric detection technique

For a linearly polarized light the initial state of electric field can be written as,

$$\begin{aligned} E &= \begin{bmatrix} E_x \\ E_y \end{bmatrix} \\ &= E_0 \begin{bmatrix} \cos \phi \\ \sin \phi \end{bmatrix} \end{aligned} \quad (\text{C.0.1})$$

where ϕ is the angle of the polarization with respect to x-axis. Now Eq.(C.0.1) can be written in terms of circular polarization basis vectors,

$$E = E_0 \frac{e^{-i\phi}}{2} \begin{bmatrix} 1 \\ i \end{bmatrix} + E_0 \frac{e^{i\phi}}{2} \begin{bmatrix} 1 \\ -i \end{bmatrix} \quad (\text{C.0.2})$$

While propagating through the cell of the length L , the different polarization components of the beam will exhibit the differential absorption and dispersion on account of the atomic medium. The electric field of the probe field is given by after passing through the atomic medium,

$$E = E_0 \left\{ \frac{e^{-i\phi}}{2} \begin{bmatrix} 1 \\ i \end{bmatrix} e^{-ik_+L - \alpha_+L/2} + E_0 \frac{e^{i\phi}}{2} \begin{bmatrix} 1 \\ -i \end{bmatrix} e^{-ik_-L - \alpha_-L/2} \right\} \quad (\text{C.0.3})$$

where, $k_{\pm} = \frac{\omega n_{\pm}}{c}$, n_{\pm} is the refractive indices for σ_{\pm} circular polarization components and

α_{\pm} is the corresponding absorption coefficient. Simplification of Eq.(C.0.3) leads to,

$$E = E_0 e^{-i\frac{\omega n L}{c}} e^{-\frac{\alpha L}{2}} \left\{ \frac{1}{2} e^{-i\phi + \frac{\omega \Delta n L}{2c}} \begin{bmatrix} 1 \\ i \end{bmatrix} + \frac{1}{2} e^{i\phi + \frac{\omega \Delta n L}{2c}} \begin{bmatrix} 1 \\ -i \end{bmatrix} \right\} \quad (\text{C.0.4})$$

where, $n = \frac{1}{2}(n_+ + n_-)$, $\alpha = \frac{1}{2}(\alpha_+ + \alpha_-)$ and $\Delta n = (n_+ - n_-)$. Eq.(C.0.4) can be rewritten as,

$$E = E_0 e^{-i\frac{\omega n L}{c}} e^{-\frac{\alpha L}{2}} \begin{bmatrix} \cos\left(\phi + \frac{\omega \Delta n L}{2c}\right) \\ \sin\left(\phi + \frac{\omega \Delta n L}{2c}\right) \end{bmatrix} \quad (\text{C.0.5})$$

Therefore, the x - component and y - component of the electric field are given by,

$$\begin{aligned} E_x &= E_0 e^{-i\frac{\omega n L}{c}} e^{-\frac{\alpha L}{2}} \cos\left(\phi + \frac{\omega \Delta n L}{2c}\right) \\ E_y &= E_0 e^{-i\frac{\omega n L}{c}} e^{-\frac{\alpha L}{2}} \sin\left(\phi + \frac{\omega \Delta n L}{2c}\right) \end{aligned} \quad (\text{C.0.6})$$

This gives the intensities in the x and y direction as,

$$\begin{aligned} I_x &\propto E_0^2 e^{-\alpha L} \cos^2\left(\phi + \frac{\omega \Delta n L}{2c}\right) \\ I_y &\propto E_0^2 e^{-\alpha L} \sin^2\left(\phi + \frac{\omega \Delta n L}{2c}\right) \end{aligned} \quad (\text{C.0.7})$$

Therefore the output intensity of the balanced homodyne detector is given by,

$$\begin{aligned} \Delta I &= I_x - I_y \\ &= I_0 e^{-\alpha L} \cos 2\left(\phi + \frac{\omega \Delta n L}{2c}\right) \end{aligned} \quad (\text{C.0.8})$$

Since we set $\phi = \pi/4$, so Eq.(C.0.8) yields,

$$\begin{aligned} \Delta I &= I_0 e^{-\alpha L} \sin \frac{\omega \Delta n L}{c} \\ &= I_0 e^{-\alpha L} \frac{\omega \Delta n L}{c} \end{aligned} \quad (\text{C.0.9})$$

This intensity depends on several system parameters e.g. frequency, ellipticity, amplitude of the electric field and also on the perturbation given to the medium.

D

Assembling magneto-optical trap (MOT)

My research work contains the study of coherence phenomena in the hot and room temperature Rb vapour. This work also involves in the development of the vacuum and the magnetic field for the magneto-optical trap (MOT) along with the planning of the optical path to get cold atoms. The detail description of designing and characterizing the quadrupole magnetic field and the description of assembling of the vacuum chamber with the pumps with a schematic presentation of the optical path are discussed with an initial introduction on MOT.

D.1 Assembling vacuum chambers for magneto-optical trap (MOT)

In this section, at first, I will explain the scattering force on atom when it interacts with a light field. The mechanism of Doppler cooling and the MOT will also be discussed qualitatively. After that, I will discuss how we achieved the ultra-high vacuum in our laboratory for this purpose. Then, the details of the magnetic coils will be presented. A schematic view of the optical path will also be presented.

D.1.1 Scattering force on an atom

There are two types of optical force when the laser interacts with atoms; they are (i) stimulated force or dipole force and (ii) spontaneous or radiation pressure force. Dipole force arises due to the induced dipole moment, i.e., the absorption of photon followed by stimulated emission. It is related to the intensity gradient of the field. Radiation pressure force arises due to the momentum transfer from the laser beam to the atom. It is related to the phase gradient of the field. This force represents the rate at which the light delivers momentum, or we can say that this equals the rate at which the light delivers energy divided by the speed of light. Therefore, the magnitude of the radiation pressure force is given by [65, 67],

$$F_{rad} = \frac{IA}{c} \quad (\text{D.1.1})$$

Where the quantity IA represents the power of radiation absorbed by the atom and c is the speed of light in vacuum. The radiation force has a significant effect on the atoms since the peak absorption cross-section is much greater than the physical size of the atom. Now, it is convenient to describe the absorption process in terms of photons. When atoms absorb photons, then each absorbed photon gives the atom a kick in the opposite direction of its motion, and spontaneously-emitted photons scatter in all directions so that the scattering of many photons gives an average force which slows down the atom. The value of this scattering force, being equal to the rate at which the absorbed photons impart momentum to the atom, is given by

$$F_s = \hbar k \times R_{scatt} \quad (\text{D.1.2})$$

where $\hbar k$ is the momentum of the photon. R_{scatt} is the scattering rate and is given by,

$$R_{scatt} = \Gamma_2 \rho_{22} = \frac{\Gamma_2}{2} \frac{\frac{\Omega_{12}^2}{2}}{\delta^2 + \frac{\Omega_{12}^2}{2} + \frac{\Gamma_2^2}{4}} \quad (\text{D.1.3})$$

with Γ_2 as the spontaneous decay rate and ρ_{22} is the excited state population of a two-level atom (discussed in chapter 3). The Rabi frequency (Ω_{12}) and the saturated intensity (I_{sat}) are related by $\frac{I}{I_{sat}} = \frac{2\Omega_{12}^2}{\Gamma_2^2}$. Now Eq.(D.1.2) can be written as,

$$F_s = \hbar k \frac{\Gamma_2}{2} \frac{\frac{I}{I_{sat}}}{1 + \frac{I}{I_{sat}} + \frac{4\delta^2}{\Gamma_2^2}} \quad (\text{D.1.4})$$

Thus for $I \rightarrow \infty$, the magnitude of the scattering force given in Eq.(D.1.4) tends to a maximum value of $F_{max} = \hbar k \frac{\Gamma_2}{2}$. For an atom of mass M , this radiation force gives maximum magnitude of acceleration (a_{max}) as,

$$a_{max} = \frac{F_{max}}{M} = \frac{\hbar k \Gamma_2}{2M} = \frac{v_r}{\tau} \quad (\text{D.1.5})$$

with τ as the lifetime of the excited state and the magnitude of the recoil velocity $v_r = \frac{\hbar k}{M} = \frac{h}{\lambda M}$ is the change in the velocity of atom for absorption or emission of a photon at wavelength λ .

D.1.2 Doppler cooling: Optical molasses

Doppler cooling technique [65, 67] uses the radiation pressure force to reduce the kinetic energy of the atoms. This technique is understandable considering three simple cases shown in the Fig.D.1.

Consider an atom cloud constrained to move in one dimension with two red detuned laser beams (Laser 1 and Laser 2) of frequency ω_L incident from either side of the atom cloud. Now for the atom at rest, photons from both the laser beams will be absorbed

equally by the atom as shown in the Fig.D.1(a), where $|1\rangle$ and $|2\rangle$ are the two energy states of the atom. Due to collection of the equal number of photons from each beam, the atom experiences an equal force in each direction, or we can say that the atom experiences the same frequency ω_L from the two lasers.

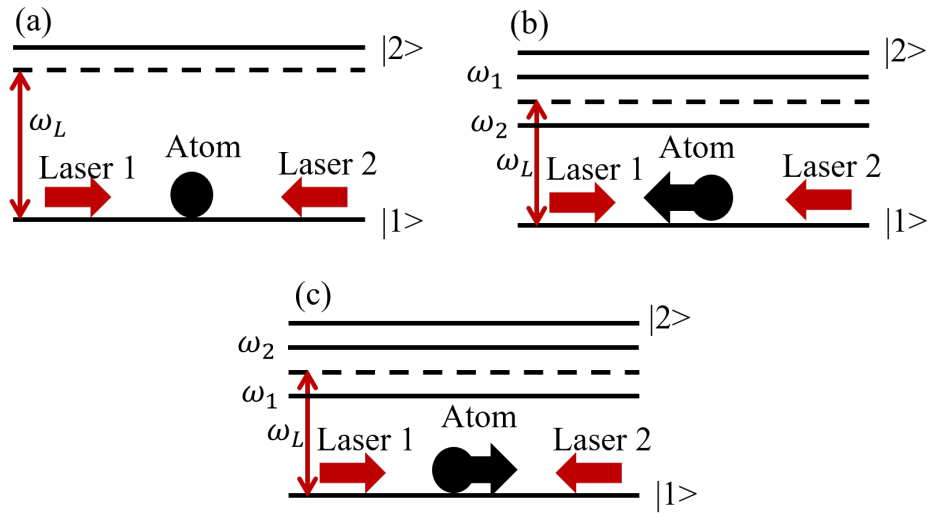


Figure D.1: Three simple cases when an atom constrained to move in one dimension interacts with two laser beams of equal frequency incident from either side of the atom : (a) atom at rest, (b) atom moving left and (c) atom moving right.

For the atom having a velocity, it experiences different frequencies from Laser 1 and Laser 2 due to the ‘Doppler shift’. If the atom is moving to the left, it sees Laser 1 with increased frequency $\omega_1 = (\omega_L + kv)$ as it is moving against Laser 1. While it experiences Laser 2 with decreased frequency $\omega_2 = (\omega_L - kv)$ because it is moving in the direction of Laser 2 as shown in Fig.D.1(b). Therefore, the atom will absorb more photons from Laser 1 than that from Laser 2. Absorbing more photons from Laser 1 effectively reduces its leftward velocity while absorbing fewer photons from Laser 2 indicates that it cannot be accelerated to the left.

Similarly, if the atom is moving to the right, it experiences Laser 1 with decreased

frequency $\omega_1 = (\omega_L - kv)$ and Laser 2 with increased frequency $\omega_2 = (\omega_L + kv)$ as shown in Fig.D.1(c). It means that the atom does not absorb nearly as many photons from Laser 1 as it does from Laser 2. It indicates that the rightward velocity of the atom is reduced and it cannot be accelerated to the right. By this process, the laser light always reduces the velocities of the atoms, but never increase them.

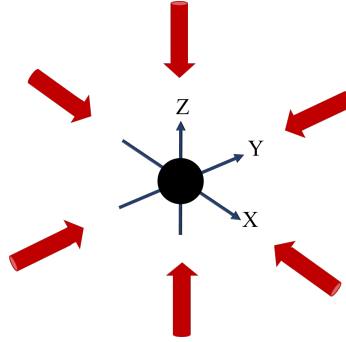


Figure D.2: Configuration for optical molasses.

Since in reality, atoms have velocities in all directions; the above idea is extended in three dimensions to reduce their temperature. This requires laser cooling with the configuration of three orthogonal standing waves, as shown in the Fig.D.2. When three pairs of laser beams propagate from each direction in space and converge on a single point, the atoms interacted with the beams are slowed down from each direction in space. The atomic sample begins to cool as the velocities of the atoms in the sample decrease. Here, the three pairs of counter-propagating beams behave like a thick liquid that hinders the motions of the atoms. Thus this situation is referred to as “optical molasses”. It attenuates the motion of the atoms in every direction in space and cools the sample.

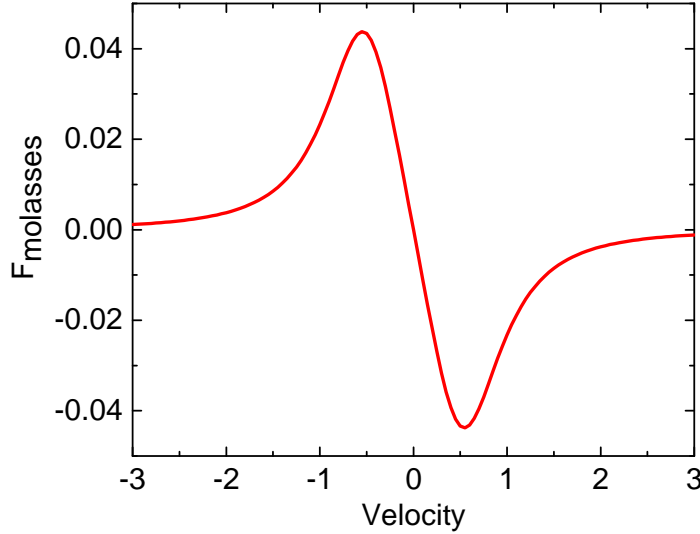


Figure D.3: The total force as a function of velocity in 1D optical molasses technique for $\delta = -\Gamma_2/2$. The force is plotted in units of $\hbar k\Gamma_2/2$, and the velocity is in units of Γ_2/k .

Considering the scattering force due to each laser beam, the above analysis of the 1D case can be quantified. The magnitude of the net force acting on an atom moving with velocity v due to two counter-propagating laser beams is given by [65, 67],

$$F_{molasses} = F_s(\omega_L - \omega_0 - kv) - F_s(\omega_L - \omega_0 + kv) \approx -2kv \frac{\partial F}{\partial \omega} = -\eta v \quad (\text{D.1.6})$$

where the damping coefficient, $\eta = 2k \frac{\partial F}{\partial \omega}$ is given by,

$$\eta = 4\hbar k^2 \frac{I}{I_{sat}} \frac{-\frac{2\delta}{\Gamma_2}}{[1 + (\frac{2\delta}{\Gamma_2})^2]^2} \quad (\text{D.1.7})$$

The damping coefficient requires a positive value. It implies $\delta = (\omega - \omega_0)$ should be negative, therefore for this purpose we need red detuned laser beams. From the above equations, we can say that for $v > 0$, $F_{molasses}$ will be negative and vice versa. So, the force decelerates the atoms. Analyzing the above equation one can get the lowest temperature, which is known as the ‘‘Doppler cooling limit’’, when the detuning, $\delta = -\Gamma_2/2$. The lowest

temperature is given as,

$$k_B T_D = \hbar \Gamma_2 / 2 \quad (\text{D.1.8})$$

In the Fig.D.3 we have plotted the magnitude of the force with $\delta = -\Gamma_2/2$ as a function of the magnitude of velocity. For very small v , the total force is linear with a negative slope. For ^{87}Rb with D_2 transition line, $\Gamma_2/2\pi = 6$ MHz, the estimated lowest temperature is $T_D = 140 \mu\text{K}$.

D.1.3 Magneto-optical Trap (MOT)

In the optical molasses technique, cold atoms, accumulating in the region where the three orthogonal pairs of laser beams intersect, take a considerable time for atoms to diffuse out. With the proper choice of polarizations for the laser beams, this configuration can be turned into a trap by the addition of a magnetic field gradient. In MOT, using a pair of anti-Helmholtz coils produces a quadrupole magnetic field which in turn creates an imbalance in the scattering forces of the laser beams, and it is the radiation force that strongly confines the atoms [66, 127].

To understand the principles of MOT [65, 67] let us consider the Fig.D.4(a) for $J = 0 \rightarrow J = 1$ transition. In this case, the magnetic field produced by the anti-Helmholtz coils is zero at the middle point of the distance between the coils and close to this zero, due to uniform field gradient, the Zeeman effect makes the energy of the sub-levels of $J = 1$ to vary linearly with the atom position as shown in the Fig.D.4(a). Here, the counter-propagating laser beams have opposite circular polarization along with slightly less frequency than the atomic resonance frequency. Now, consider an atom displaced from the centre of the trap along the z -axis with $z > 0$. The $\Delta M_J = -1$ transition move

closer to the resonance with the laser frequency.

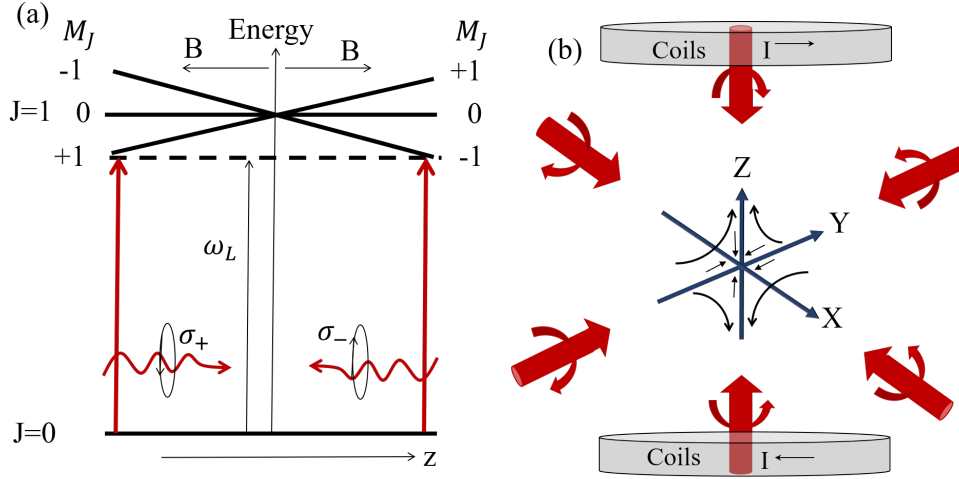


Figure D.4: (a) The mechanism of a magneto-optical trap illustrated for the case of an atom with $J = 0$ to $J = 1$ transition. In the magnetic field gradient, the Zeeman splitting of the sub-levels depends on the atom's position. (b) Configuration of a magneto-optical trap with three orthogonal pairs of laser beams which have the requisite circular polarization states and intersect at the centre of a pair of coils carrying opposite currents. The small arrows indicate the direction of the quadrupole magnetic field produced by the coils.

The selection rules favour the atom to absorb photons from the σ_- polarized laser beam and this pushes the atom back towards the trap centre generating a scattering force. A similar process happens for the displacement of the atom in the $z < 0$ direction. Here, the Zeeman shift of the transition frequency and the selection rules leads to absorption of photons from the σ_+ polarized beam; as a result, the atom is pushed back to the $z = 0$ position. Therefore here, the magnitude of the net force acting on the atom is given by [65, 67],

$$F_{MOT} = -\eta v - \frac{\eta \zeta}{k} z \quad (\text{D.1.9})$$

Therefore, from the Eq.(D.1.9) we can say that in case of MOT, the imbalance in the radiation force caused by the Zeeman effect generates a restoring force with a spring

constant $\frac{\eta\zeta}{k}$, where η is the damping coefficient as discussed in case of optical molasses, $\zeta = \frac{g\mu_B}{\hbar} \frac{dB}{dz}$ is related to the gradient of the magnetic field. So, atoms that enter the region of the intersection of the laser beams are slowed by optical molasses technique, and the position-dependent force pushes the cold atoms towards the trap centre. This combination of strong damping and trapping makes the magneto-optical trap to work. The configuration of the MOT with three-orthogonal pairs of circularly polarized laser beams with a pair of anti-Helmholtz coils is shown in the Fig.D.4(b).

D.1.4 Assembling vacuum chamber

The chamber, where the Rb atom will be loaded, should have ultra-high vacuum ($\sim 10^{-9}$ mbar) conditions. To achieve this, we have used different vacuum pumps. Rotary vane pump was used as a backing pump of a turbo molecular pump. The rotary pump has two filters connected at its output and input, respectively: 1. oil mist filter to prevent the leakage of the pump's oil vapour in the atmosphere, 2. oil trap filter to prevents the pump's oil from entering the turbo pump as the rotary pump is attached at the outlet of the turbo pump. We have used a magnetic isolator valve between the rotary and the turbo pumps and a pneumatic gate valve which allows us to isolate the vacuum chamber from the turbo pumping station. The isolation valve would protect the pumps from oil backstreaming if the roughing pump failed. In that case, the pressure would build behind the turbo pump and eventually leak into the chamber, possibly bringing in contaminants. If the turbo pump fails or there is a leakage in the chamber due to an accident, air with debris would rush in. Then the high-speed closure of the gate valve would be needed to limit the contaminants from being sucked into the vacuum chamber. This valve has a

gate that comes down fast and seals against the valve wall powered by air pressure (~ 80 psi). When the Pirani gauge pressure, connected at the outlet of the turbo pump, read 5×10^{-2} mbar, we opened the gate valve.

After that, the turbo pump was turned on. With the help of a penning gauge, the pressure inside the chamber read 1.03×10^{-7} mbar after the turbo attained full speed and ran for a few hours. After running for a day, we started baking out the whole system while the turbo pump was still on. We wrapped the vacuum chambers and the metal part of the turbo pump by heating tape and then by aluminium foil. A thermometer was used to monitor the temperature of the vacuum chamber with time. The MOT chamber was baked out for about 48 hrs upto 140°C temperature. On backing, the pressure inside the chamber will rise due to outgassing. This rise in pressure will subside with time, and the vacuum inside the chamber will get better. We baked the chamber till the time we observed no further fall in the pressure. When we stopped the process of baking out the system, the pressure of the chamber was 2×10^{-7} mbar. Baking out the system to such a high temperature to achieve low pressure while it is being pumped makes sure that the atoms and molecules stuck to the interior walls of the chamber will be removed before MOT becomes operational. It makes the bake out a necessary process for pumping the vacuum chamber down to pressures as low as possible before the MOT can begin trapping. After the successful bake-out process, we achieved 1.34×10^{-8} mbar pressure inside the chamber with only turbo pump running. Then we turned on the ion pump to get even lower pressure, and with the ion pump gauge, we read the lowest pressure as 3.2×10^{-9} mbar.

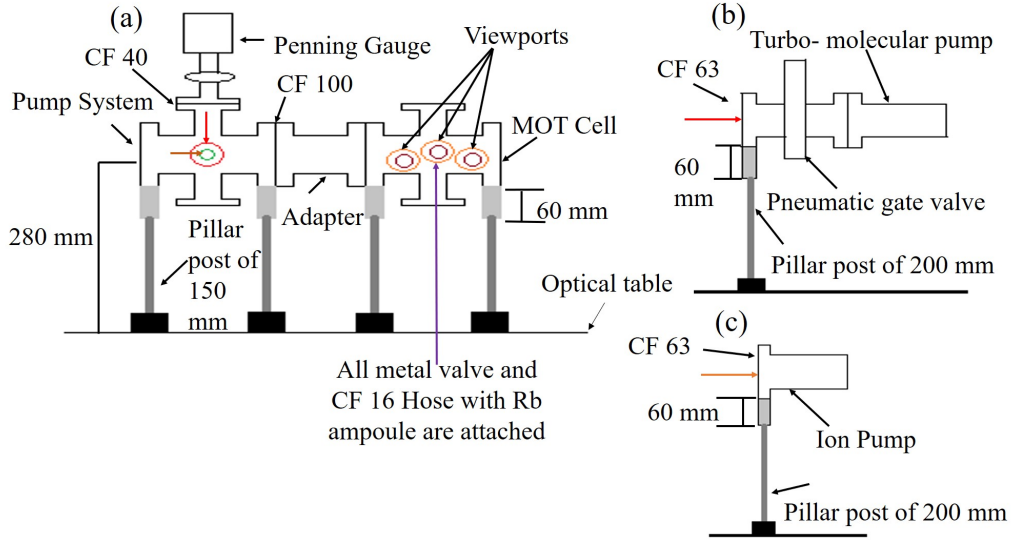


Figure D.5: (a)-(c) Schematic diagrams of the vacuum system with the MOT chamber. The ports of the MOT chamber, where these two pumps are attached, are indicated with red and orange arrows respectively in (a).

Fig.D.5(a)-(c) shows a schematic view of our design to attach the vacuum pumps with our MOT chamber. We have also used an interlock circuit connecting the rotary pump, turbo pump and the gate valve.

D.1.5 Interlock to operate the turbo pump and the gate valve

We have used an interlock circuit connecting the rotary pump, turbo pump and the gate valve. A relay circuit (say, relay A) is connected between the backing gauge of gauge controller and the turbo controller. 5×10^{-2} mbar and 8×10^{-2} mbar pressure readings are set as low and as high limit of the relay A respectively. A schematic circuit diagram is shown in the Fig.D.6(a). When the backing pressure is in 5×10^{-2} mbar via operation of the rotary pump, then the ‘NC’ (normally closed) contact opens, and turbo starts. When the turbo speeds up, the backing goes bad. If the pressure goes higher than 8×10^{-2} mbar,

the turbo controller shows the pumping unit error (PUE), and turbo turns off. Turbo restarts again only if the backing falls to 5×10^{-2} mbar. In all the above conditions, turbo pumping unit remains switched on along with the gauge controller.

There are two modes to open the pneumatic gate valve - (i) 'auto mode' and (ii) 'bypass mode'. Fig.D.6(b) shows the required circuit schematically. +24 V DC is taken from the gauge controller first to the relay C which is connected with vacuum chamber penning gauge of the gauge controller. The low and high limits are set as 5×10^{-5} mbar of the relay C. When the pressure inside the chamber is better than this, 'NO' (normally open) contact of the relay is closed, and 24 V reaches the turbo controller for full-speed contact. When the turbo reaches 80% of its maximum speed, another relay K1 inside the turbo controller closes, and 24 V comes to the coil of the gate valve relay. The coil is activated at this point and 220 V AC from the mains which is connected to 'NO', now on the closing of contact, comes live at the gate valve output and thus opens the gate valve. It is interlock operation in 'auto mode'.

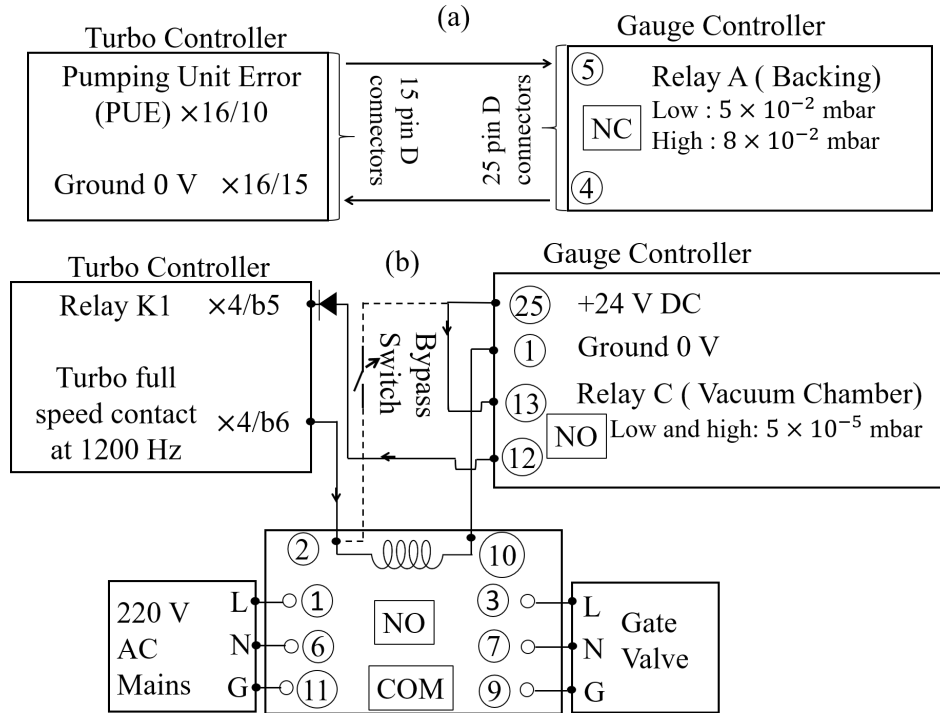


Figure D.6: Schematic diagram of home-made turbo interlock circuit. (a) Interlock for backing and (b) interlock to open the gate valve.

When power comes back after an occasional power cut, all the above logic needs to be satisfied for the gate valve to open. In ‘bypass mode’, 24 V is directly connected to the gate valve relay coil through a switch. Whenever the bypass switch is closed, the gate valve opens irrespective of the turbo and pressure conditions. But the gauge controller must always be switched on for 24V DC supply. This mode is used for initial pumping out of the chamber. In this case, without putting on the turbo, we open the gate valve, do a slow and controlled roughing of the chamber through the rotary pump. We have to get 5×10^{-2} mbar at the backing side to deactivate the PUE in turbo controller and start it. This interlock is not bypassed even in the ‘bypass mode’.

D.1.6 Design and calibration of the anti-Helmholtz coils

For the position-dependent magnetic field, we have designed a pair of anti-Helmholtz coils with 15.5 cm diameter and 15.4 cm distance between the two coils. We have simulated the magnetic field generated by the coils along its axis.

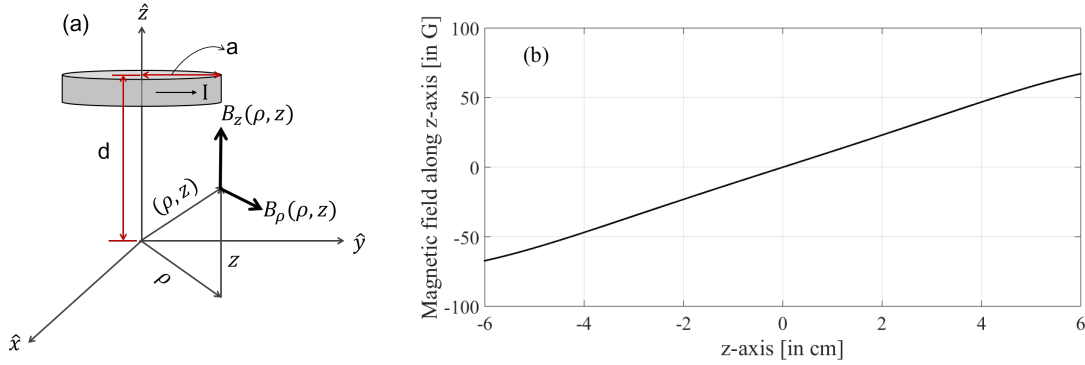


Figure D.7: (a) Cylindrical coordinates for the magnetic field of a circular coil carrying current I at the axial position (z - direction). (b) The magnetic field along the axis of the pair of anti-Helmholtz coils.

The magnetic field at a distance d along the axis of a circular coil of radius a carrying current I as shown in Fig.D.7(a) has magnetic field components given by [128]

$$B_z = \frac{\mu_0 n I}{2\pi} \frac{1}{\sqrt{(a + \rho)^2 + (z - d)^2}} \left[K(k^2) + \frac{R^2 - \rho^2 - (z - d)^2}{(a + \rho)^2 + (z - d)^2} E(k^2) \right] \quad (\text{D.1.10})$$

$$B_\rho = \frac{\mu_0 n I}{2\pi} \frac{(z - d)}{\rho \sqrt{(a + \rho)^2 + (z - d)^2}} \left[-K(k^2) + \frac{R^2 + \rho^2 - (z - d)^2}{(a + \rho)^2 + (z - d)^2} E(k^2) \right] \quad (\text{D.1.11})$$

Here, $k^2 = \frac{4a\rho}{(a + \rho)^2 + (z - d)^2}$, $K(k^2)$ and $E(k^2)$ are the first and second kind of elliptical integrals respectively [129]. Using Eq.(D.1.10) and Eq.(D.1.11), we have simulated the magnetic field along the axis of the coils with the number of turns $n = 170$ and current $I = 6.0$ A in each coil. The simulation gives the field gradient as 10.8 G/cm and the field variation along the axis (z direction) of the anti-Helmholtz coils is shown in the Fig.D.7(b).

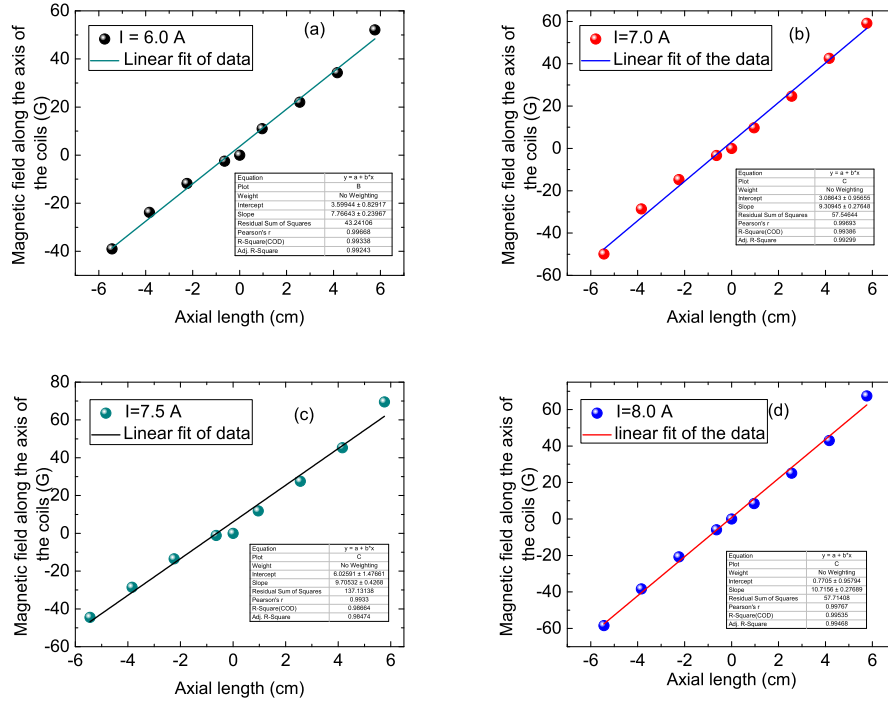


Figure D.8: Calibration of the magnetic field along the axial length of the coils in anti-Helmholtz configuration with current (a) $I = 6.0$ A, (b) $I = 7.0$ A, (c) $I = 7.5$ A, (d) $I = 8.0$ A.

We have fabricated the spools of the coils from our institute workshop. The winding of copper wire on the spools was done from the workshop of Variable Energy Cyclotron Centre (VECC), Kolkata. We have calibrated the coils in the anti-Helmholtz configuration for the separation between the coil as 15.4 cm with different sets of current through the coils by a Hall-probe with accuracy 0.01 Gauss. The calibrations are shown in the Fig.D.8. For $I = 8.0$ A we got field gradient as 10.7 G/cm.

D.1.7 Optical path for MOT

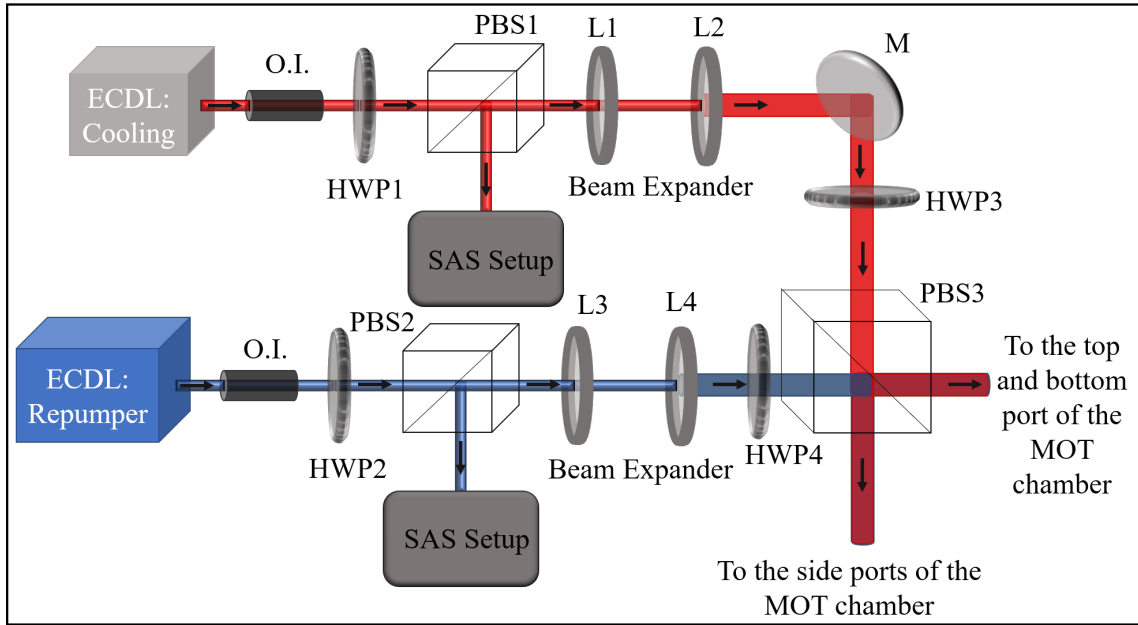


Figure D.9: Schematic presentation of the optical path from lasers to the MOT chamber. ECDC: External cavity diode laser, O.I.: Optical isolator, HWP: Half wave plate, PBS: Polarizing beam splitting cube, L: Lens, M: Mirror, SAS Setup: Saturation absorption spectroscopy setup.

I was also involved in the planning of the optical path for this purpose. Fig.D.9 represents a schematic view of the required optical path for developing MOT. We plan to take the cooling and the repumper beams from two separate ECDCs (From Moglabs:CEL002/780 and Toptica:DL100). Our required cooling transition is $F = 2 \rightarrow F' = 3$ of ^{87}Rb and the repumper beam will be locked at $F = 1 \rightarrow F' = 2$. For this, two separate SAS setups are corresponding to two ECDCs. 5% of the intensity of the beams is taken for SAS, and the rest is for MOT setup. The cooling and the repumper beams are expanded 3 times compared with initial beams' sizes. Both of the beams are mixed in PBS3. The intensities of the reflected and the transmitted part of the cooling beams are adjusted

with the help of the HWP3 as shown in the Fig.D.9.



Figure D.10: An image of the MOT setup in our laboratory.

The reflected part of the cooling beam is sent to the bottom port of the MOT chamber after making the beams circularly polarized with a quarter-wave plate (QWP). The counter-propagating beam from the top port is made opposite circularly polarized by the process of retro-reflection of the beam from the bottom port using another QWP. The transmitted part of the cooling beam is sent to the two mutually perpendicular side ports of the chamber with circular polarization created with the help of two individual QWPs. Here also the counter-propagating beams from the two opposite ports become opposite-circularly polarized with retro-reflection from a pair of mirrors and QWPs. The repumper beams follow the MOT cooling beams with the same polarization. The height of the laser beams will be adjusted accordingly to the positions of the viewports of the MOT chamber. A CCD camera is fitted to take the image of the cold Rb cloud.

Fig.D.10 shows the image of the MOT setup in our lab. Once our atom source is

ready, we can move forward to observe the cold atom with the proper characterization of its temperature using the camera and other necessary apparatus.

Bibliography

- [1] “Observation and theoretical simulation of dispersive properties of an electromagnetically induced transparent ^{87}Rb atomic medium”, A. Das, B.C. Das, S. Chakrabarti, D. Bhattacharyya and S. De, *Laser Phys.*, **2018**, *28(12)*,125205.
- [2] “Polarization rotation with electromagnetically induced transparency in a V-type configuration of Rb D_1 and D_2 transitions”, A. Das, B.C. Das, D. Bhattacharyya, S. Chakrabarti and S. De, *J. Phys. B: At. Mol. Opt. Phys.*, **2018**, *51(17)*,175502.
- [3] “Angular dependency of the polarization rotation in a coherent atomic medium”, A. Das, B.C. Das, D. Bhattacharyya and S. De, *J. Phys. B At. Mol. Opt. Phys.*, **2020**, *53(2)*,25502.
- [4] “Effects of probe ellipticity and longitudinal magnetic field on the polarization rotation in a coherently prepared atomic medium”, A. Das, B. Chandra Das, D. Bhattacharyya and S. De, *OSA Continuum*, **2021**, *4(1)*,105.
- [5] “An experimental method for the observation of r.f. transitions and laser beat resonances in oriented Na vapour”, G. Alzetta, A. Gozzini, L. Moi and G. Orriols, *Il Nuovo Cimento B Series 11*, **1976**, *36(1)*,5–20.
- [6] “Nonabsorption hyperfine resonances in a sodium vapour irradiated by a multimode dye-laser”, G. Alzetta, L. Moi and G. Orriols, *Il Nuovo Cimento B Series 11*, **1979**, *52(2)*,209–218.
- [7] “Coherent population trapping in cesium: Dark lines and coherent microwave emission”, J. Vanier, A. Godone and F. Levi, *Phys. Rev. A*, **1998**, *58(3)*,2345–2358.
- [8] “Coherent population trapping in a Λ configuration coupled by magnetic dipole interactions”, H. Kim, H.S. Han, T.H. Yoon and D. Cho, *Phys. Rev. A*, **2014**, *89(3)*,032507.

- [9] “Observation of electromagnetically induced transparency”, K.-J. Boller, A. Imamoglu and S.E. Harris, *Phys. Rev. Lett.*, **1991**, *66(20)*,2593–2596.
- [10] “Nonlinear optical processes using electromagnetically induced transparency”, S.E. Harris, J.E. Field and A. Imamoglu, *Phys. Rev. Lett.*, **1990**, *64(10)*,1107–1110.
- [11] “Observation of electromagnetically induced transparency in collisionally broadened lead vapor”, J.E. Field, K.H. Hahn and S.E. Harris, *Phys. Rev. Lett.*, **1991**, *67(22)*,3062–3065.
- [12] “Electromagnetically induced transparency: Optics in coherent media”, M. Fleischhauer, A. Imamoglu and J.P. Marangos, *Rev. Mod. Phys.*, **2005**, *77(2)*,633–673.
- [13] “Electromagnetically induced absorption and transparency due to resonant two-field excitation of quasidegenerate levels in Rb vapor”, A.M. Akulshin, S. Barreiro and A. Lezama, *Phys. Rev. A - At. Mol. Opt. Phys.*, **1998**, *57(4)*,2996–3002.
- [14] “Electromagnetically induced absorption”, A. Lezama, S. Barreiro and A.M. Akulshin, *Phys. Rev. A*, **1999**, *59(6)*,4732–4735.
- [15] “Simultaneous observations of electromagnetically induced transparency (EIT) and absorption (EIA) in a multi-level V-type system of ^{87}Rb and theoretical simulation of the observed spectra using a multi-mode approach”, B.C. Das, D. Bhattacharyya, A. Das, S. Chakrabarti and S. De, *J. Chem. Phys.*, **2016**, *145(22)*,224312.
- [16] “Interplay between electromagnetically induced transparency (EIT), absorption (EIA), and Autler-Townes (AT) splitting in an N -type atomic system: experiment and theory”, B.C. Das, A. Das, D. Bhattacharyya, S. Chakrabarti and S. De, *OSA Continuum*, **2019**, *2(3)*,994.
- [17] “Stark Effect in Rapidly Varying Fields”, S.H. Autler and C.H. Townes, *Phys. Rev.*, **1955**, *100(2)*,703–722.
- [18] “Probing, quantifying, and freezing coherence in a thermal ensemble of atoms”, A.W. Laskar, N. Singh, P. Adhikary, A. Mukherjee and S. Ghosh, *Optica*, **2018**, *5(11)*,1462.
- [19] “Observation of continuous-wave self-oscillation due to pressure-induced two-wave mixing in sodium”, D. Grandclément, G. Grynberg and M. Pinard, *Phys. Rev.*

- Lett.*, **1987**, 59(1),40–43.
- [20] “Lasers without inversion: Interference of lifetime-broadened resonances”, S.E. Harris, *Phys. Rev. Lett.*, **1989**, 62(9),1033–1036.
- [21] “Atomic coherence effects within the sodium D_1 line: Lasing without inversion via population trapping”, E.S. Fry, X. Li, D. Nikonov, G.G. Padmabandu, M.O. Scully, A.V. Smith et al., *Phys. Rev. Lett.*, **1993**, 70(21),3235–3238.
- [22] “Lasing without inversion and enhancement of the index of refraction via interference of incoherent pump processes”, M. Fleischhauer, C. Keitel, M. Scully and C. Su, *Opt. Commun.*, **1992**, 87(3),109–114.
- [23] “Lasing without inversion”, J. Mompert and R. Corbalán, *J. Opt. B Quantum Semiclassical Opt.*, **2000**, 2(3),R7–R24.
- [24] “Doppler-Free Laser Polarization Spectroscopy”, C. Wieman and T.W. Hänsch, *Phys. Rev. Lett.*, **1976**, 36(20),1170–1173.
- [25] “Frequency Stabilization of a Laser Diode with Use of Light-Induced Birefringence in an Atomic Vapor”, Y. Yoshikawa, T. Umeki, T. Mukae, Y. Torii and T. Kuga, *Appl. Opt.*, **2003**, 42(33),6645.
- [26] “Optical control of Faraday rotation in hot Rb vapor”, P. Siddons, C.S. Adams and I.G. Hughes, *Phys. Rev. A*, **2010**, 81(4),043838.
- [27] “Phase-controlled optical Faraday rotation in a closed-loop atomic system”, M. Veisi, A. Vafafard and M. Mahmoudi, *J. Opt. Soc. Am. B*, **2015**, 32(1),167–172.
- [28] “I. Experimental researches in electricity.—Nineteenth series”, M. Faraday, *Philosophical Transactions of the Royal Society of London*, **1846**, 136,1–20.
- [29] “Laser field induced birefringence and enhancement of magneto-optical rotation”, A.K. Patnaik and G. Agarwal, *Opt. Commun.*, **2000**, 179(1-6),97–106.
- [30] “Coherent control of magneto-optical rotation in inhomogeneously broadened medium”, A.K. Patnaik and G. Agarwal, *Opt. Commun.*, **2001**, 199(1-4),127–142.
- [31] “Coherent control of magneto-optic rotation”, K. Pandey, A. Wasan and V. Nataraajan, *J. Phys. B: At. Mol. Opt. Phys.*, **2008**, 41(22),225503.
- [32] M.O. Scully and M.S. Zubairy, *Quantum Optics*, Cambridge University Press (1997).

- [33] S. Stenholm, *Foundations of laser spectroscopy*, Wiley series in pure and applied optics, Wiley (1984).
- [34] “Colloquium: Trapping and manipulating photon states in atomic ensembles”, M.D. Lukin, *Rev. Mod. Phys.*, **2003**, *75(2)*,457–472.
- [35] “Atomic clocks based on coherent population trapping: a review”, J. Vanier, *Appl. Phys. B*, **2005**, *81(4)*,421–442.
- [36] “High-sensitivity magnetometer based on index-enhanced media”, M.O. Scully and M. Fleischhauer, *Phys. Rev. Lett.*, **1992**, *69(9)*,1360–1363.
- [37] “Optical magnetometry”, D. Budker and M. Romalis, *Nat. Phys.*, **2007**, *3(4)*,227–234.
- [38] “Vector magnetometry based on electromagnetically induced transparency in linearly polarized light”, V.I. Yudin, A.V. Taichenachev, Y.O. Dudin, V.L. Velichansky, A.S. Zibrov and S.A. Zibrov, *Phys. Rev. A*, **2010**, *82(3)*,033807.
- [39] “Measurements of the magnetic field vector using multiple electromagnetically induced transparency resonances in Rb vapor”, K. Cox, V.I. Yudin, A.V. Taichenachev, I. Novikova and E.E. Mikhailov, *Phys. Rev. A*, **2011**, *83(1)*,015801.
- [40] “Coherent Optical Detection of Highly Excited Rydberg States Using Electromagnetically Induced Transparency”, A.K. Mohapatra, T.R. Jackson and C.S. Adams, *Phys. Rev. Lett.*, **2007**, *98(11)*,113003.
- [41] “Temporal and Spatial Interference between Four-Wave Mixing and Six-Wave Mixing Channels”, Y. Zhang, U. Khadka, B. Anderson and M. Xiao, *Phys. Rev. Lett.*, **2009**, *102(1)*,13601.
- [42] “Quantum interface between light and atomic ensembles”, K. Hammerer, A.S. Sørensen and E.S. Polzik, *Rev. Mod. Phys.*, **2010**, *82(2)*,1041–1093.
- [43] “Light speed reduction to 17 metres per second in an ultracold atomic gas”, L.V. Hau, S.E. Harris, Z. Dutton and C.H. Behroozi, *Nature*, **1999**, *397(6720)*,594–598.
- [44] “Two-color polarization spectroscopy of rubidium”, P. Kulatunga, H.C. Busch, L.R. Andrews and C.I. Sukenik, *Opt. Commun.*, **2012**, *285(12)*,2851–2853.

-
- [45] “Polarization spectroscopy of an excited state transition”, C. Carr, C.S. Adams and K.J. Weatherill, *Opt. Lett.*, **2012**, *37(1)*,118–120.
- [46] “Onset of a collisional modification of the Faraday effect in a high-density atomic gas”, M. Kristensen, F.J. Blok, M.A. Van Eijkelenborg, G. Nienhuis and J.P. Wierdman, *Phys. Rev. A*, **1995**, *51(2)*,1085–1096.
- [47] “Resonant nonlinear magneto-optical effects in atoms”, D. Budker, W. Gawlik, D.F. Kimball, S.M. Rochester, V.V. Yashchuk and A. Weis, *Rev. Mod. Phys.*, **2002**, *74(4)*,1153–1201.
- [48] “Analysis of Resonant Voigt Effect.”, M. Yamamoto and S. Murayama, *J. Opt. Soc. Am.*, **1979**, *69(5)*,781–786.
- [49] “The Voigt effect in a dilute atomic vapour”, F. Schuller, M.J. Macpherson, D.N. Stacey, R.B. Warrington and K.P. Zetie, *Opt. Commun.*, **1991**, *86(2)*,123–127.
- [50] “Laser frequency stabilization by polarization spectroscopy of a reflecting reference cavity”, T.W. Hansch and B. Couillaud, *Optics Commun.*, **1980**, *35(3)*,441–444.
- [51] “Laser frequency offset locking by marrying modulation sideband with the two-color polarization spectroscopy in a ladder-type atomic system”, B. Yang, J. Wang, H. Liu, J. He and J. Wang, *Opt. Commun.*, **2014**, *319*,174–177.
- [52] “An analytical model for two-beam excited F2+-like color center laser”, B. Lin, *Optics Commun.*, **1996**, *124(3-4)*,400–407.
- [53] “Magnetometry based on nonlinear magneto-optical rotation with amplitude-modulated light”, S. Pustelny, A. Wojciechowski, M. Gring, M. Kotyrba, J. Zachorowski and W. Gawlik, *J. Appl. Phys.*, **2008**, *103(6)*,063108.
- [54] “Linear and nonlinear magneto-optical rotation on the narrow strontium intercombination line”, K. Pandey, C.C. Kwong, M.S. Pramod and D. Wilkowski, *Phys. Rev. A*, **2016**, *93(5)*,53428.
- [55] “Optimized ultra-narrow atomic bandpass filters via magneto-optic rotation in an unconstrained geometry”, J. Keaveney, S.A. Wrathmall, C.S. Adams and I.G. Hughes, *Opt. Lett.*, **2018**, *43(17)*,4272–4275.
- [56] “Optically controlled waveplate at a telecom wavelength using a ladder transition

- in Rb atoms for all-optical switching and high speed Stokesmetric imaging”, S. Krishnamurthy, Y. Tu, Y. Wang, S. Tseng and M. Shahriar, *Opt. Express*, **2014**, *22(23)*,28898.
- [57] “Low-frequency vacuum squeezing via polarization self-rotation in Rb vapor”, E.E. Mikhailov and I. Novikova, *Opt. Lett.*, **2008**, *33(11)*,1213–1215.
- [58] “Polarization squeezing of light by single passage through an atomic vapor”, S. Barreiro, P. Valente, H. Failache and A. Lezama, *Phys. Rev. A*, **2011**, *84(3)*,33851.
- [59] “Nonlinear optical magnetometry with accessible in situ optical squeezing”, N. Otterstrom, R.C. Pooser and B.J. Lawrie, *Opt. Lett.*, **2014**, *39(22)*,6533–6536.
- [60] “Studies of Electromagnetically Induced Transparency in Thallium Vapor and Possible Utility for Measuring Atomic Parity Nonconservation”, A.D. Cronin, R.B. Warrington, S.K. Lamoreaux and E.N. Fortson, *Phys. Rev. Lett.*, **1998**, *80(17)*,3719–3722.
- [61] “Electron-spin-reversal phenomenon in optically pumped rubidium”, E.B. Norrgard, D. Tupa, J.M. Dreiling and T.J. Gay, *Phys. Rev. A*, **2010**, *82(3)*,33408.
- [62] “Mimicking Faraday Rotation to Sort the Orbital Angular Momentum of Light”, W. Zhang, Q. Qi, J. Zhou and L. Chen, *Phys. Rev. Lett.*, **2014**, *112(15)*,153601.
- [63] “A gigahertz-bandwidth atomic probe based on the slow-light Faraday effect”, P. Siddons, N.C. Bell, Y. Cai, C.S. Adams and I.G. Hughes, *Nat. Photonics*, **2009**, *3(4)*,225–229.
- [64] “Birefringence lens effects of an atom ensemble enhanced by an electromagnetically induced transparency”, H.R. Zhang, L. Zhou and C.P. Sun, *Phys. Rev. A*, **2009**, *80(1)*,013812.
- [65] C.J. Foot, *Atomic physics*, Oxford master series in physics, Oxford University Press (2005).
- [66] “Laser cooling and trapping of atoms: Introduction”, S. Chu and C. Wieman, *J. Opt. Soc. Am. B*, **1989**, *6(11)*,2020–2022.
- [67] H. Metcalf and P. van der Straten, *Laser Cooling and Trapping*, Graduate Texts in Contemporary Physics, Springer New York (2001).
- [68] “A simple extended-cavity diode laser”, A.S. Arnold, J.S. Wilson and M.G. Boshier,

- Review of Scientific Instruments*, **1998**, 69(3),1236–1239.
- [69] “Littrow configuration tunable external cavity diode laser with fixed direction output beam”, C.J. Hawthorn, K.P. Weber and R.E. Scholten, *Review of Scientific Instruments*, **2001**, 72(12),4477–4479.
- [70] “Spectrally narrow pulsed dye laser without beam expander”, M.G. Littman and H.J. Metcalf, *Applied Optics*, **1978**, 17(14),2224.
- [71] “A compact extended-cavity diode laser with a littman configuration”, Sang Eon Park, Taeg Yong Kwon, Eun-joo Shin and Ho Seong Lee, *IEEE Transactions on Instrumentation and Measurement*, **2003**, 52(2),280–283.
- [72] H. Ghafouri-Shiraz, *Distributed Feedback Laser Diodes and Optical Tunable Filters*, Wiley (2003).
- [73] “Using diode lasers for atomic physics”, C.E. Wieman and L. Hollberg, *Rev. Sci. Instrum.*, **1991**, 62(1),1–20.
- [74] “Doppler-free saturated absorption: Laser spectroscopy”, D.W. Preston, *Am. J. Phys.*, **1996**, 64(11),1432–1436.
- [75] “Narrowing of Doppler and hyperfine line shapes of Rb - D2 transition using a Vortex beam”, B.C. Das, D. Bhattacharyya and S. De, *Chem. Phys. Lett.*, **2016**, 644,212–218.
- [76] V. Natarajan, *Modern Atomic Physics*, CRC Press (2015).
- [77] “Magnetic resonance for nonrotating fields”, F. Bloch and A. Siegert, *Phys. Rev.*, **1940**, 57(6),522–527.
- [78] “Rubidium 87 D Line Data”, D.A. Steck, *Rubidium 87 D Line Data, version 2.2.1*, 2019, . <http://www.steck.us/alkalidata/rubidium87numbers.pdf>.
- [79] “Rubidium 85 D Line Data”, D.A. Steck, *Rubidium 85 D Line Data, version 2.2.1*, 2019, . <http://www.steck.us/alkalidata/rubidium85numbers.pdf>.
- [80] “Effects of configuration interaction on intensities and phase shifts”, U. Fano, *Phys. Rev.*, **1961**, 124(6),1866–1878.
- [81] “Decaying-dressed-state analysis of a coherently driven three-level Λ system”, P. Anisimov and O. Kocharovskaya, *J. Mod. Opt.*, **2008**, 55(19-20),3159–3171.
- [82] “Objectively discerning Autler-Townes splitting from electromagnetically induced

- transparency”, P.M. Anisimov, J.P. Dowling and B.C. Sanders, *Phys. Rev. Lett.*, **2011**, 107(16),163604.
- [83] “Role of dressed-state interference in electromagnetically induced transparency”, S. Khan, V. Bharti and V. Natarajan, *Phys. Lett. A*, **2016**, 380(48),4100–4104.
- [84] M. Fox, *Quantum Optics: An Introduction*, Oxford Master Series in Physics, OUP Oxford (2006).
- [85] “Measurement of Dispersive Properties of Electromagnetically Induced Transparency in Rubidium Atoms”, M. Xiao, Y.-q. Li, S.-z. Jin and J. Gea-Banacloche, *Phys. Rev. Lett.*, **1995**, 74(5),666–669.
- [86] “Steep dispersion and group velocity below $\frac{c}{3000}$ in coherent population trapping”, O. Schmidt, R. Wynands, Z. Hussein and D. Meschede, *Phys. Rev. A*, **1996**, 53,R27–R30.
- [87] “Dispersive properties of electromagnetically induced transparency”, S.E. Harris, J.E. Field and A. Kasapi, *Phys. Rev. A*, **1992**, 46(1),R29–R32.
- [88] “Measurement of dispersive profile of a multiwindow electromagnetically induced transparency spectrum in a doppler-broadened atomic medium”, D.X. Khoa, L.C. Trung, P.V. Thuan, L.V. Doai and N.H. Bang, *J. Opt. Soc. Am. B*, **2017**, 34(6),1255–1263.
- [89] “Coherent signal amplification of refractive index spectrum in rubidium vapor using phase-shifting interferometry”, C.-Y. Liu and D.-J. Han, *J. Opt. Soc. Am. B*, **2016**, 33(6),1298.
- [90] “Pulse delay and group velocity dispersion measurement in v-type electromagnetically induced transparency of hot ^{85}Rb atom”, B.C. Das, D. Bhattacharyya, A. Das, S. Saha, S. Chakrabarti and S. De, *J. Phys. B: At. Mol. Opt. Phys.*, **2018**, 51(24),245501.
- [91] “Electromagnetically induced transparency and slow light in V-type three-level system of GaAs/AlGaAs multiple quantum wells”, W. Yan, X.-M. Li, T. Wang, C.-B. Dong and Y.-J. Jin, *J. Lumin.*, **2013**, 135(1),254–258.
- [92] “Electromagnetically induced transparency and retrieval of light pulses in a Λ -type and a V-type level scheme in $\text{Pr}^{3+}:\text{Y}_2\text{SiO}_5$ ”, F. Beil, J. Klein, G. Nikoghosyan

- and T. Halfmann, *J. Phys. B: At. Mol. Opt. Phys.*, **2008**, *41*(7),074001.
- [93] “Narrowing of electromagnetically induced transparency resonance in a Doppler-broadened medium”, A. Javan, O. Kocharovskaya, H. Lee and M.O. Scully, *Phys. Rev. A*, **2002**, *66*(1),013805.
- [94] “Buffer-gas-induced linewidth reduction of coherent dark resonances to below 50hz”, S. Brandt, A. Nagel, R. Wynands and D. Meschede, *Phys. Rev. A*, **1997**, *56*(2),R1063–R1066.
- [95] “Electromagnetically induced transparency in paraffin-coated vapor cells”, M. Klein, M. Hohensee, D.F. Phillips and R.L. Walsworth, *Phys. Rev. A - At. Mol. Opt. Phys.*, **2011**, *83*(1),013826.
- [96] “Quantum sensitivity limits of an optical magnetometer based on atomic phase coherence”, M. Fleischhauer and M.O. Scully, *Phys. Rev. A*, **1994**, *49*(3),1973–1986.
- [97] “High-sensitivity optical faraday magnetometry with intracavity electromagnetically induced transparency”, Q. Zhang, H. Sun, S. Fan and H. Guo, *J. Phys. B: At. Mol. Opt. Phys.*, **2016**, *49*(23),235503.
- [98] “Cavity-enhanced room-temperature high sensitivity optical Faraday magnetometry”, H. Sun, Y. Lei, S. Fan, Q. Zhang and H. Guo, *Phys. Lett. A*, **2017**, *381*(3),129–135.
- [99] “Two-color polarization spectroscopy in V-type configuration in rubidium”, E.H. Cha, T. Jeong and H.-R. Noh, *Opt. Commun.*, **2014**, *326*,175–179.
- [100] “Polarization-rotation resonances with subnatural widths using a control laser”, S.R. Chanu, K. Pandey, V. Bharti, A. Wasan and V. Natarajan, *Europhys. Lett.*, **2014**, *106*(4),43001.
- [101] “Polarization effects in the interaction between multi-level atoms and two optical fields”, R. Colín-Rodríguez, J. Flores-Mijangos, S. Hernández-Gómez, R. Jáuregui, O. López-Hernández, C. Mojica-Casique et al., *Phys. Scr.*, **2015**, *90*(6),068017.
- [102] “A laser spectroscopy system with combined absorption, polarization rotation and fluorescence detection to study two photon transitions in atomic rubidium”, O. López-Hernández, S. Hernández-Gómez, F.S. Ponciano-Ojeda, C. Mojica-

- Casique, R. Colín-Rodríguez, J. Flores-Mijangos et al., *J. Appl. Res. Technol.*, **2015**, *13(6)*,543–550.
- [103] “Coherence effects in electromagnetically induced transparency in V-type systems of 87Rb”, H.-J. Kang and H.-R. Noh, *Opt. Express*, **2017**, *25(18)*,21762–21774.
- [104] “Balanced detection for low-noise precision polarimetric measurements of optically active, multiply scattering tissue phantoms”, D. Cote and I.A. Vitkin, *J. Biomed. Opt.*, **2004**, *9(1)*,213.
- [105] “Thirteen pump-probe resonances of the sodium **D1** line”, V. Wong, R.W. Boyd, C.R. Stroud, R.S. Bennink and A.M. Marino, *Phys. Rev. A*, **2003**, *68(1)*,012502.
- [106] “Velocity-selective resonance dips in the probe absorption spectra of Rb D 2 transitions induced by a pump laser”, S. Chakrabarti, A. Pradhan, A. Bandyopadhyay, A. Ray, B. Ray, N. Kar et al., *Chem. Phys. Lett.*, **2004**, *399(1-3)*,120–124.
- [107] “Continuous-wave electromagnetically induced transparency: A comparison of V, Λ , and cascade systems”, D.J. Fulton, S. Shepherd, R.R. Moseley, B.D. Sinclair and M.H. Dunn, *Phys. Rev. A*, **1995**, *52(3)*,2302–2311.
- [108] “Resonant gain suppression and quantum destructive interference in a three-level open V system”, C.-L. Cui, J.-K. Jia, Y. Zhang, Y. Xue, H.-L. Xu and J.-H. Wu, *J. Phys. B: At. Mol. Opt. Phys.*, **2011**, *44(21)*,215504.
- [109] “Optically Written Waveguide in an Atomic Vapor”, A.G. Truscott, M.E.J. Friese, N.R. Heckenberg and H. Rubinsztein-Dunlop, *Phys. Rev. Lett.*, **1999**, *82(7)*,1438–1441.
- [110] “Theory of electromagnetically induced waveguides”, R. Kapoor and G.S. Agarwal, *Phys. Rev. A*, **2000**, *61(5)*,53818.
- [111] “Continuous generation of delayed light”, S. Smartsev, D. Eger, N. Davidson and O. Firstenberg, *J. Phys. B: At. Mol. Opt. Phys.*, **2017**, *50(21)*,215003.
- [112] “Angular dependence of an electromagnetically induced transparency resonance in a Doppler-broadened atomic vapor”, P.R.S. Carvalho, L.E.E. de Araujo and J.W.R. Tabosa, *Phys. Rev. A*, **2004**, *70(6)*,63818.
- [113] “Angular dependence of Dicke-narrowed electromagnetically induced transparency resonances”, M. Shuker, O. Firstenberg, R. Pugatch, A. Ben-Kish, A. Ron and

- N. Davidson, *Phys. Rev. A*, **2007**, *76*(2),23813.
- [114] “Über magnetische Beeinflussung der Polarisation der Resonanzfluoreszenz”, W. Hanle, *Zeitschrift für Physik D Atoms, Molecules and Clusters*, **1991**, *18*(1),5–10.
- [115] “Effect of ellipticity on Hanle electromagnetically induced absorption and transparency resonances with longitudinal and transverse magnetic fields”, N. Ram, M. Pattabiraman and C. Vijayan, *Phys. Rev. A*, **2010**, *82*(3),033417.
- [116] “Tuning of the Hanle effect from EIT to EIA using spatially separated probe and control beams”, M. Bhattarai, V. Bharti and V. Natarajan, *Sci. Rep.*, **2018**, *8*(1),7525.
- [117] “Coherent population trapping with losses observed on the Hanle effect of the D₁ sodium line”, F. Renzoni, W. Maichen, L. Windholz and E. Arimondo, *Phys. Rev. A*, **1997**, *55*(5),3710–3718.
- [118] “Observation of coherent population trapping in a V-type two-electron system”, A.K. Singh and V. Natarajan, *New J. Phys.*, **2015**, *17*(3),33044.
- [119] “Birefringence enhancement via quantum interference in the presence of a static magnetic field”, A. Morteza pour, A. Saleh and M. Mahmoudi, *Laser Phys.*, **2013**, *23*(6),65201.
- [120] “Magnetic resonance in the Faraday-rotation noise spectrum”, E.B. Aleksandrov and V.S. Zapasskil, *Sov. Phys. J. Exp. Thero. Phys.*, **1981**, *54*(1),64–67.
- [121] “Spin-noise spectroscopy: from proof of principle to applications”, V.S. Zapasskii, *Advances in Optics and Photonics*, **2013**, *5*(2),131.
- [122] “Measurements of spin properties of atomic systems in and out of equilibrium via noise spectroscopy”, M. Swar, D. Roy, D. D, S. Chaudhuri, S. Roy and H. Ramachandran, *Opt. Express*, **2018**, *26*(24),32168.
- [123] “Faraday rotation assisted by linearly polarized light”, J.M. Choi, J.M. Kim and D. Cho, *Phys. Rev. A*, **2007**, *76*(5),53802.
- [124] “Magneto-optical rotation and cross-phase modulation via coherently driven four-level atoms in a tripod configuration”, D. Petrosyan and Y.P. Malakyan, *Phys. Rev. A*, **2004**, *70*(2),023822.

-
- [125] “Controlled polarization rotation of an optical field in multi-Zeeman-sublevel atoms”, S. Li, B. Wang, X. Yang, Y. Han, H. Wang, M. Xiao et al., *Phys. Rev. A*, **2006**, *74*(3),033821.
- [126] “Optimization of slow and stored light in atomic vapor”, I. Novikova, A.V. Gorshkov, D.F. Phillips, Y. Xiao, M. Klein and R.L. Walsworth, *Adv. Opt. Quantum Memories Comput. IV*, **2007**, *6482*,64820M.
- [127] “Radiation force in the magneto-optical trap”, A.M. Steane, M. Chowdhury and C.J. Foot, *J. Opt. Soc. Am. B*, **1992**, *9*(12),2142–2158.
- [128] “Magnetostatic trapping fields for neutral atoms”, T. Bergeman, G. Erez and H.J. Metcalf, *Phys. Rev. A*, **1987**, *35*,1535–1546.
- [129] M. Spiegel, J. Liu and S. Lipschutz, *Mathematical Handbook of Formulas and Tables*, Schaum’s outline of theory and problems, McGraw-Hill (1999).

Thesis Highlights

Name of the Student: Arpita Das

Name of the CI/OCC: Saha Institute of Nuclear Physics **Enrolment No.:** PHYS05201504017

Thesis Title: Study of laser induced coherent phenomena in the Rubidium atomic medium

Discipline: Physical Sciences

Sub-Area of Discipline: Experimental Quantum Optics

Date of viva voce: 23/02/2021

Experiments have been performed to understand different coherent phenomena in multilevel room-temperature and hot Rb atomic vapour. For this purpose, the manipulation of the atomic states was done by applying optical fields and the magnetic field. This research work carries the experimental and the theoretical studies of polarization rotation, slow light with a coherence phenomenon in the atomic medium like electromagnetically induced transparency (EIT). Our goal is to find how the various system parameters affect the above-mentioned phenomenon when light interacts with atoms. Fig.1 describes a general experimental setup we have used for this purpose along with some results. From the experiments, we have found that the angle of polarization in a coherent medium highly depends

on the pump beam intensity, the ellipticity of the probe beam, angular mismatches between the probe and the pump beams. It also depends on the optical depth (OD), the spot size of the pump beam and the external magnetic field. From observations, we have concluded that to get an enhanced polarization rotation or to get an atomic medium with high birefringence, optimization of the pump intensity is needed and the probe beam should be linearly polarized. As angular mismatch between the probe and the pump beams is minimized, the birefringence of the medium will enhance for a higher OD and an optimum value of pump beam spot size. An additional birefringence is created when we applied an external magnetic field along with a circularly polarized pump beam. We have also

observed that the polarization rotation depends non-linearly with the magnetic field. With one of our experiments, we have carried an indirect measurement of group velocity of light with help of Mach-Zehnder interferometer. To understand all the observed phenomenon theoretically, the probe response is calculated in a semi-classical approach. The optical Bloch equations (OBE) for the multilevel atomic system has been solved analytically. The theoretical characteristics show good agreement with experimental observations. Apart from these, qualitative explanations for the experimental observations have also been given in this thesis. Studies contained in this thesis find application in optical locking, storage of light experiments, birefringence atomic lens, magnetometry etc.

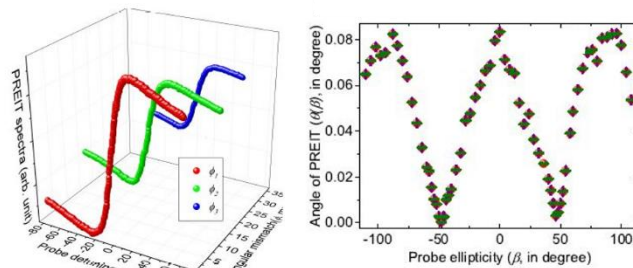
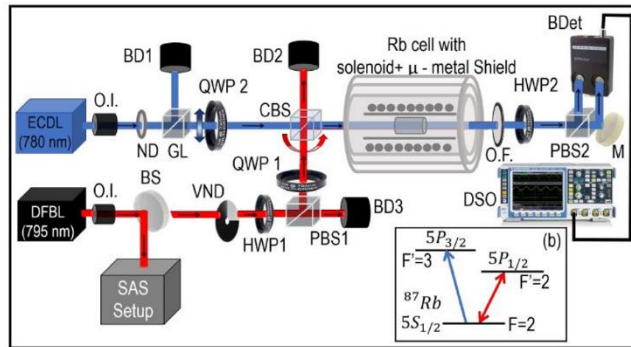


Figure 1: A general experimental setup with some experimental results.